

---

# Field-Resolved Infrared Spectroscopy

From Fundamentals towards Medical  
Applications

Marinus Huber

---



München 2020



---

# **Field-Resolved Infrared Spectroscopy**

From Fundamentals towards Medical  
Applications

**Marinus Huber**

---

Dissertation  
an der Fakultät für Physik  
der Ludwig–Maximilians–Universität  
München

vorgelegt von  
Marinus Huber  
aus Bad Aibling

München, den 21.09.2020

Erstgutachter: Prof. Dr. Ferenc Krausz

Zweitgutachter: Prof. Dr. Jürgen Popp

Tag der mündlichen Prüfung: 27. November 2020



# Zusammenfassung

Die Infrarotspektroskopie ist ein mächtiges und vielseitiges Werkzeug zur Untersuchung (organischer) Proben. Mittels einer einzigen berührungslosen Messung lassen sich umfangreiche Informationen über die molekulare Zusammensetzung einer Probe gewinnen. Diese Tatsache hat dazu geführt, dass die Infrarotspektroskopie für eine Vielzahl von biologischen, chemischen und medizinischen Anwendungen eingesetzt wird, unter anderem für die (Atem-)Gasanalyse, die Quantifizierung von klinischen Parametern in Blutproben, die Detektion von Sprengstoffen und für die Identifizierung von Mikroorganismen.

Ein besonders praxisrelevantes Anwendungsfeld der Infrarotspektroskopie ist die Analyse des molekularen Fingerabdrucks von menschlichem Blutserum/-plasma zur Krebsfrüherkennung. Obwohl bereits vielversprechende Ergebnisse bei verschiedenen Krebsarten unter Verwendung konventioneller Fourier-Transform-Infrarotspektroskopie (kurz FTIR-Spektroskopie) erzielt worden sind, muss die Effizienz der Krebserkennung noch deutlich gesteigert werden, um einen breiten Einsatz in der klinischen Praxis zu ermöglichen. Eine der Hauptlimitierungen dieser und vieler anderer Anwendungen der Infrarotspektroskopie ist die begrenzte molekulare Empfindlichkeit und Spezifität konventioneller Infrarotspektroskopie aufgrund der verfügbaren Lichtquellen und Infrarotdetektoren. Als Folge können nur hochkonzentrierte Bestandteile einer (Blut-)Probe mittels eines molekularen Fingerabdrucks erfasst werden, was wiederum die Effizienz der Krebserkennung potenziell einschränkt. Die vorliegende Dissertation befasst sich mit der Entwicklung, Untersuchung und Anwendung einer neuartigen, spektroskopischen Methodik – der feldaufgelösten Infrarotspektroskopie (*field-resolved spectroscopy*, kurz FRS) – und zeigt in Theorie und Experiment das Potenzial der FRS zur Überwindung der oben genannten Einschränkungen auf.

Im ersten Teil der Arbeit werden technische, experimentelle, konzeptionelle und theoretische Aspekte der feldaufgelösten Metrologie präsentiert und im Detail diskutiert. Die Fähigkeit, elektrische Felder von impulsiv angeregten Molekülschwingungen mittels elektro-optischer Abtastung direkt zu messen, eröffnet bisher unerschlossene Möglichkeiten für die Aufnahme von Fingerabdrücken komplexer nativer molekularer Ensembles. Vibrationsangeregte Moleküle emittieren ein kohärentes elektrisches Feld im Nachklang einer ultrakurzen Infrarot-Laseranregung, welches spezifisch für die molekulare Zusammensetzung der Probe ist. Es wird gezeigt, dass solche feldaufgelösten molekulare Fingerabdrücke (*electric-field-resolved molecular fingerprints*, kurz EMFs) mittels einer auf Empfindlichkeit optimierten elektro-optischen Abtastung direkt bis hinunter zu Feldstärken gemessen werden kann, die  $10^7$ -mal schwächer als die der Anregung sind. Zudem erlaubt die sowohl zeit- als auch feldaufgelöste Messung eine Abgrenzung vom durch die Anregung erzeugten und eigentlichen molekularen Signal. Letzteres kann somit praktisch ohne den um Größenordnungen stärkeren Hintergrund des Anregungspulses aufgenommen werden. Damit ist es erstmals möglich, auch schwächste Signale zu erfassen, die bei Anregung von in Flüssigkeiten (wie z.B. Blutserum) gelösten Molekülen im sub- $\mu\text{g}/\text{ml}$ -Bereich entstehen. Dies entspricht einer Empfindlichkeitssteigerung gegenüber kommerziellen FTIR-Spektrometern um mehr als den Faktor 40.

Darüber hinaus wird theoretisch und experimentell gezeigt, dass sich FRS insbesondere für die Untersuchung von stark absorbierenden Proben eignet. Dies lässt sich zu einen auf den Intensitätsdynamikbereich von mehr als 10 Größenordnungen und zum anderen auf die direkte Messung des elektrischen Feldes zurückführen. Letzteres impliziert, dass das Messsignal

linear mit der Feldstärke skaliert. Im Gegensatz zu einer Intensitätsskalierung, wie sie bei herkömmlicher Infrarotspektroskopie vorliegt, kann durch Feldstärkenskalierung eine erhöhte molekulare Empfindlichkeit über einen signifikant vergrößerten Bereich von Probendicken realisiert werden. Dadurch war es zum ersten Mal möglich, intakte lebendige Systeme mit Dicken in der Größenordnung von 0,1 Millimetern zu durchleuchten, was eine breitbandige infrarotspektroskopische Untersuchung von menschlichen Zellen und Pflanzenblättern erlaubt. FRS verspricht eine verbesserte molekulare Empfindlichkeit für die Untersuchung komplexer, realer biologischer und medizinischer Fragestellungen.

Der zweite Teil der Dissertation befasst sich mit der ersten praxisnahen Anwendung der FRS zur Krankheitsdiagnostik in der Onkologie mittels Flüssigkeitsbiopsie.

In einem ersten, vorbereitenden Schritt wurden hierfür unter Verwendung herkömmlicher FTIR Spektroskopie die Arbeitsabläufe zur Messung von flüssigen Serums- und Plasmaproben im Hinblick auf die Reproduzierbarkeit optimiert und die biologische Variabilität über die Zeit von molekularen Infrarot-Fingerabdrücken von gesunden, nicht-symptomatischen Probanden untersucht. Die erfassten Infrarot-Fingerabdrücke erwiesen sich über klinisch relevante Zeitskalen als hochstabil und lieferten eine Vielzahl von personenspezifischen spektralen Markern, mit denen individuelle molekulare Phänotypen erkannt und über die Zeit verfolgt werden können. Dieses bisher unbekanntes Maß an zeitlicher Stabilität und Spezifität von blutbasierten spektralen Infrarot-Fingerabdrücken bildet die Grundlage für ihre künftige Anwendung zur Gesundheits- und Krankheitsüberwachung.

Im darauffolgenden Abschnitt der Arbeit wird über die Ergebnisse einer ersten klinischen Machbarkeitsstudie berichtet, bei welcher die EMFs von flüssigem Blutserum von mehr als dreihundert Individuen mittels FRS erfasst worden sind. Algorithmen des maschinellen Lernens ermöglichten die Isolierung von Infrarotsignaturen, die aufschlussreich für die Unterscheidung von Proben von Patienten mit nicht-metastasierten Brust-, Prostata- und Lungenkarzinomen und von sorgfältig auf diese abgestimmten Kontrollpersonen sind. Die Detektionseffizienz im Bereich von 0,63-0,84 (Fläche unter der ROC-Kurve) übersteigt systematisch die Effizienz der FTIR-Spektroskopie, wenn sie auf dieselben Proben angewendet wird. Dies ist ein erster experimenteller Hinweis darauf, dass sich die verbesserte molekulare Empfindlichkeit der FRS direkt in einer höheren Effizienz bei der Erkennung von Krankheitsbildern niederschlägt. Die vorliegenden Daten belegen, dass die kohärenten elektrischen Felder, die von impulsiv angeregten Biomolekülen im Blut ausgehen, robust und zuverlässig als informative EMFs erfasst werden können. Abgesehen davon, dass sie zur Krebserkennung beitragen, dürften sie ganz allgemein neue Möglichkeiten für die künftige Phänotypisierung von Biofluiden eröffnen.

Aufgrund der bereits erzielten Ergebnisse und des Potentials die Empfindlichkeit der nächsten Generation von FRS um mehr als zwei Größenordnungen zu erhöhen, verspricht FRS sowohl existierende Anwendungen wie die Analyse von molekularen Fingerabdrücken von Blut zur Krankheitsdiagnostik weiter zu verbessern, als auch komplett neue Anwendungsbereiche in der Untersuchung von intakten biologischen Systemen zu erschließen.

# Abstract

Infrared spectroscopy is a powerful and versatile tool for the investigation of (organic) specimen. With a single non-invasive measurement, extensive information about the molecular composition of a sample can be obtained. This fact has prompted infrared spectroscopy to be employed for a wide range of biological, chemical and medical applications, including (respiratory) gas analysis, quantification of clinical parameters in blood samples, detection of explosives, and identification of microorganisms.

A particularly relevant practical application of infrared spectroscopy is the analysis of infrared molecular fingerprints of human blood serum/plasma for early cancer detection. Although promising results have already been reported for various types of cancer entities using conventional Fourier-transform infrared (FTIR) spectroscopy, the efficiency of cancer detection still needs to be significantly improved in order to enable broad application in clinical practice. One of the main challenges for this particular and many other applications of infrared spectroscopy is the limited molecular sensitivity and specificity of conventional infrared spectroscopy due to the restrictions imposed by the available light sources and infrared detectors. As a result, only highly concentrated components of a (blood) sample can be detected by molecular fingerprinting, which in turn potentially limits the efficiency of cancer detection. The present dissertation addresses the development, investigation, and application of a novel spectroscopic method – *field-resolved spectroscopy* (FRS) – and demonstrates in theory and experiment the potential of FRS to overcome the above-mentioned limitations.

In the first part of the thesis technical, experimental, conceptual, and theoretical aspects of field-resolved metrology are presented and discussed in detail. The ability to directly measure electric fields of impulsively-excited molecular vibrations by means of electro-optic sampling (EOS) opens up hitherto untapped potential for the fingerprinting of complex native molecular ensembles. Vibrationally-excited molecules emit a coherent electric field in the wake of an ultrashort infrared laser excitation, which is specific for the molecular composition of a sample. It is demonstrated that such *electric-field-resolved molecular fingerprints* (EMFs) can be measured directly down to field strengths  $10^7$ -times weaker than the excitation by employing electro-optic sampling optimised for sensitivity. In addition, a measurement, which is both time- and field-resolved, enables separation between the impulsive excitation and the coherent molecular response. The latter can thus be recorded practically without the background of the orders-of-magnitude stronger excitation pulse. As a result, it is now possible to detect even the faintest signals that are generated when molecules solved in liquids (such as blood serum) in the sub- $\mu\text{g}/\text{ml}$  range are excited. This corresponds to a sensitivity increase of more than a factor 40 compared to commercial FTIR spectrometers.

Furthermore, it is shown theoretically and experimentally that FRS is particularly suitable for the measurement of highly absorbent samples. This can be attributed to an intensity dynamic range of more than 10 orders of magnitude as well as to the ability to directly measure the electric field. The latter implies that the measurement signal scales linearly with the field strength. In contrast to intensity-scaling, which is a typical feature of conventional infrared spectroscopy, field-scaling enables to achieve increased molecular sensitivity over a significantly extended range of sample thicknesses. This made it possible for the first time to transilluminate intact living systems with thicknesses in the order of 0.1 millimetres, enabling broadband infrared spectroscopic examination of human cells and intact plant leaves. FRS promises

improved molecular sensitivity for the investigations of complex, real-world biological and medical problems.

The second part of the dissertation is devoted to the first practical application of FRS for disease detection in cancer diagnostics using liquid biopsies.

In a first, preparatory step, the workflows for the measurement of human liquid serum and plasma samples were optimised with regard to reproducibility using conventional FTIR spectroscopy. Furthermore, the biological variability of molecular infrared fingerprints of healthy, non-symptomatic subjects was investigated over time. The recorded infrared fingerprints proved to be highly stable over clinically relevant time scales and provided a variety of person-specific spectral markers that can be used to identify individual molecular phenotypes and track them over time. This previously unknown temporal stability and specificity of individual biochemical fingerprints forms the basis for future applications in health and disease monitoring.

The subsequent section of the thesis reports on the results of a first clinical proof-of-principle study in which EMFs of liquid blood sera of more than three hundred individuals were recorded with FRS. Machine learning algorithms enabled isolation of infrared signatures that are instructive for distinguishing samples of patients with therapy-naïve non-metastatic breast, prostate, and lung carcinoma from those of carefully-matched control individuals. Detection efficiencies in the range of 0.63-0.84 (area under the receiver operating characteristic curve) systematically exceeds the efficiency of FTIR spectroscopy when applied to the same samples. This is a first experimental indication that the improved molecular sensitivity of FRS directly translates into higher efficiency in the detection of disease patterns. The reported data builds evidence that the coherent electric fields emanating from impulsively-excited biomolecules in blood can be robustly and reliably captured as informative EMFs. Beyond contributing to the detection of cancer, they are likely to provide, more generally, a new framework for future phenotyping of biofluids.






Based on the achieved results and the potential to increase the sensitivity of the next generation of field-resolved spectrometers by more than two orders of magnitude, FRS holds the promise to further improve existing applications, such as the analysis of molecular fingerprints of human blood for disease diagnosis, as well as pave the way for entirely new areas of applications in the investigation of intact biological systems.

# List of included Publications

1. **M. Huber**, W. Schweinberger, F. Stutzki, J. Limpert, I. Pupeza, and O. Pronin, “*Active intensity noise suppression for a broadband mid-infrared laser source*”, *Optics Express* **25**, 22499-22509 (2017) [10.1364/OE.25.022499](https://doi.org/10.1364/OE.25.022499). – included as section 2.1
2. I. Pupeza, **M. Huber**, M. Trubetskov, W. Schweinberger, S. Hussain, C. Hofer, K. Fritsch, M. Poetzlberger, L. Vamos, E. Fill, T. Amotchkina, K. Kepesidis, A. Apolonski, N. Karpowicz, V. Pervak, O. Pronin, F. Fleischmann, A. Azzeer, M. Žigman and F. Krausz, “*Field-resolved infrared spectroscopy of biological systems*”, *Nature* **557**, 52-59 (2020) [10.1038/s41586-019-1850-7](https://doi.org/10.1038/s41586-019-1850-7). – included as section 2.2
3. **M. Huber**, M. Trubetskov, S. Hussain, W. Schweinberger, C. Hofer and I. Pupeza, “*Optimum sample thickness for trace analyte detection with field-resolved infrared spectroscopy*”, *Analytical Chemistry* **91**, 7508-7514 (2020) [10.1021/acs.analchem.9b05744](https://doi.org/10.1021/acs.analchem.9b05744). – included as section 2.3
4. **M. Huber**, K. Kepesidis, L. Voronina, M. Božić, M. Trubetskov, N. Harbeck, F. Krausz and M. Žigman, “*Stability of person-specific blood-based infrared molecular fingerprints opens up prospects for health monitoring*”, *Nature Communications* **12**, 1511 (2021) [10.1038/s41467-021-21668-5](https://doi.org/10.1038/s41467-021-21668-5). – included as section 3.1



# Contents

<b>Zusammenfassung</b>	<b>v</b>
<b>Abstract</b>	<b>vii</b>
<b>List of Publications</b>	<b>ix</b>
<b>1 Introduction and Motivation</b>	<b>1</b>
1.1 The power of infrared spectroscopy . . . . .	1
1.2 Pushing the limits of infrared spectroscopy . . . . .	5
1.3 Application of infrared spectroscopy to biofluid analysis and disease detection	8
1.3.1 Quantitative analysis of biofluids . . . . .	8
1.3.2 Functionalized infrared sensors and chips . . . . .	9
1.3.3 Infrared fingerprinting . . . . .	10
1.4 Research goals and structure of the thesis . . . . .	15
<b>2 Field-Resolved Spectroscopy</b>	<b>17</b>
2.1  Active intensity noise suppression for a broadband mid-infrared laser source	17
2.2  Field-resolved infrared spectroscopy of biological systems . . . . .	30
2.3  Optimum sample thickness for trace analyte detection with field-resolved infrared spectroscopy . . . . .	73
<b>3 Infrared Fingerprinting for Blood Profiling</b>	<b>87</b>
3.1  Stability of person-specific blood-based infrared molecular fingerprints . . . . .	87
3.2  Electric-field molecular fingerprinting to probe human disease . . . . .	108
<b>4 Conclusions and Outlook</b>	<b>135</b>
4.1 Summary . . . . .	135
4.2 Future of field-resolved spectroscopy . . . . .	139
4.3 Future of electric-field-resolved fingerprinting . . . . .	142
<b>References</b>	<b>145</b>
<b>Danksagung</b>	<b>155</b>





# Introduction and Motivation

## 1.1 The power of infrared spectroscopy

A beautiful property of light-matter interaction is that it allows virtually any material to be studied by means of a non-contact measurement. Based on the specific response of the photons to the sample under scrutiny, insights into biological, chemical, electrical, mechanical or, more generally, material properties can be gained. Thereby the frequencies of the applied electromagnetic radiation determine what kind of information can be gained. For example, the strength of the interaction of X-rays with matter depends mainly on the elemental composition of the material, but not so much on the chemical properties, since the photon energy is much higher than the chemical binding energies [1]. Consequently, X-ray spectra contain information about the different elements within a sample. When moving to the visible range, photon energies get smaller, and electronic transition in the outer orbitals of single atoms and complex molecules can be efficiently excited [1]. Well-known application examples of visible spectroscopy are the identification of chemical elements in atmospheres (e.g. Fraunhofer lines [2]) or the investigation of the photosynthetic electron transport chain [3].

However, linear absorption spectroscopy in the visible range only gives partial insight into the chemical functionality of a sample. To access this information, one has to probe the chemical bonds holding molecules together. In a simplified picture, these bonds can be considered as springs between vibrating atoms. In a quantum mechanical picture, the vibrational modes can be associated with different energy levels. The energy between transitions of different vibrational states typically ranges between 0.4 eV and 0.04 eV, which corresponds to electromagnetic frequencies in the (mid-)infrared spectral range. Whenever the vibrational movement induces a change in the dipole moment of the molecule, it can be directly excited and probed using infrared radiation [4]. Vibrational modes of molecules can also be measured by visible light via the Raman effect [4]. Depending on the type of sample, the measurement conditions, and the questions under investigation, either infrared or Raman spectroscopy offers distinct advantages in the respective situation. A detailed and critical comparison of the two techniques would go beyond the scope of this introduction. For further reading, the interested reader is referred to the relevant literature [5–8].

To understand what kind of information can be obtained by vibrational infrared spectroscopy, it is instructive to examine the simplistic picture of two vibrating atoms connected by a spring in more detail (Fig. 1.1 a). The spring constant  $k$  is determined by the strength of the chemical bond. Considering the reduced mass  $m_{eff}$  ( $1/m_{eff} = 1/m_A + 1/m_B$ ) of both atoms, a classical equation for the movement, expressed as relative distance  $x$  between the atoms, can

be written down as:

$$m_{eff}\ddot{x} + kx = 0 \quad (1.1)$$

In a quantum mechanical description, the energy of the corresponding eigenstates  $E_n$  is given by

$$E_n = \left(n + \frac{1}{2}\right) \frac{h}{2\pi} \sqrt{\frac{k}{m_{eff}}}, \quad (1.2)$$

where  $h$  denotes the Planck constant. For a transition from the ground to the first excited state due to light absorption, a photon energy  $E_{ph}$  with an optical frequency  $\nu$  of

$$E_{ph} = h\nu = \frac{1}{2} \frac{h}{2\pi} \sqrt{\frac{k}{m_{eff}}} \quad (1.3)$$

is required (Fig. 1.1 b).

By analysing this relationship, we can derive basic properties of absorption bands associated with certain vibrational modes. Increasing the mass shifts the absorption frequency to lower frequencies, while a larger ‘spring constant’ – e.g. by replacing a single with double bond – results in a higher absorption frequency. Each combination of spring constant and mass will result in a different eigenfrequency. This simple model example showcases why infrared spectroscopy allows to extract rich chemical information. In actual physical systems, even more factors contribute to the information content of infrared spectra. A molecule with  $N$  atoms has  $3N$  degrees of freedom including translation, rotation, and vibration. Taking into account translational and rotational motion as well as symmetries, the number of vibrational modes is  $3N-5$  for linear and  $3N-6$  for nonlinear molecules [4]. These vibrational modes may also be coupled to rotational energy states, resulting in a multitude of characteristic infrared absorption lines. In addition, each molecular vibration is either damped or dephases according to their specific chemical (e.g. water vs. organic solvents) or physical (e.g. temperature) environment. A detailed explanation and (theoretical) description of this is out of scope for this introduction and has already been extensively covered by others [4, 9, 10].

The aim here is to highlight the fact, that the chemical information about a molecule (strength and type of chemical bonds, mass of atoms that make up the molecules, information about the chemical and physical environment) is encoded in the associated infrared spectra (strength, width, shape, number, and position of the absorption lines). In fact, the information content is so rich, that basically any larger molecule (and even different conformations thereof) has a unique absorption spectrum in the infrared (Figure 1.1 c and d shows a few examples of characteristic infrared spectra for molecules in liquid and gas phase) [4]. Therefore, a carefully performed infrared measurement can reveal qualitative, quantitative, and/or structural information about a sample. In addition, changes in this information can be easily tracked over time, for example to follow protein folding in response to a rise in temperature [4, 9].

For more complex (especially organic) sample compositions, e.g. biological fluids or living cells, the identification and quantification of all constituents eventually becomes impossible due to overlapping spectral bands. However, it has been shown in numerous applications, that the acquired spectra of such samples still deliver highly specific information – a so called *infrared fingerprint* – about the overall chemical makeup, which can be utilized to characterize and classify given samples or sample sets [4, 9, 11]. For example, infrared fingerprints have been

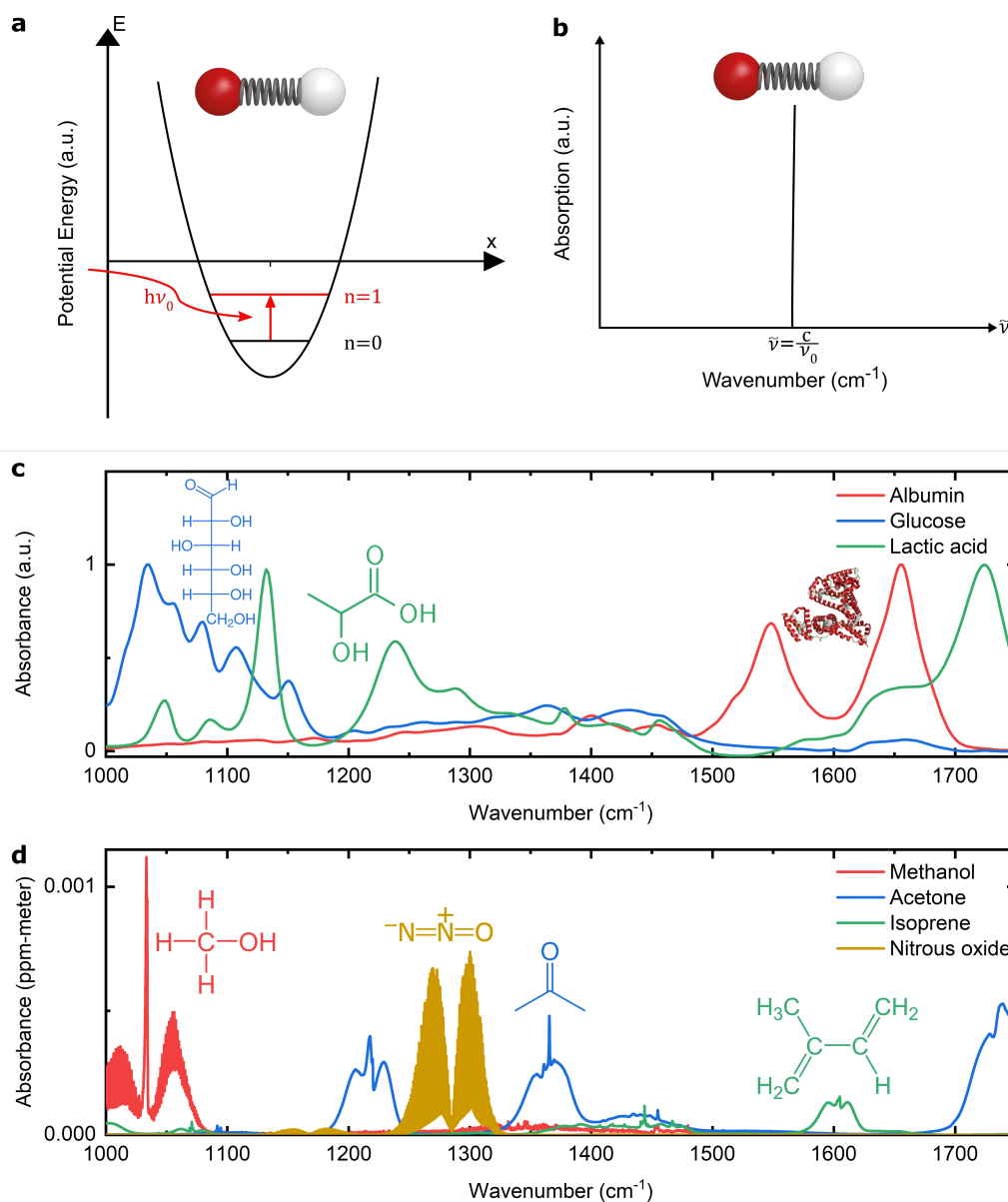


**Figure 1.1:** **a)** In a simplified quantum mechanical picture, a molecular vibration can be described as two atoms connected by a mechanical spring. The corresponding quadratic potential has discrete energy levels. If an infrared photon has an energy equal to the energy difference between the first and ground state, the molecular vibration can be excited and the photon is absorbed. **a)** The absorption spectrum belonging to this model consists of a sharp line at the absorption frequency. **c, d)** In reality, molecules have several chemical bonds that enable a multitude of vibrational, translational, and rotational movements. Therefore, the corresponding infrared spectra can have a large number of absorption lines. In a liquid environment, the vibrational motions dephase rapidly due to collisions and therefore the molecules have a rather broad absorption spectrum. **c)** Shows some examples of this. In contrast, fewer collisions occur in the gas phase, causing the corresponding absorption lines of the gases to be quite narrow, as shown in **d)**. In general, any larger molecule (may it be in the gas phase or liquid phase) offers an unique absorption spectrum in the infrared that can be e.g. used for molecular identification.

used to identify strains of bacteria [12] or cell (pheno-)types [13, 14]. It has also been shown that the analysis of infrared fingerprints of tissue sections or biofluids – such as blood serum – can assist cancer detection [11, 15–18]. Typically, the identification or classification is assisted using machine learning algorithms [11]. Such algorithms are being trained – using fingerprints from samples with known states (e.g. healthy vs. cancerous tissue) – to pick up signatures in the infrared fingerprint that are characteristic for specific sample types correlating with certain physiological states (for more details see also section 1.3).

The aim of this short introduction was to explain the basic idea of the physical principles underlying vibrational infrared spectroscopy and to emphasize why it is a powerful tool for the study, investigation, and characterization of (organic) matter. It can be applied to any type of sample, less and more complex, to living or non-living materials, while providing label-free access to the chemical composition and therefore to the functional makeup of a system as such – regardless of whether the matter of investigation is in hydrated, solid or gas state. As Peter Griffiths once put it so very aptly: “*The number of applications for which a careful measurement of the infrared spectrum will yield important qualitative, quantitative, and/or kinetic information is limited only by the imagination of the user*” [4].

## 1.2 Pushing the limits of infrared spectroscopy

One of the major goals in the development of any spectroscopy technique is to increase the sensitivity to the shot noise limit, which is set by the quantum nature of light. Whether the field-resolved metrology, which is the subject of this thesis, can reach this limit remains to be investigated. However, before discussing the latter in detail, a short overview of the history of infrared spectroscopy is given. Interestingly, in retrospect, it seems that the inherent pursuit of higher sensitivity has already come to a halt several times as the potential for further improvements seemed exhausted. But now, as it has been the case before, after years of stagnation, new technical developments have initiated the process of a further evolutionary leap.

The first commercial infrared spectrometer was released in 1913 and eventually infrared spectroscopy became widespread with the *Perkin-Elmer 21*, a commercial double-beam spectrometer introduced in 1950 [19]. Back then, infrared spectroscopy was mainly used for chemical analysis and structural determination of molecules. However, with the advent of techniques such as two-dimensional nuclear magnetic resonance spectroscopy, X-ray diffraction, and mass spectrometry, the structure of complex molecules is nowadays mostly studied using these methods [4]. In 1973, this fact has led Herbert Laitinen, who was the editor of *Analytical Chemistry* at the time, to make an analogy between the development of an analytical method and Shakespeare's concept of the 'seven ages of man' [20]. A development that spans from the recognition of a physical principle and its experimental validation for measurements in a research environment to the implementation into practical use and gradual commercialization, until it is eventually well recognized and established in a wide scope of applications. But inevitably it will one day reach its 'seventh age', in which "*other methods of greater speed, economy, convenience, sensitivity, selectivity, etc. surpass the method under consideration*" [20]. Laitinen indicated that infrared spectroscopy had reached this stage of development, which can be interpreted to mean that he did not consider infrared spectroscopy to be a relevant competitive technique in the future unless fundamental technical or theoretical developments will cause one of the earlier stages to resurge.

Retrospectively, the conclusion that infrared spectroscopy had already reached its final age would be incorrect, especially when considering that the first commercial Fourier-transform infrared (FTIR) spectrometer was introduced in 1969. Griffiths commented in his book that instead of being in his seventh and final age, infrared spectroscopy was actually in its what he calls 'second childhood', which might be defined as the rejuvenation of the analytical method [21]. The FTIR technology has enabled improvements in many technical aspects, such as greatly increased sensitivity, spectral coverage, reproducibility, and resolution while at the same time increasing the measurement speed. In addition, the FTIR devices became cheaper, smaller, and more user-friendly. Combined with the development of new sampling techniques (e.g. attenuated total reflection, multi-pass-cells, micro-spectroscopy) different sample types could now be easily investigated. This enabled the study of new research questions and has led to many applications in the fields of chemistry, biochemistry, biomedicine, environmental monitoring, and many others. Due to all these aspects, FTIR spectrometry became so dominant that many scientists now consider it equivalent to infrared spectroscopy. At present, nearly fifty years later, FTIR spectrometry is still considered to be the gold standard of infrared spectroscopy.

However, there have not been any substantial technical advances in commercially available FTIR spectrometers within the last twenty years. The initially rapid leaps in the area of improved sensitivity and other technical aspects enabled by the introduction of FTIR technology slowed down once the (fundamental) limits of what can be achieved with thermal sources and liquid-nitrogen cooled detectors were approached [4, 22]. Most likely, this was also the reason why Griffiths wrote, that infrared spectroscopy “*passed from its second childhood into its fifth age*” [4], in which the major steps of development are completed and “*applications are enlarged to an ever-widening scope of areas*” [20].

Although it is indeed a fact that FTIR spectrometers are still widely used, even Griffiths could probably not have foreseen how upcoming new laser-based light sources and new light detection schemes would have the capacity to start another evolutionary step of infrared spectroscopy towards higher sensitivity and its applicability to an even wider range of applications.

Fundamentally, the achievable sensitivity of a spectroscopic method is limited by the shot noise of the employed light source. The single-sided linear spectral density  $s_q$  of the relative quantum power noise is given by

$$s_q = \sqrt{\frac{2hc}{P\lambda}} = 1.9 \cdot 10^{-8} \text{ Hz}^{-0.5} \sqrt{\frac{1 \text{ mW}}{P}} \sqrt{\frac{1064 \text{ nm}}{\lambda}}, \quad (1.4)$$

where  $h$  is the Planck constant,  $c$  the vacuum speed of light,  $P$  is the optical power incident on the detector (assuming a detector quantum efficiency of 1), and  $\lambda$  the wavelength of the radiation [23]. In practice however, current state-of-the-art FTIR spectrometers do not operate even close to shot noise limit and are usually dominated by the detector noise [4]. Since liquid-nitrogen cooled photodetectors already operate close to the limit set by the thermal background [22], the first step towards higher sensitivity is to overcome detector noise and increase the employed light power in a spectroscopic scheme.

Apart from synchrotron sources (which will not be discussed here due to their limited availability, cost, and space requirements), the first competitive alternative to thermal-based sources became quantum cascade lasers (QCLs). Introduced in 1994 [24], they have been becoming cheaper, more compact, user-friendly, and therefore more widely applied [25–29]. Commercially available QCLs are now able to cover the entire mid-infrared (MIR) range (when multiple QCLs are combined) and deliver watt-scale powers. In parallel, coherent supercontinuum and broadband femtosecond sources in the mid-infrared have been developed, which now exceed the brilliance of thermal sources by orders of magnitude [30–33].

With these new MIR sources significant progress in infrared spectroscopy has been achieved. The properties of laser light allow to take advantage of advanced spectroscopic schemes. Multipass-configurations and enhancement cavities can now be realized more efficiently due to the spatial coherence of lasers [34, 35]. In gas spectroscopy, this allows to significantly increase the effective interaction length with the molecules of interest, and therefore enables higher detection sensitivities. By combining two coherent frequency-combs, broadband dual-comb spectroscopy can achieve orders-of-magnitude higher spectral resolution at significantly reduced acquisition times as compared to conventional FTIR spectroscopy [27, 36–38]. At the same time, the increased MIR powers of laser-based sources allow to better tolerate losses due to absorption and scattering [39]. This enables increased sensitivity in micro-spectroscopy or transmission spectroscopy of strongly absorbing or scattering samples by either increasing the effective pathlength or by increasing the number of photons reaching the detector.

Despite these advances, the increased power of MIR sources could not be fully exploited so far [28, 40, 41]. Firstly, a common issue of sensitive MIR photodetectors is their limited intensity dynamic range. Commercially available detectors saturate in the mW-range, limiting the useable MIR power for spectroscopy [22, 37]. Frequency up-conversion detectors [42, 43] with high quantum-efficiency can circumvent this problem to some extent, as orders-of-magnitude more sensitive photoreceivers with larger intensity dynamic ranges are available for visible and near-infrared light. Secondly, even assuming the availability of perfect detectors, most spectrometers would not operate at the shot noise limit, but would be heavily dominated by technical excess noise, such as relative intensity noise or interferometer instabilities. Therefore, many spectroscopic schemes either suppress or circumvent noise by various approaches, such as balanced detection, active stabilization or fast data acquisitions [35, 37, 44–46].

Later in this work, it is discussed in detail and demonstrated how field-resolved spectroscopy (FRS) of few-cycle infrared-laser-excited molecular vibrations is able to address both of the above-mentioned issues simultaneously. Sub-cycle nonlinear gating enables isolation of the molecular response from the orders-of-magnitude stronger excitation. By this, sensitivity limitations imposed by source noise and detector dynamic range can be avoided. As a result, FRS offers – already in its first implementation – a limit of detection of  $200 \text{ ng ml}^{-1}$  dimethylsulfone solved in water, outperforming state-of-the-art FTIR in sensitivity by a factor of 40 [40]. Still, there is substantial room for further improvement. Considering the same light source as used in the experiments mentioned above, a limit of detection of  $0.4 \text{ ng ml}^{-1}$  dimethylsulfone solved in water would be possible under shot-noise-limited detection with perfect detectors [37, 40].

Considering these recent advancements as well as the potential for further improvements, it is difficult to agree with Griffiths that infrared spectroscopy now is in its ‘fifth age’. Rather, I would argue that infrared spectroscopy is (once again) in its ‘second childhood’. Only when broadband infrared spectroscopy can be routinely operated at the limits set by the quantum nature of light – with average powers close to the damage threshold of the samples – could infrared spectroscopy have reached a final ‘age’ at which it can no longer be surpassed - at least according to our current understanding of the matter. The future will show whether FRS will be the technology able to achieve this ultimate goal within the field of infrared spectroscopy. But regardless of whether it will mark the final step of development, we can already state now that FRS will definitely move the field of infrared spectroscopy forward and thereby broaden the prospects for novel applications.

## 1.3 Application of infrared spectroscopy to biofluid analysis and disease detection

Due to its ability to obtain rich information about all types of molecules present within a complex sample in a rapid and label-free manner, infrared spectroscopy has always been and still is predestined for chemical, biological, and medical applications. Over the last decades all kinds of biological samples – breath [47], (human) tissue sections [15], plant leaves [48], cells [13, 14], cow's milk [49], saliva [50], blood serum [51], blood plasma [52], full blood [53], etc. – have been studied using different measurement modalities [11, 25, 54–56] – including attenuated-total-reflection, transmission, reflection, micro-spectroscopy, waveguide sensors and microfluidic chips – in order to investigate chemically, biologically, and medically relevant questions related to label-free sample identification [11, 13] as well as (cell) phenotyping [13], identification and quantification of selected molecules [52, 54, 57], disease and cancer detection [11, 15, 50, 51]. A complete comprehensive overview over all these different topics is beyond the scope of this thesis. The interested reader is kindly referred to the original works already cited as well as to dedicated books on these topics [4, 7–9].

The focus of this section of the introduction lies on the analysis of biofluids with infrared spectroscopy for biomedical applications, highlighting the potential advantages for disease and cancer detection. Towards that end, I will review three main approaches – (1) quantitative analysis, use of (2) functionalized sensors, and (3) fingerprinting approaches – and discuss their respective advantages and disadvantages for different applications.

### 1.3.1 Quantitative analysis of biofluids

A variety of analytical methods are routinely used to identify and quantify selected components of liquid samples. Among these approaches, optical methods stand out in particular, as they allow quantitative analytical measurements without direct contact or manipulation of the sample under investigation, e.g. by using additional reagents such as chemical labels. The basic concept of quantitative infrared spectroscopy is based on the fact that virtually every molecule exhibits a unique absorption spectrum in the infrared range, which can be used not only for identification but also for quantification of this specific molecule, as the absorption scales linearly with the molecular concentration (in the limit of linear spectroscopy) [4].

For complex organic biofluids, consisting of many thousand different molecular species at (often vastly) differing abundancies, the infrared molecular signal is a linear superposition of the individual molecular signals weighted according to their concentrations. Considering that these individual molecular signals range over several orders of magnitude, and that absorption spectra in the liquid or solid phase have rather broad absorption features with overlapping bands, concentration retrieval in complex substances constitutes a challenging problem. Therefore, molecular identification and quantification is assisted by so called ‘infrared chemometrics’ using advanced (machine learning) algorithms to extract, identify, and quantify features in the infrared fingerprints that belong to specific analytes. To date, parallel molecular quantification based on infrared spectroscopy has been restricted to about 10 analytes, all with concentration levels well above  $10 \mu\text{g mL}^{-1}$  in biofluids [29, 57–59]. However, it is still unclear whether the spectroscopic sensitivity, the broad absorption features, or other factors (e.g. sample preparation and measurement modalities) are currently the main limitations of this specific approach [59].



In the context of clinical diagnostics, quantitative infrared spectroscopy has significant application potential. A large number of blood parameters (e.g. erythrocytes, leukocytes, thrombocytes, haemoglobin, haematocrit, total protein content, glucose concentration) are routinely measured whenever a blood sample is drawn, either when healthy individuals undergo a medical check-up or to support the diagnosis of a disease if patients already show symptoms. If a specific disease is suspected, a targeted quantification of selected indicative marker molecules is performed (e.g. prostate specific antigen for prostate cancer). It is now understood that a single molecular marker, although highly correlative with the onset of certain diseases, is not sufficient to provide reliable diagnostic efficiency and thus multiple molecules need to be quantitatively evaluated from one and the same sample. Established enzymatic and antibody-based methods or modern omics approaches have the capability to probe and quantify an ever-wider range of molecules, but the immense number of relevant biomarking molecules in such blood-based tests causes the costs of these methods to grow prohibitively [60].

Due to its relatively cost-effective and compact instrumentation, infrared spectroscopy has distinct advantages when it comes to point-of-care capability, speed of evaluation and economic viability. In addition, the methodology for quantifying selected molecules, once established, can readily be combined with infrared fingerprinting applications, e.g. for disease detection (see section 1.3.3). This would mean great synergy effects, as quantitative clinical parameters could be obtained additionally and free of charge from the same spectra that were used for disease diagnosis based on the infrared fingerprints.

### 1.3.2 Functionalized infrared sensors and chips

A major challenge of (quantitative) infrared spectroscopy of complex biofluids is both its selectivity and sensitivity of molecular detection. As discussed in the previous section, direct sampling is usually limited to the identification and quantification of the most abundant molecules. In order to enhance selectivity and sensitivity, two concepts are mainly followed, namely molecular pre-concentration and the use of molecule-specific binding sites [25, 54, 55, 61]. Both approaches are often combined and realized on a sensor chip, to which the light is coupled in transmission, or via waveguides or via attenuated total reflection.

For example, Nabers et al. developed an attenuated total reflection infrared sensor with binding sites for the amyloid-beta peptide [62–64]. Here, the functionalized interface fulfils two tasks. On the one hand, it enables isolation of the target peptide from the complex fluid (blood serum and cerebrospinal fluid in this case). On the other hand, the peptide concentration is locally highly increased, thus facilitating optical detection. Furthermore, these authors have also shown that the measured infrared spectrum can be associated with a conformational change of amyloid-beta peptides. First results from a clinical study show that these changes can be correlated with the likelihood of developing Alzheimer's and may thus be used as a promising biomarking approach for early diagnostics [64].

The example above showcases how the sensitivity and specificity of infrared spectroscopic analysis can be increased. However, such a 'targeted' approach is only applicable if the target molecule has already been identified, which is not always the case. At the same time, in any approach that only focuses on the detection of a selected molecule, relevant information from other constituents may remain undetected. This can be disadvantageous for certain research questions or applications, since often only the interaction pattern of different molecules within

complex networks are crucially informative and the right conclusions can be often drawn only when multi-molecular analyses are available. For a more extensive overview over different types of MIR sensors and their application, the interested reader is referred to dedicated reviews on these topics [25, 54, 55, 61].

### 1.3.3 Infrared fingerprinting

Quantitative analysis of biofluids and functionalized sensors target the identification and quantification of either (pre-)selected or known molecules, and therefore require *a priori* information about molecules relevant for a specific biological or medical question. By this, a wealth of information – inherently provided by infrared molecular spectroscopy – may be neglected or missed. Infrared spectroscopy is sensitive to all molecular species. Thus, an absorption spectrum, in principle, contains information about the entire molecular landscape of a biological sample. The advantage of infrared molecular fingerprinting is that no *a priori* information about relevant molecules is required, rendering an extensive search and testing of potential candidates obsolete.

Instead of relying on the analysis of a few selected analytes, the concept of infrared molecular fingerprinting is to identify and relate specific patterns within the infrared spectra of biological samples to characteristic molecular compositions or phenotypes. Thereby, the observed pattern may originate from a combination of changes of many different molecules – something that might be missed when only specific pre-selected sets of analytes are investigated. If an infrared fingerprint is specific enough for a molecular composition, i.e. it is unambiguously correlated with a certain phenotype while being non-sensitive to other conditions, infrared fingerprinting can contribute to the detection of a given physiology. These concepts and approaches can be applied to any (biological) material, such as biofluids, tissues, or cells, and for phenotyping and sample type classification [4, 7, 8, 11, 13, 65]. In the following, I will elaborate on the application of infrared fingerprinting of biofluids for disease detection, discuss in more detail how to decode infrared molecular fingerprint information, and examine the advantages and disadvantages of this particular approach.

The incentive of molecular fingerprinting of biofluids relies on the fact that a multitude of human phenotypes, including diseases, are reflected in the molecular composition of biofluids, such as blood serum and plasma, urine, saliva, etc. In addition, biofluids can be sampled easily and repeatedly. In general, medical diagnostics would greatly benefit from liquid biopsies as they are minimally invasive as well as time- and cost-effective compared to tissue biopsy-driven diagnostics.

So far, most liquid biopsies predominantly rely on the analysis of few pre-selected analytes and biomarkers. Although the emergence of highly sensitive and molecule-specific methods in the fields of proteomics [60, 66, 67], metabolomics [68, 69], and genomics [70–72] has led to the discovery of thousands of different biomarker candidates, only a few of them could be verified and made it to the clinics. Over the last few decades, there has been a paradigm change. Instead of relying on a single molecular marker, recent research increasingly focuses on the combination of different markers, and the investigation of changes of molecular patterns in order to detect physiologies specific to a disease. However, the combination of analytical approaches, with each targeting a specific family of molecules (e.g. proteins), is still a major challenge as it requires complex and target-specific sample preparation as well as elaborate

ways combining different datasets [73–76].

Infrared fingerprinting addresses these issues by capturing the entire molecular fingerprint information in a single time- and cost-effective measurement enabling phenotyping ‘in a snapshot’. Numerous studies have already shown the potential of blood-based infrared spectroscopic molecular fingerprinting for disease detection [17, 18, 51, 77, 78]. In the following three subsections the workflow, challenges, and steps towards a clinical translation of infrared spectroscopy are outlined.

### **Considerations on the workflow and application of biofluid infrared spectroscopy**

The basic principle of infrared fingerprinting was established two decades ago [79–85] and has been refined over time. The typical workflow of biofluid infrared spectroscopy along with several application examples is reviewed in detail in several publications [17, 86–90] and can be summarized in the following steps and considerations:

1. **Study design and sample collection.** This includes considerations such as: Which medical question is to be investigated? Are proper case and control groups available to avoid bias? How homogeneous is a phenotype or condition and should relevant subgroups (e.g. different types of breast cancer) be considered accordingly? How many samples should be included in the envisioned study for the results to have sufficient statistical power? Which biofluid (e.g. serum, plasma) would be the most promising to sample and detect a given condition? Can standardized sample collection and long-term storage be ensured?
2. **Sample preparation.** The collected liquid samples are usually stored in a deep-freezer. Prior to any measurement they have to be thawed and can then be either measured in the dried or liquid state. Most infrared fingerprinting studies were performed with dried samples, as liquid water is a strong infrared absorber and therefore makes the infrared measurement more challenging. However, the drying process suffers from the so-called ‘coffee-ring effect’ [87, 90] making the obtained infrared spectra less reproducible. For both cases (dried and liquid) standardized sample preparation routines need to be established in order to minimize possible pre-analytical errors.
3. **Sample holder and spectral acquisition.** The measurement can either take place in transmission geometry or using an ATR cell. In any case, an automated sample delivery unit is preferable to increase measurement reproducibility and speed.
4. **Spectral pre-processing and outlier removal.** Infrared spectra are often affected by instrument drifts over time and/or changes in the environmental conditions. As discussed in detail by Trevisan et al. [89], spectral pre-processing can for one reduce some of these effects and for the other facilitate efficient extraction of biologically relevant information from the infrared fingerprints. Usually, this step also involves an outlier detection (often automatic) in order to remove faulty measurements.
5. **Data analysis and classification.** The goal here is to find spectral features that are linked to medically relevant questions. In general, this can be done applying unsupervised methods (e.g. principal component analysis, clustering analysis) or supervised methods

(e.g. support vector machine, random forest analysis, artificial neural networks) [11, 89]. The supervised methods are often called machine-learning algorithms. The general strategy here is that part of the dataset is used to train the algorithm to find features connected to the disease. Afterwards the trained algorithm is tested on the remaining test dataset.

6. **Classifier for diagnostics.** As a final step, the accuracy, specificity and sensitivity of the methods is evaluated.

Using these steps as a basic recipe, infrared fingerprinting of biofluids has been applied to various cancer entities (e.g. prostate, lung, breast, ovarian, brain) and other diseases (e.g. Alzheimer's, scrapie, malaria) [17, 18, 51, 77, 78, 86–88]. Although some studies show promising classification accuracies, e.g. 93.2 % sensitivity and 92.8 % specificity for the detection of brain cancer using ATR-FTIR sampling [51], none of them have been successfully transferred to clinical use so far, as difficulties arise from several aspects, which are discussed below.

### Methodological and practical challenges in applying infrared fingerprinting

There are several methodological and practical challenges that arise when applying infrared fingerprinting.

1. **Limited sensitivity and specificity** of infrared fingerprinting is one of the largest drawbacks so far. Current FTIR spectrometers have detection limits typically well above  $10 \mu\text{g mL}^{-1}$ . This renders various common biomarkers, e.g. prostate specific antigen (at a mean concentration level of  $100 \text{ ng mL}^{-1}$ ), impossible to detect [91]. Furthermore, broad spectral features result in overlapping spectra from different molecules, making it challenging to distinguish between the individual molecules. Therefore, an approach that manages to increase specificity and sensitivity without losing the ability to measure all signals simultaneously would be of great practical relevance.
2. **Biological variability** of infrared fingerprints, neither of any larger random population, nor of healthy individuals have been studied systematically. However, only with exact knowledge of the latter, one can assess whether an observed pattern is indeed abnormal, or if it still lies within the normal range for an individual.
3. **Limited insight into the (molecular) origin** (see also section 1.3.1) of the observed patterns that are relevant for classification of any specific disease makes infrared molecular fingerprinting susceptible to false positive findings due to confounding factors or non-disease specific signals (4.) and experimental bias (5.) [91].
4. **Confounding factors or non-disease specific signals.** For example, by combining proteomics and infrared spectroscopy, the Naumann group discovered that the infrared fingerprint pattern related to the presence of bovine spongiform encephalopathy (or mad cow disease) could be attributed to a change of the albumin to globulin ratio [84, 85]. The latter is known to correlate with many different diseases and disease prognosis due to a non-specific immune response [91]. Since both albumin and globulin are generally abundant in blood serum, and therefore contribute to a large extent to the infrared signal, this has to be considered before claiming to have identified any disease-specific markers.

Other confounding factors might arise due to poor study design. Especially non-balanced control and case groups (e.g. young controls and old cases) might lead to falsely assessing the actual classification performance. Thus, it is instrumental to demonstrate that a given infrared fingerprint pattern unambiguously correlates with the onset of a given condition, while not being in positive correlation with other real-life conditions.

5. **Experimental bias.** Any signal that is predominantly present in the spectra of one group (e.g. control individuals) might be taken up by the machine learning algorithm, even though it does not originate from the disease itself. In a critical commentary [91], Max Diem discusses a study, which sought to discriminate between serum samples from healthy individuals and cancer patients. He notes, that the most relevant p-values in the t-test observed for the experiment roughly follow the overall vibrational spectrum of water vapour, suggesting that an algorithm could possibly pick up an experimental artefact, possibly due to changes in the water vapour content in the room during the measurements of the different samples and sample sets. For small-scale studies, experimental bias can be largely countered by randomization in order to avoid batch effects [92]. For large-scale studies additional standardization (6.) is required.
6. **Standardization** is a prerequisite for any large-scale study as it minimizes the potential for experimental bias by standardization of workflow, sample handling, and measurements. In addition, several algorithms can be applied to the spectral data in order to minimize instrument related bias and drifts [93].

### Clinical translation as a challenge

The clinical translation presents a challenge in and of itself. It is demanding in terms of both time and cost, and in addition, it necessitates close collaboration with professionals of different backgrounds and integration of different clinical and research institutions. In a series of publications [16, 17, 87, 94–96], Matthew Baker and co-workers address the challenges and outline necessary steps towards a successful clinical translation:

1. **Small-scale pilot study.** Frequently, many studies do not progress from the pilot phase due to methodological flaws (see above), a lack of funding or the unavailability of sufficient clinical samples. Once leaving the pilot phase, the acquired results need to be confirmed in independent large-scale cohort studies (clinical validity).
2. **Investigation and demonstration of the envisioned clinical decision-making setting.** Depending on the acquired sensitivity and specificity as well as the costs of the envisioned medical test, it has to be determined in which clinical setting the new technique can be used with the most benefit (in terms of economic viability and clinical utility). For example, it might be beneficial to use a new test in conjunction with established diagnostic procedures to increase their efficiency or cost effectiveness, while others might be especially useful in a screening context. Gray et al. explored two clinical scenarios for the use of a FTIR-based blood serum test for brain cancer [97]. They concluded that whenever their test is applied to potentially avoid an expensive computed tomography scan or magnetic resonance imaging, it would not only reduce the overall costs, but also have the potential to deliver improvements in health outcomes.

3. **Commercial considerations** such as intellectual property rights, lack of funding, and competing techniques and approaches. They often represent barriers for proof-of-concept studies and are therefore crucial for a successful clinical translation [17].

A routine use of infrared biofluid analysis in a clinical context can only be established, if all these challenges are met adequately.

This thesis reports on the application of FRS, a novel technology of infrared spectroscopy, for cancer detection in liquid serum to increase the sensitivity and specificity of infrared fingerprints. Pursuing a new approach, however, also means that we were mainly confronted with methodological and practical challenges. In the following chapters I will report on how we addressed them.

## 1.4 Research goals and structure of the thesis

The investigated research goals and results presented in this cumulative thesis were driven by two overriding scientific questions:

1. *Can fs-laser technology, offering broadband few-cycle infrared pulses, and the field-resolved detection thereof with electro-optic sampling (i.e. field-resolved spectroscopy), provide the means to improve sensitivity limits as compared to other emerging and established mid-infrared spectroscopy techniques?*
2. *Can this newly developed field-resolved spectroscopy be successfully applied to the analysis of human serum in order to detect diseases such as cancer? Underlying questions include whether (i) electric-field molecular fingerprints can be obtained reliably and robustly, and whether (ii) the increased sensitivity of field-resolved infrared spectroscopy (as compared to conventional Fourier-transform infrared spectroscopy) translates to higher efficiency in cancer detection.*

Chapter 2 of this thesis addresses the first question. It focuses on the description of technical advances and theoretical aspects of field-resolved infrared spectroscopy.

As a first preparatory step I investigated and optimised the intensity noise properties of the broadband femtosecond mid-infrared source that later was employed in the field-resolved spectrometer. Excess relative intensity noise (RIN) constitutes one of the major limitations of most spectroscopic methods involving lasers. Therefore, the idea was to reduce the RIN of the employed source prior to any spectroscopic experiments. The results were summarized and published as an article in *Optics Express* [45], which is included in the corresponding section 2.1 below.

The subsequent section reports on the most fundamental and essential aspects and findings of FRS. First, conceptual advantages of field-resolved spectroscopy as compared to frequency-resolved spectroscopies are discussed. We demonstrate that these conceptual advantages can be used and employed to increase the sensitivity of FRS over FTIR by a factor of 40. Furthermore, we report how this advantage in sensitivity enables spectroscopy of strongly absorbing samples like living cells and plant tissues. These results have been published as an article in *Nature* [40], which is included in section 2.2.

The last section of chapter 2 elaborates on the benefits of FRS for the measurement of strongly absorbing samples. Fundamental advantages of techniques whose signal-to-noise ratio (SNR) scales linearly with the electric field (e.g. FRS) over those whose SNR scales linearly with radiation intensity (e.g. conventional FTIR spectroscopy) are discussed in theory and demonstrated experimentally. This beneficial scaling behaviour leads to an optimum interaction length with samples for SNR-maximized measurements that is twice the value usually considered to be optimum for FTIR devices. These results were published as an article in *Analytical Chemistry* [39], which is included in section 2.3.

Chapter 3 of this thesis addresses the application of infrared spectroscopy to the fingerprinting of human blood serum and plasma to facilitate disease detection.

In a preparatory work, I assess the (temporal) stability of infrared molecular fingerprints obtained from human serum and plasma samples from 31 healthy individuals who have provided up to 13 blood samples each over a period of 6 months. In addition, the measurement error as

well as the uncertainties due to sample handling and collection were investigated. This study was intended to serve as a framework for future studies in the field. The results are instructive to relate a potential disease related signal to the natural biological variability and the analytical errors. Furthermore, this study revealed that infrared molecular fingerprints contain highly individual-specific information. The results were summarized as an article and are currently under review by *Nature Communications* [98]. The submitted version is included in section 3.1.

Finally, we applied field-resolved spectroscopy to the analysis of over 300 individuals in a clinical study involving lung, breast, and prostate cancer patients. Applying machine learning algorithms, we find that all cancer entities can be detected with an area under the receiver operating characteristic curve of 0.63-0.84. We also find that the detection efficiencies of field-resolved spectroscopy are systematically higher than those obtained with conventional infrared spectroscopy, suggesting that the increased sensitivity of the method directly translates into a better detection efficiency. The results can be found in section 3.2.

At the end of the thesis, I summarise the main findings throughout the work in order to put them into a larger context. I discuss how the field-resolved metrology might further evolve and how this might open up new avenues for an even larger variety of applications. Specifically, I discuss the impact of these potential further developments on the future of infrared fingerprinting.



# Field-Resolved Spectroscopy

## 2.1 Active intensity noise suppression for a broadband mid-infrared laser source

**Preface:** Precision absorption spectroscopy relies on resolving minuscule intensity changes upon transmission of (laser) light through a sample. In the most simplistic implementation, linear spectroscopy employs a monochromatic source that is transmitted through a sample and measured with a photodetector. According to Beer's law, the sample attenuates the light beam by a certain value  $x$ . The resulting change in light intensity ( $1 - 1/x$ ) can only be detected if the relative intensity fluctuation of the light source is less than  $x$  throughout the measurement time. Although a large number of measurement concepts have been developed in order to circumvent the negative influence of intensity noise on the spectroscopic measurement (as it is also the case for field-resolved-spectroscopy, see section 2.2), it is always beneficial to start with a source that offers less intensity noise intrinsically [23, 35, 44, 99]. This motivated us to investigate intensity noise suppression schemes for the femtosecond mid-infrared (MIR) laser source that later was employed in the field-resolved spectrometer. We implemented an active intensity stabilization with an electronic feedback loop and an acoustic-optic modulator acting as a fast intensity modulator. With this system a relative intensity noise (RIN) suppression of the MIR pulse train of up to a factor of 20 was achieved in the band between 1 Hz and 100 kHz, resulting in a total integrated RIN of 0.07 % [45].

## **Active intensity noise suppression for a broadband mid-infrared laser source**

*as published in*

**Optics Express** (2017)

[45]

*by*

Marinus Huber, Wolfgang Schweinberger, Fabian Stutzki, Jens Limpert,  
Ioachim Pupeza, and Oleg Pronin

**Contributions:** I designed and investigated all noise suppression concepts, performed the measurements, evaluated and interpreted the data, and wrote most of the manuscript.



Research Article

Vol. 25, No. 19 | 18 Sep 2017 | OPTICS EXPRESS 22498

Optics EXPRESS

## Active intensity noise suppression for a broadband mid-infrared laser source

MARINUS HUBER,<sup>1,2,\*</sup> WOLFGANG SCHWEINBERGER,<sup>1,3</sup> FABIAN STUTZKI,<sup>4</sup>  
JENS LIMPERT,<sup>4</sup> IOACHIM PUPEZA,<sup>1,2</sup> AND OLEG PRONIN<sup>2</sup>

<sup>1</sup>Ludwig-Maximilians-Universität München, Am Coulombwall 1, 85748 Garching, Germany

<sup>2</sup>Max-Planck-Institut für Quantenoptik, Hans-Kopfermann-Straße 1, 85748 Garching, Germany

<sup>3</sup>King Saud University, Department of Physics and Astronomy, Riyadh 11451, Saudi Arabia

<sup>4</sup>Friedrich-Schiller-University Jena, Institute of Applied Physics, Albert-Einstein-Straße 15, 07745 Jena, Germany

\*marinus.huber@mpq.mpg.de

**Abstract:** Excess relative intensity noise (RIN) constitutes one of the major limitations of most spectroscopic methods involving lasers. Here, we present an active RIN suppression scheme for a coherent mid-infrared (MIR) light source (8.4–11  $\mu\text{m}$ ), based on intra-pulse difference frequency generation (DFG). Three different stabilization concepts that rely on modulating the intensity of the driving near-infrared (NIR) pulse train with an acousto-optic modulator are investigated and compared. By using the wings of the NIR spectrum to generate the error signal, a RIN suppression of the MIR pulse train of up to a factor of 20 was achieved in the band between 1 Hz and 100 kHz, resulting in a total integrated RIN of 0.07%.

© 2017 Optical Society of America

**OCIS codes:** (140.3425) Laser stabilization; (140.3070) Infrared and far-infrared lasers.

### References and links

1. P. C. Hobbs, "Ultrasensitive laser measurements without tears," *Appl. Opt.* **36**(4), 903–920 (1997).
2. J. Hodgkinson and R. P. Tatam, "Optical gas sensing: a review," *Meas. Sci. Technol.* **24**(1), 012004 (2013).
3. P. Kwee, C. Bogan, K. Danzmann, M. Frede, H. Kim, P. King, J. Pöld, O. Puncken, R. L. Savage, F. Seifert, P. Wessels, L. Winkelmann, and B. Willke, "Stabilized high-power laser system for the gravitational wave detector advanced LIGO," *Opt. Express* **20**(10), 10617–10634 (2012).
4. F. Seifert, P. Kwee, M. Heurs, B. Willke, and K. Danzmann, "Laser power stabilization for second-generation gravitational wave detectors," *Opt. Lett.* **31**(13), 2000–2002 (2006).
5. O. Pronin, M. Seidel, F. Lücking, J. Brons, E. Fedulova, M. Trubetskov, V. Pervak, A. Apolonski, T. Udem, and F. Krausz, "High-power multi-megahertz source of waveform-stabilized few-cycle light," *Nat. Commun.* **6**, 6988 (2015).
6. C. Jauregui, J. Limpert, and A. Tünnermann, "High-power fibre lasers," *Nat. Photonics* **7**(11), 861–867 (2013).
7. S. Hädrich, M. Krebs, A. Hoffmann, A. Klenke, J. Rothhardt, J. Limpert, and A. Tünnermann, "Exploring new avenues in high repetition rate table-top coherent extreme ultraviolet sources," *Light Sci. Appl.* **4**(8), e320 (2015).
8. I. Pupeza, D. Sánchez, J. Zhang, N. Lilienfein, M. Seidel, N. Karpowicz, I. Znakovskaya, M. Pescher, W. Schweinberger, V. Pervak, E. Fill, O. Pronin, Z. Wei, F. Krausz, A. Apolonski, and J. Biegert, "High-power sub-two-cycle mid-infrared pulses at 100 MHz repetition rate," *Nat. Photonics* **9**(11), 721 (2015).
9. C. Kötting and K. Gerwert, "Monitoring protein–ligand interactions by time-resolved FTIR difference spectroscopy," *Protein-Ligand Interact. Methods Appl.* **1008**, 299–323 (2013).
10. P. Lerch, P. Dumas, T. Schilcher, A. Nadji, A. Luedeke, N. Hubert, L. Cassinari, M. Boege, J. C. Denard, L. Stingelin, L. Nadolski, T. Garvey, S. Albert, Ch. Gough, M. Quack, J. Wambach, M. Dehler, and J. M. Filhol, "Assessing noise sources at synchrotron infrared ports," *J. Synchrotron Radiat.* **19**(Pt 1), 1–9 (2012).
11. S. Keiber, S. Sederberg, A. Schwarz, M. Trubetskov, V. Pervak, F. Krausz, and N. Karpowicz, "Electro-optic sampling of near-infrared waveforms," *Nat. Photonics* **10**(3), 159–162 (2016).
12. J. Zhang, J. Brons, N. Lilienfein, E. Fedulova, V. Pervak, D. Bauer, D. Sutter, Z. Wei, A. Apolonski, O. Pronin, and F. Krausz, "260-Megahertz, Megawatt-Level Thin-Disk Oscillator," *Opt. Lett.* **40**(8), 1627–1630 (2015).
13. P. Kwee, B. Willke, and K. Danzmann, "Shot-noise-limited laser power stabilization with a high-power photodiode array," *Opt. Lett.* **34**(19), 2912–2914 (2009).
14. N. R. Newbury, B. R. Washburn, K. L. Corwin, and R. S. Windeler, "Noise amplification during supercontinuum generation in microstructure fiber," *Opt. Lett.* **28**(11), 944–946 (2003).
15. U. Møller, S. T. Sørensen, C. Jakobsen, J. Johansen, P. M. Moselund, C. L. Thomsen, and O. Bang, "Power dependence of supercontinuum noise in uniform and tapered PCFs," *Opt. Express* **20**(3), 2851–2857 (2012).

#297992

<https://doi.org/10.1364/OE.25.022498>

Journal © 2017

Received 15 Jun 2017; revised 16 Aug 2017; accepted 16 Aug 2017; published 7 Sep 2017

16. A. Leitenstorfer, S. Hunsche, J. Shah, M. C. Nuss, and W. H. Knox, "Detectors and sources for ultrabroadband electro-optic sampling: Experiment and theory," *Appl. Phys. Lett.* **74**(11), 1516–1518 (1999).
17. A. A. Lanin, A. A. Voronin, A. B. Fedotov, and A. M. Zheltikov, "Time-domain spectroscopy in the mid-infrared," *Sci. Rep.* **4**(1), 6670 (2015).

## 1. Introduction

The intensity noise of the laser source represents a significant limitation on any high-precision optical measurement. While some spectroscopic measurements, such as those that employ balanced detection, rely on passive intensity noise suppression [1,2] or mitigate the influence of excess relative intensity noise (RIN) by using modulation techniques (several of which are reviewed in Ref [2].), other applications require active stabilization of the laser source itself. For instance, in gravitational wave detectors a complex active stabilization scheme is implemented which allows to suppress radiation pressure fluctuations on the mirrors that originate from laser intensity noise [3,4]. A stable laser source is also vital for driving nonlinear (optical) processes [1]. The radiation emitted by these sources (usually in the visible or near-infrared [5,6]) can be converted via nonlinear processes to achieve broad spectral coverage ranging from the extreme ultraviolet [7] to the mid- and far infrared [8]. The unique combination of high brightness with unparalleled spatial and temporal coherence makes mode-locked, MHz-repetition-rate lasers indispensable for high-precision metrology in these spectral regions.

Particularly in the mid-infrared (MIR) region, such sources are of great interest for vibrational spectroscopy. This technique allows organic compounds in gases or liquids to be identified in a label-free manner by their unique molecular fingerprints, and finds a large variety of applications in biology, chemistry, medicine and environmental monitoring. Fourier transform infrared (FTIR) spectrometers based on thermal sources ("globar") remain the instrument of choice in the field [9]. However, even though thermal sources only exhibit low intensity noise, the performance of these devices is usually limited by detector noise rather than by photon shot noise, owing to the weak light intensity of thermal sources.

Laser-based MIR sources could in principle overcome this problem thanks to their high brightness; however, one of the major limitations of these sources is their (low-frequency) RIN, which usually lies orders of magnitude above the power-equivalent shot-noise limit. In order to reduce this excess noise contribution, most MIR spectroscopic techniques (like FTIR spectroscopy) employ fast scanning (or other modulation techniques) to effectively transfer the measured spectrum into a radio frequency region with lower noise levels. With mechanical delay stages, scan speeds of 10 mm/s can easily be obtained, shifting the noise contribution for spectral components at 1000 cm<sup>-1</sup> to noise frequencies around 2 kHz [10]. However, with laser sources, noise in the kHz frequency range is normally dominated by strong excess noise, and therefore further reduction of RIN is highly desirable.

In this work, we present an active intensity noise suppression system for a coherent source of broadband MIR radiation generated by a 19-fs near-infrared (NIR) pulse train via intrapulse difference-frequency-generation (DFG), which is based on an acousto-optic-modulator (AOM). Three different stabilization concepts are investigated and compared. As direct stabilization of the generated MIR can be very challenging owing to the lack of sufficiently sensitive broadband detectors and/or active broadband optical elements in the MIR spectral range, all investigated stabilization concepts aim at stabilizing the driving source itself. In addition, the error signal for the feedback loop is generated with a pick-off from the driving NIR source. This circumvents the need for rather impractical and less sensitive liquid-nitrogen-cooled mercury cadmium telluride (MCT) photodetectors for the MIR radiation. Combined with MIR detection schemes that rely on frequency up-conversion, such as EOS [8,11], this could lead to highly sensitive MIR spectroscopy without the requirement to use MIR detectors which require liquid nitrogen cooling.

We demonstrate that the implementation of this stabilization system results in the suppression of RIN of the generated MIR by up to a factor of 20 (in the band between 1 Hz

and 20 kHz). The concept presented here can significantly broaden the application of laser-based mid-infrared sources in spectroscopy.

## 2. Experimental setup

The experimental setup is shown in Fig. 1(a). The output of an Yb:YAG Kerr-lens mode-locked thin-disc oscillator [12] (100 MHz, 260 fs, up to 70 W) is spectrally broadened in a photonic crystal fiber (PCF) and temporally compressed by chirped mirrors [5]. The resulting 19-fs pulses (measured with frequency-resolved optical gating) are focused into a 1-mm thick LiGaS<sub>2</sub> (LGS) crystal to create, via intra-pulse difference frequency generation (DFG), broadband ultrashort MIR pulses with a central wavelength of 10  $\mu\text{m}$  and an average power of 5 mW [8]. The pulse duration of 65 fs was determined via electro-optical sampling [8] and the MIR spectrum was measured with a FTIR spectrometer (Lasnix, L-FTS). To achieve optimum intensity stability, the nonlinear broadening in the PCF and the DFG process are driven at lower average powers here than in Ref [8].

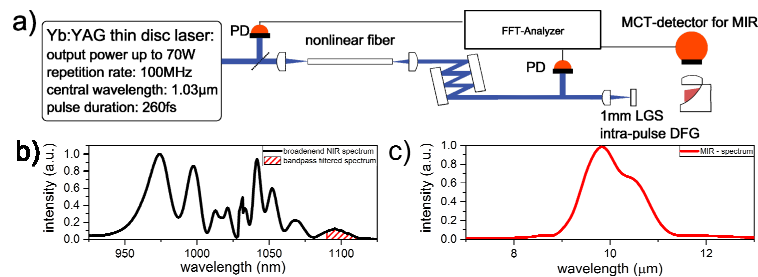


Fig. 1. a) Schematic of the free-running laser setup. The NIR pulses from the oscillator are spectrally broadened in a nonlinear fiber and temporally compressed by chirped mirrors (CM). The resulting 19-fs pulse train is focused into a LiGaS<sub>2</sub> crystal to generate MIR radiation via intra-pulse difference frequency generation. Fluctuations in the power of the free-running NIR or MIR radiation were measured with photodiodes (PD) at different positions in the setup, and the noise spectrum was recorded with a fast Fourier transform analyzer. b) Optical spectrum of the broadened NIR light. The patterned area indicates the portion of the spectrum that was used for generation of the feedback signal in stabilization concepts Ib and IIIb. c) Optical MIR spectrum measured with a FTIR.

The strategies for intensity stabilization of the MIR pulses described here rely on the use of an AOM as an active optical element to control the transmitted power. In the free-running state, 98% of the intensity is transmitted through the AOM (the 0th-order beam), while 2% is diffracted to higher orders and discarded. The error signal for the DC-coupled feedback loop is generated by diverting a fraction of the main NIR beam and detecting it with a 2-mm diameter InGaAs amplified photodiode (Thorlabs, PDA20CS).

The signal generated with the in-loop photodiode is then fed into a PI<sup>2</sup>D controller (Vescent Photonics, D2-125) which regulates the RF power of the AOM driver (Intraaction, ME-1104) and therefore provides active feedback on the transmitted laser intensity. The internal voltage reference of the D2-125 is used to define the lock point. The two integrators in the PI<sup>2</sup>D loop are set to 200 kHz and 2 MHz, respectively. The differential value and the gain (up to a maximum value of 32 dB) of the loop are then adjusted to attain the best possible noise suppression.

We implemented and compared three concepts for intensity stabilization of the MIR pulses, which differ in the placement of the AOM and the in-loop photodiode within the optical setup (see Fig. 2):

Concept I: The AOM is placed after the fiber, where generation of the error signal occurs, either without any spectral filtering (Concept Ia) or after passage through a 1100 nm ( $\pm 10$  nm) bandpass filter (Concept Ib) - Fig. 2(a)

Concept II: The AOM is placed ahead of the fiber and generation of the error signal also occurs in front of the fiber - Fig. 2(b)

Concept III: The AOM is placed ahead of the fiber, while generation of the error signal takes place downstream of the fiber, either without any spectral filtering (Concept IIIa) or after passage through a 1100 nm ( $\pm 10$  nm) bandpass filter (Concept IIIb) - Fig. 2(c)

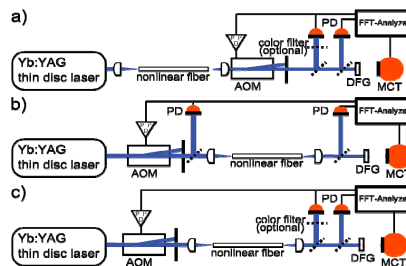


Fig. 2. Schematic of the three stabilization concepts: a) Concept I, b) Concept II, c) Concept III.

For concepts I and III, a fraction of the main beam was diverted via two subsequent 92/8 beam splitters, and an 1100-nm bandpass filter (Thorlabs, FB1100-10) was optionally placed before the photodiode to select only a part of the broadened spectrum for generation of the feedback signal (see Fig. 1(b)). In concept II, the error signal was generated based on the portion of the main beam transmitted through one of the highly reflective dielectric mirrors.

In all cases, additional neutral-density filters were employed to attenuate the laser beam used for generation of the feedback signal to an average power of about 1 mW. The spot size on the detector area (500  $\mu\text{m}$ ) was carefully aligned with the center of the diodes to minimize cross-coupling due to beam-pointing fluctuations [4,13]. Note that, in principle, one could also generate the error signal for the stabilization of the MIR intensity by directly measuring the MIR fluctuations with a mercury cadmium telluride (MCT) detector. However, this would require liquid nitrogen cooling, reduce the versatility of the approach and compromise long-term usage.

The independent (out-of-loop) MIR signal was recorded by focusing the beam onto a liquid-nitrogen-cooled MCT detector (Kolmar Technologies, KMPV11-0.25-J1/DC50). The voltage noise spectrum (in  $[V / \text{Hz}^{0.5}]$ ) up to 100 kHz was recorded with a fast Fourier transform (FFT) spectrum analyzer (Stanford Research, SR780) and normalized by the DC voltage signal to obtain the relative intensity noise spectrum  $S_{RIN}$  [in  $1 / \text{Hz}^{0.5}$ ]. The integrated root-mean-square (rms) RIN value for a given bandwidth was obtained by:

$$RIN_{rms}(f_0, f_1) = \sqrt{\int_{f_0}^{f_1} (S_{RIN}(f))^2 df} \quad (1)$$

The NIR out-of-loop signal was recorded using the same photodiode and pick-off optics as for generation of the in-loop signal. The noise suppression results for the NIR beam are discussed in more detail in the Appendix. The whole setup was encased in a housing to

minimize air fluctuations. Additionally, all photodiodes were placed in an additional housing to minimize the influence of scattered light on the noise suppression.

### 3. Results

First, the RIN spectra of the oscillator, the nonlinearly broadened NIR pulse train, the red edge of the broadened NIR pulses (at  $1100 \text{ nm} \pm 10 \text{ nm}$ ) and the MIR radiation were measured without active stabilization (see Fig. 3). The integrated RIN (rms, from 1 Hz to 100 kHz) of the oscillator (black curve) is 0.1% and the noise spectrum shows the typical  $1/f$  behavior. Nonlinear broadening does not change the RIN when the entire optical spectrum of the broadened NIR pulses is considered (blue curve, Fig. 3). However, the RIN of the edge of the broadened spectrum (at  $1100 \text{ nm} \pm 10 \text{ nm}$ , violet curve, Fig. 3) is increased by a factor of  $\sim 11$  over the measured RF spectrum. Approximately the same increase in noise was observed when the RIN of the blue edge of the NIR spectrum was measured (with a 950-nm shortpass filter, data not shown). The fact that the noise within one region of the broadened spectrum is amplified relative to the total input fluctuations is well-known, and has been reported and investigated by several groups [14,15]. In contrast, the fluctuations of the entire broadened NIR spectrum (i.e. integrated over all wavelengths) are approximately proportional to the input fluctuations (if no losses occur, the output power of the fiber is equal to the input power). The overall MIR noise spectrum (red, Fig. 3) is very similar to the noise at the edge of the spectrum. This can be attributed to the fact that, in this DFG scheme, the outer portions of the NIR spectrum are mixed.

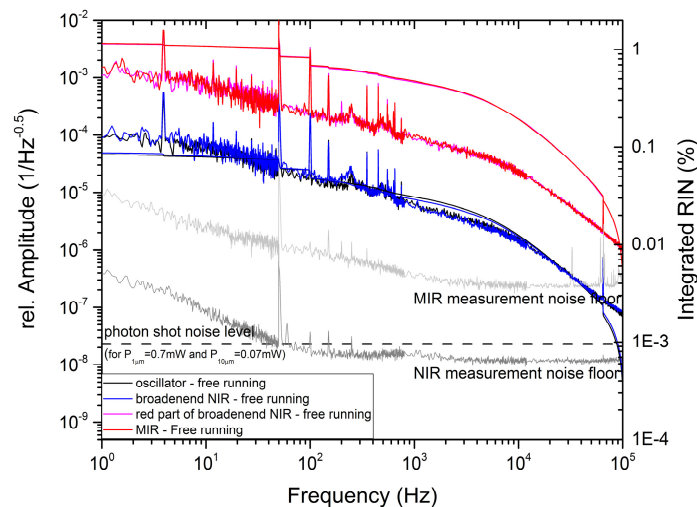


Fig. 3. Relative intensity noise and integrated noise (integration starts at 100 kHz) of the free-running system for the oscillator (black), the broadened NIR (blue), the red portion of the broadened NIR spectrum (pink) and the MIR light (red). The measurement noise floors of the InGaAs and MCT detectors are both well below the relative intensity noise of the measured radiation.

The extents of noise suppression of the MIR achieved by the three aforementioned stabilization concepts are shown in Figs. 4 and 5, respectively.

Implementation of stabilization concept I (AOM in front of the fiber and generation of the error signal in front of the fiber) reduces the MIR noise by up to a factor of 3 for frequencies below 50 kHz, while the integrated noise (rms, 1 to 100 kHz) was reduced from 1.2% to 0.5% (see Fig. 4(b)).

In concept II, the error signal generated downstream of the fiber was fed back to an AOM placed after the fiber. This signal was either obtained from the full optical NIR spectrum or produced after passage through an additional bandpass filter at 1100 nm, but no suppression of the MIR noise was observed in either of these cases (see Fig. 4(a)). In contrast, use of the same configuration to derive the error signal for NIR results in strong suppression of the RIN (see Appendix, Fig. 6(b)).

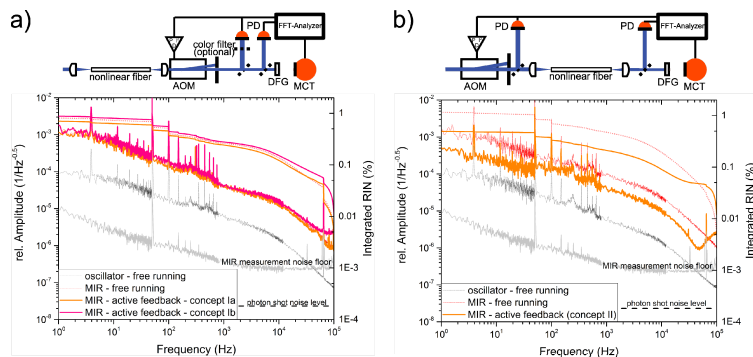


Fig. 4. MIR noise suppression by stabilization concepts I and II. No MIR noise reduction was achieved with stabilization concept I (a) while moderate suppression (by a factor of ~3) was obtained with stabilization concept II (b). A sketch of the stabilization concept employed is shown above each graph.

For stabilization concept III an error signal derived after the nonlinear broadening was fed back to the AOM in front of the fiber. As in concept I, the error signal was either generated from the full spectrum or from the red edge of the broadened spectrum. Application of the first approach suppressed the intensity noise by up to a factor of 5, whereas the second option led to noise reduction by up to a factor of 20 relative to the RIN of the free-running MIR for frequencies below 20 kHz. The corresponding integrated noise level (rms, 1 Hz to 100 kHz) was 0.3% or 0.07%, respectively (see Fig. 5(a)). Similar noise suppression is achieved when the blue edge of the spectrum is used to generate the error signal (data not shown).

In summary, stabilization concept IIIb (AOM placed in front of the fiber and generation of the error signal placed after the fiber with the edge of the optical spectrum) achieves the strongest suppression of MIR noise. Using this setup, the long-term stability of the MIR was tested. Figure 5(c) shows a normalized time trace of the MCT signal recorded, with and without active feedback, by an FFT analyzer over a period of 500s (this measurement is equal to a frequency noise bandwidth of 2 mHz to 2 Hz). The measured power fluctuations during this period are below 0.05% rms. Stabilization on longer time scales is limited by thermal drifts within the system.



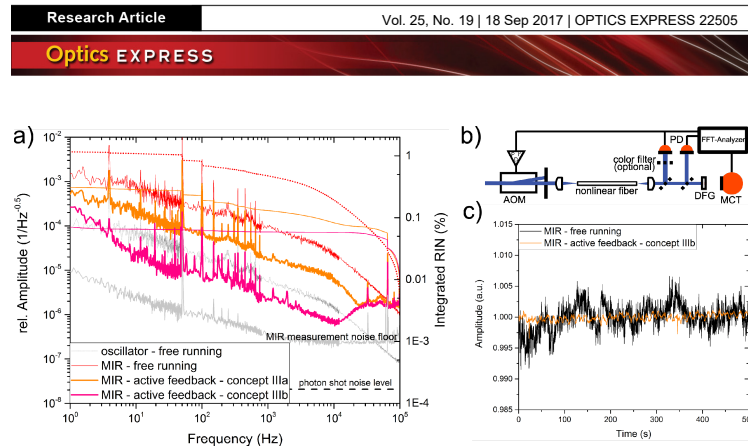


Fig. 5. a) MIR noise suppression by stabilization concept III. b) Sketch of the experimental layout for stabilization concept III. c) Normalized intensity fluctuations of the stabilized (concept IIIb) MIR beam (orange) recorded over 500s with an FFT analyzer. The rms of the intensity fluctuations of the stabilized beam is less than 0.05%.

#### 4. Discussion

The three stabilization concepts investigated here yielded very different degrees of MIR noise suppression. While concepts II and III resulted in noise reduction by factors of up to 10 and 20, respectively, no suppression of MIR noise was observed for stabilization concept I.

This outcome can be explained by variations in the magnitude of nonlinear broadening in the photonic crystal fiber, which results in corresponding differences in the amplification of noise in the broadened spectrum [14]. Moreover, the noise levels in the blue and red edges of the spectrum may be uncorrelated to some extent. An increase in input energy into the nonlinear fiber due to intensity fluctuations may thus lead to a higher power spectral density (PSD) in one part of the spectrum and to a lower PSD in another. If the AOM is placed downstream of the broadening fiber, the stabilization can act either on the noise contained in the entire optical spectrum or only on the fraction associated with the selected part of it (e.g. the red edge). Hence, this stabilization scheme does not permit one to simultaneously stabilize separate regions of the optical spectrum, which might fluctuate independently. However, simultaneous stabilization of different parts of the optical spectrum is precisely what is required to stabilize the output of an intra-pulse DFG scheme, as it is the mixing of the blue and red edges of the spectrum that leads to MIR generation.

Stabilization concept II suppresses the noise of the NIR pulse train before it enters the nonlinear fiber. Clearly, a reduction in RIN at the input of the fiber results in a reduction of noise in the broadened spectrum, and therefore suppresses MIR noise. However, as the error signal is generated upstream of the fiber, this scheme cannot compensate for nonlinear noise amplification within the fiber.

In stabilization concept III, on the other hand, the error signal is generated downstream of the fiber and fed back to the AOM, which acts prior to the fiber. First, we tried to stabilize the system using an error signal based on the full broadened optical spectrum. The RIN of the fiber output is very close to the RIN of the input beam, as can be seen in Fig. 3 (black vs. blue). Therefore, the MIR noise reduction is similar to that provided by concept II, in which the error signal was generated in front of the fiber. When only the edge of the broadened spectrum is used, the nonlinear error signal obtained is very sensitive to power fluctuations at the input of the fiber, and is also affected by nonlinear noise amplification during spectral broadening within the fiber. Stabilization of this signal leads to a reduction in the total noise, but also to a reduction in the nonlinear noise amplification during the spectral broadening. This in turn results in an overall noise reduction, which is associated with stronger

correlations between the intensity fluctuations in the different parts of the optical spectrum. As a result, the strongest suppression of the generated MIR intensity fluctuations – down to a RIN of  $\approx 6 * 10^{-7} \text{ kHz}^{-0.5}$  at 10 kHz – is achieved.

This is still a factor of 20 worse than the shot noise limit attainable for the feedback system, and this discrepancy is exacerbated at lower frequencies. The reason for this is that only the intensity fluctuations common to the measured error signal and the actual MIR signal can be canceled out [1]. Any uncorrelated noise signal which exclusively couples into either the in-loop or the out-of-loop signal will degrade the noise suppression performance. The system used here is most likely prone to such uncorrelated noise sources, as two nonlinearities (nonlinear broadening and DFG) are utilized to create the MIR radiation, while the active optical element and the photodiode for the generation of the error signal are working within the NIR wavelength region. Furthermore, due to the broadband nature of the NIR and MIR light, uncorrelated noise in different parts of the optical spectrum will degrade the overall efficiency of noise suppression.

Some additional noise sources were also identified and minimized. Any spatial dependence of the laser noise in combination with beam-pointing fluctuations can couple to the measured laser intensity due to the non-uniform response of the photodiodes [4]. As the beam pointing and the spatial response will differ for each photodiode, this will lead to uncorrelated noise that cannot be further suppressed. This noise source becomes dominant at low frequencies, due to the typical timescale of air fluctuations. In order to minimize this cross-coupling, the complete laser setup was enclosed in a housing to reduce the air fluctuations. In its absence of this precaution, the out-of-loop noise suppression was significantly degraded. Encasing the setup in a pressure-tight housing with clean air or in a vacuum enclosure might improve the noise suppression performance further.

The noise spectrum shows spikes at multiple values of 50 Hz, which indicates coupling of the power supply into the feedback loop or photodiode signals. In principle, these noise contributions can be suppressed by driving the electronics with batteries or stable DC sources. There is also a strong noise contribution at 4 Hz, which can probably be attributed to the water cooling of the laser system. Further potential noise sources include uncorrelated temperature fluctuations of both photodiodes, low-frequency noise and bias voltage fluctuations in the photodiodes, mechanical vibrations of the optics, electronic grounding noise, or polarization fluctuations [1,4,13].

As shown in Fig. 5, stabilization concept IIIb also helps to improve the long-term power stability of the MIR light generated. However, this works only over moderate time scales (10 min) before drifts in the average MIR power set in. Such drifts cannot be stabilized solely with the error signal derived from the NIR, as other effects that are independent of the NIR power also contribute. Even if the power of the NIR beam is perfectly stable, the MIR power generated might still vary slightly, as beam pointing drifts will alter the targeted position on the DFG crystal or temperature-dependent MIR generation conditions.

## 5. Conclusion

We have investigated and compared three different approaches to active intensity stabilization of a broadband MIR source driven by high-average-power femtosecond NIR pulses. The strongest MIR noise suppression – up to a factor of 20 – was attained when stabilizing to the red edge of the broadened NIR spectrum. We demonstrated a RIN of the MIR intensity of 0.05% rms over a time period of 10 min (this is equal to a frequency noise bandwidth of 2 mHz to 2 Hz). A minimal RIN value of  $6 * 10^{-7} \text{ Hz}^{-0.5}$  was obtained at 10 kHz.

MIR spectroscopic techniques, like FTIR or direct absorption spectroscopy, would directly benefit from the proposed noise suppression system, as the interfering noise frequencies are usually located at kHz frequencies and below. Additionally, the error signal for the feedback is derived from the driving NIR beam, so that no liquid-nitrogen-cooled MCT detectors are necessary. This factor, together with the reduced intensity noise and MIR

detection schemes that rely on frequency-up-conversion [8,16,17], should facilitate the realization of highly sensitive MIR spectroscopy that does not require any MIR detectors.

The stabilization schemes presented here can be easily adapted for other laser-driven light and electron sources which suffer from intensity noise and cannot easily be stabilized due to the lack of active optical elements or adequate detectors.

## 6. Appendix

### 6.1. Calculation of the shot noise limit of the stabilization scheme

Quantum or shot noise is a fundamental noise limit imposed by the photon nature of light. The relative shot noise power of a light source at a central wavelength  $\lambda$  and an average power of  $P$  can be calculated with

$$s_q = \sqrt{\frac{2hc}{P\lambda}} \quad (2)$$

where  $h$  is the Planck constant and  $c$  is the speed of light in the vacuum. For a given feedback system, the relative shot noise of the light impinging on the in-loop (with power  $P_{IL}$  and central wavelength  $\lambda_{IL}$ ) and out-of-loop (with power  $P_{OOL}$  and central wavelength  $\lambda_{OOL}$ ) photodetectors contribute to the attainable shot noise limit  $s_{tot}$  of the stabilization system [13]:

$$s_{tot} = \sqrt{\frac{2hc}{P_{IL}\lambda_{IL}} + \frac{2hc}{P_{OOL}\lambda_{OOL}}} \quad (3)$$

For the system presented here, the error signal was generated with a 0.7-mW NIR beam (at  $\approx 1 \mu\text{m}$ ) and the MIR beam (at  $\approx 10 \mu\text{m}$ ) had an average power of 0.07 mW. This gives a relative shot noise limit for the stabilization system of  $3 * 10^{-8} \text{ Hz}^{-0.5}$ .

### 6.2. Active intensity noise suppression of the near-infrared pulse train

The stabilization system for the MIR light can also be used to stabilize the intensity noise of the driving NIR light. The levels of RIN for the free-running NIR beam and the red edge of the broadened NIR spectrum are depicted in Fig. 6(a). The degrees of noise suppression attained by the different stabilization concepts are show in Fig. 6(b)-6(d) and values of the integrated noise and the noise reduction at 5 kHz are given in Table 1.

Table 1. NIR noise suppression

Stabilization concept	Noise reduction at 5 kHz	Integrated RIN (from 1Hz to 100 kHz)
Free running	-	0.1
1	30	0.021
2a	29	0.006
2b	1.7	0.04
3a	15	0.007
3b	0.08	1.3

In general, better noise suppression can be achieved for NIR than for MIR (up to a factor 30 instead of 20 and an integrated RIN of 0.006% instead of 0.07%). This is not surprising, as the error signal is derived from the very beam that is subjected to stabilization, and therefore one non-linearity less is involved. However, stabilization concept IIIb, which worked best on the MIR, yields only a small noise suppression of about a factor 2 for the NIR. Indeed, stabilization concept Ib actually worsens the RIN of the broadened NIR by a factor of 11. This effect is due to the broadband nature of the NIR radiation. Concepts Ib and IIIb both use

the red edge of the broadened spectra to generate the error signal. As discussed above, the intensity noise within the edges of the broadened spectra is nonlinearly linked to input intensity fluctuations, whereas the fluctuations of the fully broadened NIR are approximately proportional to the input fluctuations (if no losses occur, the output power of the fiber equals the input power) and therefore there may be no linear correlation between the intensity fluctuations of the full NIR beam and those of red part of the spectrum. Additionally, the RIN of the red part of the spectrum is augmented due to the fiber broadening (see Fig. 6(a), black vs gray curve). This part of the spectrum is used to generate the error signal in concept Ib. With active feedback, the AOM compensates for those fluctuations; however, as there is no correlation between the red part of the spectrum and the full spectrum, it introduces additional noise in the rest of the spectrum, as it acts on the full NIR beam. Concept IIIb also uses the red part of the spectrum. In contrast to concept Ib, the AOM is placed in front of the nonlinear fiber and therefore actively controls the input power to the fiber to stabilize the power in the red part of the broadened output spectrum. This also leads to suppression of intensity fluctuations of the integrated spectrum (see Fig. 6(d), cyan curve).

In summary, it can be concluded that the choice of a stabilization concept depends on the desired application, as they will differ in their performance. If the goal is to stabilize the NIR output energy of a nonlinear fiber, the suppression works best if the full optical spectrum of the broadened NIR beam is used for generation of the error signal. However, this does not necessarily stabilize the intensity fluctuations at the edges of the optical spectrum and, as shown in the main text (see Fig 4(a)), it might not improve the stability of a DFG output.

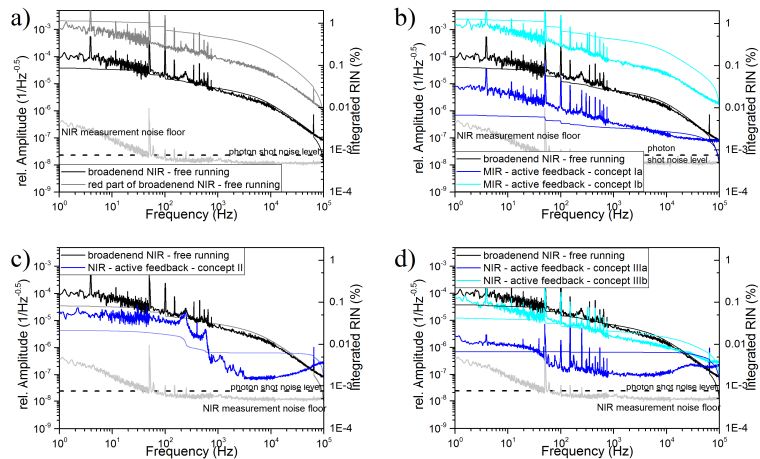


Fig. 6. a) Relative intensity noise and integrated noise (integration starts at 100 kHz) of the free running system for the oscillator (black) and the broadened NIR (gray). b)-d) NIR noise suppression for the different stabilization concepts. Strong NIR noise suppression is only obtained when stabilizing to the full (spectrally integrated) NIR signal.

If the goal is to stabilize the intensity fluctuations within different parts of the optical spectrum and therefore stabilize the spectral broadening itself, the suppression works best if one uses the edge of the broadened NIR to generate the error signal. This approach does not markedly suppress the RIN of the full NIR beam (see Fig. 6(d), cyan curve), but it does lead to a major improvement in the stability of the MIR generated via intra-pulse DFG (see Fig 4(a)).

### 6.3. Relative intensity noise of the free-running broadened NIR and MIR pulse train for frequencies up to 1 MHz

To measure the RIN spectrum of the free-running NIR or MIR beam up to 1 MHz, we used the same photodiodes as before. The noise spectrum was obtained via FFT of the photodiode signal measured with a MHz-Lock-In amplifier (Zürich Instruments, UHFLI) and is displayed in Fig. 7. The RIN of the NIR light approaches the shot noise limit around 200 kHz before the measurement is limited by the detector noise floor.

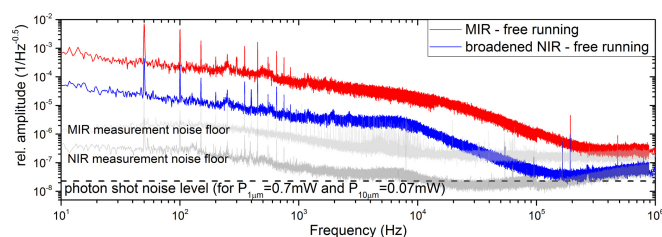


Fig. 7. Relative intensity noise spectrum free-running broadened NIR and MIR pulse train.

### Funding

Munich Centre for Advanced Photonics ([www.munich-photonics.de](http://www.munich-photonics.de)), a DFG-funded Cluster of Excellence.

## 2.2 Field-resolved infrared spectroscopy of biological systems

**Preface:** When I joined the research group of Prof. Krausz in the summer of 2015 and started to work intensively on what we now call *field-resolved spectroscopy* (FRS), we only had a vague idea about the conceptual advantages of FRS. The basic concept that electro-optic sampling (EOS) of impulsively-excited molecular vibrations with femtosecond mid-infrared pulses would allow for a ‘background-free’ measurement of the molecular response has already been the subject of intensive discussions within our group. Back then, we called it ‘zero-background-advantage’ as we expected that the molecular signal would be measured against a zero signal, which is in contrast to conventional absorption spectroscopy where a relative change of transmission is recorded.

Over the years, we obtained a more detailed understanding of the physics underlying FRS. It turned out that there is indeed something similar to a ‘zero-background-advantage’, however it turned out to be slightly different from what we originally anticipated. We realized that there is still an optical background from the near-infrared (NIR) gate pulse used in the EOS. Luckily, this NIR background proved to not be detrimental to the measurement of the MIR signals. In addition, a ‘zero-MIR-background’ can only be obtained under specific requirements, which will be discussed in more detail in the subsequent article and in section 4.2. Therefore, the measurement condition we are currently able to reach can rather be referred to as ‘MIR-reduced background’. However, this already provides distinct measurement advantages as compared to frequency-resolved spectroscopies. Firstly, it enables to drastically reduce the negative influence of intensity fluctuations (and other noise sources), and secondly, it circumvents limitations imposed by the dynamic range of the detector.

The recognition of these conceptual advantages combined with a deep understanding of electro-optic sampling – the key technique to FRS – enabled us to systematically improve the underlying technology. We took measures to compress the MIR pulse temporally in order to access the molecular response more directly [100]. We adjusted the power, shape, and size of the MIR and NIR pulses in the EOS crystal to maximize the detection sensitivity [101]. To reduce the background generated by water vapour, we placed the MIR beam path under vacuum. We optimized the interaction length with the liquid samples (see also section 2.3) to maximize the measurement signal-to-noise ratio [39]. To increase the measurement accuracy we further added active intensity stabilization and tracked the length of the interferometer [45, 102]. And to finally be in a position to adequately analyse this ‘new type’ of spectroscopic data, we developed several new numerical tools that facilitate a deeper understanding of the acquired fingerprint data [103].

All these theoretical considerations and technological developments have led to the development of a device that currently offers orders-of-magnitude higher sensitivity as compared to state-of-the-art Fourier-transform infrared (FTIR) spectroscopy. We were able to demonstrate a 40-times lower limit of detection for dimethylsulfone solved in water when applying FRS. A similar detection limit could be shown for blood serum, which is extremely relevant for infrared fingerprinting of biofluids (see also chapter 3). In addition, we demonstrated an intensity dynamic range of more than 10 orders of magnitude, outperforming conventional FTIR by five orders of magnitude. This puts us in the unique position to probe highly absorbent biological samples, such as living cells and plant tissues.

Considering all this, we believe that the presented results can significantly advance the field of infrared spectroscopy and that FRS will provide the basis for establishing a variety of new applications. This view was also shared by a wider audience and the respective findings were published in *Nature* [40].

## Field-resolved infrared spectroscopy of biological systems

*as published in*

**Nature** (2020)

[40]

*by*

Ioachim Pupeza, Marinus Huber, Michael Trubetskov, Wolfgang  
Schweinberger, Syed A. Hussain, Christina Hofer, Kilian Fritsch, Markus  
Poetzlberger, Lenard Vamos, Ernst Fill, Tatiana Amotchkina, Kosmas V.  
Kepesidis, Alexander Apolonski, Nicholas Karpowicz, Vladimir Pervak, Oleg  
Pronin, Frank Fleischmann, Abdallah Azzeer, Mihaela Žigman, and Ferenc  
Krausz

**Contributions:** I made substantial contributions to the design of the experiments and contributed significantly to the theoretical and conceptual description of the FRS. I took all measurements presented in this work and helped with the writing of the manuscript.



## Article

# Field-resolved infrared spectroscopy of biological systems

<https://doi.org/10.1038/s41586-019-1850-7>

Received: 1 February 2019

Accepted: 29 October 2019

Published online: 1 January 2020

Ioachim Pupeza<sup>1,2,5\*</sup>, Marinus Huber<sup>1,2,5</sup>, Michael Trubetskov<sup>2</sup>, Wolfgang Schweinberger<sup>1,3</sup>, Syed A. Hussain<sup>1,2</sup>, Christina Hofer<sup>1,2</sup>, Kilian Fritsch<sup>1</sup>, Markus Poetzlberger<sup>2</sup>, Lenard Vamos<sup>2</sup>, Ernst Fill<sup>1</sup>, Tatiana Amotchkina<sup>1</sup>, Kosmas V. Kepesidis<sup>1</sup>, Alexander Apolonski<sup>1</sup>, Nicholas Karpowicz<sup>2</sup>, Vladimir Pervak<sup>1,2</sup>, Oleg Pronin<sup>1,2</sup>, Frank Fleischmann<sup>2,4</sup>, Abdallah Azzeer<sup>3</sup>, Mihaela Žigman<sup>1,2,4</sup> & Ferenc Krausz<sup>1,2,4\*</sup>

The proper functioning of living systems and physiological phenotypes depends on molecular composition. Yet simultaneous quantitative detection of a wide variety of molecules remains a challenge<sup>1–8</sup>. Here we show how broadband optical coherence opens up opportunities for fingerprinting complex molecular ensembles in their natural environment. Vibrationally excited molecules emit a coherent electric field following few-cycle infrared laser excitation<sup>9–12</sup>, and this field is specific to the sample's molecular composition. Employing electro-optic sampling<sup>10,12–15</sup>, we directly measure this global molecular fingerprint down to field strengths  $10^7$  times weaker than that of the excitation. This enables transillumination of intact living systems with thicknesses of the order of 0.1 millimetres, permitting broadband infrared spectroscopic probing of human cells and plant leaves. In a proof-of-concept analysis of human blood serum, temporal isolation of the infrared electric-field fingerprint from its excitation along with its sampling with attosecond timing precision results in detection sensitivity of submicrograms per millilitre of blood serum and a detectable dynamic range of molecular concentration exceeding  $10^5$ . This technique promises improved molecular sensitivity and molecular coverage for probing complex, real-world biological and medical settings.

The molecular composition of living organisms is a sensitive indicator of their physiological states. Even apparently simple physiological transitions are often connected to highly multivariate concurrent molecular changes. Therefore, the capability to simultaneously observe changes in concentrations of a variety of molecules embedded in complex organic consortia is likely to be instrumental in advancing biology and medical diagnostics systems.

Many biologically relevant changes occur at concentration levels that are often not detectable in system-wide molecular milieu owing to the vast dynamic range of molecular concentrations<sup>1</sup>. Simultaneous quantitative probing of multiple molecules within a complex consortium relies on either biochemical separation of certain types of molecules or depletion of highly abundant ones<sup>16</sup>. Such approaches are time-consuming or expensive or suffer from poor reproducibility, impeding robust, high-throughput implementations. Here we harness broadband optical coherence to address this challenge directly.

Optical spectroscopy of biological samples interrogates the chemical substructures of intact molecules (molecular fragments<sup>17</sup>) rather than molecules as a whole<sup>18,19</sup> by detecting their resonant vibrational response to infrared or Raman excitation. Occurrence of the same or similar fragments in different biomolecules and rapid dephasing results in overlapping temporal and spectral responses and hampers

the identification of individual molecules<sup>2–4</sup> in complex samples. However, the detected superposition of the responses of all fragments is characteristic of molecular composition, representing what may be referred to as the global molecular fingerprint (GMF) of the sample.

Higher excitation power increases the GMF signal, making smaller changes in the sample's molecular composition detectable. In spectroscopies that capture time-integrated fields<sup>11,20–23</sup>—that is, frequency-resolved spectroscopy—the GMF signal hits the detector along with the (much stronger) excitation transmitted through the sample. This has far-reaching implications. First, in the limit of strong excitation, the weakest molecular signal detectable tends to be limited by the technical noise of the excitation source<sup>22,24</sup>. Second, and more fundamentally, even in the absence of technical noise, saturation of the detector (elements) places a limit on the sensitivity<sup>11,22,24</sup>. These limitations are schematically illustrated in Fig. 1a, see 'Frequency-resolved spectroscopy'.

In this work, we show how time-resolved sampling of the electric field emitted by impulsively excited molecular vibrations allows us to overcome these limitations by isolating the retarded molecular signal from any excitation background. We term the technique field-resolved spectroscopy (FRS). Sensitive sampling of the isolated molecular signal generated by a powerful, ultrashort-pulsed infrared source enables broadband transmission spectroscopy of biological systems in their

<sup>1</sup>Ludwig Maximilians University München, Garching, Germany. <sup>2</sup>Max Planck Institute of Quantum Optics, Garching, Germany. <sup>3</sup>King Saud University, Department of Physics and Astronomy, Riyadh, Saudi Arabia. <sup>4</sup>Center for Molecular Fingerprinting, Budapest, Hungary. <sup>5</sup>These authors contributed equally: Ioachim Pupeza, Marinus Huber. \*e-mail: ioachim.pupeza@mpq.mpg.de; krausz@lmu.de

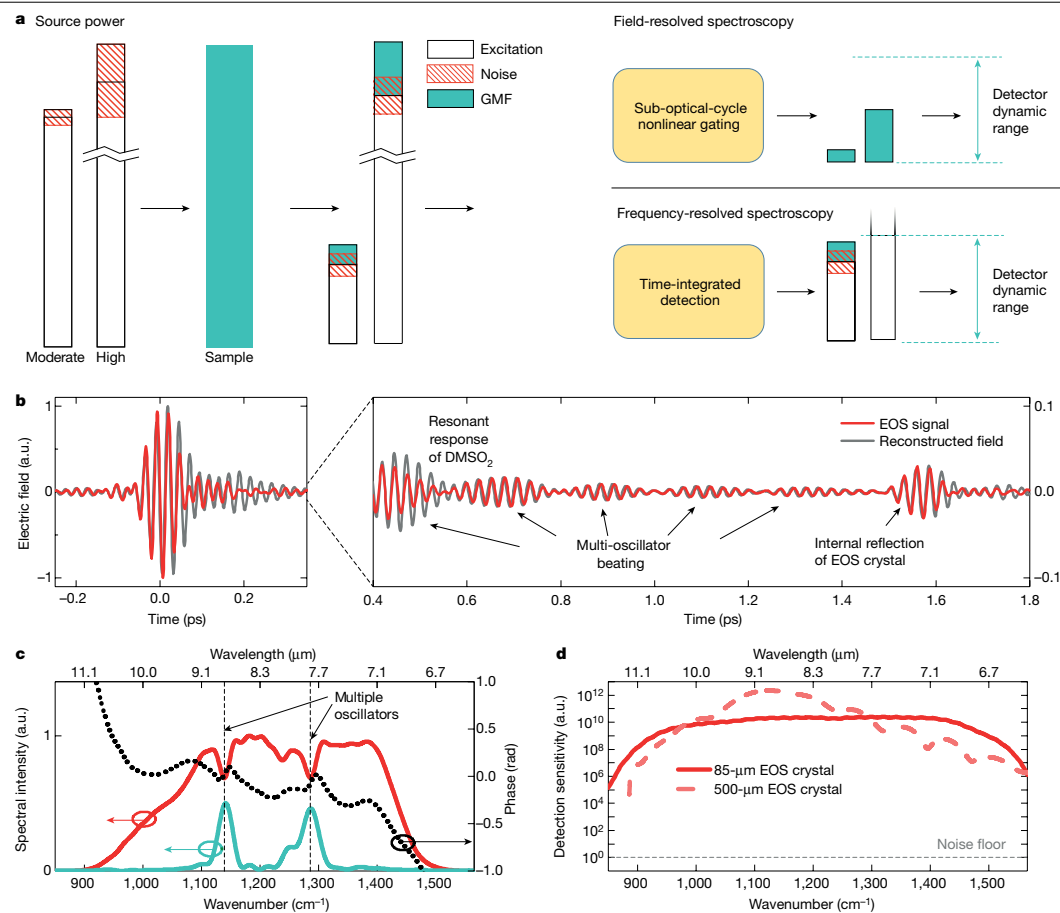


**Fig. 1 | Infrared FRS.** **a**, Schematic comparison of spectroscopic techniques. Infrared light (white bar length indicates source power) with intensity noise (technical noise, red hatching) is transmitted through a sample, acquiring GMF information (cyan shading). For frequency-resolved spectroscopy, the GMF signal is detected 'on top' of the excitation signal transmitted through the sample. As a consequence, (1) the GMF signal needs to surpass the excitation noise (surviving balanced detection) and (2) enhancing the GMF signal by increasing the excitation power is limited by the detector's dynamic range. For FRS, following a few-cycle excitation, sub-optical-cycle nonlinear gating isolates ultrabrief fractions of the GMF from any infrared background, avoiding both requirement (1) and limit (2); see Methods. **b**, Infrared electric field as reconstructed from the measured electro-optic sampling (EOS) trace using an 85-μm-thick GaSe EOS crystal (Supplementary Information section I) after transmission through a solution of 10 mg ml<sup>-1</sup> DMSO<sub>2</sub> in water.

The reconstructed electric field strongly resembles the EOS signal, owing to the broadband instrument response function. The resonant sample response is temporally well separated from the non-resonant response (incorporating the excitation) and exhibits 'beating' of several oscillation frequencies. **c**, Fourier transform of the EOS trace shown in **b**, truncated at 1.5 ps to exclude spectral modulations caused by the echo in the EOS crystal. The solid red line shows the spectral intensity, revealing absorption dips associated with vibrational modes of DMSO<sub>2</sub> molecules; the black dashed line shows the spectral phase; the cyan line shows the spectral intensity of the signal in the time window 380–1,500 fs, showing time-filtered GMF information. **d**, Spectral detection sensitivity above the detection noise floor (3-ps time window, 25-s measurement time, transmission through cuvette filled with water). The solid and dashed lines are the bandwidth-optimized versus quantum-efficiency-maximized EOS (Supplementary Information section I), respectively.

natural, aqueous environment (see 'Field-resolved spectroscopy' in Fig. 1a).

### Field-resolved molecular spectroscopy

Fourier-transform infrared (FTIR) spectrometers employing thermal radiation sources<sup>20</sup> are the gold standard for broadband vibrational spectroscopy<sup>2–4,7,8,19,24–33</sup>. In liquid samples, they have detected

concentration levels down to several micrograms per millilitre<sup>3,25,27,30,33,34</sup>. This limitation has so far been overcome only by sample drying<sup>33</sup> or targeted detection with functionalized optical biosensors<sup>34,35</sup>.

Recently, tunable quantum cascade lasers<sup>23,24,27,36,37</sup> and femtosecond laser sources<sup>15,38–40</sup> have dramatically enhanced the excitation brilliance. For the reasons sketched in Fig. 1a and explained in the Methods, frequency-resolved spectroscopies have not been able to fully capitalize on this to achieve improved sensitivity and specificity in molecular

## Article

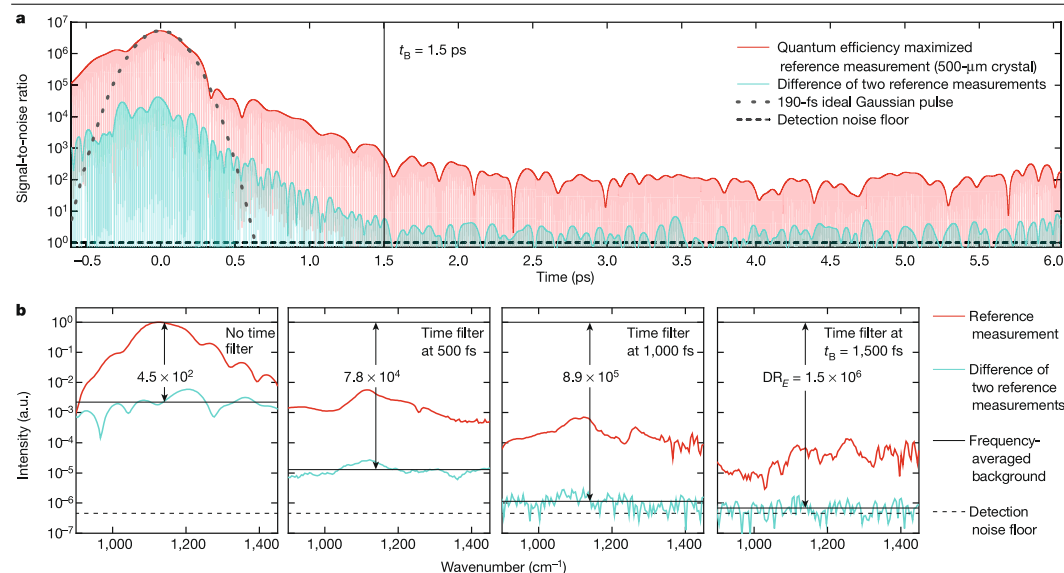


**Fig. 2 | Background quantification for detection of resonant molecular responses.** **a**, The red line is the time-resolved magnitude of the EOS signal (revealing field oscillations) related to the detection noise floor (signal-to-noise ratio), for a reference measurement of pure water (quantum-efficiency-maximized detection setting, 37-s effective measurement time). Following the excitation, the molecular signal from residual atmospheric background in the beam path is observed. The cyan line is the numerical difference of two independent reference measurements. The recorded traces were frequency-

filtered by a 20th-order super-Gaussian filter suppressing any noise outside the spectral window 900–1,450  $\text{cm}^{-1}$ . The grey dotted line is the 190-fs (full-intensity-width-at-half-maximum duration) ideal Gaussian pulse, for comparison. **b**, Frequency-domain definition of DR<sub>E</sub> and  $t_B$ . The magnitudes of the Fourier transforms of the traces in a are shown for different numerical high-pass time filter values. Setting the filter at  $t_B$  (the beginning of the background-free time-domain measurement, rightmost panel) yields an electric-field peak dynamic range of DR<sub>E</sub> =  $1.5 \times 10^6$  around 1,140  $\text{cm}^{-1}$ .

detection<sup>24,27</sup>. Here, we show how FRS of few-cycle infrared-laser-excited molecular vibrations enables us to take advantage of the temporal structure and power of laser-driven few-cycle infrared sources.

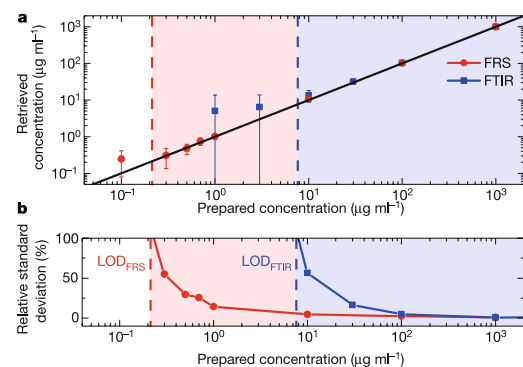


**Fig. 3 | Limit of detection of DMSO<sub>2</sub> molecules dissolved in water.** **a**, Results of the concentration retrieval (see Supplementary Information section IV) with quantum-efficiency-optimized FRS (red data points) and FTIR (blue data points). The dots indicate the mean values obtained from at least five measurements per concentration and the error bars show the absolute standard deviation. **b**, Relative standard deviation for the retrieved values. LOD, limit of detection. The coloured shading indicates the range of concentrations exceeding the LOD of each instrument.

The experimental setup is described in the Methods and in Supplementary Information section I (see also Extended Data Figs. 3, 4). In short, waveform-stable, few-cycle mid-infrared (MIR) pulses abruptly excite molecular vibrations by resonant absorption. The sample-specific electric field (previously referred to as GMF) emitted in the wake of the excitation pulse (Supplementary Video 1 and Methods) is detected via EOS<sup>10,13–15</sup> (Fig. 1b, c). The thickness of the electro-optic crystal controls a trade-off between the bandwidth and the sensitivity of detection (Fig. 1d).

The nonlinear frequency conversion underlying EOS sequentially isolates ultrabrief fractions of the GMF from any infrared background—including the excitation pulse transmitted through the sample, and the thermal background (see Fig. 1a and Methods). Drawing on preliminary experiments<sup>41,42</sup>, here we report a direct measurement of MIR molecular electric fields emanating from biological samples.

### Detection of time-gated molecular signals

In any scheme measuring time-integrated fields, the minimum detectable absorbance, MDA<sub>FD</sub>, defining the minimum detectable depth of the dips in the red line in Fig. 1c, is given by (Supplementary Information section II):

$$\text{MDA}_{\text{FD}} \approx \sigma \quad (1)$$

where  $\sigma$  represents the relative fluctuations of the measured signal in the considered spectral element. Here,  $\sigma$  incorporates contributions from excitation and detection noise, as well as from the limited detector dynamic range<sup>22</sup>.

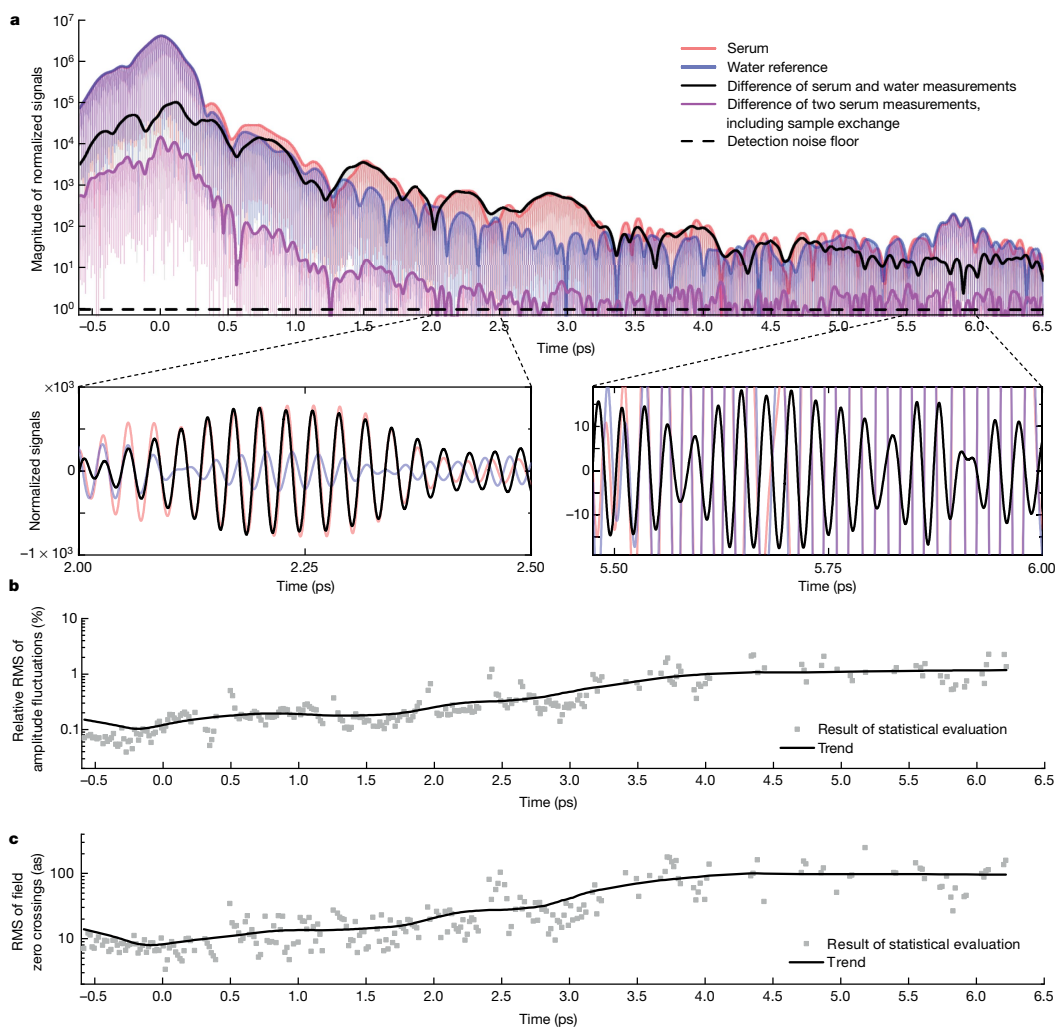


**Fig. 4 | GMFs of human blood serum and their reproducibility.** **a**, Magnitude of the EOS signals, recorded with quantum-efficiency-optimized FRS (see key). The insets show linear-scale representations of the signals depicted in the main panel in two different time windows. **b**, **c**, Relative (**b**) and absolute (**c**) root-mean-square (RMS) of oscillation amplitude and zero crossings of five hundred measurements of the GMF of a serum sample (without sample exchange) (see Supplementary Information section V).

In FRS, temporal isolation of (wave-cycle-scale) fractions of the GMF renders the weakest detectable molecular response largely immune against the noise of excitation intensity, as is apparent from the cyan line in Fig. 1c. This is indicated by the expression for the MDA obtained by time-domain modelling of the molecular system with an isolated Lorentzian oscillator of dephasing time  $T_L$  (Supplementary Information section II):

$$\text{MDA}_{\text{FRS}} = \frac{2}{\text{DR}_E} \exp\left(\frac{t_B}{T_L}\right) \quad (2)$$

Here, the dynamic range  $\text{DR}_E$  is defined as the ratio of the spectral amplitude of the electric field of the overall signal reaching the detector at the centre frequency of the Lorentzian oscillator to that of the weakest

signal detectable after passage through a temporal filter opening at  $t_B$ . The parameter  $t_B$  is defined as the instant when the temporal window for an infrared-background-free measurement begins.

This is the case when the numerical difference between two subsequent measurements (in this case, of liquid water) reaches the detection noise floor (Fig. 2a). In our proof-of-principle measurement with the quantum-efficiency-maximized FRS setting, this occurs at about  $t_B = 1,500$  fs, yielding a value of  $\text{DR}_E$  in excess of  $10^6$  for absorptions with centre frequencies between  $1,080 \text{ cm}^{-1}$  and  $1,190 \text{ cm}^{-1}$  (for a 7-ps time window and 37-s effective measurement time, see right panel of Fig. 2b). For a dephasing time of the order of a picosecond, typical for an aqueous environment<sup>8</sup>, equation (2) predicts a minimum detectable absorbance of the order of  $10^{-6}$ .

## Article

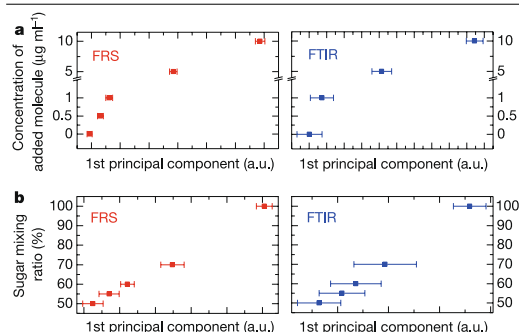


**Fig. 5 | Sensitivity and specificity of FRS of complex fluids performed with bandwidth-optimized sampling.** **a**, Principal component analysis results (separation along the 1st principal component) for a human blood serum sample containing an added aqueous solution of decreasing DMSO<sub>2</sub> concentration, and fingerprinted with FRS using quantum-efficiency-optimized detection (left panel) and with FTIR (right panel). The plots show the mean and relative standard deviation of the values of the 1st principal component for data classes obtained by repeated measurements of samples with nominally identical added DMSO<sub>2</sub> concentration. **b**, Principal component analysis results for a mixture of two sugars dissolved in water with constant total concentration and varying relative concentration (see text), and fingerprinted with FRS using bandwidth-optimized detection (left panel) and with FTIR (right panel).

For experimental verification, we investigated methylsulfonylmethane (DMSO<sub>2</sub>) dissolved in deionized water. FRS was benchmarked against a state-of-the-art FTIR spectrometer equipped with a thermal infrared source (MIRA Analyzer, Micro Biolytics; see Supplementary Information section III). With both instruments, at least five aliquots of concentrations ranging from 1 mg ml<sup>-1</sup> to 100 ng ml<sup>-1</sup> were measured over a duration of  $T = 45$  s each, with a spectral resolution of 4 cm<sup>-1</sup> (realized in FRS by setting the duration of the temporal window of measurement equal to 8.3 ps). Reference measurements of solvent only (deionized water) were performed in alternating order. The concentration values retrieved from the measured data (see Supplementary Information section IV) are summarized in Fig. 3. The limit of detection is defined as the concentration retrieved with a relative standard deviation of 100%. Our study yields an FRS limit of detection of 200 ng ml<sup>-1</sup>, by a factor of 40 lower than that obtained with the FTIR spectrometer (8 µg ml<sup>-1</sup>). This is in agreement with the prediction of equation (2); see Supplementary Information section IV and Extended Data Fig. 7. We estimate a limit of detection of approximately 7 µg ml<sup>-1</sup> for Fourier-transform spectroscopy (FTS)<sup>22</sup> performed with our coherent infrared source and state-of-the-art infrared photodetectors (see Methods).

The exponential dependence of the detection limit on  $t_b$  in equation (2) emphasizes how FRS is fundamentally different from any frequency-domain spectroscopy, where  $t_b$  is irrelevant (see also Methods). To investigate this dependence—and thereby this hitherto unexplored advantage—we repeated the DMSO<sub>2</sub> dilution series measurement with shorter, sub-60-fs infrared excitation pulses (Supplementary Information section I) and the bandwidth-optimized detection setting of the FRS instrument (Fig. 1d, continuous line). This combination substantially improved the opening time for background-free detection to  $t_b = 450$  fs (Supplementary Information section IV). The improvement came at the expense of a factor-of-ten reduction of DR<sub>c</sub> (Fig. 1d). This reduction would, in its own right, result in a factor-of-ten increase of the minimum detectable concentration, according to equation (2). By contrast, we observe an increase from 200 ng ml<sup>-1</sup> to 450 ng ml<sup>-1</sup> only, mainly due to shortening  $t_b$  from 1.5 ps to 0.45 ps (Supplementary

Information section IV). This corroborates the predicted sensitivity of  $\text{MDA}_{\text{FRS}} \propto t_b$ .

A more powerful broadband few-cycle infrared source<sup>40</sup> will improve DR<sub>c</sub> while preserving the full bandwidth along with the reduced  $t_b$ . This holds promise for a detection limit below 50-ng ml<sup>-1</sup> in combination with super-octave spectral coverage.

## Attosecond-timed molecular signals

For the investigation of complex molecular consortia, the sensitivity and specificity of FRS-based molecular fingerprinting depends critically on the temporal coherence of the GMF signal and its reproducibility over extended measurement time. In gas-phase samples, vibrational dephasing occurs on the nanosecond scale and the required long acquisition delays are advantageously realized with two asynchronous femtosecond oscillators<sup>12,21,43,44</sup>, harnessing optical frequency-comb techniques<sup>45,46</sup>. By contrast, in the liquid phase the coherent molecular signal survives only for several picoseconds<sup>9</sup>. To efficiently use measurement time and ensure attosecond delay precision, we implemented waveform sampling with a mechanical delay line equipped with interferometric delay tracking<sup>47</sup>. Figure 4a shows the field-resolved GMF of a human blood serum sample, as representative of a cell-free bioliquid routinely used in biomedical profiling. The insets in Fig. 4a, b show the differential GMF of the biomolecular ensemble in the sample, as a result of subtracting the signal obtained from pure water from the one of the sample. This ‘pure’ biomolecular signal decays by a few orders of magnitude within 5 ps (compare the left and right panels in Fig. 4b), revealing a dephasing time of collective biomolecular vibrations in human blood serum far below 1 ps.

Five hundred consecutive measurements of the same serum sample yield a relative root-mean-square deviation of the field oscillation amplitude from its mean value of around 0.2% and an absolute root-mean-square of the zero crossings of the infrared GMF field in the range of 20 as, within the first two picoseconds following the excitation (Fig. 4c, d). It is this reproducibility that enables suppression of the electric field background by up to three orders of magnitude via comparison with a reference field (Figs. 2a and 4a), opening the window for background-free measurement less than 2 ps after the excitation pulse peak, even in a highly complex sample such as blood serum (Fig. 4a, magenta line).

## Sensitivity and specificity of FRS

In real-world applications<sup>2–4,26,27</sup>, molecular fingerprinting of complex biofluids will need to probe minuscule changes in the sample’s chemical composition, often caused by low-abundance molecules. The method’s utility for biological or medical applications will be greatly dependent on the smallest changes in molecular concentration that can cause a detectable distortion of the field-resolved GMF. To assess this concentration level, we added controlled amounts of DMSO<sub>2</sub> to the serum sample fingerprinted in Fig. 4a. The results of a principal component analysis of the infrared fingerprints of these samples, measured with our FRS and FTIR devices (Supplementary Information section VI and Extended Data Fig. 8) are shown in Fig. 5a. The plots show the mean and the spread of the data classes of repeated measurements of samples with different concentrations of the added molecule, along the first principal component. FRS appears to clearly separate the sample containing additional DMSO<sub>2</sub> molecules at a concentration of 500 ng ml<sup>-1</sup> from the reference sample. Moreover, the error bars suggest that FRS is capable of detecting changes in molecular concentration down to the 200 ng ml<sup>-1</sup> level in human blood serum, an improvement of nearly an order of magnitude compared to state-of-the-art FTIR spectrometry.

Hence, the smallest changes currently detectable are more than five orders of magnitude below the concentration of the most highly

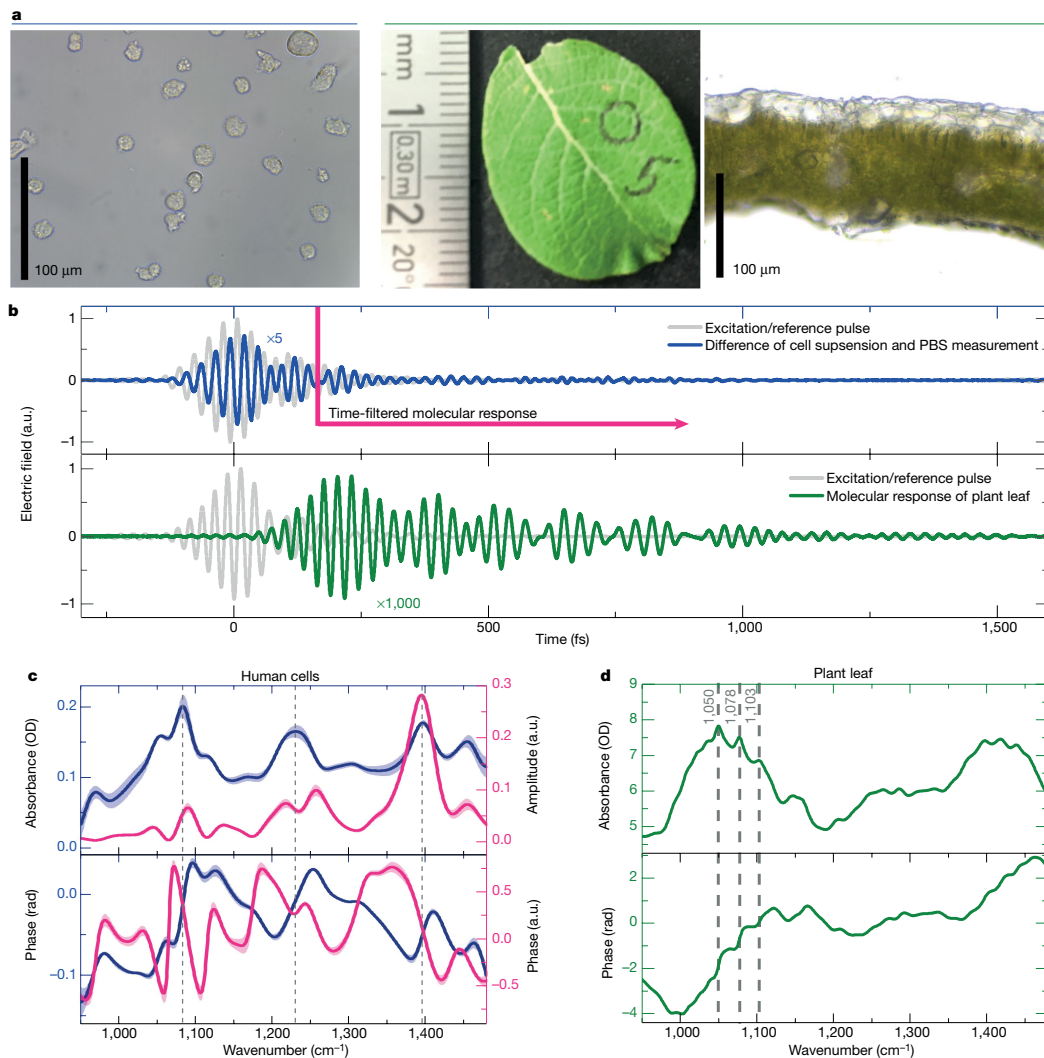


**Fig. 6 | FRS of strongly absorbing living systems.** **a**, The blue-outlined (left) panel is an optical microscope image of cultured human THP-1 cells. The green-outlined panel (right) shows the top and lateral views of a leaf from *Salix caprea*. The measurement of the intact hydrated leaf was performed 5 min after collection, within the marked area. **b**, The upper panel shows GMF of THP-1 cells in suspension, contained in a 100-μm-thick cuvette (blue line) referenced by numerical subtraction to the signal of the suspension medium (phosphate-buffered saline, PBS; grey line). The lower panel shows the molecular response obtained after transmission through a 120-μm-thick leaf of *Salix caprea* (green

line) with air reference (grey line). **c**, Absorption (top panel) and phase (lower panel) spectra of five measurements of human THP-1 cells (blue lines) along with the amplitude and phase of temporally-filtered GMFs (magenta lines). Absorption and phase spectra of the plant leaf are shown in **a**. The standard deviations of multiple measurements in **c** and **d** are indicated by the shaded areas (see Supplementary Information section VII for data processing). We note that the error corridor of the measurement in **d** is smaller than the line thickness and therefore not visible. The grey dotted lines in **c** and **d** indicate prominent absorption peaks.

abundant molecules of blood serum, albumin<sup>1</sup>. This implies a detectable concentration dynamic range in excess of  $10^5$ .

Although the relative intensity noise of the excitation does not affect the FRS limit of molecular detection with a spectrally isolated feature, the lowest detectable concentration of the same molecule in a complex environment is limited by the relative intensity noise of the overall GMF

signal. This, in turn, is likely to be dominated by the noise of the excitation source. As an important consequence, the current FRS concentration dynamic range of  $10^5$  offers substantial room for further improvement by suppressing the noise of the GMF signal. An efficient measure to this end may be 'freezing' the excitation source noise by scanning faster than the characteristic time of low-frequency intensity fluctuations<sup>22,48</sup>.



## Article

To test the specificity of the measured fingerprints, that is, the sensitivity to small changes in relative concentrations, we prepared aqueous solutions of two different sugar molecules of constant total concentration and varying relative concentrations (Supplementary Information section VI). The total concentration of  $100 \mu\text{g ml}^{-1}$  was chosen to be well above the limit of detection of both instruments. To challenge the method, we used two molecules, maltose and melibiose, which have very similar absorption characteristics (Supplementary Information Section VI and Extended Data Fig. 9). The data in Fig. 5b reveal that FRS outperforms FTIR spectrometry in sensing not only small absolute changes but is also sensitive to relative changes in concentration of molecules of a complex ensemble.

### Probing of intact biological systems

Non-invasive, quantitative probing of intact biological systems would benefit a diversity of biological, biomedical, pharmaceutical and ecological applications. To circumvent sensitivity limitations caused by the strong absorption of infrared radiation in liquid water, so far the majority of studies of biological matter have drawn on sample preparations<sup>7,8,28,29</sup> that substantially alter the state of the sample (such as drying, fixation, slicing, chemical extraction, homogenization and so on). Direct interrogation of intact living systems with infrared spectroscopy has been limited to interaction lengths of the order of  $10 \mu\text{m}$  (or less), either in attenuated-total-reflection geometry<sup>28</sup> or by using extremely thin microfluidic cuvettes<sup>31,32</sup>. Both implementations prevent the majority of living cells from being studied in vivo (for example, human cells are on average larger than  $10 \mu\text{m}$  in diameter). More recently, quantum-cascade lasers have enabled infrared transmission measurements of living systems with path lengths of several tens of micrometres, albeit with restrictions on the bandwidth and with modest signal-to-noise ratios<sup>36,37</sup>.

The unparalleled dynamic range of FRS implemented with a powerful few-cycle infrared source enables these restrictions to be overcome. Here we present the feasibility of infrared fingerprinting of living human cells (THP-1 leukaemic-monocyte-like cell line) cultured and measured directly in suspension (Fig. 6a, left panel) by transillumination of a 0.1-mm-thick flow-through cuvette (see also Supplementary Information section VII). In spite of the order-of-magnitude increase in interaction length as compared to previous broadband measurements of cells from the same cell line<sup>49</sup>, the differential signal originating from the molecules of the cells (blue line in Fig. 6b) is acquired with a high signal-to-noise ratio (Supplementary Information section VII). The corresponding absorption and phase spectra are depicted in Fig. 6c (blue lines), with the former reflecting well the spectral signatures featured by THP-1 cells when squeezed into a  $7\text{-}\mu\text{m}$ -thick cuvette<sup>49</sup>. Temporal gating of the molecular signal (magenta lines in Fig. 6c) uncovers the splitting of the absorption lines at approximately  $1,080 \text{ cm}^{-1}$  and  $1,230 \text{ cm}^{-1}$ , along with relevant phase oscillations—features that are not apparent in the time-integrated spectra (blue lines). This underlines the power of isolating the molecular signal from an (inherently) noisy excitation, offered by FRS.

We have further tested the ability of FRS to acquire transmission spectra of strongly absorbing samples by transilluminating intact plant leaves from the goat willow (*Salix caprea*), a common deciduous tree, with a thickness of approximately  $120 \mu\text{m}$  (Fig. 6a, right panel). The spectra in Fig. 6d feature clearly discernible absorption bands at  $1,050 \text{ cm}^{-1}$ ,  $1,078 \text{ cm}^{-1}$  and  $1,103 \text{ cm}^{-1}$ , corresponding to the C–O stretching motion characteristic of carbohydrates<sup>7,50</sup> widespread in cell walls and cellular compartments of plant leaves. The spectrally resolved attenuation ranges from 5 to 8 orders of magnitude, which is orders of magnitude higher than previously demonstrated in a broadband infrared transmission measurement. In addition, it shows the instrument's ability to resolve absorption over several orders of magnitude in strength without the need to adjust the light power reaching the detector<sup>24</sup>.

### Conclusions and outlook

We have measured infrared-electric-field molecular fingerprints of organic molecules in aqueous solution and in human blood sera. In both settings, the limit of detecting changes in concentration of individual molecules lies in the range of hundreds of nanograms per millilitre for less than one minute of data acquisition time. The amplitude of the coherent emission carrying the GMF of human blood serum was observed to decay by a few orders of magnitude within a few picoseconds. The reproducibility of electric-field oscillations was found to be in the range of tens of attoseconds over a temporal span exceeding six picoseconds following the excitation.

These findings emphasize the performance of FRS of impulsively excited molecular vibrations for GMF of complex biofluids and uncover potential for its further improvement. First, the extremely fast (much less than a picosecond) decay of vibrational coherence in human blood serum suggests an exponential improvement of the detection limit with further steepening of the temporal decay of the excitation transmitted through the sample. Second, the coherence of the recorded molecular signal over spans of several picoseconds along with reduced source-noise-induced GMF noise, by rapid scanning<sup>48</sup>, for example, will increase the detectable range of concentrations in biofluids. The capability of simultaneous probing of multi-molecular changes over a dynamic range of detectable concentration changes in excess of  $10^5$  holds promise for applications in the life sciences and medical diagnostics.

Last, broadband infrared fingerprinting of physiologically relevant living human cells is now feasible in transmission, opening the door for combining infrared fingerprinting with standard flow cytometry. The unparalleled dynamic range of FRS implemented with powerful few-cycle light promises a new regime of transmission-mode vibrational spectroscopy and spectro-microscopy of intact living systems: individual biological cells, bulk-cell and tissue cultures, organs such as plant leaves—all settings in which excessive water absorption has so far constituted a major obstacle.

### Online content

Any methods, additional references, Nature Research reporting summaries, source data, extended data, supplementary information, acknowledgements, peer review information; details of author contributions and competing interests; and statements of data and code availability are available at <https://doi.org/10.1038/s41586-019-1850-7>.

- Geyer, P. E., Holdt, L. M., Teupser, D. & Mann, M. Revisiting biomarker discovery by plasma proteomics. *Mol. Syst. Biol.* **13**, 942 (2017).
- Barth, A. & Hais, P. I. *Biological and Biomedical Infrared Spectroscopy* (IOS Press, 2009).
- Lasch, P. & Kneipp, J. *Biomedical Vibrational Spectroscopy* (Wiley, 2010).
- Baker, M. J. et al. Developing and understanding biofluid vibrational spectroscopy: a critical review. *Chem. Soc. Rev.* **45**, 1803–1818 (2016).
- Hasin, Y., Seldin, M. & Lusa, A. Multi-omics approaches to disease. *Genome Biol.* **18**, 83 (2017).
- Chen, R. et al. Personal omics profiling reveals dynamic molecular and medical phenotypes. *Cell* **148**, 1293–1307 (2012).
- Türker-Kaya, S. & Huck, C. A review of mid-infrared and near-infrared imaging: principles, concepts and applications in plant tissue analysis. *Molecules* **22**, 168 (2017).
- Doherty, J., Cinque, G. & Gardner, P. Single-cell analysis using Fourier transform infrared microspectroscopy. *Appl. Spectrosc. Rev.* **52**, 560–587 (2017).
- Laubereau, A. & Kaiser, W. Vibrational dynamics of liquids and solids investigated by picosecond light pulses. *Rev. Mod. Phys.* **50**, 607–665 (1978).
- Sell, A., Scheu, R., Leitenstorfer, A. & Huber, R. Field-resolved detection of phase-locked infrared transients from a compact Er-fiber system tunable between 55 and 107 THz. *Appl. Phys. Lett.* **93**, 251107 (2008).
- Coddington, I., Swann, W. C. & Newbury, N. R. Time-domain spectroscopy of molecular free-induction decay in the infrared. *Opt. Lett.* **35**, 1395–1397 (2010).
- Kowligy, A. S. et al. Infrared electric field sampled frequency comb spectroscopy. *Sci. Adv.* **5**, eaaw8794 (2019).
- Wu, Q. & Zhang, X.-C. Free-space electro-optic sampling of terahertz beams. *Appl. Phys. Lett.* **67**, 3523–3525 (1995).
- Nahata, A., Weling, A. S. & Heinz, T. F. A wideband coherent terahertz spectroscopy system using optical rectification and electro-optic sampling. *Appl. Phys. Lett.* **69**, 2321–2323 (1996).

15. Pupeza, I. et al. High-power sub-two-cycle mid-infrared pulses at 100 MHz repetition rate. *Nat. Photon.* **9**, 721–724 (2015).
16. Gianazza, E., Miller, I., Palazzolo, L., Parravicini, C. & Eberini, I. With or without you—proteomics with or without major plasma/serum proteins. *J. Proteomics* **140**, 62–80 (2016).
17. Dębska, B. & Guzowska-Swider, B. Fuzzy definition of molecular fragments in chemical structures. *J. Chem. Inf. Comput. Sci.* **40**, 325–329 (2000).
18. Demtröder, W. *Molecular Physics* (Wiley, 2005).
19. Movasaghi, Z., Rehman, S. & ur Rehman, Dr. I. Fourier transform infrared (FTIR) spectroscopy of biological tissues. *Appl. Spectrosc. Rev.* **43**, 134–179 (2008).
20. Griffiths, P. R. & De Haseth, J. A. *Fourier Transform Infrared Spectrometry* (Wiley, 2007).
21. Keilmann, F., Gohle, C. & Holzwarth, R. Time-domain mid-infrared frequency-comb spectrometer. *Opt. Lett.* **29**, 1542–1544 (2004).
22. Newbury, N. R., Coddington, I. & Swann, W. Sensitivity of coherent dual-comb spectroscopy. *Opt. Express* **18**, 7929–7945 (2010).
23. Villares, G., Hugi, A., Blaser, S. & Faist, J. Dual-comb spectroscopy based on quantum-cascade-laser frequency combs. *Nat. Commun.* **5**, 5192 (2014).
24. Schwaighofer, A. et al. Beyond Fourier transform infrared spectroscopy: external cavity quantum cascade laser-based mid-infrared transmission spectroscopy of proteins in the amide I and amide II region. *Anal. Chem.* **90**, 7072–7079 (2018).
25. Haas, J., Catalán, E. V., Piron, P., Karlsson, M. & Mizaikoff, B. Infrared spectroscopy based on broadly tunable quantum cascade lasers and polycrystalline diamond waveguides. *Analyst* **143**, 5112–5119 (2018).
26. Ollesch, J. et al. An infrared spectroscopic blood test for non-small cell lung carcinoma and subtyping into pulmonary squamous cell carcinoma or adenocarcinoma. *Biomed. Spectrosc. Imaging* **5**, 129–144 (2016).
27. Brandstetter, M., Volgger, L., Gerner, A., Jungbauer, C. & Lendl, B. Direct determination of glucose, lactate and triglycerides in blood serum by a tunable quantum cascade laser-based mid-IR sensor. *Appl. Phys. B* **110**, 233–239 (2013).
28. Baker, M. J. et al. Using Fourier transform IR spectroscopy to analyze biological materials. *Nat. Protocols* **9**, 1771–1791 (2014).
29. Martin, M. C. et al. 3D spectral imaging with synchrotron Fourier transform infrared spectro-microtomography. *Nat. Methods* **10**, 861–864 (2013).
30. Rohleder, D. et al. Comparison of mid-infrared and Raman spectroscopy in the quantitative analysis of serum. *J. Biomed. Opt.* **10**, 031108 (2005).
31. Bhargava, R. Infrared spectroscopic imaging: the next generation. *Appl. Spectrosc.* **66**, 1091–1120 (2012).
32. Quaroni, L., Zlateva, T., Wehbe, K. & Cinque, G. Infrared imaging of small molecules in living cells: from *in vitro* metabolic analysis to cytopathology. *Faraday Discuss.* **187**, 259–271 (2016).
33. Bonnier, F. et al. Ultra-filtration of human serum for improved quantitative analysis of low molecular weight biomarkers using ATR-IR spectroscopy. *Analyst* **142**, 1285–1298 (2017).
34. Haas, J. & Mizaikoff, B. Advances in mid-infrared spectroscopy for chemical analysis. *Annu. Rev. Anal. Chem.* **9**, 45–68 (2016).
35. Lu, R. et al. High-sensitivity infrared attenuated total reflectance sensors for in situ multicomponent detection of volatile organic compounds in water. *Nat. Protocols* **11**, 377–386 (2016).
36. Haase, K., Kröger-Lui, N., Pucci, A., Schönhals, A. & Petrich, W. Advancements in quantum cascade laser-based infrared microscopy of aqueous media. *Faraday Discuss.* **187**, 119–134 (2016).
37. Haase, K., Kröger-Lui, N., Pucci, A., Schönhals, A. & Petrich, W. Real-time mid-infrared imaging of living microorganisms. *J. Biophoton.* **9**, 61–66 (2016).
38. Gaida, C. et al. Watt-scale super-octave mid-infrared intrapulse difference frequency generation. *Light Sci. Appl.* **7**, 94 (2018).
39. Seidel, M. et al. Multi-watt, multi-octave, mid-infrared femtosecond source. *Science Advances* **4**, eaq1526 (2018).
40. Butler, T. P. et al. Watt-scale 50-MHz source of single-cycle waveform-stable pulses in the molecular fingerprint region. *Opt. Lett.* **44**, 1730–1733 (2019).
41. Pupeza, I. et al. Field-resolved spectroscopy in the molecular fingerprint region. In *Lasers and Electro-Optics Europe & European Quantum Electronics Conf. (CLEO/Europe-EQEC)* <https://doi.org/10.1109/CLEO-EQEC.2017.8086859> (IEEE, 2017).
42. Huber, M. et al. Detection sensitivity of field-resolved spectroscopy in the molecular fingerprint region. In *Lasers and Electro-Optics Europe & European Quantum Electronics Conference (CLEO/Europe-EQEC)* <https://doi.org/10.1109/CLEO-EQEC.2017.8086921> (IEEE, 2017).
43. Timmers, H. et al. Molecular fingerprinting with bright, broadband infrared frequency combs. *Optica* **5**, 727–732 (2018).
44. Muraviev, A. V., Smolski, V. O., Loparo, Z. E. & Vodopyanov, K. L. Massively parallel sensing of trace molecules and their isotopologues with broadband subharmonic mid-infrared frequency combs. *Nat. Photon.* **12**, 209–214 (2018).
45. Udem, T., Holzwarth, R. & Hänsch, T. W. Optical frequency metrology. *Nature* **416**, 233–237 (2002).
46. Ye, J. & Cundiff, S. T. *Femtosecond Optical Frequency Comb: Principle, Operation, And Applications* (Springer, 2005).
47. Schweinberger, W. et al. Interferometric delay tracking for low-noise Mach-Zehnder-type scanning measurements. *Opt. Express* **27**, 4789–4798 (2019).
48. Schubert, O. et al. Rapid-scan acousto-optical delay line with 34 kHz scan rate and 15 ns precision. *Opt. Lett.* **38**, 2907–2910 (2013).
49. Birarda, G. et al. IR-Live: fabrication of a low-cost plastic microfluidic device for infrared spectromicroscopy of living cells. *Lab Chip* **16**, 1644–1651 (2016).
50. Max, J.-J. & Chapados, C. Glucose and fructose hydrates in aqueous solution by IR spectroscopy. *J. Phys. Chem. A* **111**, 2679–2689 (2007).

**Publisher's note** Springer Nature remains neutral with regard to jurisdictional claims in published maps and institutional affiliations.

© The Author(s), under exclusive licence to Springer Nature Limited 2019



## Article

### Methods

#### Nonlinear time-domain gating in FRS

Here, we elucidate the qualitative differences between FRS and traditional, frequency-resolved spectroscopy. For the latter, we choose FTS as the perhaps most advanced form of frequency-resolved infrared spectroscopy, in particular in the dual-frequency-comb implementation<sup>11,21,22</sup>. Furthermore, the interferograms obtained by FTS performed either with ultrashort pulses<sup>11,21,22</sup> or with broadband, incoherent light<sup>51</sup> resemble the electric field emerging from a sample after resonant excitation with a few-cycle infrared pulse, which FRS samples with sub-optical-cycle resolution by means of nonlinear optics (see Fig. 1b). To understand the important performance differences between the two techniques, it is essential to recognize the conceptual differences in the acquisition of these time-domain signals. First, using simple formalisms for the signals acquired in FTS and FRS, we reveal two major advantages introduced by the time-domain, nonlinear-conversion-based gating of the sampled electric field in FRS over FTS: the robustness of detection sensitivity against technical noise of the MIR excitation transmitted through the sample, and the mitigation or circumvention of the detector-dynamic-range limitation of sensitivity inherent to FTS<sup>22</sup>. Then, we evaluate the performance of FTS achievable with our coherent infrared source and state-of-the-art infrared detection (both described in Supplementary Information section I), employing a well established frequency-domain formalism<sup>22</sup>. Contrasting the results with those of FRS presented in this work, we observe detection sensitivities higher by more than a factor of 30 for FRS of impulsively excited molecular signals decaying with a time constant on the order of 1 ps, as is typical for liquid-phase samples—owing to the above-mentioned advantages.

Extended Data Fig. 1a illustrates the working principle of FTS. Here, we consider an ultrashort-pulsed MIR excitation source. Its broadband pulses are sent along two arms of an interferometer, one of which contains the sample and one of which acts as a ‘local oscillator’ for homodyne (or heterodyne) detection. The field transmitted through the sample is the convolution of the sample response with the incident excitation field<sup>22</sup>  $E_{\text{ex}}(t)$ . It can be written as the sum of (1) a non-resonant response representing an attenuated (and temporally altered) version of  $E_{\text{ex}}(t)$ , which for simplicity we approximate here as  $aE_{\text{ex}}(t)$ , with a scalar  $a < 1$ , and (2) the response  $E_{\text{GMF}}(t)$  of the resonantly excited molecules (a more rigorous treatment of the sample response is given in Supplementary Information section II). The field  $R_{\text{LO}}(t-\tau)$  in the local oscillator arm is a copy of  $E_{\text{ex}}(t)$ , delayed by a variable time  $\tau$ . FRS implemented with EOS (Extended Data Fig. 1b) employs a near-infrared (NIR) gate pulse  $E_{\text{g}}(t-\tau)$  fulfilling two functions<sup>32</sup> (see also Supplementary Information section I). First, this pulse ‘carves out’ an ultrashort portion of the sample response, for instance via a second-order nonlinear upconversion process. Second, it acts as a local oscillator in the homodyne/heterodyne detection of this upconverted signal.

In both schemes, at each delay  $\tau$ , the superposition of the sample response (time-gated and upconverted in the case of FRS) and local oscillator fields is sent to (usually two)  $t$ -integrating intensity detectors placed at each of the sum and difference ports of the beam combiner. In the wake of the excitation, where the strength of  $aE_{\text{ex}}(t)$  can be neglected against that of  $E_{\text{GMF}}(t)$ , the resulting signals recorded by the two respective detectors read:

$$I_{\text{FTS},1,2}(\tau) \propto \int [aE_{\text{ex}}(t) + E_{\text{GMF}}(t)]^2 dt + \int E_{\text{LO}}^2(t-\tau) dt \pm 2 \int E_{\text{GMF}}(t) E_{\text{LO}}(t-\tau) dt \quad (1a)$$

$$I_{\text{FRS},1,2}(\tau) \propto \int [\chi E_{\text{g}}(t-\tau) E_{\text{GMF}}(t)]^2 dt + \int E_{\text{g}}^2(t-\tau) dt \pm 2 \int \chi E_{\text{GMF}}(t) E_{\text{g}}^2(t-\tau) dt \quad (1b)$$

where  $\chi E_{\text{g}}(t-\tau) E_{\text{GMF}}(t)$  is a qualitative expression for the time-gated, upconverted sample response in FRS, neglecting effects such as phase matching or depletion/saturation. The first two right-hand-side terms of equation (1a, b) represent a background (direct-current baseline) around which the third term, containing the spectroscopic information, oscillates. A major difference stems from the first background term in the two equations and immediately becomes apparent after two approximations. In equation (1a), this term can be approximated by  $\int [aE_{\text{ex}}(t)]^2 dt$ , which is typically orders of magnitude larger than the (time-integrated) GMF signal. In equation (1b), owing to temporal gating, the first right-hand-side term is orders of magnitude smaller than the other two terms (see Extended Data Fig. 1c), and can be neglected. With these two approximations, equation (1a, b) becomes:

$$I_{\text{FTS},1,2}(\tau) \propto \int [aE_{\text{ex}}(t)]^2 dt + \int E_{\text{LO}}^2(t-\tau) dt \pm 2 \int E_{\text{GMF}}(t) E_{\text{LO}}(t-\tau) dt \quad (2a)$$

$$I_{\text{FRS},1,2}(\tau) \propto \int E_{\text{g}}^2(t-\tau) dt \pm 2 \int \chi E_{\text{GMF}}(t) E_{\text{g}}^2(t-\tau) dt \quad (2b)$$

The fact that in FTS the time-integrated excitation transmitted through the sample always impinges on the detector(s), whereas in FRS this background term is negligible in the wake of an impulsive excitation, illustrated by equation (2a, b), has two far-reaching implications, described as follows.

**Robustness of FRS against excitation noise.** Although for both schemes the contribution of the local-oscillator term to the background can be readily reduced to the shot-noise/detector-noise level, for example, via lock-in detection (see Supplementary Information section I), in FTS the minimum detectable molecular signal is directly affected by the technical noise of the MIR excitation, whose contribution to the recorded signal is constant along the entire delay range. This requires its suppression by sophisticated fast scanning methods<sup>22</sup> and/or balancing techniques<sup>53,54</sup>. In spite of all these efforts, photon quantum-noise-limited sensitivity<sup>54</sup> has not been experimentally demonstrated for broadband measurements for wavenumbers shorter than 2,000  $\text{cm}^{-1}$ , to the best of our knowledge. In FRS, by contrast, excitation-background-free detection of the molecular signal in the wake of an impulsive excitation implies a sensitivity that is ultimately limited by the quantum noise of the NIR gating field but largely immune to the noise of the MIR excitation.

**Circumvention or mitigation of detector-dynamic-range-induced sensitivity limitation.** In FTS, the usable input power is restricted by the excitation, transmitted through the sample, saturating the detector(s); see the first right-hand-side term of equation (2a). This implies a severe detector-dynamic-range-induced sensitivity limit<sup>11,22</sup> that can only be circumvented/mitigated by techniques such as spectral multiplexing<sup>22</sup> or building the difference between a sample and a reference response to the same excitation interferometrically, before detection<sup>55,56</sup>. This adds substantial complexity to any detection scheme and has not been widely used so far. In FRS, for a fixed local-oscillator power (set to be below the detector saturation level), the signal-to-noise ratio can readily be increased by increasing the excitation field, which linearly increases the sought-for molecular signal  $E_{\text{GMF}}(t)$  in the third right-hand-side term in equation (2b). Because the excitation signal transmitted through the sample is eliminated by the femtosecond temporal gate, the molecular signal can, in principle, be increased up to levels at which  $aE_{\text{ex}}(t)$  vastly exceeds the saturation level of any available detector.

**Sensitivity estimation of FTS implemented with our infrared source**  
Here, we calculate the expected sensitivity for an FTS implementation employing our infrared radiation source and state-of-the-art MIR

detectors. Because of the delay-independent contribution of excitation noise to the recorded signal (see above), time-domain filtering of the recorded signal does not have such a dramatic effect as in FRS, and well established frequency-domain models for FTS lend themselves for a sensitivity estimation. Here we use the model of Newbury et al.<sup>22</sup> who derived an expression for the frequency-domain signal-to-noise ratio in dependence of detector noise, shot noise, excess laser relative intensity noise (RIN) and detector dynamic range. Although the formula was derived for dual-comb spectroscopy, it can be readily applied to FTS with (slow) mechanical scan, with our experimental parameters (see Supplementary Information section I, Extended Data Fig. 5 and summary in Extended Data Table 1). In addition, we assume no limitations due to digitization, no sequential or parallel multiplexed acquisition and a duty cycle of 1. The power level in both the signal and the local oscillator arms was set to 0.45 mW, limited by detector saturation and well within the range of our source.

For direct comparison with our FRS results, we consider the absorption of DMSO<sub>2</sub> solved in water, spectrally centred at 1,139 cm<sup>-1</sup> (see Extended Data Fig. 6 and parameters in Extended Data Table 1). According to equation (4) of ref.<sup>22</sup>, for these parameters we obtain a limit of detection of 7 µg ml<sup>-1</sup> of DMSO<sub>2</sub> dissolved in water for FTS, which is a factor of 35 above what is demonstrated here with FRS.

#### Experimental setup

The instrument (see also Supplementary Information section I for a detailed description) is based on a Kerr-lens mode-locked thin-disk Yb:YAG oscillator<sup>57</sup> emitting a 28-MHz repetition-rate train of 220-fs pulses, spectrally centred at 1,030 nm. After temporal compression via nonlinear spectral broadening based on multi-pass self-phase modulation in bulk fused silica followed by chirped-mirror compressors<sup>58</sup>, the resulting NIR pulses are 16 fs long, with an average power of 60 W. These pulses drive intrapulse difference-frequency generation (optical rectification) in a 1-mm-thick LiGaS<sub>2</sub> crystal. The emerging MIR radiation with an average power of the order of 100 mW is spectrally tunable with a coverage of nearly one octave around a central frequency of 1,200 cm<sup>-1</sup>. After the crystal, the NIR pulse is recycled and used for gating in the EOS detection of the MIR waveforms. Balanced detection in EOS is optimized close to the NIR shot-noise limit, with an impinging NIR power on the GaSe EOS crystal of 420 mW. In order to reduce phase artefacts introduced by variations of the mutual delay between the MIR sampled wave and the NIR sampling pulse, we track this delay interferometrically, with an additional continuous-wave laser<sup>57</sup>. In this manner, data can be recorded with few-nanometre delay precision and a temporal duty cycle close to 100% during forward as well as backward scans. Starting with the last NIR pulse compression stage, all the beams are enclosed in vacuum chambers at a background pressure in the 1-mbar range. Further measures of stabilization include an acousto-optical-modulator-based active noise eater<sup>59</sup> and lock-in detection employing mechanical chopping of the MIR beam.

#### Dynamic range of FRS

The 500-µm-thick GaSe electro-optic crystal constitutes a trade-off between a high quantum efficiency and broad bandwidth (Fig. 1d). In addition, it avoids internal reflections within the measurement time window. This quantum-efficiency-optimized apparatus resulted in a linearity of the instrument response over more than seven orders of magnitude of electric-field strength and, moreover, the intensity dynamic range scales linearly with measurement time (Extended Data Fig. 2). Thus, sampling of the oscillating electric field rather than its cycle-averaged intensity<sup>60</sup> results in an unprecedented linear-response intensity dynamic range of >10<sup>14</sup>, vastly exceeding that of infrared spectroscopy so far, to our knowledge<sup>2</sup>. This enables transillumination of aqueous samples of several tens of micrometres in thickness while maintaining a high signal-to-noise ratio.

#### Measurement principle and the nature of the signal

FRS molecular fingerprinting relies on the generation of ultrashort infrared pulses with identically repeating electric-field waveforms (in our setup, 28 million such pulses per second). These pulses are transmitted through the sample under investigation, and the waveforms emerging from this interaction are recorded with EOS (see Supplementary Information section I). The spatial distribution of microscopic electric charges (that is, electrons and nuclei) in organic molecules is (1) inhomogeneous and (2) characteristic of the molecular species. Because of (1), when the electric field of the above-mentioned infrared pulses interacts with the molecules, it induces microscopic spatial charge separations (due to the existence of electric dipole moments). These charge separations evolve in time, driven by the oscillating electric field. Because of (2), these microscopic charge oscillations occur with characteristic magnitudes and frequencies—albeit having a fixed mutual timing, set by the common excitation field. In particular, resonant vibrations oscillate long after the excitation by the few-cycle infrared waveform, emanating a GMF. This resonant response is the coherent superposition of the fields of all sample-specific oscillations, thus containing most of the sample-specific information. Importantly, at the centre frequency of any such oscillation, the emission of light as a consequence of the resonant excitation by a light field occurs with opposing phase to the latter<sup>9</sup>. Consequently, the coherent superposition of the GMF and the excitation transmitted through the sample results in a destructive interference at these frequencies, leading to the typical ‘absorption dips’ observed in frequency-domain spectroscopy; see Fig. 1c.

#### Data availability

The data that support the findings of this study are available from the corresponding author upon reasonable request.

- Tsurumachi, N., Fujii, T., Kawato, S., Hattori, T. & Nakatsuka, H. Interferometric observation of femtosecond free induction decay. *Opt. Lett.* **19**, 1867–1869 (1994).
- Gallot, G. & Grischkowsky, D. Electro-optic detection of terahertz radiation. *J. Opt. Soc. Am. B* **16**, 1204–1212 (1999).
- Hobbs, P. C. D. Ultrasensitive laser measurements without tears. *Appl. Opt.* **36**, 903–920 (1997).
- Foltynowicz, A., Ban, T., Mastowski, P., Adler, F. & Ye, J. Quantum-noise-limited optical frequency comb spectroscopy. *Phys. Rev. Lett.* **107**, 233002 (2011).
- Buberl, T. Broadband interferometric subtraction of optical fields. *Opt. Express* **27**, 2432–2443 (2019).
- Tomberg, T., Muraviev, A., Ru, Q. & Vodopyanov, K. L. Background-free broadband absorption spectroscopy based on interferometric suppression with a sign-inverted waveform. *Optica* **6**, 147–151 (2019).
- Fritsch, K., Poetzlberger, M., Pervak, V., Brons, J. & Pronin, O. All-solid-state multipass spectral broadening to sub-20 fs. *Opt. Lett.* **43**, 4643–4646 (2018).
- Schulte, J., Sartorius, T., Weitenberg, J., Vernaleken, A. & Russbuedelt, P. Nonlinear pulse compression in a multi-pass cell. *Opt. Lett.* **41**, 4511–4514 (2016).
- Huber, M. et al. Active intensity noise suppression for a broadband mid-infrared laser source. *Opt. Express* **25**, 22499–22509 (2017).
- Lanin, A. A., Voronin, A. A., Fedotov, A. B. & Zheltikov, A. M. Time-domain spectroscopy in the mid-infrared. *Sci. Rep.* **4**, 1–8 (2014).

**Acknowledgements** We thank D. Gerz, A. Zigman Kohlmaier, L. Fuerst and I. Kosse for their contributions and help with the measurements. We acknowledge the support of the Max Planck Society, the Center for Advanced Laser Applications of the Ludwig-Maximilians University and the King Saud University via the Researchers Supporting Project (NSRSP-2019/1).

**Author contributions** I.P., M.H., M.T., W.S., S.A.H., C.H., E.F., A. Apolonski, A. Azzeer, M.Z. and F.K. conceived the experiments. I.P., M.H., M.T., W.S., S.A.H., C.H., K.F., M.P., L.V., T.A., K.V.K., N.K., V.P., O.P., M.Z. and F.K. designed the experiments and analysed the experimental data. M.H., F.F. and M.Z. prepared the living systems. S.A.H., K.F., M.P. and O.P. designed and built the few-cycle near-infrared femtosecond laser source. I.P., M.H., W.S., S.A.H., C.H., L.V., V.P. and N.K. developed the optical system for the generation and electro-optic detection of waveform-stable MIR radiation. All authors contributed to evaluating the results and writing the manuscript.

**Competing interests** The authors declare no competing interests.

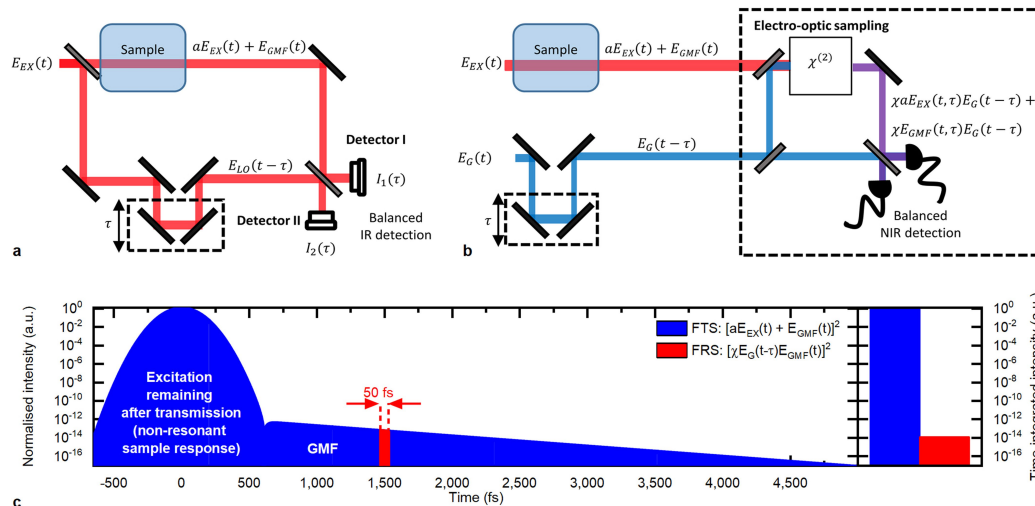
#### Additional information

**Supplementary information** is available for this paper at <https://doi.org/10.1038/s41586-019-1850-7>.

**Correspondence and requests for materials** should be addressed to I.P. or F.K.

**Reprints and permissions information** is available at <http://www.nature.com/reprints>.

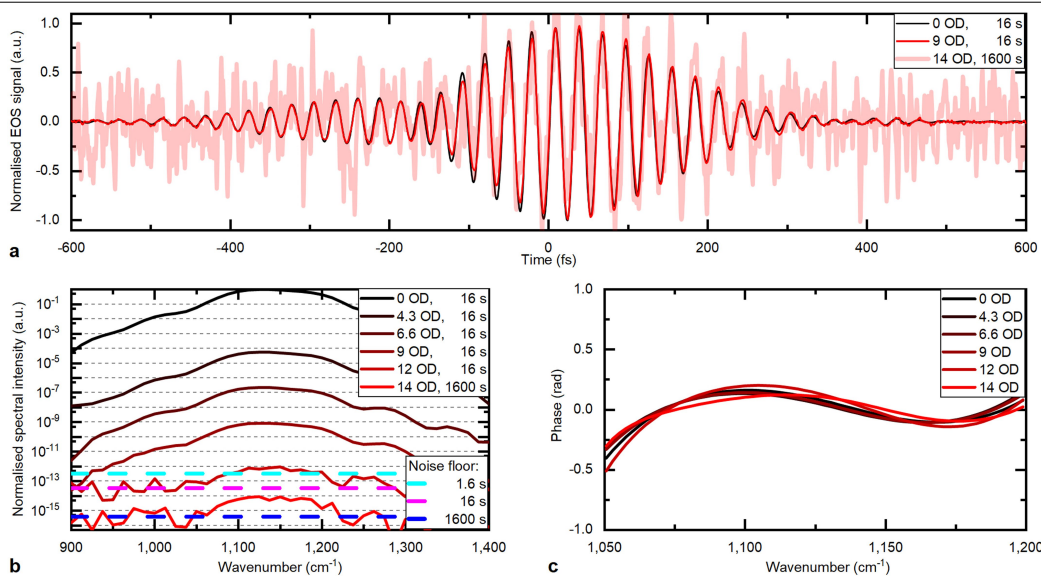
## Article



**Extended Data Fig. 1 | Comparison of FTS with FRS.** **a**, Schematic of FTS.

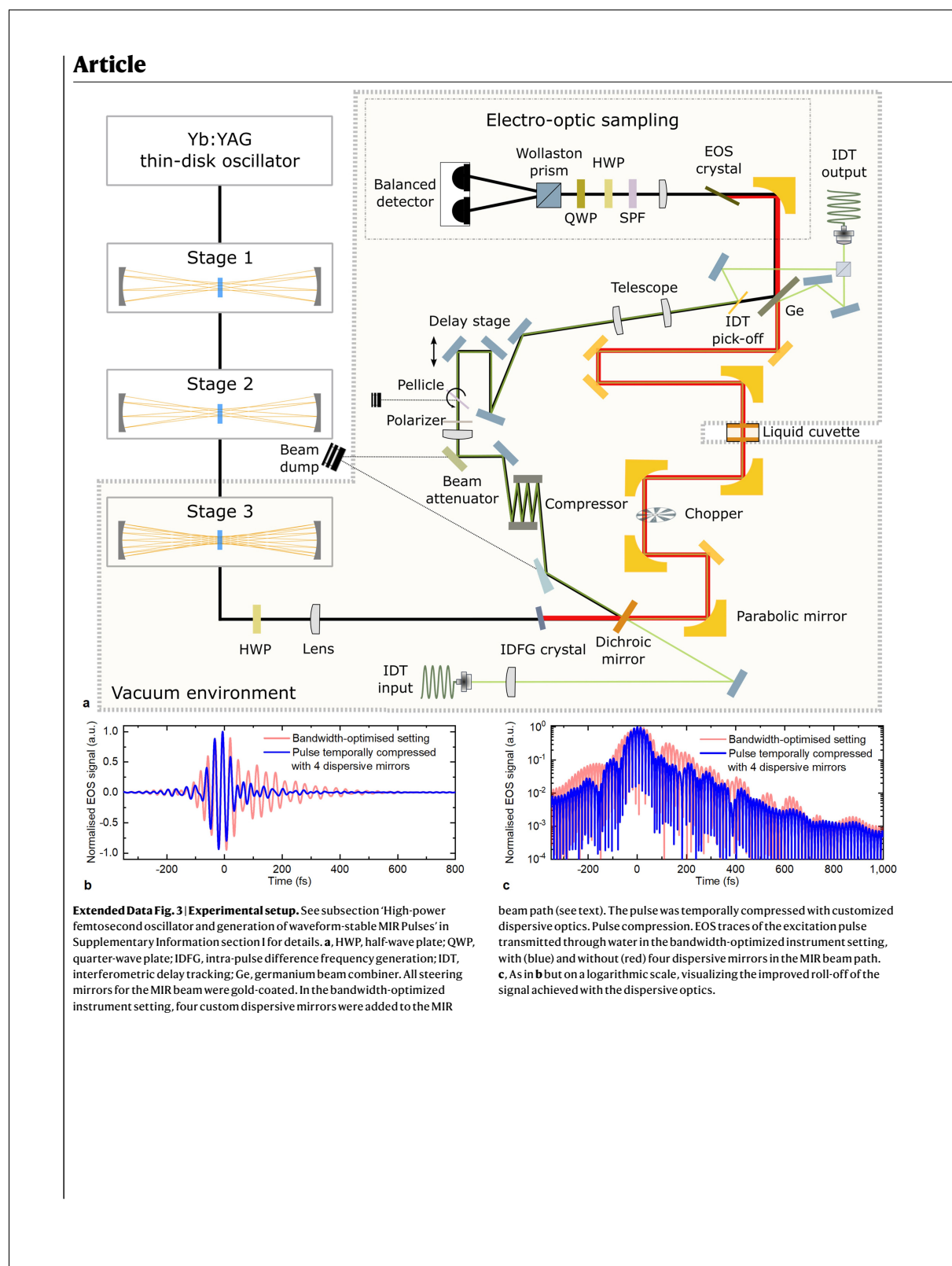
**b**, Schematic of FRS. **c**, Portions of the background signal contributed by the sample response to the FTS (blue, first right-hand-side term of equation (1a)) and to the FRS (red, first right-hand-side term of equation (1b)) signals at a fixed

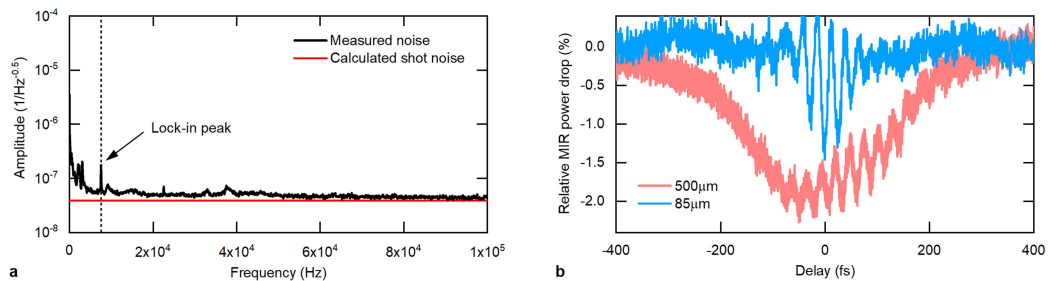
delay ( $\tau=1,500$  fs). For illustration purposes, the nonlinear upconversion efficiency was set to 1 and the 'carved out' effective window time length to 50 fs (without loss of generality). Example parameters: 190-fs Gaussian excitation pulse and  $1,139\text{-cm}^{-1}$  DMSO<sub>2</sub> absorption (see Extended Data Table 1).



**Extended Data Fig. 2 | Detection dynamic range and linearity of the instrument response.** **a**, Infrared excitation pulse (normalized to maximum), recorded with attenuating optical density (OD) filters instead of the cuvette in the beam path, for increasing attenuation and measurement time  $T$ . A 1,200-fs scan range and  $T=16$  s and  $T=1,600$  s were considered. Small variations of the pulse shape for different attenuations are attributed to slight dispersion variations among the OD filters. The attenuation-independent pulse shape

confirms the instrument linearity over the entire parameter range considered. **b, c**, Spectral intensity (normalized to the maximum of the attenuation-free measurement) and phase of the signals in **a**, respectively. The detection noise floors in **b** were obtained by blocking the MIR signal and evaluating the mean of the (white) noise in the considered spectral range, and confirm the linear decrease of the noise floor with  $T$ . For the data in **c**, for all time-domain waveforms a super-Gaussian filter (width 700 fs, order 20) was applied.

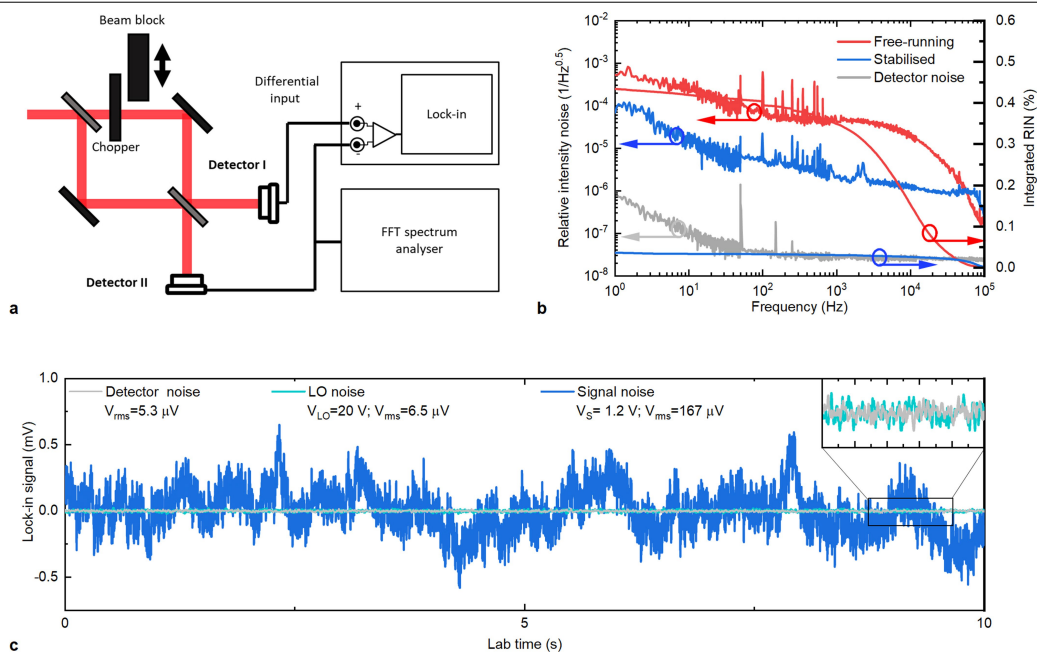




**Extended Data Fig. 4 | Contributions to quantum efficiency in electro-optic sampling.** **a**, Frequency-resolved measurement of the noise of the balanced detection (black), and calculated shot noise (red). The dashed line indicates the lock-in frequency, and its peak stems from the chopper. **b**, Comparison of MIR

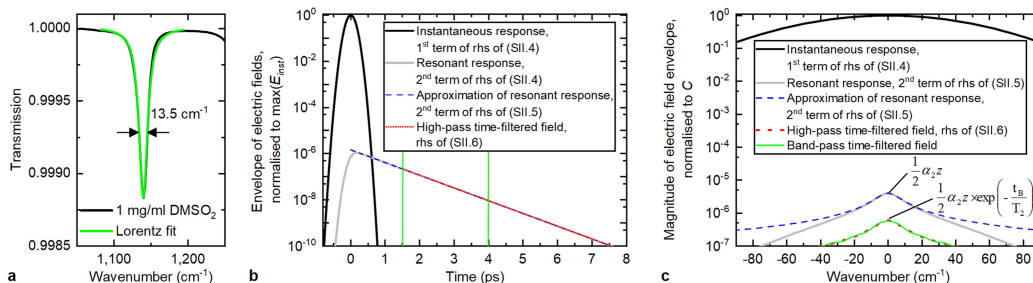
power depletion after EOS crystal for the two different crystal thicknesses. The oscillations originate from interferences of the MIR pulse incident to the EOS crystal and MIR radiation generated therein (these oscillations do not affect the performance of EOS detection).

## Article



**Extended Data Fig. 5 | Measurement of noise contributions for the estimation of the performance of FTS with our femtosecond-laser-based source, our mechanical scan, and state-of-the-art infrared detection.** **a**, The setup mimics a FTS setup in the Mach-Zehnder configuration, with balanced lock-in detection. For lock-in frequency modulation, a mechanical chopper is placed in the 'sample arm'. The two arms are recombined with a 50:50 beam splitter. The two outputs are detected with two independent MIR detectors (see text for details). The power impinging on each detector was limited to 450 mW, corresponding to a detector output voltage of 20 V. The relative intensity noise (RIN) spectrum of the source is recorded with an FFT-Analyser in the range 0.1–100 kHz (before balanced detection). Balanced lock-in

detection is performed with a lock-in amplifier with differential input. The beam block was used in the measurements shown in **c**. **b**, RIN spectrum of the free-running (red curve) and intensity-stabilized (blue curve) MIR beam (before the interferometer). The integrated RIN of the stabilized source from 1 Hz and 100 kHz is as low as 0.04%. **c**, Demodulated (after lock-in detection with a time constant of 1.6 ms and 4th-order filter) time-domain trace of detector noise (grey), local-oscillator signal with sample arm blocked (turquoise) and of the combination of both interferometer arms impinging on the balanced detection (blue). The inset shows a 1-second section of the signals, for a detailed comparison of the local-oscillator noise and the detector noise.

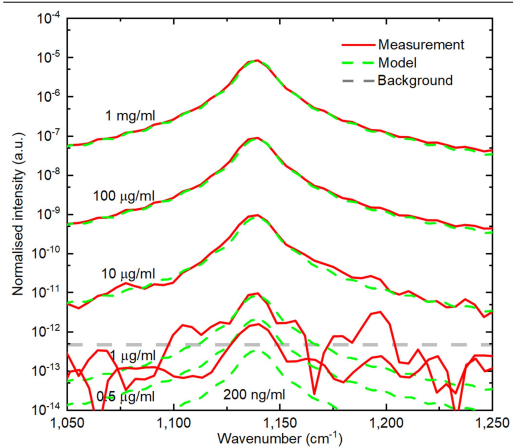


**Extended Data Fig. 6 | Simulations of time-domain decay of a molecular Lorentzian oscillator.** **a.** Fit of a Lorentzian oscillator to the 1,139 cm<sup>-1</sup> absorption of (low-concentration) DMSO<sub>2</sub>. Black line, intensity transmission through pure, molecular DMSO<sub>2</sub>, determined by referencing the transmission spectrum of a 1 mg ml<sup>-1</sup> solution to that of water, measured via FTIR, and normalizing to a 1-μm path. Green line, least-squares fit (1,080–1,190 cm<sup>-1</sup>) of a Lorentzian oscillator to the 1,139 cm<sup>-1</sup> absorption, yielding a full width at half depth of 13.47 cm<sup>-1</sup> and an absorption coefficient  $\alpha = 11.96$  cm<sup>-1</sup>. The numerical example shows the instantaneous and resonant parts of the electric field as described by equations (1) to (4) in Supplementary Information section II. The initial pulse is a Gaussian pulse with an intensity envelope (full width at half maximum) of 190 fs. The Lorentzian absorption band has a peak of  $\alpha_2 z$  with  $\alpha_2 = 0.0024$  cm<sup>-1</sup>, corresponding to a 200 ng ml<sup>-1</sup> solution of DMSO<sub>2</sub> in water, and a width  $\delta\nu = 13.47$  cm<sup>-1</sup>. These values were obtained from fitting a

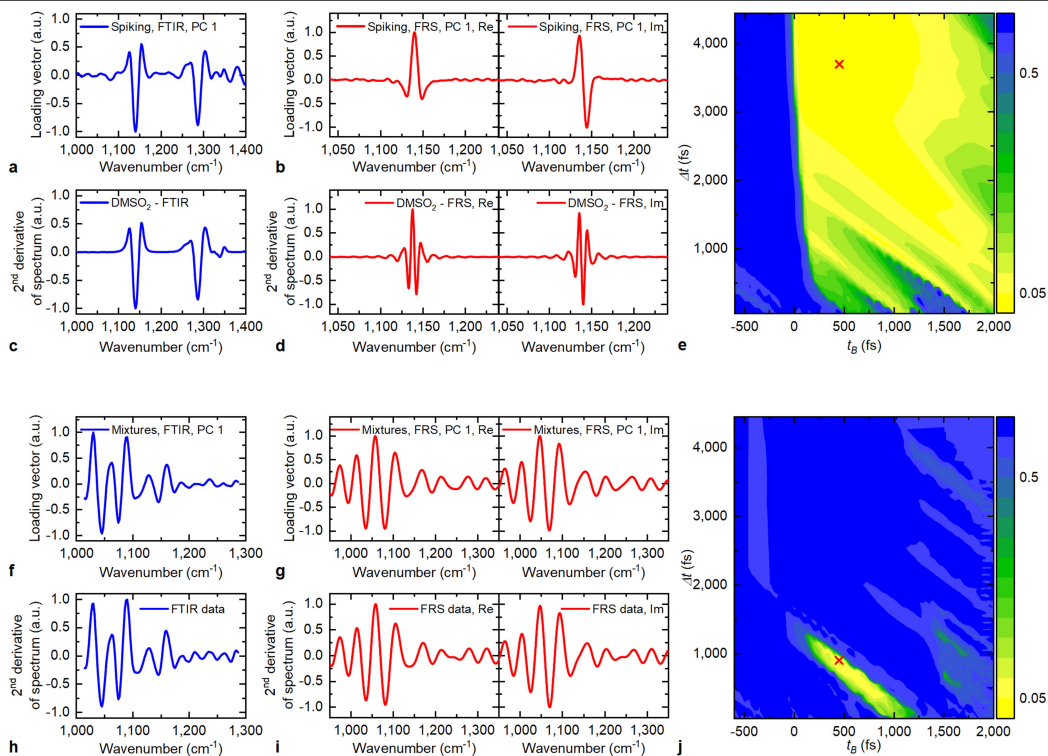
Lorentzian absorber to the 1,139 cm<sup>-1</sup> band of the transmission spectrum of a 1 mg ml<sup>-1</sup> solution obtained with FTIR and linear extrapolation to a concentration 5,000 times lower. **b.** Time-domain representation of the normalized envelope functions of the electric fields described (see key). A value of  $t_B = 1.5$  ps is chosen. The green vertical bars indicate the boundaries of the band-pass-filtered resonant response shown in green: 1.5 ps and 4 ps. **c.** Magnitudes of the Fourier transforms of the envelopes shown in **a**, normalized to **C**. At the absorption maximum, the discrepancy between the resonant response as in Supplementary Information section 2 and its approximation as in Supplementary Information section 3 is 1%, justifying this convenient approximation. The error introduced by band-pass filtering the resonant response between 1.5 ps and 4 ps compared to the high-pass time-filtered signal is 4%.



## Article



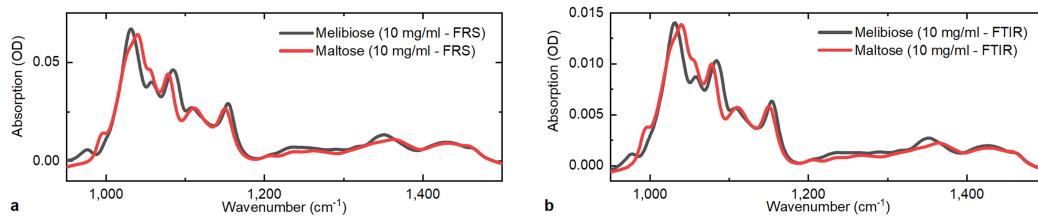
**Extended Data Fig. 7 | Spectral intensity of the Fourier-transformed temporal fingerprints of DMSO<sub>2</sub>.** Spectral intensity is shown for different concentrations, after high-pass-time-filtering at  $t_0 = 1,500$  fs and subtraction of pure water reference, normalized to the spectral intensity of the reference pulse. Green dashed lines, modelled Lorentzian oscillator with the parameters derived from the fit in Extended Data Fig. 6. This model agrees excellently with the measured fingerprints, and confirms the minimum detectable absorbance predicted by equation (2) as well as the linear response of the instrument.



**Extended Data Fig. 8 | Principal component analysis.** **a-d**, Comparison of the loading vectors for the first principal component for the FTIR data (**a**) and the FRS data (**b**) from the serum spiking experiment, with the pre-processed GMF data (see text) of the FTIR (**c**) and FRS (**d**) measurements of a  $1 \text{ mg ml}^{-1}$  DMSO<sub>2</sub> solution. We note that the FRS spectra are complex, so the real and imaginary parts were considered separately (and stitched to single vectors). **e**, Figure of merit (FOM) (colour scale in arbitrary units; see Supplementary Information section VI) quantifying the separation of classes according to the first principal component (the lower the FOM, the better the separation), evaluated for a large

range of the beginning time  $t_b$  and time window length  $\Delta t$ . The cross indicates parameters yielding optimum separation. **f-i**, Comparison of the loading vectors for the first principal component for the FTIR data (**f**) and the FRS data (**g**) from the sugar mixture experiment, with the pre-processed GMF data of the FTIR (**h**) and FRS (**i**). For the latter, the difference of the spectra of the 50/50 mixture and the pure maltose solution is shown. The real and imaginary parts were considered separately. **j**, FOM quantifying the separation of classes according to the first principal component, in analogy to **e**.

## Article



**Extended Data Fig. 9 | Absorption spectra of 10 mg ml<sup>-1</sup> aqueous solutions of maltose and melibiose, measured by FRS and FTIR.** The difference in total absorption is due to the differing cuvette thickness. **a**, FRS; **b**, FTIR. OD, optical density.

**Extended Data Table 1 | Parameters for numerical estimation of the sensitivity of FTS implemented with our infrared source**

Parameter	Quantity	Comment
Central wavelength	$\lambda_c = 8.5 \mu m$	
Spectral width	$\Delta\nu_{FWHM} = 180 \text{ cm}^{-1}$	
MIR power (FTS)	$P_{LO} = P_S = 0.45 \text{ mW}$	Maximum incident power limited by detector saturation
MIR detector noise	$NEP_{MCT} = 2.5 \text{ pW/Hz}^{0.5}$	e.g.: InfraRed Associates; MCT-13-1.00
Relative intensity noise	$RIN = 2.7 \times 10^5 \text{ 1/Hz}^{0.5}$	
FTS detector efficiency	$\eta_{FTS} = 1$	Quantum efficiency is not stated in the detector datasheet
Measurement time	$T = 37 \text{ s}$	Measurement time for sample and reference measurement
Spectral resolution	$\nu_{RES} = 4.7 \text{ cm}^{-1}$	This corresponds to a scan time window of 7 ps
<b>DMSO<sub>2</sub> absorption line at <math>\nu_{DMSO_2} = 1139 \text{ cm}^{-1}</math></b>		
Absorptivity	$\alpha_{DMSO_2} = 12.92 \text{ cm}^{-1}$	For 1 mg/ml DMSO <sub>2</sub> solution
Line width	$\nu_{FWHM} = 13.47 \text{ cm}^{-1}$	This corresponds to a dephasing time $T_2$ of ~770 fs

**nature**

<https://doi.org/10.1038/s41586-019-1850-7>

**Supplementary information**

---

# Field-resolved infrared spectroscopy of biological systems

---

In the format provided by the authors and unedited

Joachim Pupeza, Marinus Huber, Michael Trubetskov, Wolfgang Schweinberger, Syed A. Hussain, Christina Hofer, Kilian Fritsch, Markus Poetzlberger, Lenard Vamos, Ernst Fill, Tatiana Amotchkina, Kosmas V. Kepesidis, Alexander Apolonski, Nicholas Karpowicz, Vladimir Pervak, Oleg Pronin, Frank Fleischmann, Abdallah Azzeer, Mihaela Žigman & Ferenc Krausz

## I. Experimental Setup

### High-power femtosecond oscillator and generation of waveform-stable MIR Pulses

A detailed sketch of the setup is shown in Extended Data Fig. 3. An initial near-infrared (NIR) 28-MHz-repetition-rate train of 220-fs (intensity envelope full width at half maximum, FWHM) pulses spectrally centred at a wavelength of 1030 nm ( $9709\text{ cm}^{-1}$ ) and with an average power exceeding 100 W is provided by a Kerr-lens modelocked thin-disk Yb:YAG oscillator<sup>1</sup>. At a peak power of 14 MW, these pulses are sent to three nonlinear spectral broadening and compression stages, based on self-phase modulation in bulk media (fused silica) inside of Herriott-type multi-pass cells, followed by chirped-mirror compressors. The dispersive mirrors of the multi-pass cells were designed to compensate for the material dispersion of the broadening medium, targeting a constant pulse duration and peak power during all passes. Upon each pass, a moderate nonlinear phase-shift (0.5 rad for each of the first two stages and 0.6 rad for the third stage) is accumulated.

The pulse durations after the three compression stages (measured via second-harmonic frequency-resolved optical gating, FROG) were 84 fs, 43 fs and 16 fs, respectively, at Fourier-transform limits of 80 fs, 40 fs and 15 fs, respectively<sup>1</sup>. The 16-fs output pulses spectrally cover 920 to 1180 nm ( $10870\text{ cm}^{-1}$  to  $8475\text{ cm}^{-1}$ , at -20 dB level), with an average power of 60 W.

For intrapulse difference-frequency generation (IDFG), the NIR pulse train is focused down to  $330\text{-}\mu\text{m}$  ( $1/e^2$ -intensity diameter), corresponding to a peak intensity of  $180\text{ GW}/\text{cm}^2$ , onto a LiGaS<sub>2</sub> (LGS) crystal (1-mm thick, anti-reflection-coated for the NIR beam on the front surface). The polarisation of the incident NIR pulse train and the orientation of the LGS crystal were arranged for type-I phase-matched IDFG<sup>2</sup>. The emerging p-polarised mid-infrared (MIR) radiation was spectrally tuneable with a coverage of nearly one octave around a central frequency of  $1200\text{ cm}^{-1}$  (see Fig. 1d). After the crystal, the incident NIR and the generated MIR beams were separated with a custom-designed dichroic mirror, with an average transmittance of > 80 % in the bandwidth between 5 and  $12\text{ }\mu\text{m}$  ( $2000\text{ cm}^{-1}$  and  $833\text{ cm}^{-1}$ ) and a total reflection of > 99 % for the NIR pulses. The MIR beam was chopped at a frequency of 7.5 kHz for lock-in-amplified detection, and focused down to a spot diameter of  $420\text{ }\mu\text{m}$  (with a Rayleigh length of 17 mm), for transmission through the liquid cuvette. At the cuvette, a MIR average power of 50 mW was measured.

The liquid cuvette (Micro Biolytics GmbH) consisted of two parallel 2-mm ZnSe windows, enclosing a  $34\text{-}\mu\text{m}$ -long propagation path through the sample liquid. Filling of the cuvette was performed with a fully automated microfluidic delivery unit.

After reflection off the dichroic mirror, NIR pulses were recycled and used to sample the MIR waveforms electro-optically. Their polarisation was filtered with a wire-grid polariser and the pulses were temporally recompressed with dispersive mirrors down to 16 fs. The average power of the sampling beam was

adjusted (see below) via reflection off two transmitting optics and fine adjustment was implemented via transmission through a 100-nm-thin  $\text{Si}_3\text{N}_4$  pellicle. A variable delay between the MIR waveform and the sampling pulses was achieved with a mechanical stage (PI-Micos, L-511). In order to determine the mutual delay change during a measurement scan, the beam of a frequency-controlled distributed-feedback laser diode at 1550 nm was co-propagated along the MIR and NIR paths, after being split at the dichroic mirror.

Interferometric delay tracking<sup>3</sup> was achieved by modulating the frequency of the laser and by demodulating the resulting interference signal at two different frequencies that can be phase shifted with respect to each other to construct a quadrature signal. In contrast to a simple interference signal, this allows for a constant position sensitivity and for a directionality of the measurement. The implemented system was based on a commercial interferometer (Smaract PICOSCALE). All data was taken with a common clock. Synchronisation of the electro-optic sampling (EOS) and delay data information was realised by recording forward and backward scans and shifting the entire data sets by a constant time value such that the forward and backward traces become congruent.

Starting with the last NIR pulse compression stage, all the beams were enclosed in vacuum chambers. A background pressure of a few mbar was maintained over all measurements (except for the dynamic range evaluation and the measurements of living systems). The vacuum level was limited by the air-tightness of the custom-made liquid cuvette.

In the bandwidth-optimised detection setting of the FRS instrument (see next section), custom dispersive optics were employed to temporally compress the (non-resonant) response of pure water, together with the dispersion of the MIR pulse upon propagation through the ZnSe windows of the liquid cuvette (with a total thickness of 4 mm). Specifically, 4 identical multilayer mirrors (not shown in Extended Data Figure 3) were placed under small angles of incidence ( $\sim 7$  degrees). The customised optics enable the compensation of relative phase delays of up to  $\sim 400$  fs over the almost-octave-spanning range between 6.5 and 11.5  $\mu\text{m}$ , leading to a reduction of FWHM pulse duration from 78 fs to 56 fs (Extended Data Fig. 3b) and – essential for the sensitivity of FRS – to a significantly steeper roll-off of the measured non-resonant response of liquid water (Extended Data Fig. 3c). The layer materials for these mirrors were Ge and  $\text{YbF}_3$ , affording a significantly broader bandwidth than previous dispersive multilayer optics in this spectral range<sup>4</sup>. A detailed description will be given in a future publication.

#### **Electro-optic sampling**

The MIR and NIR beams were spatially recombined with a germanium plate: the MIR beam was transmitted at Brewster's angle and the NIR sampling beam was reflected off the surface (see Extended Data Fig. 3). Both beams were focused to the electro-optic sampling (EOS) crystal. We used a 85- $\mu\text{m}$  and a 500- $\mu\text{m}$ -thick GaSe crystal, placed at 52° and 55°, respectively (cf. spectra in Fig. 1d). The thinner crystal

was used for EOS providing a waveform close to the generated electric field (Fig. 1b) and the thicker crystal for quantum-efficiency-optimised detection.

The dispersion of the beam splitter (1-mm ZnSe substrate), liquid cuvette walls (4 mm of ZnSe) and the GaSe EOS crystal was balanced by choosing a suitable thickness of the germanium NIR-MIR beam combiner (5 mm) under the constraints of geometrical feasibility. This resulted in an intensity-envelope FWHM duration of the instantaneous response of the liquid cuvette with water of 56 fs and 190 fs for the 85- $\mu\text{m}$  and 500- $\mu\text{m}$  thick EOS crystal, respectively

EOS can be understood as a two-step process<sup>5,6</sup> (see also Extended Data Fig. 1b): first, the two participating fields are mixed in a second-order ( $\chi^{(2)}$ ) nonlinear process (here, we phase-matched sum-frequency generation, SFG). In a second step, the resulting SFG photons are detected in a balanced, heterodyne detection scheme, using the unconverted NIR beam as a local oscillator. Assuming that the detection noise is dominated by the shot noise of the local oscillator, the power of the sampling pulse train  $P_s$  should be maximised because the signal-to-noise ratio (SNR) increases with  $\sqrt{P_s}$  according to the contribution of the increasingly efficient SFG<sup>6</sup>. An upper limit to this scaling is set by undesired nonlinearities in the EOS crystal, eventually culminating in damage. The focus diameter of the MIR beam achieved with a 50-mm-focal-length off-axis parabolic mirror was 80  $\mu\text{m}$  (averaged over the entire spectrum). The spot size of the NIR beam was adjusted to the same value with a two-lens telescope before the beam combiner. The sampling pulse power was adjusted to  $\sim 85\%$  of the crystal damage threshold. This resulted in an average power of the sampling pulses of 430 mW.

A short-pass filter at 912 nm was used<sup>6</sup> for enhancing the SNR of the EOS. A half-wave plate and a quarter-wave plate were used for optimising the balancing on the difference photodiode, for which the beam was split with a Wollaston prism. The signal was detected with a self-built balanced detector, consisting of two photodiodes (first sensor, series 7, chip PC10-7), followed by a low-noise current amplifier (femto DLPCA-200). The diodes were reverse-biased with 15 V and the amplification was set as high as possible without saturating the lock-in amplifier (integration time 186  $\mu\text{s}$  with 6<sup>th</sup> order filtering at a mechanical chopping frequency of 7.5 kHz). The resulting noise floor was a factor of 1.6 above the shot noise level of the NIR beam, see Extended Data Fig. 4a. Assuming a DC signal due to averaging over several pulses, the theoretical value for the single-sided linear spectral density  $s_q$  of the relative quantum power noise was calculated according to<sup>7</sup>:

$$s_q = 1.9 \times 10^{-8} \text{Hz}^{-\frac{1}{2}} \times \sqrt{\frac{1\text{mW}}{P}} \times \sqrt{\frac{1064\text{nm}}{\lambda}}, \quad (\text{SI. 1})$$

where  $P$  is the optical power incident on the detector,  $\lambda$  the wavelength of the radiation, and a detector quantum efficiency of 1 is assumed.



The NIR pulse duration, power, focus size on the EOS crystal and the crystal thickness were all optimised for maximum quantum efficiency, in order to upconvert and detect as many MIR photons as possible. The detection of the MIR waveform is confined to the temporal window determined by the propagation of the sampling pulse through the EOS crystal. This results in a temporal gating both of the nonlinear interaction and of the MIR background (both from the MIR excitation and thermal background noise).

To estimate the efficiency of MIR photon detection, we first measured the MIR power transmitted through the EOS crystal, while scanning over the EOS signal. Extended Data Fig. 4b shows the comparison of the MIR depletion for the two different crystal thicknesses used in this paper. For the 500- $\mu\text{m}$  crystal, the maximum MIR depletion corresponds to a relative change in photon number (or MIR power) of 2.27 %. Considering that the interaction window for the delay corresponding to maximum depletion is approximately 88 % of the MIR pulse duration, the quantum efficiency is effectively 2.6 %.

As we were using a short-pass filter in the EOS configuration, we determined the number of transmitted SFG photons by measuring the SFG spectrum with and without the filter and by calculating the spectrally integrated power transmission through the short-pass filter, to be roughly 60 %. Furthermore, the percentage of detected photons is reduced by the spatial overlap of near-infrared (NIR) and SFG (95 %) and the factor above shot noise in intensity ( $1.6^2$ ). The resulting 0.6 % of detected MIR photons matches the value determined from dividing the EOS intensity dynamic range (normalised to one second measurement time) by the average mid-infrared photon number in the interaction window.

The electric field was reconstructed from the EOS trace using a calculated frequency-domain instrument response function<sup>8</sup> (IRF). The EOS signal was calculated<sup>5</sup> as the superposition of the sum frequency, generated in the EOS crystal and the remaining NIR, serving as a local oscillator. The SFG was calculated with a 1D model for the nonlinear generation, using the first-order propagation equation<sup>8,9</sup>:

$$\frac{\partial E_{\omega}(z)}{\partial z} = -ik_{\omega}E_{\omega}(z) - \frac{i\omega}{2n(\omega)\epsilon_0 c}P_{\omega}^{NL}(z). \quad (\text{SI. 2})$$

Here,  $E_{\omega}$  is the electric field for the frequency component  $\omega$ , evolving spatially in  $z$  direction,  $k_{\omega}$  is the wave vector,  $n(\omega)$  the frequency dependent refractive index and  $P_{\omega}^{NL}$  the second-order nonlinear polarisation. The MIR pulse employed (generic transform-limited super-Gaussian spectrum, covering the experimental spectral width) was assumed to propagate on the extraordinary crystal axis and the NIR pulse (with an intensity envelope as measured with FROG) on the ordinary one, leading to type II phase matching, with the 52- $\mu\text{m}$  long crystal rotated at 52°. The frequency-domain IRF was then calculated as the ratio of the Fourier transforms of the EOS trace and the MIR input field.

In the bandwidth-optimised implementation, the “echo” of the excitation, appearing  $\sim 1.6$  ps after the maximum of the main pulse as a consequence of an internal reflection inside the thin EOS crystal limits the time window of sensitive GMF detection. However, this is not a fundamental limitation, and several

potential solutions might provide a workaround in the near future. The potentially more favourable bandwidth-versus-quantum-efficiency trade-off with ultrashort 2- $\mu\text{m}$  sampling pulses<sup>10</sup> promising to allow for a thicker sampling crystal, impedance-matched reduction of the echo<sup>11</sup>, and geometrical separation of the echo (e.g., wedged crystal) are potential solutions.

For a quantitative interpretation of EOS traces, knowledge of the IRF is necessary. While a complete reconstruction of the electric field, as illustrated in Fig. 1b requires precise, quantitative knowledge of the latter, for the quantitative interpretation of linear (i.e.,  $\chi^{(1)}$ ) interactions directly from the measured EOS traces, only the linearity of the instrument response function is necessary, not its precise knowledge. In the case of a linear light-matter interaction, which can be fully described in the frequency domain by multiplication of the input electric field  $E_0(\omega)$  by a sample response function  $H_s(\omega)$ , a linear IRF  $H_i(\omega)$  results in the (time-domain) measurement of the complex function  $EOS_s(\omega) = E_0(\omega)H_s(\omega)H_i(\omega)$ . Rearranging the rhs of this expression to  $[E_0(\omega)H_i(\omega)]H_s(\omega)$  and noting that a reference measurement without sample in place leads to a trace corresponding to  $EOS_0(\omega) = E_0(\omega)H_i(\omega)$ . Thus, the sample measurement can be described by  $EOS_s(\omega) = EOS_0(\omega)H_s(\omega)$ , and therefore describes the linear response of the sample to an excitation field equal to  $EOS_0(\omega)$ .

#### Relative intensity noise of the MIR beam

In order to assess the contribution of technical noise to the SNR of FTS (See Methods), we evaluated the RIN under typical measurement conditions using a setup akin to FTS (see Extended Data Fig. 5a). The MIR beam of our laser system was split in a Mach-Zehnder configuration into two arms, one acting as the LO and the other as the sample arm. The sample arm was mechanically chopped at 10 kHz. The two arms were re-combined with a 50:50 beam splitter for balanced detection with two state-of-the-art MCT detectors (InfraRed Associates; MCT-13-1.00). For optimum noise performance, we took additional technical measures, namely active intensity stabilization of the MIR beam<sup>12</sup> and lock-in detection to minimize the contribution of low-frequency RIN.

The RIN spectra of our free-running MIR source and with active intensity stabilization, measured at 0.45 mW with one of the MCT detectors are plotted in Extended Data Fig. 5b. The measurement reveals a relative standard deviation of 0.04 % integrated in the band from 1 Hz to 100 kHz.

Next, we applied balanced detection in the MIR. To this end, we split the MIR output of our coherent source with a 50:50 beam splitter and used a polariser for the fine adjustment of the power. The output of the two detectors was then recorded with a two-channel lock-in amplifier with internal subtraction. For frequencies above 10 kHz, the RIN of the LO can be suppressed by more than a factor of 500 compared to the free-running laser, down to a white noise floor with at  $6 \times 10^{-8} \text{Hz}^{-0.5}$ . Together with lock-in detection, this enables measurement of the homodyne/heterodyne signal (i.e., sample beam) with very

small noise contribution from the LO (Extended Data Fig. 5c, turquoise line), i.e. comparable to the detector-noise level (Extended Data Fig. 5c, grey line).

However, the total noise within the trace drastically increases when also the noise contributions of the sample beam are considered (see Extended Fig. 5c, blue line). The noise-filtering properties of the lock-in detection act on the LO only, but not on the signal. Therefore, low-frequency noise contributions from the sample beam affect the recorded trace. For a 10-s measurement (typical time-scale for a scan in our system), we observe a ~26 times higher time-domain root-mean-square value in comparison to the LO noise. In FRS, nonlinear time-domain gating would avoid these noise contributions (see Extended Data Fig. 1).

At a total power of 0.450 mW impinging on each detector, in our experiment the power in the signal arm was 17 times smaller than that in the LO due to limitations of the lock-in electronics. Accounting for this, we estimate a RIN of the sample beam of  $17 \times 26 \times 6 \times 10^{-8} \text{ Hz}^{-0.5} = 2.7 \times 10^{-5} \text{ Hz}^{-0.5}$ .

## II. Derivation of Equations (1) and (2)

### Derivation of Equation (1)

In traditional frequency-domain spectroscopies, molecular absorption is measured as the frequency-resolved intensity attenuation of the source. Thus, for each spectral element of the instrument (for a given spectral resolution), the weakest detectable molecular signal is limited by the intensity variation from measurement to measurement. The main causes of these variations are intensity and shot noise of the source, and detector noise. Assuming a statistical behaviour of the measurement-to-measurement variations, for a given spectral element these can be quantitatively described by their relative standard deviation  $\sigma$ . Thus, for a mean reference intensity  $I_0$ , an absorption leading to an intensity smaller than  $I_0(1 - \sigma)$  can be regarded as detectable, while a weaker absorption would lead to an intensity within the error bar of the measurement of  $I_0$ .

Beer's absorption law for an absorption coefficient  $\alpha$  and a propagation length  $z$  reads:

$$I_s = I_0 e^{-\alpha z}, \quad (\text{SII.1})$$

where  $I_s$  is the intensity of the spectral element, with the sample in the beam path. Thus, for the absorption to be detectable, the following inequality needs to hold:

$$e^{-\alpha x} \leq 1 - \sigma \Leftrightarrow \alpha x \geq \ln\left(\frac{1}{1 - \sigma}\right). \quad (\text{SII.2})$$

For small values of  $\sigma$ , the rhs of this inequality can be approximated by the linear terms of the Taylor expansions for  $1/x$  and  $\ln(x)$  yielding:  $\ln\left(\frac{1}{1-\sigma}\right) \approx \ln(1+\sigma) \approx \sigma$ . In conclusion, the minimum detectable absorbance (MDA) is  $\sigma$ , see Eq. (1).

### Derivation of Equation (2)

The propagation of an ultrashort IR pulse through a molecular sample in the electronic ground state, exhibiting both resonant and non-resonant absorption can be modelled semiclassically by solving the wave equation with an adequate polarization response of the sample<sup>13</sup>. In the following, we consider the linear interaction of an ultrashort excitation pulse with an initial electric field amplitude envelope  $E_0(t) = E(z=0, t)$  propagating along the spatial coordinate  $z$  through a medium with a constant absorption coefficient  $\alpha_1$  describing the nonresonant (instantaneous) part of the interaction with the field, and a resonant vibrational absorption. We describe the latter<sup>13</sup> as a homogeneously broadened, Lorentzian-shaped absorption band having a peak absorption  $\alpha_2$  and an effective dephasing time  $T_2$ . Homogeneous broadening is a pertinent assumption due to the large number of molecules involved in the experiments considered here, and due to the comparatively long integration time per measurement point. Furthermore, the Lorentzian model describing the temporal evolution of a two-level system is in accordance with the linearity of all measurements presented in this paper.

We first consider the case in which this band is centred at the carrier frequency of the excitation pulse and later discuss the generalization to an arbitrary central frequency. Thus, the intensity of the initial pulse at its central wavelength is attenuated by  $\exp[(\alpha_1 + \alpha_2)z]$ , and  $T_2$  can be estimated from the full-width-at-half-depth value  $\delta\nu$  of the power spectral density (PSD) absorption line (given in wavenumbers,  $\text{cm}^{-1}$ ) in the frequency domain (FD), cf. Extended Data Fig. 6a, according to  $\delta\nu = (\pi c T_2)^{-1}$ , where  $c$  is the speed of light (see Eq. (88) in Laubereau and Kaiser<sup>13</sup>). Furthermore, we assume that the duration of the excitation pulse is smaller than the dephasing time  $T_2$ . Under these conditions, the electric field envelope in the time domain (TD) as a function of  $z$  and  $t$  is described by (Eq. (90) in Laubereau and Kaiser<sup>13</sup>):

$$E(z, t) = E_0(t) e^{-\frac{1}{2}\alpha_1 z - \varepsilon \cdot \exp\left(-\frac{1}{2}\alpha_1 z - \frac{t-t_{max}}{T_2}\right)} \cdot \frac{J_1(\sqrt{2\varepsilon(t-t_{max})})}{\sqrt{2\varepsilon(t-t_{max})}} \int_{-\infty}^t E_0(t') dt', \quad (\text{SII.3})$$

where  $t_{max}$  denotes the time instant of the maximum of  $E_0(t)$ ,  $J_1$  denotes the first-order Bessel function and  $\varepsilon = \frac{\alpha_2 z}{T_2}$ . Under the assumption of a weak resonant absorption, i.e.,  $\alpha_2 z \ll 1$ , the term  $\frac{J_1(\sqrt{2\varepsilon(t-t_{max})})}{\sqrt{2\varepsilon(t-t_{max})}}$  can be approximated by  $\frac{1}{2}$ . With the notation  $E_{inst}(z, t) = E_0(t) \exp\left(-\frac{1}{2}\alpha_1 z\right)$ , Eq. (SII.3) becomes:

$$E(z, t) \approx E_{inst}(z, t) - \frac{1}{2} \frac{\alpha_2 z}{T_2} \exp\left(-\frac{t-t_{max}}{T_2}\right) \cdot \int_{-\infty}^t E_{inst}(z, t') dt'. \quad (\text{SII.4})$$

The first term on the rhs of Eq. (SII.4),  $E_{inst}(z, t)$ , corresponds to the instantaneous (non-resonant) sample response. Due to the short duration of the exciting pulse, the envelope of this term decays very fast in time (see example in Extended Data Fig. 6b). The second term describes the macroscopic (ensemble-integrated) electric field emitted by the coherent oscillations of the resonantly excited molecular dipoles, modelled by the Lorentz oscillator. The strength of these oscillations (dubbed “dark waves” by Lanin et al.<sup>14</sup>) is proportional to the number of emitters ( $\propto \alpha_2 z$ ) and decays exponentially with the effective dephasing time  $T_2$ . The phase of this field is opposite to that of the instantaneous response, which is reflected in the opposite sign with respect to  $E_{inst}(z, t)$  and which leads to the appearance of a Lorentzian “absorption dip” in the FD representation of the total field after traversing the sample<sup>13</sup>. Extended Data Fig. 6c shows the magnitudes of the Fourier transforms of the two individual terms of the rhs of Eq. (SII.4). Note that the central frequency here is 0 since the electric field envelope is considered (rather than the full, oscillating, electric field).

With the condition  $\alpha_2 z \ll 1$ , a second approximation can be readily performed, namely that on the time scale of the excitation pulse, the field is not attenuated by the resonant absorption<sup>14</sup>. In analogy to Eq. (8) in Lanin et al.<sup>14</sup>, Eq. (SII.4) becomes:

$$E(z, t) \approx E_{inst}(z, t) - \frac{1}{2} \frac{\alpha_2 z}{T_2} \Theta(t - t_{max}) \exp\left(-\frac{t - t_{max}}{T_2}\right) \cdot \int_{-\infty}^{\infty} E_{inst}(z, t') dt', \quad (\text{SII.5})$$

where  $\Theta(t)$  denotes the Heaviside step function. The approximation in (SII.5) improves for shorter initial pulse duration and longer  $T_2$ . The example given in Extended Data Fig. 6 illustrates that this approximation is very good for the regime in this paper. Thus, the second term of the rhs of Eq. (SII.5) is a good approximation for the field emitted by the resonantly excited polarization, corresponding to a Lorentzian emission line with a spectral maximum (absolute value of the electric field envelope) of  $\frac{1}{2} \alpha_2 z C$  with  $C = \int_{-\infty}^{\infty} E_{inst}(z, t') dt'$ .

A (small) portion of the resonant sample response overlaps in time with the instantaneous response. To minimize the contribution of the latter to the recorded signal, and capture mostly the resonant response in a background-free manner, a high-pass time filter beginning at the time  $t_B$  can be applied to the electric field envelope expressed by (SII.5). Assuming that the contribution of  $E_{inst}(z, t)$  is negligible after  $t_B$ , we obtain the following expression for the time-filtered resonant response:

$$\Theta(t - t_B) E(z, t) \approx -\frac{1}{2} \frac{\alpha_2 z}{T_2} \Theta(t - t_B) \exp\left(-\frac{t - t_B}{T_2}\right) \exp\left(-\frac{t_B}{T_2}\right) \cdot C. \quad (\text{SII.6})$$

In analogy to the second term in (SII.5), this expression is a good approximation for a Lorentzian emission line, whose field is delayed by the time  $t_B$  and whose maximum spectral amplitude is attenuated by the factor  $\exp\left(-\frac{t_B}{T_2}\right)$ , see Extended Data Fig. 6c.

At the central frequency ( $\omega = 0$  Hz, corresponding to  $0 \text{ cm}^{-1}$ ), the magnitude of the Fourier transform of  $E_{inst}(z, t)$  is:  $\int_{-\infty}^{\infty} E_{inst}(z, t) \exp(-i\omega t) dt = \int_{-\infty}^{\infty} E_{inst}(z, t) dt = C$ . In conclusion, the magnitude ratio of the field envelopes corresponding to the resonant and the high-pass time-filtered instantaneous responses amounts to  $\frac{1}{2} \alpha_2 z \exp\left(-\frac{t_B}{T_2}\right)$ .

The observable in FRS is the oscillating electric field (rather than its envelope). The electric field can be obtained by multiplying the envelope  $E(z, t)$  by an oscillating function  $\cos(\omega_0 t)$  at the carrier angular frequency  $\omega_0$  (here, we omit the carrier-envelope phase for simplicity). According to basic Fourier transform laws, this results in a two-sided FD spectrum, consisting of two copies of the spectrum of  $E(z, t)$ , shifted to the wavenumbers corresponding to  $-\omega_0$  and  $\omega_0$ , respectively, each with a magnitude decreased by  $\frac{1}{2}$ . Since this reduction of magnitude applies for both the resonant and instantaneous parts of the response, their magnitude ratio remains the same.

Assuming a noise (background signal) level  $N$ , the MDA for FRS at the frequency  $\omega_0$  can be defined as the value  $\alpha_2 z$ , at which the high-pass time-filtered signal emitted upon resonant excitation equals this level ( $S/N = 1$ ). Normalizing this equality by the magnitude of the instantaneous field, we obtain:

$$\frac{1}{2} \alpha_2 z \exp\left(-\frac{t_B}{T_2}\right) = \frac{1}{DR_E}, \quad (\text{SII.7})$$

where  $DR_E$  denotes the magnitude ratio of the instantaneous field to the background in the FD at the carrier frequency  $\omega_0$  and can therefore be interpreted as the dynamic range of the measurement at this frequency. Eq. (2) immediately follows from (SII.7) (note that in Eq. (2) the dephasing time  $T_2$  is denoted  $T_L$ ).

The parallel between Eq. (SII.3) and Beer's law is noteworthy and readily justifies the extension of the MDA criterion in Eq. (2) to all optical frequencies within the spectrum of the initial pulse. Considering in the FD the instantaneous response as a reference, the magnitude of the envelope of its electric field  $|\mathcal{E}_{inst}(z, \omega)|$  at  $\omega = 0$  is attenuated by  $\exp\left(-\frac{1}{2} \alpha_2 z\right)$ . For  $\alpha_2 z \ll 1$  the exponential function is well approximated by the first-order term in its Taylor expansion and we obtain:

$$|\mathcal{E}(z, 0)| \approx |\mathcal{E}_{inst}(z, 0)| \left(1 - \frac{1}{2} \alpha_2 z\right). \quad (\text{SII.8})$$

With  $|\mathcal{E}_{inst}(z, 0)| = C$ , the second term on the rhs of Eq. (SII.8) corresponds to the maximum of the Lorentzian emission peak obtained by Fourier transforming the rhs of Eq. (SII.3). Spectrally shifting the same Lorentzian absorber in the FD to a different frequency  $\omega \neq 0$  results in the TD in a Lorentzian exponential decay whose amplitude is scaled to  $|\mathcal{E}_{inst}(z, \omega)|$  and with a phase shift given by the frequency shift in the FD which does not affect the MDA criterion derived here. In analogy to (SII.6), high-pass time-filtering this signal starting at  $t_B$  results in a further attenuation by  $\exp\left(-\frac{t_B}{T_2}\right)$ . In conclusion, equations (SII.7) and (1) can be extended to all frequencies  $\omega$  by extending the definition of  $DR_E$  as the

magnitude ratio of the measured field of the instantaneous response (i.e.  $\frac{1}{2}|\mathcal{E}_{inst}(z, \omega)|$ ) to the  $\omega$ -dependent background level.

### III. Benchmarking with Fourier-transform infrared (FTIR) spectrometry

The FTIR spectrometer-based instrument (in the following, briefly “FTIR”) used for all benchmarking measurements reported in this paper was a commercial, research-grade device (MIRA Analyzer, Micro Biolytics GmbH). The thermal source sends milliwatt-level broadband radiation to the 8- $\mu\text{m}$ -thick liquid cuvette. The cuvette is filled by an automated microfluidic system. The cuvette thickness was chosen by the manufacturer for high sensitivity with the FTIR device. For the Sterling-motor-cooled detector with an area of  $7.85 \times 10^{-3} \text{ cm}^2$ , the manufacturer provided a peak detectivity  $D^* = 45.59 \times 10^9 \text{ cm } \sqrt{\text{Hz}}/\text{W}$  at the wavelength of 10.49  $\mu\text{m}$ , a frequency of 10 kHz, and a bias voltage of -25mV.

To compare the performance of our FTIR device with the state of the art reported in literature, we evaluated the RMS (root-mean-square) noise of the 100 % lines of water in the spectral region between 1600 and 1700  $\text{cm}^{-1}$ , in analogy to the measurement reported in Schwaighofer et al.<sup>15</sup> performed with the high-end Bruker Vertex 80v device employing a liquid-nitrogen-cooled MIR. The latter device yielded an RMS noise of  $2.75 \times 10^{-5}$  (evaluated as the RMS of the nominally 0 absorbance across the above-mentioned 100- $\text{cm}^{-1}$  spectral window) at a spectral resolution of 2  $\text{cm}^{-1}$  and a measurement time of 53 s, without exchange of the water sample in the 8- $\mu\text{m}$ -thick cuvette. With our FTIR device and comparable parameters (spectral resolution: 4  $\text{cm}^{-1}$ , measurement time: 45 s, 8- $\mu\text{m}$ -thick cuvette), a similar value of  $2.8 \times 10^{-5}$  was obtained, albeit with exchanging the water sample in the cuvette between the reference and sample measurement. Thus, the differences between the performances of the two high-end FTIRs are minor.

The spectral coverage of the FTIR instrument is broader than that of the FRS instrument, and all of the FTIR measurements reported in this paper were performed with the full spectral coverage of the FTIR. To exclude an unfair comparison between the performance of FRS and that of FTIR due to this discrepancy in bandwidth (in particular a decrease in sensitivity due to the broader bandwidth for the FTIR), we compared the noise RMS of the 0-absorption line with and without a 7.3- $\mu\text{m}$  long-pass filter (Edmund Optics). The detector-limited spectrum of the FTIR reaches up to 12  $\mu\text{m}$ , such that with the long-pass filter the spectral coverage of the two instruments was very similar. Because our FTIR is a sealed commercial product (customised for liquid-phase measurements), the insertion of the long-pass filter in our instrument was not feasible. Instead, this comparison measurement was performed by the device manufacturer with an identical device. With parameters optimised for each setting, a decrease of the RMS-SNR of the 0-absorption line to 75% was observed with the long-pass filter in the beam (in the spectral range from 1020 to 1220  $\text{cm}^{-1}$ ). Thus, while a slight improvement is indeed detectable, the

expected sensitivity improvement in this bandwidth-filtered case is marginal (e.g., a limit of detection of 6  $\mu\text{g}/\text{ml}$  instead of 8  $\mu\text{g}/\text{ml}$  is expected for  $\text{DMSO}_2$  solved in water).

An identical microfluidic system, including the cuvette was adapted for the FRS measurements. For FRS, we used a thicker liquid layer (i.e., larger distance between the cuvette walls), as allowed by the higher dynamic range of our instrument.

#### IV. Sample preparation, retrieval of concentrations and experimental validation of Eq. (2)

For this experiment, we prepared a dilution series of methylsulfonylmethane solved in pure water (Millipore, Check System). First, we prepared 50 ml of 10 mg/ml  $\text{DMSO}_2$  in water, serving as a stock solution for the preparation of the dilution series. Next, the stock solution was watered down in several steps to obtain concentrations of 1000, 30, 10, 3, 1, 0.7, 0.5, 0.3, 0.1  $\mu\text{g}/\text{ml}$ . Each concentration was prepared in a large volume ( $\sim 10$  ml) and with a maximal dilution factor of 10, in order to minimize errors in the obtained concentrations due to sample handling.

For each prepared concentration, more than 5 aliquots were measured under identical conditions with FRS and FTIR. Concentrations above 10  $\mu\text{g}/\text{ml}$  were measured 5 times and smaller concentrations were measured more than 10 times to obtain sufficient statistics. The nominal spectral resolution of both measurements was 4  $\text{cm}^{-1}$  and the duration of each measurement was set to 45 s, over which several individual scans were averaged, for both instruments.

The FTIR spectrometer (described in Supplementary Section III) is a fully automated, commercial product. The raw output data consists in absorbance spectra (for the pre-defined spectral resolution and measurement time). With the absorbance spectrum measured at a calibration concentration well above the instrument noise floor (1 mg/ml), for each individual measurement we extracted the solution concentration via a 1-parameter least-squares fit using Beer's law, fitting the spectrum with the unknown concentration to the spectrum with the calibration concentration of 1 mg/ml.

The raw time-domain data recorded with the FRS instrument were truncated to the temporal window between 1.5 and 4 ps (referenced to the pulse envelope maximum). To isolate the response of the molecular signal of interest, all sample measurements were referenced to pure water measurements by subtracting the time-domain trace of a reference measurement from the time-domain trace of the sample measurement. Like in the case of the FTIR data processing, a calibration measurement at a concentration of 1 mg/ml was performed, and used for retrieving the concentrations of the individual samples via 1-parameter fits. To this end, the bandpass-filtered time-domain data were Fourier-transformed and the wavenumber range 950 – 1350  $\text{cm}^{-1}$  was considered. As opposed to a fit of the raw time-domain data, the latter operation excludes noise/measurement errors outside this spectral window containing molecular signal.



Due to the relatively low calibration concentration, the resonant response of the DMSO<sub>2</sub> molecules to the impulsive excitation is in very good approximation linear in concentration (cf. derivation in Supplementary Section II). For the bandwidth-optimised setting, the narrowband fit (capturing mainly the absorption at 1139 cm<sup>-1</sup>) was performed in the wavenumber range 1080 – 1200 cm<sup>-1</sup>, and the broadband fit in the range 950 – 1500 cm<sup>-1</sup>.

By performing statistics on the retrieved concentrations, we obtained the mean and standard deviation values for the retrieved concentrations for each set of samples with nominally identical DMSO<sub>2</sub> concentration. The results are plotted in Fig. 3.

It is noteworthy that the modelled resonant response at 1139 cm<sup>-1</sup>, using only the width and strength of the absorption line (as determined from an FTIR measurement at a calibration concentration), and linearly scaled to the nominal concentrations of the samples measured with FRS, is in excellent agreement with the measured response of the latter, as can be seen in Extended Data Fig. 7. In addition, the modelled response for a 200-ng/ml solution yields a maximum spectral intensity which coincides with the measured noise floor, demonstrating the consistency between the LOD determination by the statistics of the concentration retrieval (Fig. 3) and that given by Eq. (2).

Using the sub-60-fs infrared excitation pulses (Supplementary Information Section I) and the bandwidth-optimised detection setting of the FRS instrument (Fig. 1d, continuous line) yields an experimentally determined value of  $t_B = 450$  fs at the expense of a factor-of-ten reduction of  $DR_E$  (Fig. 1d). The lowered  $DR_E$  would, in its own right, result in an increase of the minimum detectable concentration by the same factor, according to Eq. (2). This is toned down to a factor of three by shortening  $t_B$  from 1.5 ps to 0.45 ps, predicting 600 ng/ml as the new limit of detection. This value is in excellent agreement with the experimentally determined value when considering the single oscillator centred at 1139 cm<sup>-1</sup> for concentration retrieval, corroborating the sensitivity of  $MDA_{FRS}$  to  $t_B$ . In reality, the broadband excitation brings more than one vibrational mode into oscillation (see also temporal “beating” in Fig. 1b as well as the multiple “absorption dips” in Fig. 1c), resulting in a further decrease of the limit of detection to 450 ng/ml.

#### V. Statistics of the waveform stability of human blood serum

The statistics shown in Fig. 4c, d were obtained by evaluating 500 individual scans of the same blood serum sample (each scan taking 4.5 s). The individual EOS traces were aligned in time using a one-parameter (time shift) optimisation. Furthermore, a one-parameter amplitude correction of all traces to the maximum amplitude of the first measurement was performed, allowing for a compensation of minor, slow drifts of the laser intensity with time. Subsequently, the traces were frequency-filtered by a 20<sup>th</sup>-order super-Gaussian filter suppressing any noise outside the spectral window 900 – 1450 cm<sup>-1</sup>.

For each trace, in steps of a few field oscillations, a sinus curve of  $\sim 1.5$  oscillations was fitted with respect to 4 parameters: amplitude, amplitude offset, frequency and phase. The relative amplitude noise and the absolute timing jitter of the zero crossings, shown in Fig. 4c and d, respectively, were obtained by evaluating the statistics of the amplitude and phase fit parameters, respectively. Because the oscillating EOS trace exhibits regions of strong deviation from a sinus function (e.g., due to the temporal evolution of the GMF), we excluded fits with relative errors larger than 3 %. This resulted in the grey dots in Fig 4c, d. The black, continuous lines indicate a trend, calculated by interpolating the grey points with an 82-point LOWESS filter (OriginPro 2017).

#### **VI. Sample preparation and data processing for complex samples – human blood serum spiked with aqueous DMSO<sub>2</sub> solutions, and mixtures of maltose and melibiose solved in water**

##### **Spiked serum**

Spiked serum samples were prepared using pooled human serum (BioWest, Nuaille, France). For each prepared concentration, 900  $\mu\text{l}$  of serum was mixed with 100  $\mu\text{l}$  of DMSO<sub>2</sub> in pure water. Subsequently, 1000, 100, 50, 10, 5 and 0  $\mu\text{g/ml}$  of DMSO<sub>2</sub> solution were used to obtain spiked sera samples with 100, 10, 5, 1, 0.5, 0  $\mu\text{g/ml}$  DMSO<sub>2</sub> concentrations, respectively. In order to avoid systematic effects in the sample preparation that might lead to a separation in the subsequent principal component analysis, each concentration of spiked serum was prepared 5 times independently. Concentrations below 10  $\mu\text{g/ml}$  were measured at least 8 times. For FTIR measurements 0.5  $\mu\text{g/ml}$  was excluded, as the previous experiment showed that this is below the limit of detection of our FTIR.

While the measurement time (45 s) and the spectral resolution ( $4\text{ cm}^{-1}$ ) were set equal for both instruments, due to the different nature of the two measurement devices, the output data which we further used for principal component analysis (PCA), were of different nature. To minimize the effect of pure data processing on the difference in the classification performance with the two instruments (cf. Fig. 5) we chose similar data processing parameters for both instruments wherever possible. In the following, the data processing steps for both instruments are described.

The absorbance spectra were measured with FTIR in the spectral range  $930 - 3050\text{ cm}^{-1}$ . In order to reduce the influence of a fluctuating baseline (which is a well-known problem in FTIR data processing<sup>16</sup>), and to sharpen essential spectral features, we performed standard FTIR data processing steps of smoothing with a Savitzky–Golay filter (with the width of 15 data points) and calculated the 2<sup>nd</sup> derivative of the absorption spectra. After vector normalization, the spectra were truncated to the spectral range from  $1000$  to  $1400\text{ cm}^{-1}$ , where essential spectral features of the DMSO<sub>2</sub> are located. After this pre-processing, the obtained vectors

were analysed with PCA. We emphasize that among a multitude of pre-processing routines, these above-listed pre-processing steps led to the best separation performance with PCA.

The FRS apparatus presented in this paper delivers raw data recorded as described in Supplementary Information Section I. In analogy to the FRS data processing described in the previous section, first, all spiked serum sample measurements were referenced to pure water samples (measured in alternating order to the sample measurements) by subtraction of time-domain data. Subsequently, for the compatibility with FTIR data processing, the data in a temporal window in the wake of the pulse were Fourier-transformed. The Savitzky–Golay filter was applied to the real and imaginary part of the complex vectors independently and the 2<sup>nd</sup> derivative of the spectra was calculated. After vector normalization the spectra were truncated to the spectral range from 1000 to 1300 cm<sup>-1</sup>. PCA was applied to the complex-valued result of the Fourier-transformed time-domain data.

In all our measurements whose results were evaluated with PCA, the nominal variation among different classes of samples can be parametrised by one parameter. Thus, for simplicity, for the PCA results reported in the main text, we considered the first principal component only, for both instruments, which is expected to describe the maximum separation of differing classes. This expectation is confirmed by the similarity of the first loading vector to the pre-processed data for each instrument (Extended Data Figure 8a-d).

For the more complex samples (here, both spiked serum and a mixture of sugars solved in water), the choice of the time values for the beginning and end of the temporal window considered for processing GMFs is not obvious, and an optimum choice might depend on the specific experiment. For the case of the FRS data obtained from the measurements of the spiked serum samples, we therefore varied these two important free parameters over broad ranges (beginning time  $t_B$  from -0.5 ps to 2 ps with respect to the envelope maximum of the time-domain signal, and time window length  $\Delta t$  from 0.05 ps to 4.5 ps with respect to the beginning time  $t_B$ ) and evaluated a figure of merit (FOM) for the quality of separation of classes (defined by the spiking concentration). The FOM evaluates the average spread (root mean square) of classes normalised to the maximum distance of the centroids of the 0  $\mu\text{g}/\text{mL}$  class and 10  $\mu\text{g}/\text{mL}$  class, with respect to the first principal component.

The result is shown in Extended Data Figure 8e. The regions of good separation are located in both cases at positive  $t_B$  values, confirming that noise of the excitation affects the separation performance.

#### **Aqueous solution of maltose and melibiose**

For this experiment, two sugars, maltose (D-Maltose; Serva Electrophoresis GmbH) and melibiose (D-(+)-Melibiose; Sigma-Aldrich) were mixed in pure water at a constant total concentration of 100  $\mu\text{g}/\text{ml}$  and at varying relative concentrations, using the procedure described in Section IV. The two sugars were chosen to exhibit similar spectral fingerprints, see Extended Data Figure 9.

In order to capture absorption features in a wavenumber band as broad as possible, this measurement was performed with the bandwidth-optimised setting of our instrument, covering the spectral range between  $900\text{ cm}^{-1}$  and  $1524\text{ cm}^{-1}$  at  $-20\text{-dB}$  intensity, cf. Fig. 1d. With this setting, the intensity dynamic range of detection was roughly 100 times lower than with the previous setting. Furthermore, the recorded EOS traces exhibit a strong signal from the internal reflection of the thinner EOS at  $1.6\text{ ps}$  after the excitation pulse, see Fig. 1b.

With the same data processing as for the previous experiment, the loading vectors for PCA and result of the separation FOM are shown in Extended Data Fig. 8f-i and j, respectively. We considered concentration ratios of 50/50, 55/45, 60/40, 70/30, and 100/0. Like in the case of the spiked serum, for both instruments the first principal component resembles the processed spectral data representing the single-parameter nominal variation among the classes. As in the previous experiments, regions of good PCA separation are located at positive  $t_B$  values. In addition, both FOM maps indicate a sharp upper bound of the corridor of good separation at  $t_B + \Delta t = 1.5\text{ ps}$ , which is the temporal value for the beginning of the strong internal reflection. This observation confirms the detrimental effect of excitation noise on the performance of FRS and justifies future efforts addressing both the suppression of multiple reflections, and of further temporal compression of the excitation.

For the PCA results shown in Fig. 5, for both instruments the same nominal concentrations were used in both experiments, except for not including serum spiked with  $0.5\text{ }\mu\text{g/ml}$  DMSO<sub>2</sub> in the FTIR measurement due to this concentration being below the LOD of the instrument. In Fig. 5, the mean values and standard deviations of the 1<sup>st</sup> principal component value are shown.

#### VII. Measurements of living human cells and plant leaves

THP-1 human leukemic cells (ATCC® TIB-202™) were cultured under standard culture conditions in RPMI 1640 Complete medium (EMD Millipore Corp.) supplemented with 10% fetal calf serum (FCS; EMD Millipore Corp.). Prior to measurements cells were washed twice with phosphate buffered saline (PBS; Sigma), resuspended and measured in PBS, prepared at a density of about  $10 \times 10^6$  cells/ml. Resuspended cells were kept at  $37\text{ }^\circ\text{C}$  until measurement.

Measurements were performed with a  $100\text{-}\mu\text{m}$  thick flow-through measurement cell (cuvette) consisting of two  $5\text{-mm}$  anti-reflection-coated germanium windows (Spectral Systems, LLC). The cell suspension was injected using a  $1\text{-ml}$  manual syringe. The interrogation volume was around  $25$  nanoliters, thus probing on average  $250$  cells per measurement. As reference, PBS only (without cells) was measured. The flow-through measurement cell and adjacent tubing were cleaned between measurements, using deionized water. The total integration time per measurement was  $48$  seconds with a nominal spectral resolution of  $8$

$\text{cm}^{-1}$ . The five measurements, shown in Fig. 6c, were prepared from 4 independent tissue culture flasks, and each measurement was repeated 5 times.

On average, the power spectral density (i.e., intensity) of the GMF signal of the living human cells, obtained by subtracting the FRS signal of a PBS only (reference) measurement from a cell-based sample measurement (THP-1 human cells resuspended in PBS) lies 7 orders of magnitude (averaged in the range between 900 and 1500  $\text{cm}^{-1}$ ) above the detection noise floor. This illustrates the capability of FRS to investigate strongly absorbing samples in transmission, without a significant reduction of the signal-to-noise ratio due to either the low level of the transmitted power, or to detector noise.

The absorbance and phase spectra in Fig. 6c were calculated after removing the multiple reflection artefact located at 1500 fs via truncation of the raw time domain traces at 1400 fs. The time-filtered spectra were obtained by subtracting the THP-1 cell measurement from the respective reference PBS measurement using a temporal filter opening at 325 fs and closing at 1400 fs, before applying the Fourier transform. All resulting THP-1 spectra were rescaled by normalizing their respective area under the curve to their average value. The standard deviation of the THP-1 measurements shown in Fig. 6c was calculated after rescaling. The obtained spectra are well reproducible for different experiments, performed on THP-1 cells cultured and measured on different days.

The measurement uncertainty was defined as the root-mean-square noise of the baseline between 1000 and 1480  $\text{cm}^{-1}$  and was evaluated from multiple PBS measurements that were referenced to PBS (including sample exchange). The average signal-to-noise ratio (SNR) is obtained by dividing the maximum absorbance/power spectral density by the measurement noise. We evaluated an average SNR of 61 for the absorbance spectra and an SNR of 102 for the time-filtered spectra. Note that these values include significant signal variations due to sample exchange.

Transmission measurements of leaves from *Salix caprea*, a common tree plant, were performed immediately after collection. The leaves were mounted in a free-standing geometry using a leaf clip. The total measurement time was 1.5 min with a spectral resolution of 8  $\text{cm}^{-1}$ . The absorbance and phase spectra were calculated after removing the multiple reflection artifacts located at 1500 fs via truncation of the raw time domain traces at 1400 fs. Although only the spectra of one leaf at one position are shown in Fig. 6d, we were able to obtain very similar spectra from different positions on the leaf and from different leaves of the same tree, as well as those of leaves from the same tree measured on other days. After the optical measurement, the leaf was sliced and its thickness was measured using an optical microscope, shown in Fig. 6a.

**References for Supplementary Information**

1. Fritsch, K., Poetzlberger, M., Pervak, V., Brons, J. & Pronin, O. All-solid-state multipass spectral broadening to sub-20 fs. *Optics Letters* **43**, 4643–4646 (2018).
2. Pupeza, I. *et al.* High-power sub-two-cycle mid-infrared pulses at 100 MHz repetition rate. *Nature Photonics* **9**, 721–724 (2015).
3. Schweinberger, W., Vamos, L., Xu, J., Baune, C. & Rode, S. Interferometric delay tracking for low-noise Mach-Zehnder-type scanning measurements. *Optics Express* **27**, 4789–4798 (2019).
4. Habel, F. & Pervak, V. Dispersive mirror for the mid-infrared spectral range of 9–11.5  $\mu\text{m}$ . *Applied Optics* **56**, C71–C74 (2017).
5. Gallot, G. & Grischowsky, D. Electro-optic detection of terahertz radiation. *Journal of the Optical Society of America B* **16**, 1204–1212 (1999).
6. Porer, M., Ménard, J.-M. & Huber, R. Shot noise reduced terahertz detection via spectrally postfiltered electro-optic sampling. *Optics Letters* **39**, 2435–2438 (2014).
7. Kwee, P., Willke, B. & Danzmann, K. New concepts and results in laser power stabilization. *Applied Physics B* **102**, 515–522 (2011).
8. Keiber, S. *et al.* Electro-optic sampling of near-infrared waveforms. *Nature Photonics* **10**, 159–162 (2016).
9. Brabec, T. & Krausz, F. Intense few-cycle laser fields: Frontiers of nonlinear optics. *Reviews of Modern Physics* **72**, 545–591 (2000).
10. Butler, T. P. *et al.* Watt-scale 50-MHz source of single-cycle waveform-stable pulses in the molecular fingerprint region. *Optics Letters* **44**, 1730–1733 (2019).
11. Knorr, M. *et al.* Ultrabroadband etalon-free detection of infrared transients by van-der-Waals contacted sub-10- $\mu\text{m}$  GaSe detectors. *Optics Express* **26**, 19059–19066 (2018).
12. Huber, M. *et al.* Active intensity noise suppression for a broadband mid-infrared laser source. *Optics Express* **25**, 22499–22509 (2017).
13. Laubereau, A. & Kaiser, W. Vibrational dynamics of liquids and solids investigated by picosecond light pulses. *Reviews of Modern Physics* **50**, 607–665 (1978).
14. Lanin, A. A., Voronin, A. A., Fedotov, A. B. & Zheltikov, A. M. Time-domain spectroscopy in the mid-infrared. *Scientific Reports* **4**, 6670, 1–8 (2014).

15. Schwaighofer, A. *et al.* Beyond Fourier Transform Infrared Spectroscopy: External Cavity Quantum Cascade Laser-Based Mid-infrared Transmission Spectroscopy of Proteins in the Amide I and Amide II Region. *Analytical Chemistry* **90**, 7072–7079 (2018).
16. Baker, M. J. *et al.* Using Fourier transform IR spectroscopy to analyze biological materials. *Nature Protocols* **9**, 1771–1791 (2014).





## 2.3 Optimum sample thickness for trace analyte detection with field-resolved infrared spectroscopy

**Preface:** Field-resolved spectroscopy gives direct access to the electric field. This implies that the measurement signal scales linearly with the electric field strength. This simple fact has important consequences for the measurement of strongly attenuating samples – a common challenge in infrared spectroscopy as water is a strong absorber and present in many systems.

For any spectroscopic measurement it is desirable to record the molecular signal with the highest possible signal-to-noise ratio (SNR). A general approach to obtaining a stronger molecular signal is to increase the interaction length with the analyte under test. However, this brings about an attenuation of the light intensity and, in the case of long path lengths, ultimately a reduction in the (relative) measurement SNR. It is therefore desirable to optimize the interaction length with the sample under this boundary condition.

For most of the established infrared spectroscopies, the measurement SNR scales linearly with the light intensity. Consequently, if the sample attenuates the light intensity by for example two orders of magnitude, the SNR is also reduced by the same amount. Therefore, any recommendations for the optimum or suggested sample thickness have been based on this assumption so far [104, 105]. In contrast to that the SNR in FRS scales linearly with the electric field. Considering the same example as above, i.e. if the sample attenuates the light intensity by two orders of magnitude, the SNR is reduced by only one order of magnitude.

Based on these considerations, we theoretically evaluated the limit of detection (LOD) of a given analyte in dependence of the light attenuation. We show that for field-scaling – in comparison to intensity-scaling – a lower LOD can be achieved for a much wider range of interaction lengths. This effectively increases the useable range of path lengths in applications. In addition, we find that the theoretical optimum sample thickness in FRS [39] is twice the length considered optimal for FTIR measurements [104, 105]. We believe these features of FRS will be advantageous for existing applications of infrared spectroscopy, but will also broaden the potential field of applications due to the relaxed sample thickness requirements.

## Optimum sample thickness for trace analyte detection with field-resolved infrared spectroscopy

*as published in*

**Analytical Chemistry** (2020)

[39]

*by*

Marinus Huber, Michael Trubetskov, Syed A. Hussain, Wolfgang  
Schweinberger, Christina Hofer, and Ioachim Pupeza

**Contributions:** I worked out most of the theoretical considerations, took all the measurements included in this paper, and wrote most of the manuscript.

This is an open access article published under a Creative Commons Attribution (CC-BY) License, which permits unrestricted use, distribution and reproduction in any medium, provided the author and source are cited.



analytical  
chemistry

pubs.acs.org/ac

Article

## Optimum Sample Thickness for Trace Analyte Detection with Field-Resolved Infrared Spectroscopy

Marinus Huber,\* Michael Trubetskov, Syed A. Hussain, Wolfgang Schweinberger, Christina Hofer, and Joachim Pupeza\*



Cite This: <https://dx.doi.org/10.1021/acs.analchem.9b05744>



Read Online

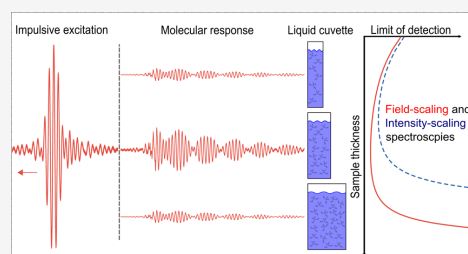
ACCESS |

Metrics & More

Article Recommendations

Supporting Information

**ABSTRACT:** The strong absorption of liquid water in the infrared (IR) molecular fingerprint region constitutes a challenge for applications of vibrational spectroscopy in chemistry, biology, and medicine. While high-power IR laser sources enable the penetration of ever thicker aqueous samples, thereby mitigating the detrimental effects of strong attenuation on detection sensitivity, a basic advantage of heterodyne-measurement-based methods has—to the best of our knowledge—not been harnessed in broadband IR measurements to date. Here, employing field-resolved spectroscopy (FRS), we demonstrate in theory and experiment fundamental advantages of techniques whose signal-to-noise ratio (SNR) scales linearly with the electric field over those whose SNR scales linearly with radiation intensity, including conventional Fourier-transform infrared (FTIR) and direct absorption spectroscopy. Field-scaling brings about two major improvements. First, it squares the measurement dynamic range. Second, we show that the optimum interaction length with samples for SNR-maximized measurements is twice the value usually considered to be optimum for FTIR devices. In order to take full advantage of these properties, the measurement must not be significantly affected by technical noise, such as intensity fluctuations, which are common for high-power sources. Recently, it has been shown that subcycle, nonlinear gating of the molecular fingerprint signal renders FRS robust against intensity noise. Here, we quantitatively demonstrate this advantage of FRS for thick aqueous samples. We report sub- $\mu\text{g}/\text{mL}$  detection sensitivities for transmission path lengths up to  $80\ \mu\text{m}$  and a limit of detection in the lower  $\mu\text{g}/\text{mL}$  range for transmission paths as long as  $200\ \mu\text{m}$ .



Molecular vibrational spectroscopies, such as Raman and infrared (IR) spectroscopies, are versatile tools for delivering chemical and molecular information on complex samples in a fast, reliable, and label-free manner.<sup>1</sup> Every molecule exhibits a unique spectrum of vibrational eigenstates,<sup>2</sup> leading to highly specific signals when a molecular ensemble (for instance biofluids or tissue) is subjected to spectroscopic interrogation. This “spectral fingerprint” contains a wealth of information about the molecular composition, structure, and conformation.<sup>1,2</sup> This underlies numerous applications in biology and medicine, such as comprehending protein dynamics and folding,<sup>3</sup> identifying cell phenotypes,<sup>4</sup> quantifying blood-based clinical parameters,<sup>5</sup> and detecting cancerous states in tissues<sup>6</sup> and biofluids.<sup>7,8</sup>

Typically, the study of biological systems is preferably performed in their natural aqueous environment. While Raman spectroscopy is well suited for transmission measurements thereof, it suffers from weak signals.<sup>1</sup> Broadband IR spectroscopy, on the other hand, profits from large interaction cross sections, potentially affording a unique combination of detection sensitivity and molecular coverage.<sup>1</sup> However, the strong absorbance of (liquid) water in this spectral range has

severely limited the applicability of IR vibrational spectroscopy (and microscopy) in transmission geometry so far. In fact, in table-top Fourier-transform IR (FTIR) spectrometry setups, the most commonly employed technology, the transmission path length needs to be limited to  $<10\ \mu\text{m}$  due to the modest brightness of the source and the lack of high-sensitivity mid-infrared (MIR) detectors.<sup>3,9</sup> This implies severe practical complications and limitations.

First, when studying living cells or (complex) biofluids, sophisticated cell holders and/or microfluidic systems have to be utilized, with small flow cross sections, complicating sample handling and increasing the danger of clogging.<sup>10</sup> Second, strong water absorption prevents the investigation of thick samples in transmission, such as large biological cells, cell

Received: December 20, 2019

Accepted: April 30, 2020

Published: April 30, 2020



ACS Publications

© XXXX American Chemical Society

A

<https://dx.doi.org/10.1021/acs.analchem.9b05744>  
Anal. Chem. XXXX, XXX, XXX–XXX

complexes (e.g., 3D cell cultures), and (aqueous) tissue. To circumvent the strong water absorption, attenuated total reflection techniques<sup>11</sup> are often applied, albeit at the cost of even smaller penetration depths. Alternatively, the sample can be dried, which excludes the study of live organisms and strongly alters the sample.<sup>12</sup>

In order to work with larger path lengths and to mitigate the loss in signal-to-noise ratio (SNR) due to strong water absorption, it is necessary to use high-brightness sources like synchrotrons or quantum cascade lasers (QCL). By utilizing their increased MIR power, determination of glucose, lactate, and triglycerides in blood serum with path lengths above 100  $\mu\text{m}$  (1030–1230  $\text{cm}^{-1}$ )<sup>5</sup> and spectroscopy of proteins in aqueous solution in the Amide I and II region with path lengths as large as 32  $\mu\text{m}$ <sup>13</sup> have been demonstrated. However, power scaling is limited, because the strong water absorption eventually results in heating of the samples. Therefore, a further increase of the path length and/or sensitivity is not readily achievable when the remaining transmitted intensity is directly measured with (noisy) MIR photodetectors.

In this work, we demonstrate in theory and experiment the potential of field-resolved infrared spectroscopy (FRS)<sup>14</sup> to overcome these long-standing limitations. FRS relies on the excitation of resonant molecular vibrations with waveform-stable, broadband MIR pulses and electric-field-resolved detection of the emerging fingerprint waveforms. This brings about two major advantages. First, the measurement signal scales linearly with the electric field and, therefore, it decreases with the square root of intensity attenuation. This effectively squares the measurement intensity dynamic range, which is usually limited by the detector dynamic range.<sup>15–17</sup> Second, temporal isolation of the resonant molecular signal from the impulsive excitation renders FRS robust against fluctuations of the latter.<sup>14</sup>

Together, these properties result in linear scaling of the measurement SNR with the electric field. In the following, we refer to this scaling behavior as *field-scaling* in order to distinguish it from *intensity-scaling* techniques whose SNR scales linearly with the light intensity reaching the detector (e.g., conventional FTIR spectrometry). Although field-scaling is not unique to FRS, with other methods, the presence of the time-integrated sample signal (containing all noise contribution from the source) on the detector(s) makes it much more challenging to achieve this regime, especially in conjunction with high-power MIR sources. When applicable, field-scaling of the SNR brings about fundamental advantages for measurements of strongly absorbing samples.

For each SNR-scaling regime, we derive scaling laws for the limit of detection (LOD) of a given analyte in a matrix material (e.g., liquid water) having the absorption coefficient  $\alpha_M$  and considering the total interaction length  $x$ . We show that for field-scaling—in comparison to intensity-scaling—a lower LOD can be obtained for a significantly wider range of interaction lengths, which effectively increases the useable range of path lengths in applications (Figure 1). We find that the theoretical optimum sample thickness is twice the length considered optimum for FTIR measurements.<sup>18,19</sup> Finally, we experimentally validate this formula, demonstrating that field-scaling and intensity-noise robust detection can be achieved in practice.

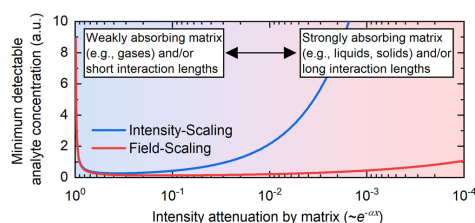


**Figure 1.** Theoretical limit of detection (LOD) of a given analyte embedded within a matrix substance for field- and intensity-scaling techniques. The theoretical LOD values were calculated assuming a spectrometry device for both approaches offering the same SNR for a non-attenuated beam. For weak attenuations by the matrix, the LOD of field-scaling and intensity-scaling techniques are comparable. For strong attenuations, field-scaling is advantageous.

## SCALING LAWS AND OPTIMUM INTERACTION LENGTH

For a spectroscopic measurement, the optimum path length depends on the SNR-scaling with intensity  $I$ . Typically, a distinction into one of the three following scaling-regimes is possible:<sup>2,20</sup>

- (1) Square-root-scaling ( $\text{SNR} \sim \sqrt{I}$ )
- (2) Linear scaling ( $\text{SNR} \sim I$ )
- (3) Constant ( $\text{SNR} \sim \text{const}$ )

The majority of MIR spectroscopies operate either in the second or the third regime. For a given setup, the “operating regime” often depends on the average signal power reaching the detector.<sup>20</sup> Usually, a system is intensity–noise limited at high optical powers and, for decreasing power, eventually becomes detector–noise limited. This has to be considered when choosing the interaction length. By contrast, FRS has been demonstrated to afford field-scaling operation for a range of powers extending from a few hundred photons per second to tens of milliwatts<sup>14</sup> and, potentially, to Watt-level average powers.<sup>21</sup>

For all scaling regimes, derivations of the optimum sample thickness can be found in the [Supporting Information](#). In the following, we focus on the discussion of scaling laws for FRS (i.e., field-scaling). Subsequently, we discuss to what extent these apply to other spectroscopic techniques and how they compare to those of conventional FTIR spectroscopy.

For any spectroscopic measurement, it is desirable to record the molecular signal with the highest possible SNR. A general approach to gaining a stronger signal is to increase the interaction length with the analyte under test. However, this brings about an attenuation of the light intensity due to interaction with the matrix containing the analyte and, for large path lengths, eventually decreases the (relative) measurement SNR. This is particularly severe for aqueous solutions, as the strong IR absorption of water is, unlike the molecules dissolved in it, mostly of little spectroscopic interest. Therefore, it is desirable to optimize the interaction length with the sample under this condition.

According to Beer’s absorption law, the light intensity  $I$  (at a certain frequency) after passing through a medium with absorption coefficient  $\alpha$  and propagation length  $x$  is given by  $I = I_0 e^{-\alpha x}$ , where  $I_0$  denotes the intensity before the medium. For the case of a field-scaling time-domain measurement, we

have previously derived a simple formula for the minimum value of  $(\alpha x)_{\min}$  detectable for a particular absorption line of a molecule:<sup>14</sup>

$$(\alpha x)_{\min} = \frac{2}{\text{DR}_E} \exp\left(\frac{t_B}{T_L}\right) \quad (1)$$

Here, the electric-field dynamic range  $\text{DR}_E$  is defined as the ratio of the spectral amplitude of the electric field to the detection noise for a given instrument setting (total measurement time, etc.);  $T_L$  denotes the dephasing time of the considered absorption line. For a Lorentzian-shaped absorption with a spectral width  $\nu$ , the decay time is  $T_L = (\pi c \nu)^{-1}$ , with  $c$  being the speed of light. The parameter  $t_B$  is defined as the instant when the temporal window for an infrared-background-free measurement begins.<sup>14</sup>

Now, let  $\alpha_M$  denote the absorption of water (or any other matrix substance) and  $\alpha_A$  the absorption of analyte molecules. By increasing the interaction length  $x$ , the MIR beam is mainly attenuated due to water absorption according to Beer's law. The electric field dynamic range for a certain optical frequency  $\nu$  scales as  $\text{DR}_E(\nu) = \text{DR}_E^0 \times \exp\left(-\frac{\alpha_M(\nu)x}{2}\right)$  with  $\text{DR}_E^0$  being the dynamic range for the measurement of the unattenuated radiation. Equation 1 now writes:

$$\alpha_A x = \frac{2}{\text{DR}_E^0 e^{(-\alpha_M x)/2}} \exp\left(\frac{t_B}{T_L}\right) \quad (2)$$

The minimum for  $\alpha_A$  is reached for (see the Supporting Information):

$$x = x_{\text{opt}}^F = \frac{2}{\alpha_M} \quad (3)$$

According to eq 3, the optimum interaction length is independent of the system's dynamic range and source intensity noise. Therefore, for any FRS system, the choice of an optimum liquid cuvette will depend not on the particular specifications of the system but on only the absorption coefficient  $\alpha_M$  of the matrix substance at the desired wavelength.

For broadband spectroscopy, the choice of interaction length becomes more complicated as  $\alpha_M$  might vary within the spectral range of interest. This is for instance the case for aqueous samples, for which MIR spectroscopy is most informative between 1000 and 3000  $\text{cm}^{-1}$ . Due to the strong water absorption band at 1640  $\text{cm}^{-1}$  (HOH bending vibration), the optimum interaction length for FRS is 7.4  $\mu\text{m}$ , while at 2630  $\text{cm}^{-1}$ , it is 178  $\mu\text{m}$  (Figure 2). In order to maintain good measurement performance over the entire spectral range, we suggest choosing a path length of  $\sim 25 \mu\text{m}$ . This keeps the expected LOD within 33% of the optimum value at all wavenumbers (see the Supporting Information).

It is noteworthy that similar scaling laws apply to any spectroscopic method whose SNR scales linearly with the field strength. For example, Withayachumnankul et al.<sup>22</sup> obtained a similar expression for the optimum path length in THz time-domain spectroscopy.<sup>23</sup> However, their derivation assumes that multiplicative noise (i.e., relative intensity noise) from the source is negligible, without discussing under what circumstances this condition is met.

Similar considerations can be applied to asymmetric FTIR spectrometers where the sample is placed in one arm of the interferometer.<sup>20</sup> However, due to limited dynamic range and

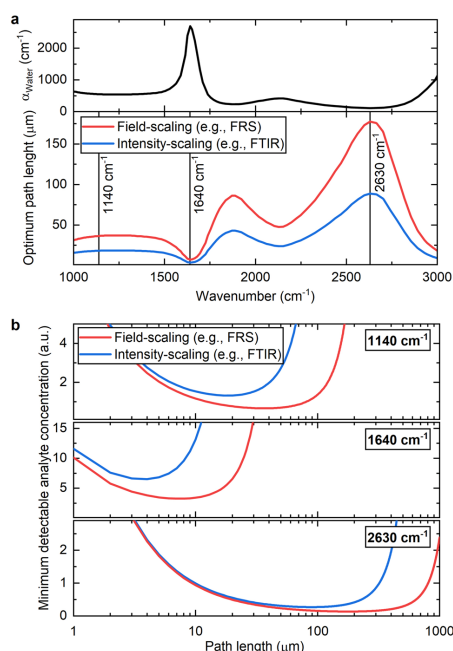


**Figure 2.** (a) Optimum sample thickness for measurements in aqueous media in dependence of the wavenumber for field-scaling (blue) and intensity-scaling (red) techniques. The absorption coefficient of water (top panel) determines the path length for optimum sensitivity. (b) Theoretical limit of detection (LOD) of a given analyte dissolved in water in dependence of the thickness of the measurement cuvette at the different wavenumbers.

poor noise performance of the available MIR detectors as well as due to source intensity noise, the favorable scaling behavior with intensity attenuation may either not be reached at all or only within a smaller range.

The discussed scaling laws and optimum interaction lengths are in sharp contrast to spectroscopic methods whose SNR is linearly proportional to the light intensity, as is the case for conventional (i.e., symmetric) FTIR spectrometers.<sup>2</sup> For the comparison of the two scaling regimes, in the following, we consider field- and intensity-scaling devices (e.g., a symmetric and an asymmetric FTIR) with the same performance in terms of minimum detectable absorption difference for non-attenuated beams.

For weak attenuation (i.e., short path length and/or weakly absorbing matrix), the LOD is comparable (Figures 1 and 2b). For strong attenuation by the matrix (i.e., long path length and/or strongly absorbing matrix), field-scaling is clearly advantageous. This becomes particularly important for samples with nonuniform thickness (e.g., biological tissue or living cells) or varying total absorption and/or water content. In addition, the field-scaling device inherently reaches a twice as low LOD at an optimum path length that is twice the one of the intensity-scaling devices (Figure 2a and the Supporting Information).

In principle, SNR-scaling with field strength can also be obtained with direct absorption spectroscopy (DAS) in the MIR range. However, in practice, for DAS, this is only applicable when MIR shot-noise-limited performance can be reached over the entire measurement dynamic range. This is technologically very challenging due to typically orders of magnitude stronger source intensity noise. Additionally, shot-noise-limited performance can only be achieved for high MIR powers, as the noise-equivalent shot-noise power has to overcome the noise of the MIR photodetectors. When Brandstetter et al.<sup>5</sup> investigated the path length with maximum measurement SNR for a QCL-based DAS setup, they found it to be 140  $\mu\text{m}$ , determined by the intensity noise of the source. In general, when a spectroscopic system is intensity-noise limited, the full potential of the light source (set by photon shot noise) cannot be exploited and the SNR-maximized path length in experiment will be longer than the optimum value in a detection-limited setting (see the Supporting Information).

### EXPERIMENTAL SETUP

In the remainder of the paper, we verify these theoretical considerations experimentally, employing the mid-infrared field-resolving spectrometer described in detail in our previous work<sup>14</sup> (see Figure 3). In short, a Kerr-lens mode-locked

IPDFG stage, the NIR pulses are separated from the MIR beam *via* a custom-designed dichroic mirror, recompressed to 16 fs, and optically delayed with respect to the MIR transients *via* a mechanical stage. After passing through a chopper wheel modulating the signal at 10 kHz for lock-in detection, the MIR radiation traverses a liquid cuvette for transmission measurements. Custom multilayer optics were used to compensate for the dispersion of the MIR pulse upon propagation through the ZnSe windows of the liquid cuvette and temporally compressed the MIR pulse to 59 fs (intensity envelope full width at half-maximum).<sup>26</sup>

The MIR and NIR beams are temporally and spatially recombined at a germanium plate and sent to an electro-optic sampling detection system<sup>14,27,28</sup> that allows for recording the MIR waveform. To increase measurement stability, the entire MIR beam path was put under vacuum conditions and an active intensity noise stabilization<sup>29</sup> as well as interferometric delay tracking<sup>30</sup> of the interferometer were implemented.

### RESULTS

The power spectrum (Figure 3b) was obtained *via* Fourier transforming the recorded time trace (Figure 4a). After passing through liquid cuvettes with path lengths of 7, 34, and 50  $\mu\text{m}$ , we obtained peak intensity dynamic range values of  $5 \times 10^{10}$ ,  $2 \times 10^{10}$ , and  $0.5 \times 10^{10}$  for a total measurement time of 20 s with a spectral resolution of 10  $\text{cm}^{-1}$ , respectively. The wide intensity dynamic range renders the instrument advantageous for measurements of strongly absorbing (aqueous) samples. This is also illustrated in Figure 3b, showing the calculated power spectral density of the spectrum after transmission through 100, 200, and 300  $\mu\text{m}$  of water.

In addition to the instrument's ability to detect electric fields with high sensitivity, the time-domain nature of FRS renders the detection of molecular emission robust against fluctuations of the excitation. This advantage is described in detail in our previous work<sup>14</sup> and will be illustrated here for the example of dimethyl sulfone ( $\text{DMSO}_2$ ), a test molecule used for the measurements presented in this work. The spectral absorption and phase information on  $\text{DMSO}_2$  can be obtained from the corresponding reference and sample measurements (Figure 4a,b). However, this procedure becomes unstable for small absorptions due to signal fluctuations in the range of the excitation, affecting the (complex) Fourier-transformed spectra.

Measuring the time-domain response to an ultrashort MIR excitation pulse allows for the temporal separation of the sample response of the molecules under investigation and the—orders of magnitude stronger—excitation energy remaining after transmission through the sample. Consequently, the noise power carried by the excitation can be temporally separated from the molecular signal. For substances in aqueous environments, the resonant molecular response usually spans over a few picoseconds. In the case of  $\text{DMSO}_2$ , the dephasing time of the absorption line at 1139  $\text{cm}^{-1}$  is  $\sim 0.8$  ps, which is significantly longer than the full-width at half-maximum of 59 fs of the excitation pulse (Figure 4a). Already 500 fs after the pulse, the signal from the reference pulse drops to  $\sim 0.5\%$  of the peak value. Within this strongly reduced background, a significantly weaker signal of the excited molecules can be detected, as the detrimental influence of the excitation fluctuations is strongly reduced.

This becomes apparent when extracting the resonant molecular response by subtracting a reference from a sample

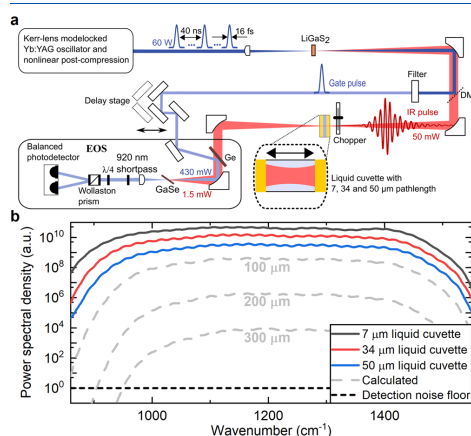


**Figure 3.** (a) Layout of the field-resolved spectrometer. For this experiment, measurement cuvettes with 7, 34, and 50  $\mu\text{m}$  path lengths were used. (b) Intensity dynamic range of the FRS spectrometer after passing through water layers of 7, 34, and 50  $\mu\text{m}$  thicknesses, measured over 20 s, with a spectral resolution of 10  $\text{cm}^{-1}$ . The gray dashed lines show the expected dynamic range after transmission through 100, 200, and 300  $\mu\text{m}$  of water, respectively.

Yb:YAG thin-disc oscillator emits a 28 MHz repetition-rate train of 220 fs pulses spectrally centered at 1030 nm, with an average power of 100 W. The near-infrared (NIR) pulses are spectrally broadened in three nonlinear multipass bulk-transmission stages<sup>24</sup> and temporally compressed to 16 fs.<sup>25</sup> Few-cycle mid-infrared pulses, spectrally covering the 910–1530  $\text{cm}^{-1}$  range at  $-20$  dB spectral intensity with an average power of 50 mW, are obtained *via* intrapulse difference frequency generation (IPDFG) in a LiGaS<sub>2</sub> crystal. After the

D

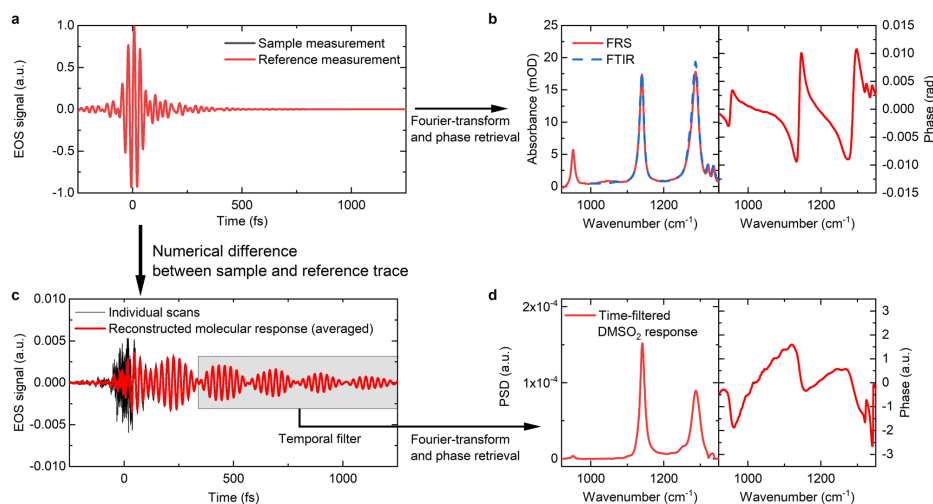


**Figure 4.** FRS measurement of a solution of DMSO<sub>2</sub> in water. (a) EOS traces of a reference and a test sample (liquid cuvette filled with pure water and one with a 1 mg/mL solution of DMSO<sub>2</sub> in water, respectively). The difference between the two traces is miniscule (cannot be discerned by eye). (b) Amplitude and phase spectra obtained *via* Fourier transform (FT) of the traces in (a), permitting the calculation of conventional absorption and phase spectra of the analyte DMSO<sub>2</sub> in its aqueous environment. For comparison, an absorption spectrum of the same solution, measured with a commercial FTIR spectrometer device, is shown. (c) Time-domain molecular response of DMSO<sub>2</sub> was obtained *via* numerical subtraction of the sample from the reference trace, as shown in (a). Due to fluctuations in the excitation remaining after transmission through the sample (induced by intensity and phase noise of the source, by interferometer fluctuations etc.), the reconstruction of the molecular response is noisy in time windows with large EOS signal—in particular during the excitation pulse centered around 0 fs. After several hundred femtoseconds, this detrimental influence of source noise on the subtraction result becomes negligible because of the rapid decay of the excitation pulse. This opens up the window for background-free measurements of the molecular signal. (d) Similar to the conventional spectra shown in (b), one can obtain analyte-specific amplitude and phase spectra of the time-filtered sample response *via* FT of the truncated time-domain difference trace.

measurement (Figure 4c). During the excitation, source intensity fluctuations hinder the clean subtraction, i.e., referencing, of two strong signals, leading to noise in the signal of interest in this time window. After a few hundred femtoseconds, the excitation pulse has decayed either below the detection noise floor or it has become weak enough to be subtracted (or referenced out). Note that a signal of the excited matrix molecules might be spanning over several picoseconds and therefore potentially masking the molecular signal of the analyte. However, vibrations of liquid water dephase within tens of femtoseconds and therefore do not affect the detection of the resonant analyte response in the wake of the excitation. In practice, this means that after a certain time  $t_B$ , the detection of the molecular signal is only limited by the detection noise and not by any technical noise of the driving laser or of the interferometer.<sup>14</sup>

In our case, the window for background-free access to resonant analyte response opens up approximately 500 fs after the peak of the excitation pulse. Fourier-transforming the time-filtered molecular signal delivers a sample-specific “resonant fingerprint”, i.e., a power and a phase spectrum (Figure 4d). Even though its appearance differs from that of conventional spectra, the main spectral features are contained and can be used for quantitative identification of the analyte.

In order to validate eq 2, we evaluated the LOD for DMSO<sub>2</sub> dissolved in water in a dilution series, using liquid cuvettes with thicknesses of 7 (commonly used in FTIR spectrometers), 34, and 50  $\mu\text{m}$ . To retrieve the concentration of DMSO<sub>2</sub> for each

sample, a calibration measurement at a concentration of 1 mg/mL was performed for each thickness and used for 1-parameter fits yielding the concentrations of the individual samples.<sup>14</sup>

For a spectral resolution of 4 cm<sup>-1</sup> (corresponding to an 8.3 ps time window) and a total effective measurement time of 90 s per injected sample (45 s each for reference and sample measurement), we experimentally obtained LOD values of 1.6, 0.6, and 0.7  $\mu\text{g}/\text{mL}$  for increasing cuvette thickness, respectively (Figure 5). The theoretical LOD curve was calculated using the absorption coefficient of DMSO<sub>2</sub> of 12.92 cm<sup>-1</sup> for 1 mg/mL at 1139 cm<sup>-1</sup>, a decay time  $T_1$  of 770 fs, the absorption coefficient of water of 537 cm<sup>-1</sup>,<sup>31</sup> and a field

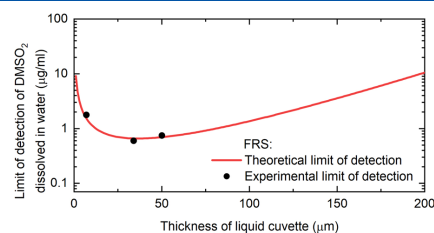


**Figure 5.** Theoretical vs experimental limits of detection (LOD) for DMSO<sub>2</sub> dissolved in water in dependence of the thickness of the measurement cuvette.



dynamic range  $DR_E^0$  of the non-attenuated beam of  $3.0 \times 10^5$ . This theoretical curve is in very good agreement with the experimentally obtained values for the LOD.

### CONCLUSION AND OUTLOOK

We have demonstrated that broadband field-resolved MIR spectroscopy can offer an intensity dynamic range in excess of  $10^{10}$  over more than  $460 \text{ cm}^{-1}$  (without measurement cuvette) for a measurement time of less than 1 min, rendering it applicable for the investigation of strongly absorbing (aqueous) samples. The ability of FRS to measure the temporally retarded sample response separated from the nonresonant response (i.e., excitation remaining after transmission through the sample) grants access to the—orders of magnitude smaller—molecular signal in a background-reduced manner, rendering the measurement SNR virtually independent from excitation fluctuations. This enables detection sensitivities in the sub-microgram/milliliter range for molecules solved in water. Furthermore, the signal strength and SNR scale linearly with the electric field of the excitation source. Based on these properties, we theoretically derived and experimentally confirmed that in FRS the optimum interaction length with a sample,  $x_{\text{opt}} = 2/\alpha_M$ , only depends on the absorption coefficient  $\alpha_M$  of the matrix substance.

For many biological samples, the matrix substance is water, therefore, we further analyzed this case and evaluated the measurement performance in dependence of wavelength and thickness. We found that sub-microgram/milliliter detection sensitivities can be maintained for samples as thick as  $80 \mu\text{m}$  and that, even for  $0.2 \text{ mm}$  thick samples, LOD values in the range of  $10 \mu\text{g/mL}$  are feasible, which is the level achieved by state-of-the-art research-grade FTIR instruments,<sup>14</sup> albeit under the stringent condition of sub- $10 \mu\text{m}$  sample thickness. In the fingerprint region from  $1000$  to  $3000 \text{ cm}^{-1}$ , the measurement performance can be kept within 33% of the peak performance at all wavenumbers by choosing a sample thickness around  $25 \mu\text{m}$ . Rapid advances of femtosecond technology hold promise for the extension of FRS to the coverage of the entire molecular fingerprint region in the near future.<sup>32,33</sup> At the same time, further improvement of the sensitivity of electro-optic sampling will push the limit of detection to the low nanogram/milliliter range or below.<sup>34</sup>

Compared to conventional (i.e., symmetric) FTIR spectrometers, the scaling laws of FRS for the sensitivity in dependence of the sample thickness and total absorption are highly advantageous. The relaxed requirements to the sample thickness enable a more flexible design of liquid cuvettes and microfluidic chips for MIR spectroscopic applications. In addition, the increased SNR for the measurement of thick aqueous samples will be beneficial for MIR transmission spectroscopy and spectroscopy–microscopy of biological samples, such as living cells, bulk cells, and tissue cultures as well as biological tissues, in their natural (hydrated) state.

### ASSOCIATED CONTENT

#### Supporting Information

The Supporting Information is available free of charge at <https://pubs.acs.org/doi/10.1021/acs.analchem.9b05744>.

Discussions of scaling laws for the limit of detection in aqueous media for intensity- and field-scaling spectroscopic methods and relative-intensity noise dominated measurements (PDF)

### AUTHOR INFORMATION

#### Corresponding Authors

**Marinus Huber** – Max Planck Institute of Quantum Optics, Garching 85748, Germany; Ludwig Maximilians University München, Garching 85748, Germany; [orcid.org/0000-0001-5309-4475](https://orcid.org/0000-0001-5309-4475); Email: [marinus.huber@mpq.mpg.de](mailto:marinus.huber@mpq.mpg.de)

**Ioachim Pupeza** – Max Planck Institute of Quantum Optics, Garching 85748, Germany; Ludwig Maximilians University München, Garching 85748, Germany; [orcid.org/0000-0001-8422-667X](https://orcid.org/0000-0001-8422-667X); Email: [ioachim.pupeza@mpq.mpg.de](mailto:ioachim.pupeza@mpq.mpg.de)

#### Authors

**Michael Trubetskov** – Max Planck Institute of Quantum Optics, Garching 85748, Germany

**Syed A. Hussain** – Max Planck Institute of Quantum Optics, Garching 85748, Germany; Ludwig Maximilians University München, Garching 85748, Germany

**Wolfgang Schweinberger** – Max Planck Institute of Quantum Optics, Garching 85748, Germany; Department of Physics and Astronomy, King Saud University, Riyadh 11451, Saudi Arabia

**Christina Hofer** – Max Planck Institute of Quantum Optics, Garching 85748, Germany; Ludwig Maximilians University München, Garching 85748, Germany

Complete contact information is available at:

<https://pubs.acs.org/10.1021/acs.analchem.9b05744>

#### Notes

The authors declare no competing financial interest.

### REFERENCES

- (1) Diem, M.; Griffiths, P. R.; Chalmers, J. M. *Vibrational Spectroscopy for Medical Diagnosis*; Wiley: Chichester, 2008; Vol. 40.
- (2) Griffiths, P. R.; De Haseth, J. A. *Fourier Transform Infrared Spectrometry*; John Wiley & Sons, 2007; Vol. 171.
- (3) Yang, H.; Yang, S.; Kong, J.; Dong, A.; Yu, S. *Nat. Protoc.* **2015**, *10* (3), 382–396.
- (4) Martin, F. L.; Kelly, J. G.; Llabiani, V.; Martin-Hirsch, P. L.; Patel, I. J.; Trevisan, J.; Fullwood, N. J.; Walsh, M. J. *Nat. Protoc.* **2010**, *5* (11), 1748–1760.
- (5) Brandstetter, M.; Volgger, L.; Genner, A.; Jungbauer, C.; Lendl, B. *Appl. Phys. B: Lasers Opt.* **2013**, *110* (2), 233–239.
- (6) Movasaghi, Z.; Rehman, S.; Ur Rehman, D. I. *Appl. Spectrosc. Rev.* **2008**, *43* (2), 134–179.
- (7) Ollesch, J.; Theegarten, D.; Altmayer, M.; Darwiche, K.; Hager, T.; Stamatis, G.; Gerwert, K. *Biomed. Spectrosc. Imaging* **2016**, *5* (2), 129–144.
- (8) Hands, J. R.; Clemens, G.; Stables, R.; Ashton, K.; Brodbelt, A.; Davis, C.; Dawson, T. P.; Jenkinson, M. D.; Lea, R. W.; Walker, C.; Baker, M. J. *J. Neuro-Oncol.* **2016**, *127* (3), 463–472.
- (9) Rogalski, A. *Infrared Detectors*; CRC press, 2010.
- (10) Vaccari, L.; Birarda, G.; Businaro, L.; Pacor, S.; Greci, G. *Anal. Chem.* **2012**, *84* (11), 4768–4775.
- (11) Kazarian, S. G.; Chan, K. L. A. *Analyst* **2013**, *138* (7), 1940.
- (12) Cameron, J. M.; Butler, H. J.; Palmer, D. S.; Baker, M. J. *J. Biophotonics* **2018**, *11* (4), No. e201700299.
- (13) Schwaighofer, A.; Montemurro, M.; Freitag, S.; Kristament, C.; Culzoni, M. J.; Lendl, B. *Anal. Chem.* **2018**, *90* (11), 7072–7079.
- (14) Pupeza, I.; Huber, M.; Trubetskov, M.; Schweinberger, W.; Hussain, S. A.; Hofer, C.; Fritsch, K.; Poetzlberger, M.; Vamos, L.; Fill, E.; Amotchkina, T.; Kepesidis, K. V.; Apolonski, A.; Karpowicz, N.; Pervak, V.; Pronin, O.; Fleischmann, F.; Azzeer, A.; Zigman, M.; Krausz, F. *Nature* **2020**, *577* (7788), 52–59.
- (15) Snyder, J. J. *Appl. Opt.* **1988**, *27* (21), 4465.
- (16) Jarry, G.; Poupinet, L.; Watson, J.; Lepine, T. *Appl. Opt.* **1995**, *34* (12), 2045.



- (17) Liukaityte, S.; Lequime, M.; Zerrad, M.; Begou, T.; Amra, C. *Opt. Lett.* **2015**, *40* (14), 3225.
- (18) Jensen, P. S.; Bak, J. *Appl. Spectrosc.* **2002**, *56* (12), 1600–1606.
- (19) Mark, H. L.; Griffiths, P. R. *Appl. Spectrosc.* **2002**, *56* (5), 633–639.
- (20) Newbury, N. R.; Coddington, I.; Swann, W. *Opt. Express* **2010**, *18* (8), 7929.
- (21) Butler, T. P.; Gerz, D.; Hofer, C.; Xu, J.; Gaida, C.; Heuermann, T.; Gebhardt, M.; Vamos, L.; Schweinberger, W.; Gessner, J. A.; Siefke, T.; Heusinger, M.; Zeitner, U.; Apolonski, A.; Karpowicz, N.; Limpert, J.; Krausz, F.; Pupeza, I. *Opt. Lett.* **2019**, *44* (7), 1730.
- (22) Withayachumnankul, W.; Fischer, B. M.; Abbott, D. *Opt. Express* **2008**, *16* (10), 7382.
- (23) Jepsen, P. U.; Cooke, D. G.; Koch, M. *Laser Photon. Rev.* **2011**, *5* (1), 124–166.
- (24) Schulte, J.; Sartorius, T.; Weitenberg, J.; Vernaleken, A.; Russbuehler, P. *Opt. Lett.* **2016**, *41* (19), 4511.
- (25) Fritsch, K.; Poetzlberger, M.; Pervak, V.; Brons, J.; Pronin, O. *Opt. Lett.* **2018**, *43* (19), 4643.
- (26) Amotchkina, T.; Trubetskov, M.; Hussain, S. A.; Hahner, D.; Gerz, D.; Huber, M.; Schweinberger, W.; Pupeza, I.; Krausz, F.; Pervak, V. *Opt. Lett.* **2019**, *44* (21), 5210.
- (27) Gallot, G.; Grischkowsky, D. *J. Opt. Soc. Am. B* **1999**, *16* (8), 1204.
- (28) Wu, Q.; Zhang, X. *Appl. Phys. Lett.* **1995**, *67* (24), 3523–3525.
- (29) Huber, M.; Schweinberger, W.; Stutzki, F.; Limpert, J.; Pupeza, I.; Pronin, O. *Opt. Express* **2017**, *25* (19), 22499.
- (30) Schweinberger, W.; Vamos, L.; Xu, J.; Hussain, S. A.; Baune, C.; Rode, S.; Pupeza, I. *Opt. Express* **2019**, *27* (4), 4789.
- (31) Segelstein, D. J. *The Complex Refractive Index of Water*. University of Missouri: Kansas City, 1981.
- (32) Butler, T. P.; Lilienfein, N.; Xu, J.; Nagl, N.; Hofer, C.; Gerz, D.; Mak, K. F.; Gaida, C.; Heuermann, T.; Gebhardt, M.; Limpert, J.; Krausz, F.; Pupeza, I. *J. Phys. Photonics* **2019**, *1* (4), 044006.
- (33) Wang, Q.; Zhang, J.; Kessel, A.; Nagl, N.; Pervak, V.; Pronin, O.; Mak, K. F. *Opt. Lett.* **2019**, *44* (10), 2566.
- (34) Hofer, C.; Hussain, S. A.; Schweinberger, W.; Huber, M.; Butler, T. P.; Gerz, D.; Karpowicz, N.; Krausz, F.; Pupeza, I. Quantum-Efficiency and Bandwidth Optimized Electro-Optic Sampling. *2019 Conference on Lasers and Electro-Optics Europe & European Quantum Electronics Conference (CLEO/Europe-EQEC)*; IEEE, 2019; p 1.

Supporting Information for:

## Optimum Sample Thickness for Trace Analyte Detection with Field-Resolved Infrared Spectroscopy

Marinus Huber,<sup>\*,†,‡</sup> Michael Trubetskov,<sup>†</sup> Syed A. Hussain,<sup>†,‡</sup> Wolfgang Schweinberger,<sup>†,§</sup> Christina Hofer,<sup>†,‡</sup> and Ioachim Pupeza,<sup>\*,†,‡</sup>

<sup>†</sup>Max Planck Institute of Quantum Optics, Hans-Kopfermann-Straße 1, 85748, Garching, Germany

<sup>‡</sup>Ludwig Maximilians University München, Am Coulombwall 1, 85748, Garching, Germany

<sup>§</sup>Department of Physics and Astronomy, King Saud University, PO Box 2455, Riyadh 11451, Saudi Arabia

\*Email: [marinus.huber@mpq.mpg.de](mailto:marinus.huber@mpq.mpg.de).

\*Email: [ioachim.pupeza@mpq.mpg.de](mailto:ioachim.pupeza@mpq.mpg.de).

### Table of contents:

*S1 Signal-to-noise scaling and limit of detection in dependence of the path length*

*S1.1 Field-scaling (e.g., FRS)*

*S1.2 Intensity-scaling*

*S1.3 Direct comparison of field- and intensity-scaling*

*S1.4 Relative-intensity noise dominated measurements*

*References*

### S1 Signal-to-noise scaling and limit of detection in dependence of the path length

In the following, we derive scaling laws for the signal-to-noise-ratio (SNR) and the limit of detection (LOD) of an analyte in dependence of the interaction length for different classes of spectroscopic techniques. Thereby, we classify the latter according to their SNR-scaling with the excitation intensity  $I$ . For most methods, a distinction in one of the three following regimes is possible:<sup>1,2</sup>

- (1) **Square-root-scaling ( $SNR \sim \sqrt{I}$ ):** This applies for techniques whose signal scales with the electric field and for which the dominating noise source is intensity-independent, e.g., for field-resolved spectroscopy<sup>3</sup>. This scaling also applies to linear techniques that achieve photon-shot-noise-limited detection (shot noise scales proportionally to  $\sqrt{I}$ ).<sup>4</sup> However, while shot-noise-limited spectroscopy has been demonstrated in the visible and near-infrared spectral ranges, it has not – to the best of our knowledge – been demonstrated in the mid-infrared range, mainly due to the lack of sensitive MIR detectors and low-noise high-brilliance infrared sources.
- (2) **Linear scaling ( $SNR \sim I$ ):** Applies for techniques whose signal scales with intensity and for which the dominating noise source is intensity-independent (e.g., detector noise). This usually is the case for commercial Fourier-transform-infrared (FTIR) spectrometers employing thermal sources.<sup>1</sup>
- (3) **Constant ( $SNR \sim const.$ ):** Applies when relative-intensity noise (RIN) is the dominating noise source. This is usually the case for high-power laser sources.

For the derivations of the scaling laws, we consider the case in which an analyte with absorption coefficient  $\alpha_A$  is embedded in a matrix substance with absorption coefficient  $\alpha_M$ . For many applications, this matrix substance is water and  $\alpha_A \ll \alpha_M$  can be assumed. The minimum detectable absorption  $(\alpha_A x)_{min}$  at a given frequency is inversely proportional to the SNR:<sup>2</sup>

$$(\alpha_A x)_{min} \sim \frac{1}{SNR} \quad (S.1)$$

The discussion is structured as follows. Section S1.1 and S1.2 contains all derivations for (1) field-scaling and (2) intensity-scaling, respectively. In section S1.3 we compare how those two regimes compare for a weakly and strongly absorbing matrix. In the last section, we discuss how relative intensity noise affects the optimum interaction length.

#### S1.1 Field-scaling (e.g., FRS)

For field-scaling spectroscopic techniques the measurement SNR scales proportionally to the electric field strength ( $SNR_F \sim E \sim \sqrt{I}$ ). According to eq. (S.1) the minimum absorption sensitivity  $(\alpha_A x)_{F,min}$  now reads:

$$(\alpha_A x)_{F,min} = \frac{c^*}{E}, \quad (S.2)$$

where  $c^*$  is an instrument and method dependent constant. Note that the field dynamic range  $DR_E$  in eq. (1) is proportional to  $E$  and all other terms on the r.h.s. of eq. (1) account for the constant  $c^*$  in time-gated FRS. For other instruments  $c^*$  might be different.

After passing through a distance  $x$  of the matrix substance the electric field strength is decreased according to Beer's law  $E = E_0 \times \exp\left(-\frac{\alpha_M x}{2}\right)$ . The subscript "0" denotes the non-attenuated beam. The LOD can now be written as:

$$\alpha_A = \frac{c^*}{xE_0 e^{-\frac{\alpha_M x}{2}}} \quad (S.3)$$

The minimum of  $\alpha_A$  is reached when the function

$$g(x) = \frac{e^{-\frac{\alpha_M x}{2}}}{x} \quad (S.4)$$

reaches a minimum. To find this value we compute the first derivative and set it to 0:

$$e^{-\frac{\alpha_M x}{2}} \left( -\frac{1}{x^2} + \frac{1}{x} \cdot \frac{\alpha_M}{2} \right) = 0 \quad (S.5)$$

The optimum sample thickness  $x_{opt,F}$  is reached for:

$$x_{opt,F} = 2/\alpha_M \quad (S.6)$$

Note that the absence of any instrument-specific noise terms (e.g. detector noise) in this expression reflects the scaling of the SNR with the field. Next, we investigate by which factor  $f$  the LOD changes for the case when  $x \neq x_{opt,F}$ :

$$f(x) = \frac{\alpha_A(x)}{\alpha_A(x_{opt,F})} = \frac{x}{x_{opt,F}} \exp\left(1 - \frac{x}{x_{opt,F}}\right) \quad (S.7)$$

Using this expression, we can calculate the lower and upper limit for the thickness  $x$  for which the LOD increases by a maximum factor  $f$  :

$$x_{f,\pm} = -x_{opt,F} W_{\frac{0}{-1}}\left(-\frac{f}{e}\right), \quad (S.8)$$

where  $W_{\frac{0}{-1}}$  denotes the Lambert W function.

For broadband measurements, one faces the problem that an optimum interaction length  $x_{opt,F}$  cannot be chosen for all wavelengths simultaneously, as  $\alpha_M$  also changes over the spectrum. To maintain best measurement performance over the entire spectral range, we apply the condition that the deviation from the optimum LOD for the smallest and highest absorption coefficient of water is the same:

$$f_{\alpha_{M,min}} = f_{\alpha_{M,max}} \quad (S.9)$$

This yields the optimum interaction length  $x_{B,F}$  for broadband measurements:

$$x_{B,F} = 2 \frac{\ln\left(\frac{\alpha_{M,max}}{\alpha_{M,min}}\right)}{\alpha_{M,max} - \alpha_{M,min}} \quad (S.10)$$

In the case of water, the minimum and maximum absorption coefficient is  $1640 \text{ cm}^{-1}$  and  $2630 \text{ cm}^{-1}$  within the fingerprint region ( $1000 \text{ cm}^{-1}$  and  $3000 \text{ cm}^{-1}$ ). Correspondingly, a good compromise for the interaction length is to choose a thickness of  $24.5 \text{ }\mu\text{m}$ . This results in a maximum increase of the LOD by a factor of 3 within the entire range.

### S1.2 Intensity-scaling

For intensity-scaling spectroscopic techniques the measurement SNR scales proportionally to the light intensity ( $SNR_I \sim I$ ). According to eq. (S.1) the minimum absorption sensitivity  $(\alpha_A x)_{\min,I}$  now reads:

$$(\alpha_A x)_{\min,I} = \frac{c^{**}}{I}, \quad (S.11)$$

where  $c^{**}$  is an instrument and method dependent constant. For conventional FTIR spectrometers equipped with a black-body source,  $c^{**}$  typically depends on the employed detector properties, optical etendue, optical efficiency, spectral resolution and acquisition time.<sup>1</sup> According to Beer's law,  $I = I_0 \times \exp(-\alpha_M x)$  is the intensity after passing through a thickness of  $x$  of the matrix substance. Inserting this scaling into eq. (S.11) yields

$$\alpha_A = \frac{c^{**}}{x I_0 e^{-\alpha_M x}} \quad (S.12)$$

and reaches its minimum for

$$x_{opt,I} = 1/\alpha_M \quad (S.13)$$

In analogy to the derivations in section S1.1, we can derive formulas for the optimum interaction length  $x_{B,I}$  for broadband measurements as well as for the upper and lower thickness limit  $x_{f,\pm}$  in order to reach an LOD below a given value, that is increased by a factor  $f$  with respect to the optimum value:

$$f = \frac{x}{x_{opt,I}} \exp\left(1 - \frac{x}{x_{opt,I}}\right) \quad (S.14)$$

$$x_{f,\pm} = -x_{opt,I} W_{\frac{0}{-1}}\left(-\frac{f}{e}\right) \quad (S.15)$$

$$x_{B,I} = \frac{\ln\left(\frac{\alpha_{M,max}}{\alpha_{M,min}}\right)}{\alpha_{M,max} - \alpha_{M,min}} \quad (S.16)$$

### S1.3 Direct comparison of field- and intensity-scaling

The main difference in the experimental setup between a symmetric (intensity-scaling) and asymmetric (field-scaling) FTIR is, that in the former the sample is placed outside the interferometer and for the latter in one of the interferometer arms. Therefore, in many cases, an asymmetric FTIR can easily be converted into a symmetric one and vice-versa. Often, the symmetric layout is preferred, as it is considered to be more user-friendly.<sup>5</sup> In addition, they have basically the same performance in terms of minimum detectable absorption difference for un-attenuated beams or very weak absorption (Fig. 1). Therefore, for the investigation of weakly absorbing substances, such as gases, the symmetric and asymmetric FTIR perform similarly. This changes dramatically when the analyte is contained within a strongly absorbing matrix such as liquid water. For this case, field-scaling is clearly advantageous (Fig. 1).

Furthermore, a better LOD can be achieved with field-scaling devices. For the derivation, we assume a field- and an intensity-scaling spectrometer, respectively, with the same performance in terms of minimum detectable absorption difference for un-attenuated beams:

$$(\alpha_A x)_{F,min} = (\alpha_A x)_{I,min} \quad (S.17)$$

$$\frac{c^*}{E_0} = \frac{c^{**}}{I_0} \quad (S.18)$$

Next, we compare the smallest detectable molecular absorption coefficient  $\alpha_{A,F}$  and  $\alpha_{A,I}$  for optimum interaction length in both cases.

$$\begin{aligned} \alpha_{A,F}(x_{opt,F}) &= \frac{c^*}{x_{opt,F} E_0 e^{-\frac{\alpha_M x_{opt,F}}{2}}} \\ \alpha_{A,F}(x_{opt,F}) &= \frac{1}{x_{opt,F} e^{-1}} \frac{c^*}{E_0} \\ \alpha_{A,F}(x_{opt,F}) &= \frac{1}{x_{opt,F} e^{-1}} \frac{c^{**}}{I_0} \\ \alpha_{A,F}(x_{opt,F}) &= \frac{1}{2} \frac{c^*}{x_{opt,I} I_0 e^{-\alpha_M x_{opt,I}}} = \frac{1}{2} \alpha_{A,I}(x_{opt,I}) \end{aligned} \quad (S.19)$$

Thus, the LOD of field-scaling techniques is two times smaller than for intensity-scaling.

### S1.4 Relative-intensity noise dominated measurements

Here, we consider a measurement situation in which a linear system is dominated by RIN at high powers/intensities and becomes detector-noise limited when the beam gets attenuated. In this case, the SNR can be expressed as:<sup>2</sup>

$$SNR \sim \frac{I}{\sqrt{(RIN \times I)^2 + n_D^2}} \quad (S.20)$$

where  $n_D$  denotes the detector noise and  $RIN \times I$  describes the fluctuations caused by intensity noise. In analogy to the derivation in Section S1.1, the LOD reads:

$$\alpha_A = \frac{c^{***}}{x} \left( \frac{I_0 e^{-\alpha_M x}}{\sqrt{(RIN \times I_0 e^{-\alpha_M x})^2 + n_D^2}} \right)^{-1} \quad (S.21)$$

This expression reaches its minimum for:

$$x_{opt,RIN} = \frac{W\left(\frac{2}{e^2} \left(\frac{I_0}{n_D} RIN\right)^2\right) + 2}{2\alpha_M}, \quad (S.22)$$

with  $W$  denoting the Lambert W function.

Finally, we consider the following (numerical) example. We have a system with a RIN of  $10^{-4}$  and a (relative) detector noise level of  $n_D = 10^{-6}I_0$  (both for a given measurement time, spectral resolution etc.). This yields a RIN-optimized path length that is approximately 4 times larger as compared to the (preferable) detection-noise limited case. At the same time, only 10 times larger LOD can be reached.

#### References

- (1) Griffiths, P. R.; De Haseth, J. A. *Fourier Transform Infrared Spectrometry*; John Wiley & Sons, 2007; Vol. 171.
- (2) Newbury, N. R.; Coddington, I.; Swann, W. Sensitivity of Coherent Dual-Comb Spectroscopy. *Opt. Express* **2010**, *18* (8), 7929. <https://doi.org/10.1364/OE.18.007929>.
- (3) Pupeza, I.; Huber, M.; Trubetskov, M.; Schweinberger, W.; Hussain, S. A.; Hofer, C.; Fritsch, K.; Poetzlberger, M.; Vamos, L.; Fill, E.; Amotchkina, T.; Kepesidis, K. V.; Apolonski, A.; Karpowicz, N.; Pervak, V.; Pronin, O.; Fleischmann, F.; Azzeer, A.; Žigman, M.; Krausz, F. Field-Resolved Infrared Spectroscopy of Biological Systems. *Nature* **2020**, *577* (7788), 52–59. <https://doi.org/10.1038/s41586-019-1850-7>.
- (4) Kwee, P.; Willke, B.; Danzmann, K. New Concepts and Results in Laser Power Stabilization. *Appl. Phys. B* **2011**, *102* (3), 515–522. <https://doi.org/10.1007/s00340-011-4399-1>.
- (5) Birch, J. R. Dispersive Fourier Transform Spectroscopy. *Mikrochim. Acta* **1987**, *93* (1–6), 105–122. <https://doi.org/10.1007/BF01201686>.

# Infrared Fingerprinting for Blood Profiling

## 3.1 Stability of person-specific blood-based infrared molecular fingerprints

**Preface:** A prerequisite for any medical diagnosis is a well-defined state of health and disease. In many cases a medical diagnosis relies on one or multiple parameters (markers) that are not binary but can take on any value (e.g. fasting glucose concentration). For such cases it is common practice to study the variation of these markers in both a control and disease population and define normal and abnormal ranges that correspond to the healthy or abnormal state, respectively [106, 107]. Thereby, the distribution of these markers arises from the natural biological variability between individuals.

The recording of an infrared molecular fingerprint of blood serum represents a simultaneous assessment of a multitude of blood-based markers. Although it has been demonstrated in many proof-of-principle studies that infrared fingerprints contain disease related information, which can successfully be used for diagnostics, no systematic investigation of the biological variation of infrared fingerprints had been conducted when we started our own endeavour to apply electric-field-resolved fingerprinting to disease detection. Therefore, we set up a study to investigate biological variability of infrared molecular fingerprints between healthy subjects and within individuals over time. In the same study we also investigated and quantified analytical and sample handling errors. The idea was that both aspects, the knowledge about biological variability and analytical errors arising from sample handling and blood drawing, will help to define normal and abnormal ranges for infrared spectral signatures for any future disease detection application. When we performed the study, the field-resolved spectrometer was not available for high-throughput measurements yet. Therefore, the results were only obtained with Fourier-transform infrared spectroscopy. Nevertheless, the results of this study represent a valuable foundation for electric-field-resolved fingerprinting of human biofluids, as biological variabilities should be independent of the measurement technique.

A surprising result for us was the fact that the obtained molecular infrared fingerprints of individuals proved to be very stable over clinically relevant time scales and could be used to efficiently track a person over time. This previously unknown temporal stability motivated us to apply blood-based spectral infrared fingerprinting measurements for health and disease monitoring in longitudinal settings. Although these results are not part of the work presented in this thesis, they triggered new clinical studies that are currently underway to further investigate the applicability of infrared fingerprinting to blood-based fingerprinting for monitoring of human health.

## **Stability of person-specific blood-based infrared molecular fingerprints opens up prospects for health monitoring**

*as published in*

**Nature Communications (2021)**

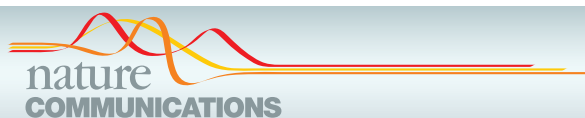
[98]

*by*

Marinus Huber, Kosmas Kepesidis, Liudmila Voronina, Masa Božić, Michael Trubetskov, Nadia Harbeck, Ferenc Krausz, and Mihaela Žigman

**Contributions:** I took part in designing and conducting the study as well as in performing the subsequent experiments. I took all measurements included in this paper and wrote the majority of the manuscript.





## ARTICLE

<https://doi.org/10.1038/s41467-021-21668-5>

OPEN

# Stability of person-specific blood-based infrared molecular fingerprints opens up prospects for health monitoring

Marinus Huber <sup>1,2</sup>✉, Kosmas V. Kepesidis<sup>1</sup>, Liudmila Voronina <sup>1,2</sup>, Maša Božić<sup>1</sup>, Michael Trubetskov <sup>2</sup>, Nadia Harbeck<sup>3</sup>, Ferenc Krausz<sup>1,2,4</sup> & Mihaela Žigman <sup>1,2,4</sup>✉

Health state transitions are reflected in characteristic changes in the molecular composition of biofluids. Detecting these changes in parallel, across a broad spectrum of molecular species, could contribute to the detection of abnormal physiologies. Fingerprinting of biofluids by infrared vibrational spectroscopy offers that capacity. Whether its potential for health monitoring can indeed be exploited critically depends on how stable infrared molecular fingerprints (IMFs) of individuals prove to be over time. Here we report a proof-of-concept study that addresses this question. Using Fourier-transform infrared spectroscopy, we have fingerprinted blood serum and plasma samples from 31 healthy, non-symptomatic individuals, who were sampled up to 13 times over a period of 7 weeks and again after 6 months. The measurements were performed directly on liquid serum and plasma samples, yielding a time- and cost-effective workflow and a high degree of reproducibility. The resulting IMFs were found to be highly stable over clinically relevant time scales. Single measurements yielded a multiplicity of person-specific spectral markers, allowing individual molecular phenotypes to be detected and followed over time. This previously unknown temporal stability of individual biochemical fingerprints forms the basis for future applications of blood-based infrared spectral fingerprinting as a multiomics-based mode of health monitoring.

<sup>1</sup>Department of Physics, Ludwig Maximilian University of Munich, Garching, Germany. <sup>2</sup>Max Planck Institute of Quantum Optics, Garching, Germany. <sup>3</sup>Department of Obstetrics and Gynecology, Breast Center and Comprehensive Cancer Center (CCLMU), Hospital of the Ludwig Maximilian University (LMU), Munich, Germany. <sup>4</sup>Center for Molecular Fingerprinting (CMF), Budapest, Hungary. ✉email: [huber.marinus@physik.uni-muenchen.de](mailto:huber.marinus@physik.uni-muenchen.de); [mihaela.zigman@mpq.mpg.de](mailto:mihaela.zigman@mpq.mpg.de)

## ARTICLE

NATURE COMMUNICATIONS | <https://doi.org/10.1038/s41467-021-21668-5>

Probing of systemic human biofluids such as blood serum and plasma offers a potential means of monitoring the health status of individuals<sup>1,2</sup>. Molecular fingerprinting of blood-based biopsies via infrared vibrational spectroscopy<sup>3–6</sup> constitutes one possible way of realizing this potential. However, whether or not infrared molecular fingerprints (IMFs) are sufficiently stable over time to allow for health monitoring has not yet been assessed, nor have standard ranges for IMFs of healthy populations been determined. Human blood composition is influenced not only by a multitude of physiological states, but also by genotypic variation, lifestyle, age, environmental factors, nutritional status, drug consumption, and even metabolites produced by the symbiotic microflora<sup>7–10</sup>. Hence, any liquid-biopsy-based approach to health state monitoring must take natural biological variability, and the reference ranges for parameters that are sensitive to the physiological state of the organism, into account<sup>2,8–10</sup>. These parameters can be either individual analytes or specific features in a spectral fingerprint. The aim of this study is to evaluate the stability of IMFs and their spectral markers over time and provide a general understanding of the range of blood-based biological variability across molecular species, which is a vital prerequisite for any future application of molecular fingerprinting in health monitoring or disease detection.

Analytical “omics” approaches for molecular profiling, such as mass spectrometry (MS), nuclear magnetic resonance (NMR) spectroscopy, or DNA/RNA-sequencing methods, have led to the discovery of numerous blood-based biomarkers as candidates for disease detection and treatment monitoring<sup>1,11–18</sup>. Although sensitive and specific, most of these techniques focus on a single molecular group in a given context: i.e., they measure either proteins<sup>12</sup>, or small molecule metabolites<sup>13</sup>, or lipids<sup>14</sup>, or DNA<sup>15</sup>, or RNA<sup>16</sup>. However, probing of different molecular classes in parallel (“multiomics”) may better capture patterns of characteristic molecular changes and thus allow one to define significant pathophysiological transitions<sup>1,17,18</sup>. Infrared vibrational spectroscopy<sup>3–6</sup> probes vibrations of the structural backbones of all molecular species in a sample. The frequencies of those vibrations depend on the atomic composition, structure, and strength of the chemical bonds in the molecules. Thus, infrared spectroscopy has the inherent advantage of being sensitive to all functional groups in organic samples<sup>5,6</sup>. Unfortunately, spectral overlap of molecular responses and limited sensitivity of commercially available infrared spectrometers allows vibrational spectroscopy to quantify only the most abundant substances of highly complex biofluids so far<sup>19,20</sup>. However, new spectroscopic schemes allow to overcome current limitations in sensitivity and have the potential to significantly increase the range of detectable molecular concentrations<sup>21,22</sup>.

When applied to liquid biopsies, vibrational spectroscopy provides an IMF, which is potentially specific for a molecular blood phenotype and can therefore serve as a marker for an individual’s state of health. Fourier-transform infrared (FTIR) spectroscopy has demonstrated the potential of spectral fingerprints for disease diagnostics (e.g., Alzheimer’s disease<sup>23–25</sup>, prostate<sup>26</sup>, lung<sup>27</sup>, breast<sup>28</sup>, liver<sup>29</sup>, and brain cancers<sup>30</sup>) as well as for tracing the evolution of metabolic changes under exercise-induced conditions in athletes (sports medicine)<sup>31–33</sup>. FTIR spectroscopy of biofluids also has been used for disease monitoring in animal models<sup>34,35</sup> and blood biopsies from patients<sup>36,37</sup>. However, to the best of our knowledge, no attempts have yet been made to assess the stability of IMFs of a healthy, non-symptomatic human population over time. Thus, the inevitable biological variability of human biopsies relevant to any health monitoring approach remains unexplored.

This study addresses questions that are fundamental for the applicability of infrared fingerprinting in health monitoring: First,

we test whether infrared spectral fingerprints can be reproducibly and directly obtained from bulk liquid blood serum and plasma samples, and we determine the range of natural biological variation of IMFs from individual volunteers over time (within-person variation). Second, we quantitatively relate the variation of the IMFs over time for any given individual to the degree of variability between different individuals (between-person variation) and to operational variabilities inherent to clinical practice. We address these questions in a prototypical human clinical study cohort, quantify the analytical measurement error, and relate this to the variation between four different clinical centers (inter-clinical variability). Our study provides evidence for the existence of detectable person-specific IMFs of liquid-phase human blood samples. This lays the foundations for IMF as a promising discriminative and non-invasive method for health monitoring in the future.

### Results

To assess whether infrared vibrational spectra obtained from human blood in the liquid phase have properties that permit its use for health monitoring, we systematically quantify the within-person and the between-person variabilities of IMFs and relate these to the analytical and the clinical error. To this end, we analyzed prospectively collected samples of blood serum and blood plasma from 31 healthy, non-symptomatic human individuals. A detailed breakdown of the study participants is given in Supplementary Table 1. Blood was drawn from each individual in the cohort on 13 different days over a period of 7 weeks (once every 3–4 days), and once or twice after 6 months (Fig. 1a and Supplementary Table 2). In addition, the influence of measurement variability as well as blood collection and sample-handling processes were characterized. This combined error was evaluated in a separate study by comparing blood samples obtained at four different clinics from five individuals within <4 h. Well-defined standardized protocols for blood drawing, sample processing, and sample storage, applicable to routine medical practice were used throughout the study. This allowed us to evaluate variability caused by variations in blood drawing and sample processing, as well as short-term changes in blood composition<sup>38</sup>. The chosen study design represents a typical prospective longitudinal clinical study setting for health monitoring.

### Infrared molecular fingerprints of liquid blood plasma and serum.

We measured the infrared absorption spectra of blood serum and plasma samples with an automated FTIR device. Serum and plasma were transilluminated as native liquids in a thin flow-through cuvette (~8 μm path length) to mitigate the effects of strong absorption by water (see also Supplementary Figure 1). A measurement of a single sample took <5 min. In comparison with measurements of dried serum/plasma, this approach avoids major sample preparation steps and artefacts (e.g., the coffee-ring effect<sup>4,39</sup>) and preserves the native secondary protein structure, altogether increasing the reproducibility of the measurements as previously shown<sup>40</sup>. With this approach, we can record IMFs in a time- and cost-effective manner, with minimal sample preparation. The IMFs obtained covered the spectral range between 950 and 3000 cm<sup>-1</sup>, which includes absorption bands characteristic for proteins (amide I/II, predominantly at 1548 cm<sup>-1</sup> and 1654 cm<sup>-1</sup>), carbohydrates (mainly between 1000 and 1200 cm<sup>-1</sup>), and lipids (1741 cm<sup>-1</sup>, 2854 cm<sup>-1</sup>, and 2929 cm<sup>-1</sup>) (Fig. 1b).

There was an overall resemblance between the infrared spectra obtained from all study participants (Fig. 1b). The IMFs of blood plasma and serum are similar in overall shape, featuring the same characteristic absorption bands. This is not surprising, since

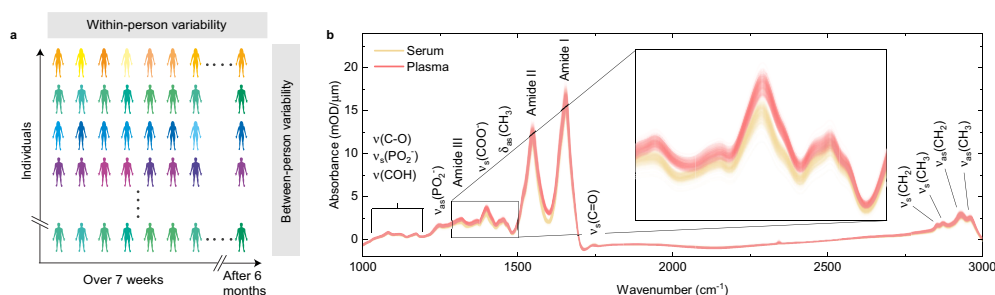


**Fig. 1 Study setup and overview.** **a** Experimental setup used for profiling of FTIR blood serum and plasma drawn from 31 healthy, non-symptomatic volunteers at up to 15 consecutive time points over the course of >6 months (see also Supplementary Table 2 for detailed information about the sampling time points). Same individuals are indicated as different shades of the same colors. **b** Unprocessed infrared absorption spectra of liquid blood sera (yellow) and plasma samples (red) measured from all individuals enrolled in the study. Inset: Close-up showing 636 individual traces of 318 measurements of blood sera and plasma each. Absorption peaks are associated with major molecular vibrations:  $\nu$  stretching,  $\delta$  bending,  $s$  symmetric, and  $as$  asymmetric vibrations.

plasma and serum share the vast majority of their molecular components. We find that the major difference between serum and plasma spectra is attributable to the ethylenediaminetetraacetic acid, which is added during plasma preparation and whose spectral features were readily recognizable (Supplementary Figure 2).

**Spectrally resolved variability of IMFs.** First, we determined the impact of natural biological variation on the acquired IMFs. To assess this variation quantitatively, we evaluated the magnitude of the time-dependent change (day-to-day and month-to-month) in the IMF of every single individual in our study cohort (within-person variability) and the spread among individuals within the same population (between-person variability). Second, we compared them with variations arising from (minor) differences in blood collection and sample-handling processes (inter-clinical error) and to the evaluated error of the spectroscopic measurement.

Unprocessed infrared absorption spectra and their standard deviation owing to the variabilities caused by the above-mentioned effects show a similar dependence on wavenumber (Fig. 2a). This suggests that the variation of IMFs is dominated by differences in the total amount of molecules in the samples (e.g., owing to disparities in details of collection, handling, and processing) rather than by changes in their relative molecular composition. These uncertainties can be substantially reduced by additional spectral pre-processing, in particular by normalization of the measured IR spectra<sup>41</sup> (see Methods for details). When applied, this step reduces the relative inter-clinical variability and the relative measurement error to <1% and 0.1%, respectively, in most spectral ranges (Fig. 2b). Overall, the reproducibility of the measurements achieved here is better than what was previously shown with liquid or dried serum or plasma<sup>40,42</sup>. We, therefore, use pre-processed spectra for all further analyses.

Removing variations in overall biomolecular content brings to light the fact that within-person variation of molecular composition is much smaller than its spread across the cohort of healthy, non-symptomatic individuals, and that the inter-clinical variation is significantly lower than any of these biological variabilities in most of the spectral regions. We found only a few spectral regions in which the inter-clinical variability and within-person variability are comparable (Fig. 2b), and should thus be considered carefully when included further for analysis. Although the inter-clinical variability may be further reduced by improved protocols for sample collection, the spectral variability is already on a level,

which allows characterization of the change of a person's molecular IR fingerprint over time.

**Comparison of biological variability in blood serum and plasma.** To evaluate whether blood serum or blood plasma might be better suited for IMF-based clinical diagnostics, we compared the magnitude of biological variability in the two biofluids after pre-processing their measured infrared absorption spectra. Spectrally resolved variability was averaged over the whole spectrum and the within-person variability for each person was evaluated individually. Although levels of between-person and inter-clinical variability were approximately the same for serum and plasma, the within-person variability of plasma was, on average, 24% higher than for serum samples (with a statistical significance of  $p = 2.7 \times 10^{-4}$ ) (Fig. 2c). This shows that IMFs of plasma samples captures more of the variations in molecular composition over time than IMFs of serum samples do. Depending on whether this additional biological information is desired for the envisioned monitoring or diagnostic application, the use of one or the other medium may be preferable.

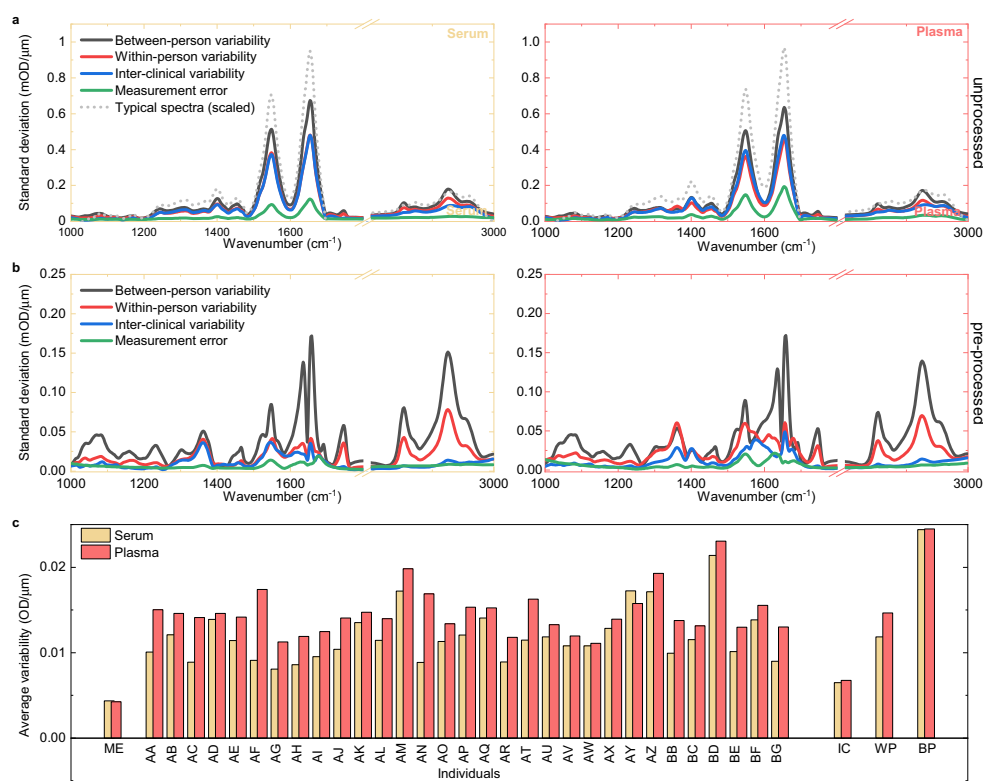
**Within-person and between-person variability of spectral markers.** Measuring the dependence of the precise abundance of a single analyte on physiological conditions in humans (e.g., given protein in states A, B, C) is known to be notoriously challenging. It is even more difficult to quantify concurrent changes in the abundance of many different substances belonging to distinct molecular classes (e.g., lipids and proteins) in a single experiment. Owing to its cross-molecular coverage, broadband infrared spectroscopy is able to make a valuable contribution here. Relative concentration changes of different molecular classes, in comparison with each other, can be estimated from the relative change in the ratio of the intensity of absorption bands, which are dominated by specific molecular classes and can therefore be assigned to them<sup>23,34,35,37,43–53</sup>. Table 1 shows a selection of peak ratios (together with their respective assignments) previously proposed as markers for physiological states, disease diagnostics, and monitoring.

We analyzed the within- and between-person variability of these ratios and evaluated their Index of Individuality ( $II$ ), which is defined as the ratio of the average within-person variability  $S_W$  and between-person variability  $S_B$ <sup>9,10</sup>:

$$II = S_W/S_B \quad (1)$$

When a molecular marker has an  $II < 0.6$ , it is considered to be

## ARTICLE

NATURE COMMUNICATIONS | <https://doi.org/10.1038/s41467-021-21668-5>

**Fig. 2 Biological variability of IMFs.** Spectrally resolved variability of **a** unprocessed and **b** pre-processed IR fingerprints obtained from serum and plasma samples: Standard deviation of the measurement error (green line), between-person (gray line), within-person (red line), and inter-clinical variability (blue line) are plotted against wavenumber. **c** Total variability of pre-processed spectra integrated over the whole spectral range (ME measurement error, IC inter-clinical variability, WP within-person variability, BP between-person variability).

specific to an individual<sup>9</sup> and can in principle be used to track the physiological state of an individual. In the context of disease detection, a low *II* also implies that the level of a marker may be within the normal range for one person, while the same values might be abnormal for another individual. In case-control scenarios, this may lead to deviations being erroneously identified as anomalies, which underlines the importance of quantitatively evaluating both the within- and between-person variability<sup>9,10</sup>.

As a case example, the ratio of the intensity of the amide I main peak to that of its shoulder ( $I_{1635}/I_{1654}$ —Fig. 3a) contains information about the relative amounts of alpha-helix and beta-sheet structures<sup>34,45,54</sup>. This parameter was used in classical case-control studies<sup>44,45</sup> as well as for longitudinal disease monitoring<sup>34,35</sup>. We found its within-person variation to be up to five times smaller than the variation between subjects, as reflected in its low *II* of 0.23 and 0.27 for serum and plasma, respectively. The high degree of individuality of this ratio suggests that it may be most helpful in health monitoring, as IMFs are to be referenced to those previously acquired from the same individual.

Generally, we find that intensity ratios of plasma and serum spectra behave in a similar fashion over time, which emphasizes the fact that serum and plasma share the vast majority of their

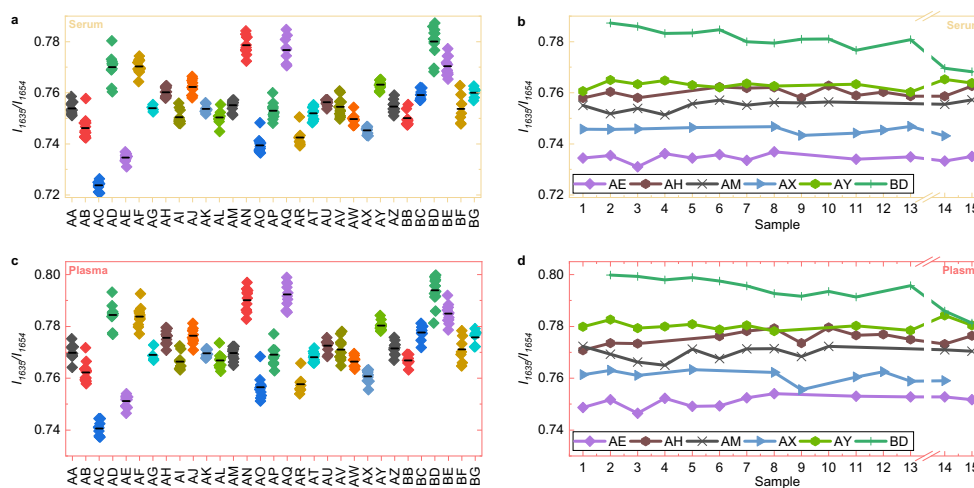
molecular components and therefore provide similar information. We found that most of the peak ratios are rather stable over time, whereas for some individuals (e.g.,  $I_{1635}/I_{1654}$  of the subject BD, Fig. 3b, d) we observed a significant change over time. This shows on the one hand that these spectral markers can be measured reliably and stably over time, but also that changes of these markers over time (potentially due to a disease) can be detected. In general, many peak ratios are found to have a rather low Index of Individuality (Table 1), which makes their biological variability comparable to commonly measured clinical variables<sup>55</sup>. This connects IMFs to other analytical approaches and highlights its value as a source of highly specific and individual molecular information.

**Identification of person-specific IMFs in the liquid phase of human blood.** Several spectral features of the IMFs are found to exhibit a low Index of Individuality, which renders them highly person-specific. This raises the intriguing question whether IMFs permit identification of individual molecular phenotypes, despite the inevitable background of biological variability. Although NMR and mass-spectroscopic fingerprints of human urine<sup>56</sup>, saliva<sup>57</sup>, blood serum<sup>58</sup>, and plasma<sup>59</sup> were found to possess this

**Table 1 Selected IR peak ratios with their assignments to respective physiological conditions.**

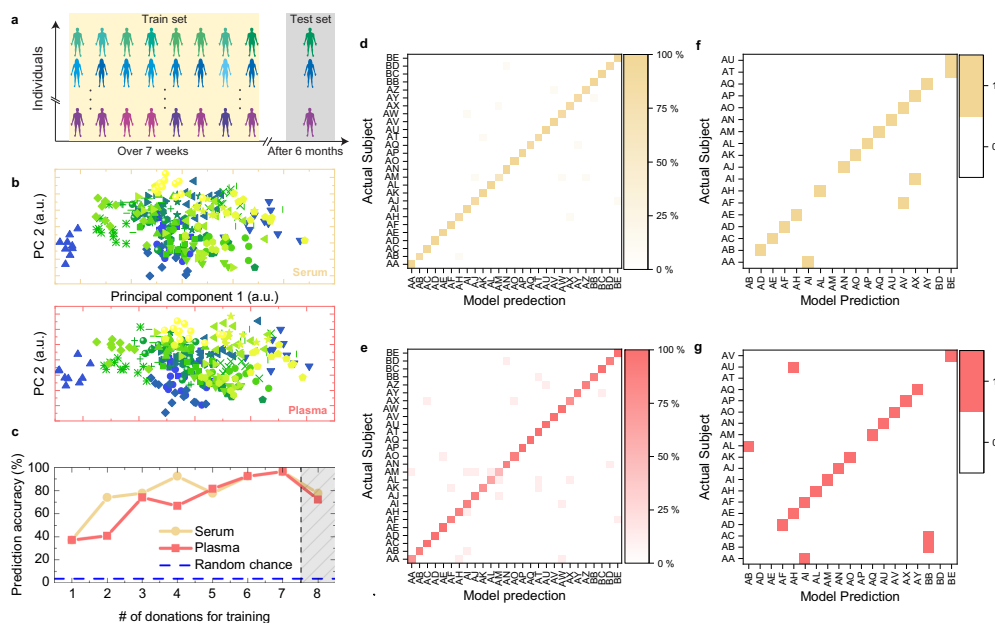
Peak ratio	Serum		Plasma		Assignment/applications
	Value ± S <sub>p</sub> <sup>2</sup>	//	Value ± S <sub>p</sub> <sup>2</sup>	//	
$I_{1635}/I_{1654}$	0.756 ± 0.012	0.23	0.771 ± 0.012	0.27	Ratio of β-sheet to α-helix secondary structures; <sup>34,35,45,49</sup> proposed marker for colitis; <sup>35</sup> determination of albumin-to-globulin ratio; <sup>44</sup> indicator of lymphoma and melanoma in a mouse model <sup>45</sup>
$I_{1546}/I_{1655}$	0.635 ± 0.003	0.61	0.638 ± 0.003	1.2	Amide I to amide II ratio; <sup>37,46,49,51</sup> alternation of secondary structure; <sup>46,51</sup> formation of protein fibrils <sup>46</sup>
$I_{1655}/(I_{1655}+I_{1548})$	0.610 ± 0.001	0.63	0.608 ± 0.001	1.2	Ratio of α-helix structure to total proteins <sup>47</sup>
$I_{1684}/(I_{1655}+I_{1548})$	0.213 ± 0.002	0.48	0.218 ± 0.002	0.69	Ratio of antiparallel β-sheet structure to total proteins <sup>47</sup>
$I_{1515}/(I_{1655}+I_{1548})$	0.174 ± 0.002	0.27	0.175 ± 0.002	0.34	Ratio of tyrosine-rich proteins to total proteins <sup>47</sup>
$I_{2959}/I_{2931}$	0.993 ± 0.020	0.52	1.005 ± 0.019	0.50	$\nu_{as}(CH_2)$ -to- $\nu_{as}(CH_2)$ ratio; length of lipid chains; <sup>51</sup> correlates with gastric cancer <sup>51</sup>
$(I_{2855}+I_{2927})/(I_{2962}+I_{2871})$	0.952 ± 0.023	0.55	0.942 ± 0.021	0.52	Elongation of fatty acids; <sup>34,46</sup> correlates with breast cancer progression <sup>34</sup>
$(I_{2851}+I_{2927})/(I_{1655}+I_{1548})$	0.178 ± 0.007	0.48	0.179 ± 0.007	0.46	Lipid-to-protein ratio <sup>47</sup>
$I_{1239}/(I_{2851}+I_{2927})$	0.424 ± 0.013	0.54	0.422 ± 0.011	0.52	Ratio of phospholipids to total lipids <sup>47</sup>
$I_{1740}/I_{1640}$	0.029 ± 0.003	0.59	0.029 ± 0.002	0.57	Lipid-to-protein ratio; <sup>52</sup> correlation with apoptotic cells <sup>52</sup>
$I_{1740}/I_{1400}$	0.118 ± 0.012	0.59	0.107 ± 0.009	0.59	Lipid-to-protein ratio; <sup>37,52</sup> correlation with tumor progression in tissues <sup>52</sup>
$I_{2852}/I_{1400}$	0.500 ± 0.018	0.54	0.454 ± 0.014	0.56	Lipid-to-protein ratio <sup>37</sup>
$I_{1450}/I_{1539}$	0.287 ± 0.003	0.30	0.297 ± 0.003	0.34	Lipid-to-protein ratio <sup>23</sup>
$I_{1240}/I_{1517}$	0.408 ± 0.004	0.51	0.407 ± 0.004	0.57	Degree of phosphorylation of tyrosine <sup>46</sup>
$I_{1045}/I_{1545}$	0.109 ± 0.003	0.41	0.109 ± 0.003	0.48	Phosphate-to-carbohydrate ratio <sup>23</sup>
$I_{1080}/I_{1550}$	0.145 ± 0.004	0.40	0.143 ± 0.004	0.44	Phosphate-to-amide II ratio <sup>37,49,51</sup>
$I_{1060}/I_{1230}$	0.705 ± 0.013	0.43	0.697 ± 0.012	0.55	$\nu_s(PO_2^-)$ -to- $\nu_{as}(PO_2^-)$ ratio <sup>23</sup>
$I_{1170}/I_{1080}$	0.905 ± 0.017	0.50	0.918 ± 0.016	0.54	Relative content of nucleic acids; distinguishes sera of lung cancer patients from those of healthy individuals <sup>49</sup>
$I_{1030}/I_{1080}$	0.626 ± 0.006	0.81	0.636 ± 0.005	1.01	Glycogen/phosphate ratio; indicator of metabolic turnover in cells <sup>43,48,53</sup>
$I_{1080}/I_{1243}$	0.726 ± 0.014	0.46	0.717 ± 0.013	0.56	$\nu_s(PO_2^-)$ -to- $\nu_{as}(PO_2^-)$ ratio <sup>49</sup>
$I_{1587}/(I_{1655}+I_{1548})$	0.145 ± 0.002	0.45	0.178 ± 0.002	0.56	Ratio of free amino acids to proteins <sup>47</sup>
$I_{1156}/I_{1171}$	0.894 ± 0.007	0.45	0.898 ± 0.006	0.49	Change of carbohydrate moieties in plasma globulins; correlates with Alzheimer's disease <sup>50</sup>
$I_{1243}/I_{1314}$	0.856 ± 0.013	0.41	0.802 ± 0.013	0.56	Reflects changes in protein and nucleic acid levels <sup>51</sup>
$I_{1453}/I_{1400}$	0.801 ± 0.006	0.43	0.737 ± 0.007	0.61	$\delta_{as}(CH_2)$ -to- $\delta_s(CH_2)$ ratio <sup>51</sup>

S<sub>p</sub><sup>2</sup> between-person variability, // index of Individuality,  $\nu$  stretching,  $\delta$  bending, s symmetric, as asymmetric vibrations.



**Fig. 3 Stability of blood-based infrared spectral markers over time.** Ratios between amide I main and side peak ( $I_{1635}/I_{1654}$ ) for **a, c** all individuals and for **b, d** six selected individuals representing detectable patterns of changes over time are shown. For most of the participants, the  $I_{1635}/I_{1654}$ -ratio was stable over time, while the pattern for e.g., subject BD (dark green line) was different over time. Each data point represents one blood sample. Blood samples 14 and 15 were collected 6 months after the previous ones.

## ARTICLE

NATURE COMMUNICATIONS | <https://doi.org/10.1038/s41467-021-21668-5>

**Fig. 4 Identification of person-specific IMFs.** **a** Experimental setup with training and test sets used for comparative analysis of IR fingerprints (see also Supplementary Table 2). **b** Prediction accuracy of the random-forest classifier. The accuracy increases as more blood samples are used for training. When applied to IMFs that were sampled 6 months after the training IMFs, the accuracy of the classifier drops to slightly below 80% (shaded area). **c** Principal component analysis (PC1 versus PC2) of the 293 normalized IR spectra (for serum and plasma each) of the 27 individuals that were included in the machine-learning evaluation. All IMFs of one person are depicted by the same color and symbol. **d, e** Confusion matrix of the prediction density of a random-forest classifier, for each individual, using seven blood draws for training and one for testing and eightfold cross-validation (repeated eight times with different combinations of training/test sets). **f, g** Confusion matrix of the prediction accuracy for blood draws obtained 6 months after the initial sampling. The random-forest classifier was trained on the first eight blood samples (initial sampling). Serum results are displayed in orange **d, f** and plasma results in red **e, g**.

capability, analogous evidence for infrared fingerprints of human biofluids is lacking. To assess the existence of highly personalized IMFs, we examined the IMFs from participants who all provided blood samples at least eight times within the first 7 weeks of the sampling period in more detail (Supplementary Table 2). Using a descriptive investigation—with principal component analysis (PCA) of all 293 IMFs (for serum and plasma each) of the 27 individuals—we found that the infrared spectra of certain subjects can be readily distinguished, whereas others overlap significantly (Fig. 4c). The separation can be improved when higher principal components (PCs) are included in the analysis; however, perfect separation of all cases was not attained. Although PCs depict the maximum variance, these are not necessarily the “directions” in multi-dimensional space of IMF spectral amplitudes that maximize the inter-group separation<sup>56</sup>.

Applying a random-forest machine-learning algorithm<sup>60</sup> (similar results can be also obtained with k-nearest neighbors<sup>61</sup> and XGBoost<sup>62</sup>, Supplementary Figure 3 and Methods), we performed predictive analysis to derive classification models. The data for the first  $N$  blood samples (for  $N = 1 \dots 8$ ) per individual were used for training, and these classifiers were then tested on the data obtained from the following blood draw,  $N + 1$  (Fig. 4a). The accuracy of the prediction is shown in Fig. 4c. If the classifier were predicting randomly, the accuracy would be 3.7%, as data from 27 participants were used in the training step. We show that training the algorithm with data from seven blood draws each, results in a prediction accuracy of >96%. Figure 4d, e shows the

result of a prediction-error analysis of a random-forest-based classification model for all individuals when seven blood draws per participant were used for training and one for testing, and when the data were subjected to eightfold cross-validation (repeated eight times with different combinations of training/test sets).

We observe that the vast majority of predictions lie on the diagonal of the confusion matrix (Fig. 4d, e), which demonstrates that the classifier is highly accurate, independently of the selection of the training set. This suggests the existence of highly person-specific IMFs that reflect the molecular phenotypes of individual donors, which are highly stable and reproducible over several independent blood draws (at least over 6 weeks). Investigation of the features that primarily contribute to successful classification revealed that the peaks that exhibit high-levels of between-person variation (e.g.,  $1747 \text{ cm}^{-1}$ ,  $2854 \text{ cm}^{-1}$ ,  $2929 \text{ cm}^{-1}$ —mostly lipid absorption) most extensively contributed to the uniqueness of a person-specific IR fingerprints (Supplementary Figure 4).

In addition, we tested the possibility of deriving a multiclass classification model based on the intensity ratios (Table 1), again by using the random forests algorithm. We found that the average accuracy of the classifiers was 85% for serum and 75% for plasma. The full list of results—for both training and test sets—is provided in Supplementary Table 4. This outcome implies that intensity ratios capture a large fraction—but not all—of the relevant information contained in the spectra, thus highlighting the need for broadband infrared coverage. Notably, intensity



ratios ranked as highly important by this independent classifier coincide with those having a low Index of Individuality (Supplementary Table 3). It should also be noted that a fraction of these intensity ratios can be categorized as redundant, as many of them are highly correlated with others and thus provide no significant information gains (Supplementary Tables 5 and 6)—in contrast to the PCs which are by definition uncorrelated.

**Testing the long-term stability of infrared fingerprints.** Finally, we investigated the stability of IMFs on medically relevant timescales. Here, the prediction accuracy of sera and plasma sampled 6 months after the initial training sampling period was evaluated. Most of the individuals were still classified correctly. The number of misclassifications increased after 6 months, reducing the identification accuracy to ~80% (Fig. 4f, g). Considering the fact that part of the misclassification may have been caused by changes in the overall physiological states (e.g., lifestyle, new drug intake) of some of the subjects, which have not been investigated for this study, the overall chemical composition of human blood is remarkably stable even over a half a year. This finding emphasizes the method's suitability for health monitoring.

#### Discussion

This proof-of-concept study demonstrates that (1) IMFs are robustly and directly measurable in liquid blood samples in a time- and cost-effective manner, (2) a single vibrational spectroscopic measurement provides access to multiple person-specific markers, and (3) infrared molecular phenotypes can be captured and monitored over time. Taken together, these findings suggest the possible applicability of blood-based infrared spectral fingerprinting for clinical health monitoring.

Routine blood profiling often focuses on the detection of defined analytes (e.g., molecule- or gene-based). However, broadband vibrational spectroscopy has the capacity to capture signals from all classes of biomolecular species. Thus, changes in any types of biomolecules, metabolic reaction products, or enzyme activities in human blood (e.g., elicited by a transition in health status) may lead to a change in the molecular phenotype of blood that may be reflected in the individual's IMFs. If so, regular, repeated sampling should enable any "abnormal" deviation in a molecular phenotype to be effectively detected by comparisons with previously recorded IMFs obtained from the same subject (self-referencing). In addition, any infrared measurement could represent a useful extension to current blood-based analytics, and could be followed up by well-established analytical approaches for deeper understanding. However, for the role proposed for IMFs in health monitoring here, it is not necessary to understand the molecular origins of changes in IMFs, as long as the characteristic deviation is specific and significant enough relative to its natural biological variability.

Although FTIR technology has been employed for case-control studies using dried serum and plasma samples<sup>23–30</sup>, its applicability for human health monitoring has not been previously evaluated. Here, we applied FTIR to native liquid samples in a longitudinal study setting, and followed healthy, non-symptomatic individuals in order to quantitatively evaluate variations in the IMFs over time. We have shown that well-defined blood collection and processing workflows yield IMFs with a high degree of reproducibility, which allows cross-comparability across different clinical sites. Importantly, we find that the relative variations detected in IMFs are comparable to the variability of molecular concentrations measured with conventional analytical methods<sup>63</sup>. Furthermore, we demonstrate that many infrared spectral markers exhibit Indices of Individuality lower than 0.6,

placing them within the range of variability typically found for blood analytes routinely used in diagnostic medical laboratory facilities<sup>65</sup>. This demonstrates the ability of infrared fingerprinting to obtain highly person-specific information. More generally, our findings lay the foundation for a robust assessment of the existence of disease-specific infrared spectral features for health monitoring and disease detection.

Sampling individuals repeatedly over time, as we did here, can greatly enhance the capacity of infrared phenotypes to identify relevant information by eliminating the influence of day-to-day, within-person biological variability. In addition, any molecular phenotype may be more accurately detected in the context of longitudinal studies with self-referencing<sup>2</sup>. Such an approach will also eliminate the major source of "biological noise", namely between-person variability. This might be especially useful for diseases with the highest mortality rates (e.g., cancer, cardiovascular conditions), which often develop over the course of years or even decades, and where self-referencing based on IMFs could be particularly valuable. However, the answer to the question whether particular infrared spectral changes can be definitively linked to the onset or progression of a given disease is beyond the scope of the current work. For this purpose, sufficiently large cohort strata combined with clinical information are needed.

The data reported here show that the infrared molecular phenotype of an individual can be effectively followed over time. This is an essential prerequisite for future health monitoring and detection of medical phenotypes by infrared broadband vibrational spectroscopy, circumventing the need for any a priori knowledge about the molecular identity or causal origin of deviations from the normal physiological range.

#### Methods

**Enrollment of study participants and blood sampling.** The study was reviewed and approved by "Ethikkommission bei der LMU München" (EK 20170820—Nr.: 17-532), and was conducted according to Good Clinical Practice (ICH-GCP), the principles of the Declaration of Helsinki, and all applicable legislations and regulations. Informed consent was obtained from all participants prior to blood collection.

Prior to the study, a statistical power calculation was performed to determine the sample size required to assess the mean and variance of the IMFs within a certain bound on accuracy, assuming a normal distribution. For the determination of the mean value of IMFs over all individuals at each wavenumber, a bound on accuracy of 0.025 mOD/ $\mu\text{m}$  with 95% confidence was set, resulting in a required minimum sample size of 26 individuals. The actual precision for the estimation of the mean is much higher than the stated limit, as several measurements per person were made and used for the analysis of the mean. For the estimation of the variabilities (between-person and within-person variability) we assumed that 26 persons donated 10 times. Thus, corresponding variabilities can be estimated within 35% of their true values and this can be achieved with a 95% confidence. To account for possible drop-outs over the course of the study, >30 individuals (31 individuals in total) were recruited.

Before each blood withdrawal, the participants were questioned about their health status and previous meals. Thirty-one adults were recruited for the longitudinal study and fasting blood samples were collected at the same site throughout the study. Within the first 7 weeks of the study, blood was sampled every 3–4 days. After 6 months, each participant again gave their blood two more times. Thus, each participant provided up to 15 samples over a period of >6 months (see also Supplementary Table 2). Ages of the participants ranged from 20 to 71 years with a mean of 39.6 years ( $\pm 14.0$  years, STD). 54.5% of the participants were female. None of the participants had any overt symptoms or severe diseases. Some of the participants were overweight, had allergies, food intolerances, or hypertension, which are all typical for a cross-section of the population at large (see Supplementary Table 1 for detailed information on subjects).

To evaluate the inter-clinical variability, five individuals volunteered to take part in an additional separate experiment. They gave blood at four different clinical sites within 4 h. No food was consumed during this time or within 6 h prior to the first sampling time.

**Standard operating procedures for serum and plasma sample collection, preparation, and storage.** Blood samples were collected, processed, and stored using defined standard operating procedures. Fasting blood was obtained between 9 am and 2 pm using Safety-Multifly needles of 21 G (Sarstedt), and transferred to

## ARTICLE

NATURE COMMUNICATIONS | <https://doi.org/10.1038/s41467-021-21668-5>

4.9-ml serum and 4.9-ml plasma Monovettes (Sarstedt). Special care was taken to make the different blood collections as comparable as possible. This meant that the same type of cannula was always used, the tubes were always filled to the recommended maximum filling level, serum was always collected first, and then plasma. For the blood clotting process to take place, the tubes were stored upright for at least 20 min and then centrifuged at 2,000 g for 10 min at 20 °C. The supernatant was carefully aliquoted and frozen at –80 °C within 3 h after collection.

After all, samples were collected, the aliquots used for the actual FTIR measurement were prepared. One tube out of each of the smaller tube-sets was thawed and again centrifuged for 10 min at 2000 g. The supernatant was distributed into the measurement tubes (50 µl per tube) to be refrozen at –80 °C. All the FTIR measurements were performed upon two freeze–thaw cycles within the same measurement campaign.

To measure experimental errors during the experiment, quality-control (QC) samples from pooled human serum (BioWest, Nuaille, France) were used<sup>64</sup>.

**FTIR measurements.** The samples were measured in random order to reduce systematic effects. The spectroscopic measurements were performed in liquid phase with an automated FTIR device (MIRA-Analyzer, micro-biolytics GmbH) with a flow-through transmission cuvette (CaF<sub>2</sub> with ~8 µm path length). The spectra were acquired with a resolution of 4 cm<sup>-1</sup> in a spectral range between 950 cm<sup>-1</sup> and 3050 cm<sup>-1</sup>. Note, that in comparison with measurements of dried serum, strong water absorption hinders the recording of the spectra over the entire mid-infrared range spanning from 400 cm<sup>-1</sup> to 4000 cm<sup>-1</sup> (see Supplementary Figure 1). After sample exchange, a water reference spectrum was measured to reconstruct the IR absorption spectrum. After every five samples, a QC measurement was performed. Each measurement sequence usually contained up to 40 samples resulting in measurement times of up to 3 h. Experiments on QC showed that the change in IMFs of serum and plasma is negligible for the time span of a regular measurement sequence.

**Pre-processing of infrared absorption spectra.** All spectra were grouped according to the respective measurement day. The measured QC spectra of the different measurement days were compared with identifying small instrument drifts, and all the other spectra were corrected accordingly. “Negative” absorption, which occurs if the hydrated sample contains less water than the reference (pure water), was corrected for<sup>65</sup>. It is known from measurements of dried serum or plasma, that there is no significant absorption in the wavenumber region 1850–2300 cm<sup>-1</sup>, resulting in a flat absorption baseline. We used this fact as a criterion for adding to each spectrum a water absorption spectrum taken from literature<sup>66</sup> to account for the missing water in the sample measurement and minimize the average slope in this region in order to obtain a flat baseline (Supplementary Figure 1). The same wavenumber region was subsequently utilized to compensate for baseline drifts, and all spectra were truncated to 1000–3000 cm<sup>-1</sup>. Finally, all spectra were normalized as vectors, using Euclidean (or  $L_2$ ) norm. To avoid  $y$  axis scale change caused by Euclidean normalization, we computed average differences between maximum and minimum values of all spectra before normalization and then rescaled all normalized spectra to restore this averaged difference. This allowed us to preserve the average swing of the spectra and to correctly compare the variabilities of the pre-processed spectra.

**Evaluation of between- and within-person variability.** To obtain the within-person variability, we calculated the standard deviation of the participants’ spectra over time and used all individual standard deviations to calculate the mean of the within-person variability. Between-person variability was obtained by averaging all spectra of a given individual and then calculating the standard deviation of these averaged spectra from different individuals. The inter-clinical variability was calculated in a similar manner from blood samples collected at different clinical sites and with standard deviations averaged to obtain the mean inter-clinical variation. The analytical error was estimated by repeatedly measuring quality-control serum samples and calculating the reproducibility of the obtained infrared spectra.

**Machine-learning analysis and classification.** After all samples and subject-related data were collected, the two following criteria led to the decision of the subset of 27 individuals to be considered in the machine-learning analysis:

1. Include at least 26 individuals (see also sample size calculation).
2. Include as many donations per individual as possible.

To meet both the above-listed criteria, we included only participants who have provided blood samples at least eight times within the first 7 weeks of the sampling period for the analysis of person-specific IMFs.

To reduce the dimension of data sets and explain the variance with a small number of linearly uncorrelated variables—PCs—we used PCA. When a significant fraction of the total variance is captured by the first two PCs, the separation between different classes can be conveniently represented by 2D scatter plots. As PCA is unsupervised, it is often used as the first analysis applied to a new data set<sup>41</sup>.

For the derivation of classification models, we used Scikit-Learn<sup>67</sup> (v. 0.20.3), an open-source machine-learning framework in Python (v.3.6.8). We trained various

models based on three algorithms: Random forests<sup>60</sup>, k-Nearest-Neighbors<sup>61</sup>, and XGBoost<sup>62</sup>. The purpose of classification is to predict and test the identity of individuals using multiclass classification models. It turned out that a random-forest-based model (an ensemble of 3160 decision trees) provided the highest accuracy. The prediction accuracy is defined as the proportion of individuals who are correctly classified according to the model applied. Information on the optimal values of model parameters can be found in the SI (caption of Supplementary Figure 3). The search for the optimal hyperparameters was performed using grid-search. Performance evaluation was carried out using cross-validation and its visualization using the notion of the confusion matrix.

Owing to the high dimensionality of the spectral data, and the high degree of correlation among the original features, the machine-learning algorithms were not applied directly to original data but rather to features extracted from them. The following approaches to feature extraction were used:

- a. dimensionality reduction using PCA (described above). Thereby, the PCs transformation was fit on the training set only and used to transform both training and test set. The minimum number of PCs required to preserve 99.9% of the explained variance was kept.
- b. manual extraction of spectral-intensity ratios.

In addition, we have evaluated the relative importance of each feature by measuring how much the tree nodes that use a particular feature reduce the average impurity (Gini impurity<sup>68</sup>) across all trees in the ensemble. This quantity is known as the Gini importance<sup>69,70</sup>. Gini importance is a way to measure the relative importance of each feature (in this case, wavenumbers) with a model build using the random-forest algorithm. Intuitively, it measures how much the tree nodes, across all trees of a random forest, reduce class impurity on average. By average, it is meant a weighted average, where each node’s weight is equal to the number of training examples that are associated with it.

**Reporting summary.** Further information on research design is available in the Nature Research Reporting Summary linked to this article.

**Data availability**

The authors declare that the main data supporting the findings of this study are available within the article and in Supplementary Data 1. Any additional information, data, and the statistical-analysis code are available upon request.

**Code availability**

The custom code used for the production of the results presented in this manuscript is stored in a persistent repository at the Leibniz Supercomputing Center of the Bavarian Academy of Sciences and Humanities (LRZ), located in Garching, Germany. The code can be only shared upon reasonable request, as its correct use depends on the settings of the experimental setup and the measuring device and should therefore be clarified with the authors.

Received: 28 January 2020; Accepted: 3 February 2021;

Published online: 08 March 2021

**References**

1. Chen, R. et al. Personal omics profiling reveals dynamic molecular and medical phenotypes. *Cell* **148**, 1293–1307 (2012).
2. Schüssler-Fiorenza Rose, S. M. et al. A longitudinal big data approach for precision health. *Nat. Med.* **25**, 792–804 (2019).
3. Bunaciu, A. A., Fleschin, Ş., Hoang, V. D. & Aboul-Enein, H. Y. Vibrational spectroscopy in body fluids analysis. *Crit. Rev. Anal. Chem.* **47**, 67–75 (2017).
4. Baker, M. J. et al. Developing and understanding biofluid vibrational spectroscopy: a critical review. *Chem. Soc. Rev.* **45**, 1803–1818 (2016).
5. Lasch, P. & Kneipp, J. *Biomedical Vibrational Spectroscopy*. (Wiley-Interscience, 2008).
6. Barth, A. & Haris, P. I. *Biological and Biomedical Infrared Spectroscopy*. 2 (IOS press, 2009).
7. Enroth, S., Johansson, Å., Enroth, S. B. & Gyllensten, U. Strong effects of genetic and lifestyle factors on biomarker variation and use of personalized cutoffs. *Nat. Commun.* **5**, 4684 (2014).
8. Liu, Y. et al. Quantitative variability of 342 plasma proteins in a human twin population. *Mol. Syst. Biol.* **11**, 786 (2015).
9. Fraser, G. G. & Harris, E. K. Generation and application of data on biological variation in clinical chemistry. *Crit. Rev. Clin. Lab. Sci.* **27**, 409–437 (1989).
10. Hawkrige, A. M. & Muddiman, D. C. Mass spectrometry-based biomarker discovery: toward a global proteome index of individuality. *Annu. Rev. Anal. Chem.* **2**, 265–277 (2009).
11. Kulasingam, V. & Diamandis, E. P. Strategies for discovering novel cancer biomarkers through utilization of emerging technologies. *Nat. Clin. Pract. Oncol.* **5**, 588–599 (2008).



12. Belczacka, I. et al. Proteomics biomarkers for solid tumors: current status and future prospects. *Mass Spectrom. Rev.* **38**, 49–78 (2019).
13. Zhang, A., Sun, H., Qiu, S. & Wang, X. Metabolomics in noninvasive breast cancer. *Clin. Chim. Acta* **424**, 3–7 (2013).
14. Qiu, Y. et al. Mass spectrometry-based quantitative metabolomics revealed a distinct lipid profile in breast cancer patients. *Int. J. Mol. Sci.* **14**, 8047–8061 (2013).
15. Heitzer, E. & Speicher, M. R. One size does not fit all: size-based plasma DNA diagnostics. *Sci. Transl. Med.* **10**, eaav3873 (2018).
16. Andersen, G. B. & Tost, J. Circulating miRNAs as Biomarker in Cancer. in *Tumor Liquid Biopsies*, 277–298 (Springer, 2020).
17. Yoo, B. C., Kim, K.-H., Woo, S. M. & Myung, J. K. Clinical multi-omics strategies for the effective cancer management. *J. Proteom.* **188**, 97–106 (2018).
18. Zachariou, M., Minadakis, G., Oulas, A., Afxenti, S. & Spyrou, G. M. Integrating multi-source information on a single network to detect disease-related clusters of molecular mechanisms. *J. Proteom.* **188**, 15–29 (2018).
19. Perez-Guaita, D., Garrigues, S. & Guardia, De. La, M. Infrared-based quantification of clinical parameters. *TRAC Trends Anal. Chem.* **62**, 93–105 (2014).
20. Brandstetter, M. et al. Reagent-free monitoring of multiple clinically relevant parameters in human blood plasma using a mid-infrared quantum cascade laser based sensor system. *Analyst* **138**, 4022–4028 (2013).
21. Akhgar, C. K. et al. The next generation of IR spectroscopy: EC-QCL-based mid-IR transmission spectroscopy of proteins with balanced detection. *Anal. Chem.* **92**, 9901–9907 (2020).
22. Pupeza, I. et al. Field-resolved infrared spectroscopy of biological systems. *Nature* **577**, 52–59 (2020).
23. Paraskevaidi, M. et al. Differential diagnosis of Alzheimer's disease using spectrochemical analysis of blood. *Proc. Natl Acad. Sci.* **114**, E7929–E7938 (2017).
24. Nabers, A. et al. Amyloid- $\beta$ -secondary structure distribution in cerebrospinal fluid and blood measured by an immuno-infrared-sensor: a biomarker candidate for Alzheimer's disease. *Anal. Chem.* **88**, 2755–2762 (2016).
25. Carmona, P. et al. Discrimination analysis of blood plasma associated with Alzheimer's disease using vibrational spectroscopy. *J. Alzheimer's Dis.* **34**, 911–920 (2013).
26. Krafft, C. et al. A specific spectral signature of serum and plasma-derived extracellular vesicles for cancer screening. *Nanomed. Nanotechnol. Biol. Med.* **13**, 835–841 (2017).
27. Ollesch, J. et al. An infrared spectroscopic blood test for non-small cell lung carcinoma and subtyping into pulmonary squamous cell carcinoma or adenocarcinoma. *Biomed. Spectrosc. Imaging* **5**, 129–144 (2016).
28. Zelig, U. et al. Early detection of breast cancer using total biochemical analysis of peripheral blood components: a preliminary study. *BMC Cancer* **15**, 408 (2015).
29. Thumanu, K. et al. Diagnosis of liver cancer from blood sera using FTIR microspectroscopy: a preliminary study. *J. Biophotonics* **7**, 222–231 (2014).
30. Butler, H. J. et al. Development of high-throughput ATR-FTIR technology for rapid triage of brain cancer. *Nat. Commun.* **10**, 4501 (2019).
31. Petitbois, C. & Délérès, G. Analysis and monitoring of oxidative stress in exercise and training by FTIR spectrometry. *Int. J. Sports Physiol. Perform.* **3**, 119–130 (2008).
32. Petitbois, C., Cazorla, G. & Délérès, G. The biological and metabolic adaptations to 12 months training in elite rowers. *Int. J. Sports Med.* **24**, 36–42 (2003).
33. Délérès, G. & Petitbois, C. Applications of FT-IR spectrometry to plasma contents analysis and monitoring. *Vib. Spectrosc.* **32**, 129–136 (2003).
34. Blat, A. et al. Fourier transform infrared spectroscopic signature of blood plasma in the progression of breast cancer with simultaneous metastasis to lungs. *J. Biophotonics* **12**, 1–11 (2019).
35. Ghimire, H., Jayaweera, P. V. V. & Perera, A. G. U. Longitudinal analysis of molecular alteration in serum samples of dextran sodium sulfate-induced colitis mice by using infrared spectroscopy. *Infrared Phys. Technol.* **97**, 33–37 (2019).
36. Medipally, D. K. R. et al. Monitoring radiotherapeutic response in prostate cancer patients using high throughput FTIR spectroscopy of liquid biopsies. *Cancers (Basel)* **11**, 925 (2019).
37. Sahu, R. K. et al. Continuous monitoring of WBC (biochemistry) in an adult leukemia patient using advanced FTIR-spectroscopy. *Leuk. Res.* **30**, 687–693 (2006).
38. Lippi, G., Salvagno, G. L., Montagnana, M., Brocco, G. & Guidi, G. C. Influence of short-term venous stasis on clinical chemistry testing. *Clin. Chem. Lab. Med.* **43**, 869–875 (2005).
39. Ollesch, J. et al. FTIR spectroscopy of biofluids revisited: an automated approach to spectral biomarker identification. *Analyst* **138**, 4092 (2013).
40. Fabian, H., Lasch, P. & Naumann, D. Analysis of biofluids in aqueous environment based on mid-infrared spectroscopy. *J. Biomed. Opt.* **10**, 031103 (2005).
41. Trevisan, J., Angelov, P. P., Carmichael, P. L., Scott, A. D. & Martin, F. L. Extracting biological information with computational analysis of Fourier-transform infrared (FTIR) biospectroscopy datasets: current practices to future perspectives. *Analyst* **137**, 3202 (2012).
42. Lovergne, L. et al. Investigating optimum sample preparation for infrared spectroscopic serum diagnostics. *Anal. Methods* **7**, 7140–7149 (2015).
43. Movasaghi, Z., Rehman, S. & ur Rehman, D. I. Fourier transform infrared (FTIR) spectroscopy of biological tissues. *Appl. Spectrosc. Rev.* **43**, 134–179 (2008).
44. Lasch, P., Beekes, M., Fabian, H. & Naumann, D. Antemortem Identification of Transmissible Spongiform Encephalopathy (TSE) from Serum by Mid-infrared Spectroscopy. *Handbook of Vibrational Spectroscopy*, <https://doi.org/10.1002/0470027320.s8925> (2001).
45. Ghimire, H., Venkataramani, M., Bian, Z., Liu, Y. & Perera, A. G. U. ATR-FTIR spectral discrimination between normal and tumorous mouse models of lymphoma and melanoma from serum samples. *Sci. Rep.* **7**, 16993 (2017).
46. Staniszevska-Slezak, E. et al. A possible Fourier transform infrared-based plasma fingerprint of angiotensin-converting enzyme inhibitor-induced reversal of endothelial dysfunction in diabetic mice. *J. Biophotonics* **11**, e201700044 (2018).
47. Staniszevska-Slezak, E., Mateuszuk, L., Chlopicki, S., Baranska, M. & Malek, K. Alterations in plasma biochemical composition in NO deficiency induced by L-NAME in mice analysed by fourier transform infrared spectroscopy. *J. Biophotonics* **9**, 1098–1108 (2016).
48. Gazi, E. et al. Applications of Fourier transform infrared microspectroscopy in studies of benign prostate and prostate cancer. A pilot study. *J. Pathol.* **201**, 99–108 (2003).
49. Wang, X., Shen, X., Sheng, D., Chen, X. & Liu, X. FTIR spectroscopic comparison of serum from lung cancer patients and healthy persons. *Spectrochim. Acta Part A Mol. Biomol. Spectrosc.* **122**, 193–197 (2014).
50. Carmona, P., Molina, M., López-Tobar, E. & Toledano, A. Vibrational spectroscopic analysis of peripheral blood plasma of patients with Alzheimer's disease. *Anal. Bioanal. Chem.* **407**, 7747–7756 (2015).
51. Sheng, D. et al. Comparison of serum from gastric cancer patients and from healthy persons using FTIR spectroscopy. *Spectrochim. Acta Part A Mol. Biomol. Spectrosc.* **116**, 365–369 (2013).
52. Paraskevaidi, M., Martin-Hirsch, P. L. & Martin, F. L. ATR-FTIR Spectroscopy Tools for Medical Diagnosis and Disease Investigation. In *Nanotechnology Characterization Tools for Biosensing and Medical Diagnosis* 163–211 (Springer, 2018).
53. Smith, B. R. et al. Combining random forest and 2D correlation analysis to identify serum spectral signatures for neuro-oncology. *Analyst* **141**, 3668–3678 (2016).
54. Barth, A. & Zscherp, C. What vibrations tell us about proteins. *Q. Rev. Biophys.* **35**, 369–430 (2002).
55. Lacher, D. A., Hughes, J. P. & Carroll, M. D. Estimate of biological variation of laboratory analytes based on the third national health and nutrition examination survey. *Clin. Chem.* **51**, 450–452 (2005).
56. Assfalg, M. et al. Evidence of different metabolic phenotypes in humans. *Proc. Natl Acad. Sci.* **105**, 1420–1424 (2008).
57. Wallner-Liebmann, S. et al. Individual human metabolic phenotype analyzed by 1 H NMR of saliva samples. *J. Proteome Res.* **15**, 1787–1793 (2016).
58. Yousri, N. A. et al. Long term conservation of human metabolic phenotypes and link to heritability. *Metabolomics* **10**, 1005–1017 (2014).
59. Draisma, H. H. M. et al. Hierarchical clustering analysis of blood plasma lipidomics profiles from mono- and dizygotic twin families. *Eur. J. Hum. Genet.* **21**, 95–101 (2013).
60. Breiman, L. Random forests. *Mach. Learn.* **45**, 5–32 (2001).
61. Altman, N. S. An introduction to kernel and nearest-neighbor nonparametric regression. *Am. Stat.* **46**, 175–185 (1992).
62. Chen, T. & Guestrin, C. Xgboost: A Scalable Tree Boosting System. In *Proceedings of the 22nd acm sigkdd international conference on knowledge discovery and data mining* 785–794 (2016).
63. Ricós, C., Alvarez, V., Cava, F. & Garcia-Lario, J. V. Current databases on biological variation: pros, cons and progress. *Scand. J. Clin. Lab. Invest.* **59**, 491–500 (1999).
64. Sangster, T., Major, H., Plumb, R., Wilson, A. J. & Wilson, I. D. A pragmatic and readily implemented quality control strategy for HPLC-MS and GC-MS-based metabolomic analysis. *Analyst* **131**, 1075 (2006).
65. Yang, H., Yang, S., Kong, J., Dong, A. & Yu, S. Obtaining information about protein secondary structures in aqueous solution using Fourier transform IR spectroscopy. *Nat. Protoc.* **10**, 382–396 (2015).
66. Segelstein, D. J. *The complex refractive index of water*. M.S. Thesis, University of Missouri (1981).
67. Pedregosa, F., Weiss, R. & Brucher, M. Scikit-learn: machine learning in Python. *J. Mach. Learn. Res.* **12**, 2825–2830 (2011).

## ARTICLE

NATURE COMMUNICATIONS | <https://doi.org/10.1038/s41467-021-21668-5>

68. Quinlan, J. R. Induction of decision trees. *Mach. Learn.* **1**, 81–106 (1986).
69. Menze, B. H. et al. A comparison of random forest and its Gini importance with standard chemometric methods for the feature selection and classification of spectral data. *BMC Bioinformatics* **10**, 213 (2009).
70. Menze, B. H., Petrich, W. & Hamprecht, F. A. Multivariate feature selection and hierarchical classification for infrared spectroscopy: serum-based detection of bovine spongiform encephalopathy. *Anal. Bioanal. Chem.* **387**, 1801–1807 (2007).

**Acknowledgements**

We thank Jacqueline Hermann, Katja Leitner, Sigrid Auweter, Daniel Meyer, Beate Rank, and Incinur Zellhuber for their help with this study. In particular, we acknowledge the efforts of many individuals who participated as volunteers in the clinical study reported here. We also want to thank Alexander Zigman Kohlmaier and Frank Fleischman for their feedback on the manuscript.

**Author contributions**

M.H. and M.Ž. designed the research plan; M.Ž. and F.K. initiated and led the study plan; N.H. led the clinical study; M.H., M.B. performed the measurements; M.H., K.V.K., M.B., L.V., and M.T. analyzed the data; M.H., M.Ž., K.V.K., L.V., and F.K. wrote the paper.

**Funding**

Open Access funding enabled and organized by Projekt DEAL.

**Competing interests**

The authors declare no competing interests.

**Additional information**

**Supplementary information** The online version contains supplementary material available at <https://doi.org/10.1038/s41467-021-21668-5>.

**Correspondence** and requests for materials should be addressed to M.H. or M.Ži.

**Peer review information** *Nature Communications* thanks the anonymous reviewer(s) for their contribution to the peer review of this work. Peer reviewer reports are available.

**Reprints and permission information** is available at <http://www.nature.com/reprints>

**Publisher's note** Springer Nature remains neutral with regard to jurisdictional claims in published maps and institutional affiliations.



**Open Access** This article is licensed under a Creative Commons Attribution 4.0 International License, which permits use, sharing, adaptation, distribution and reproduction in any medium or format, as long as you give appropriate credit to the original author(s) and the source, provide a link to the Creative Commons license, and indicate if changes were made. The images or other third party material in this article are included in the article's Creative Commons license, unless indicated otherwise in a credit line to the material. If material is not included in the article's Creative Commons license and your intended use is not permitted by statutory regulation or exceeds the permitted use, you will need to obtain permission directly from the copyright holder. To view a copy of this license, visit <http://creativecommons.org/licenses/by/4.0/>.

© The Author(s) 2021

**Stability of person-specific blood-based infrared molecular fingerprints opens up prospects for health monitoring**

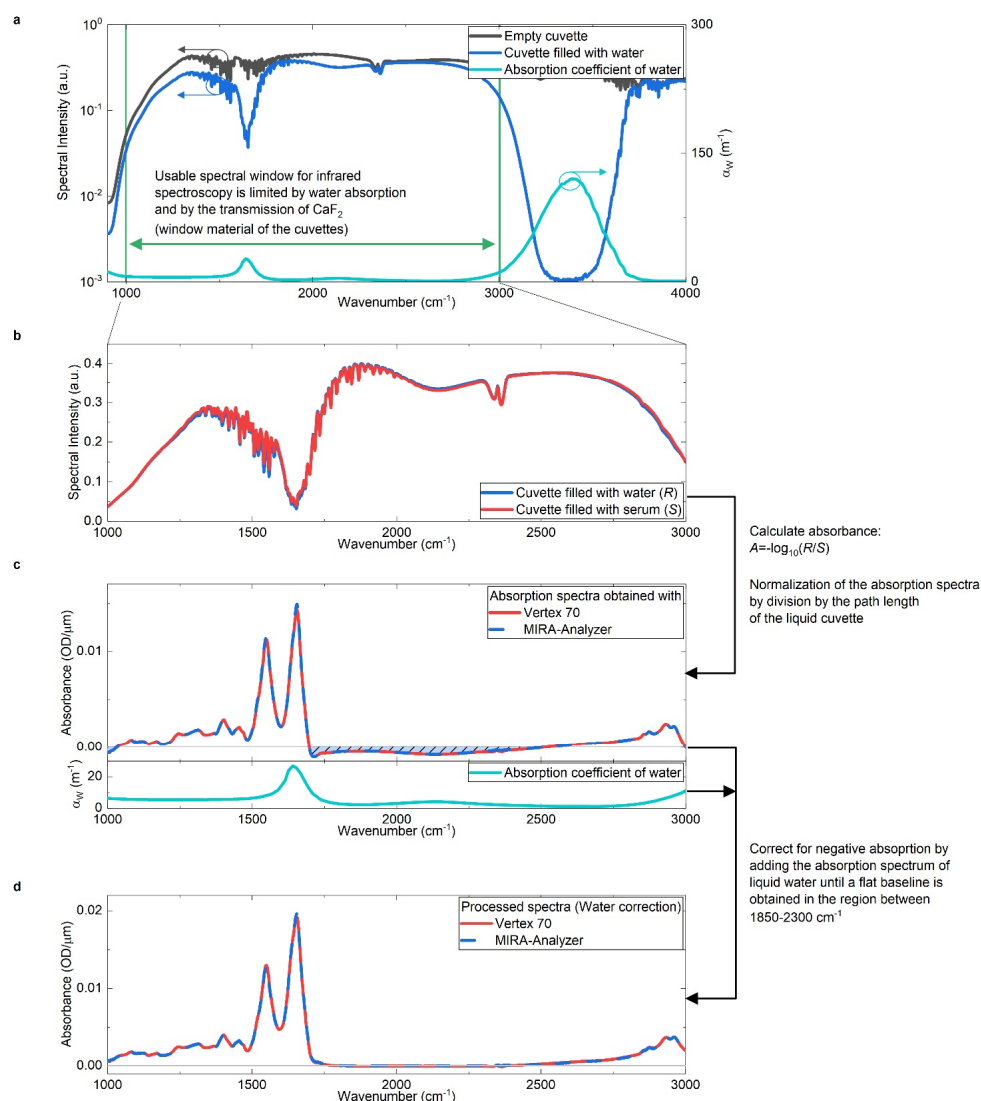
**SUPPLEMENTARY INFORMATION**

**Supplementary Table 1:** *Breakdown of the cohort of study participants. Apart from the listed comorbidities, none of the participants had a known disease or showed any symptoms of any disease.*

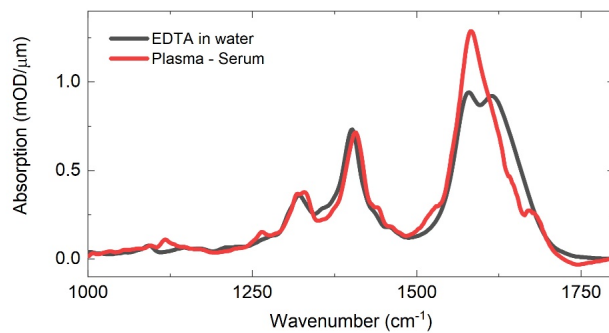
ID	Sex	Age	BMI	Smoking Status	Comorbidities
AA	female	28	n/a	n/a	
AB	female	54	23.1	non-smoker	
AC	male	29	n/a	n/a	
AD	female	54	21.2	active-smoker	
AE	female	55	22.4	active-smoker	high blood pressure
AF	female	24	26.6	non-smoker	allergies
AG	female	23	n/a	n/a	
AH	female	31	18.4	non-smoker	
AI	female	45	22.4	non-smoker	allergies
AJ	female	39	n/a	non-smoker	
AK	female	24	n/a	n/a	
AL	male	55	21.8	non-smoker	
AM	male	20	20.6	non-smoker	allergies
AN	female	42	20.2	non-smoker	
AO	male	46	23.4	non-smoker	
AP	female	28	22.8	non-smoker	
AQ	male	39	25.7	non-smoker	
AR	male	28	22.2	non-smoker	
AT	male	32	n/a	non-smoker	
AU	male	58	28.6	non-smoker	
AV	female	26	19.5	non-smoker	fibroma
AW	male	61	n/a	non-smoker	
AX	male	32	25	non-smoker	
AY	male	56	24.1	active-smoker	psoriasis
AZ	male	32	n/a	non-smoker	
BB	female	27	n/a	n/a	
BC	male	70	n/a	non-smoker	
BD	female	19	18.2	non-smoker	
BE	female	38	38.8	non-smoker	
BF	male	53	31.8	ex-smoker	
BG	male	27	n/a	non-smoker	

**Supplementary Table 2:** Overview of the sampling time of all collected blood samples. Since one serum and one plasma sample was collected per individual at a time, the absolute number of samples is 636. Depending on the number of blood samples per individual, the corresponding data were used for different types of evaluation. All data were taken into account when calculating the between- and within person variability of the infrared fingerprints and its associated spectral markers. Only data from individuals with more than 7 blood draws within the first 7 weeks were included in the training and test of the classification models for the identification of individuals (green shaded entries). The test of the long-term stability of infrared fingerprints was only performed on data from individuals that donated again 6 months after the first sampling period (dark green shaded areas).

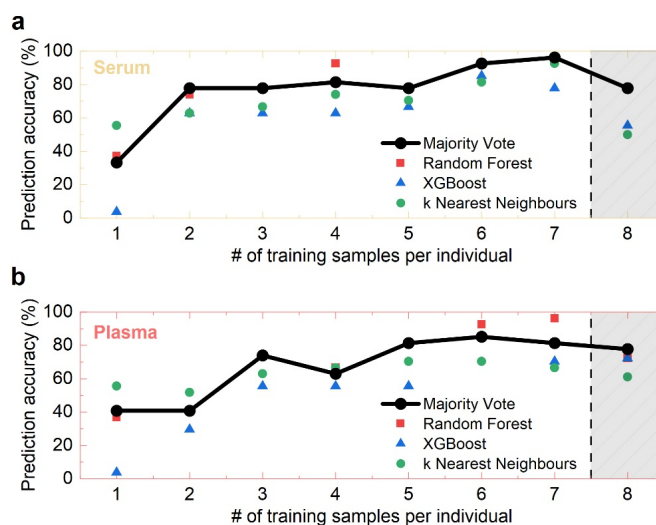
ID	Day(s) in the course of the study															Total number of blood draws	
	1	7	9	14	17	21	24	28	31	35	38	42	45	233	238	Day 1-45	Day 233-238
AA		x	x	x	x	x		x		x	x	x				9	0
AB				x	x	x	x	x	x	x	x	x	x	x	x	10	2
AC	x	x	x	x	x			x	x	x	x					9	0
AD	x	x	x		x	x	x	x					x	x	x	8	2
AE	x	x	x	x	x	x	x	x			x		x	x	x	10	2
AF	x	x	x	x	x	x		x	x	x	x		x	x		11	1
AG	x	x	x	x												4	0
AH	x	x	x			x	x	x	x	x	x	x	x	x	x	11	2
AI	x	x	x	x	x			x	x	x	x	x	x	x	x	10	1
AJ	x	x	x	x		x	x	x	x	x	x					10	0
AK	x	x			x	x		x	x	x	x	x				9	0
AL	x	x	x	x	x	x	x					x	x	x		9	1
AM	x	x	x	x	x	x	x	x	x	x				x	x	10	2
AN	x	x	x	x	x	x	x					x	x	x	x	9	2
AO	x			x	x	x	x	x	x	x	x	x		x	x	10	2
AP	x	x	x		x		x	x	x	x	x			x	x	9	2
AQ	x	x	x	x	x		x	x	x	x				x		9	1
AR	x	x	x	x	x	x								x	x	6	2
AT	x	x	x	x	x	x		x	x	x	x	x	x			12	0
AU	x	x	x	x	x		x	x	x	x				x	x	9	2
AV	x	x	x	x	x		x			x	x	x	x	x	x	10	2
AW	x	x		x	x	x	x	x	x	x						9	0
AX	x	x	x		x			x	x		x	x	x	x		9	1
AY	x	x	x	x	x	x	x	x			x		x	x	x	10	2
AZ	x	x	x	x	x	x	x	x	x		x	x				11	0
BB	x	x	x					x	x	x	x		x			8	0
BC		x		x	x	x	x	x	x	x	x		x			10	0
BD		x	x	x	x	x	x	x	x	x	x		x	x	x	11	2
BE			x	x	x	x	x	x	x	x	x	x	x	x		11	1
BF				x	x	x		x		x	x			x		6	1
BG						x	x	x	x		x		x			6	0



**Supplementary Figure 1:** Acquisition and pre-processing of infrared spectra of liquid samples. **a:** Spectral intensity of the infrared light source after passing through the empty measurement cuvette (black line) and when it is filled with water (blue line). The strong absorption of liquid water (turquoise line) and the limited transmission of the window material (CaF<sub>2</sub> – not shown) limits the useable spectral window for spectroscopy (green double-headed arrow). Any incomplete filling or drying of the sample would be detectable by a strong change of the spectra in comparison to the water reference (blue line). **b:** Spectral intensity of the infrared light source when the cuvette is filled with water (blue line) and with blood serum (red line). Please note that the power spectra shown in **a** and **b** are for demonstration purposes only, and had to be performed with a different measurement cuvette (AquaSpec™, Bruker) and a different spectrometer (Vertex 70, Bruker) for technical reasons. This setup is similar to the experimental setup (MIRA-Analyzer, microbiolytics GmbH) used throughout the measurements presented in this work and provides qualitatively the same results (**c** and **d**). **c:** The resulting absorption spectra of quality control serum. Negative absorption is caused by the fact that the number of water molecules in the measurement volume is lower in the serum sample than in pure water, and therefore at some wavenumbers, less light is absorbed by the sample than in the reference. This measurement artefact can be compensated by adding a known water absorption spectrum<sup>1</sup> (**c** – turquoise line) until (**d**) a flat baseline in the range of 1850-2300 wavenumbers is reached.

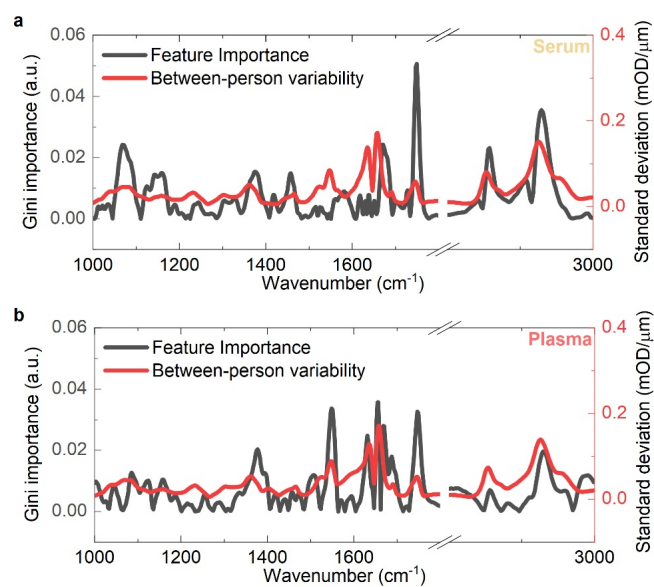


**Supplementary Figure 2:** Difference between the average serum and plasma infrared (IR) spectrum compared to the absorption IR spectrum of EDTA-Ca<sup>2+</sup> dissolved in water.



**Supplementary Figure 3:** Learning curves of prediction models generated using different algorithms (random forests, gradient boosted trees (XGBoost) and  $k$ -nearest neighbours) based on infrared molecular fingerprints (IMFs) of (a) blood serum and (b) plasma. Note that the accuracy of person identification increases when data of more blood draws are included for training and drops to slightly below 80% (shaded area) when applied to IMFs sampled 6 months later, resembling the difference between the shorter- and longer-term biological variability. The selected classification models for these plots are obtained by tuning the algorithms' hyperparameters to the following sets of values:

- Random Forest:  $n\_estimators=3160$ , others at default values of Scikit-Learn (v. 0.20.3) [see <https://scikit-learn.org/stable/modules/generated/sklearn.ensemble.RandomForestClassifier.html> for more information]
- XGBoost:  $n\_estimators=100$ , others at default values of XGBoost (v. 0.80) [see <https://xgboost.readthedocs.io/en/latest/parameter.html> for more information]
- K-NN:  $n\_neighbors=1$ , others at default values of Scikit-Learn (v. 0.20.3) [see <https://scikit-learn.org/stable/modules/generated/sklearn.neighbors.KNeighborsClassifier.html#sklearn.neighbors.KNeighborsClassifier> for more information]



**Supplementary Figure 4:** Gini importance (mean decrease in Gini impurity) of infrared spectral features (grey line) extracted by application of random forest algorithm used for Fig. 4d compared to the between-person variability (red line) of (a) serum and (b) plasma IMFs.



**Supplementary Table 3:** Gini importance (mean decrease in Gini impurity) of infrared intensity ratios – extracted by application of random forest algorithm – when the classification of individuals is based on intensity ratios instead of entire full infrared fingerprint spectra. Note that ratios with low Index of Individuality (II) correlate with high Gini importance. Gini importance provides a means of measuring the relevance of each spectral feature with regard to the classification. It can be interpreted as a relative (and not absolute) measure of the importance of each feature and thus its values can be interpreted as high or low only relative to each other. Green-shaded cells correspond to larger numbers, while the red-shaded cells correspond to low numbers.

Peak ratio:	Serum			Plasma		
	Value $\pm S_B^2$	II	Gini Importance	Value $\pm S_B^2$	II	Gini Importance
$I_{1635}/I_{1654}$	0.756 $\pm$ 0.012	0.231	0.086	0.771 $\pm$ 0.012	0.274	0.082
$I_{1546}/I_{1655}$	0.635 $\pm$ 0.003	0.613	0.034	0.638 $\pm$ 0.003	1.231	0.018
$I_{1655}/(I_{1655}+I_{1548})$	0.610 $\pm$ 0.001	0.625	0.033	0.608 $\pm$ 0.001	1.232	0.018
$I_{1684}/(I_{1655}+I_{1548})$	0.213 $\pm$ 0.002	0.481	0.038	0.218 $\pm$ 0.002	0.687	0.031
$I_{1515}/(I_{1655}+I_{1548})$	0.174 $\pm$ 0.002	0.268	0.071	0.175 $\pm$ 0.002	0.339	0.068
$I_{2959}/I_{2931}$	0.993 $\pm$ 0.020	0.521	0.025	1.005 $\pm$ 0.019	0.496	0.029
$(I_{2855}+I_{2927})/(I_{2962}+I_{2871})$	0.952 $\pm$ 0.023	0.547	0.026	0.942 $\pm$ 0.021	0.518	0.030
$(I_{2851}+I_{2927})/(I_{1655}+I_{1548})$	0.178 $\pm$ 0.007	0.484	0.026	0.179 $\pm$ 0.007	0.459	0.034
$I_{1239}/(I_{2851}+I_{2927})$	0.424 $\pm$ 0.013	0.542	0.025	0.422 $\pm$ 0.011	0.521	0.035
$I_{1741}/I_{1640}$	0.029 $\pm$ 0.003	0.592	0.030	0.029 $\pm$ 0.002	0.573	0.034
$I_{1740}/I_{1400}$	0.118 $\pm$ 0.012	0.589	0.027	0.107 $\pm$ 0.009	0.590	0.033
$I_{2852}/I_{1400}$	0.500 $\pm$ 0.018	0.539	0.025	0.454 $\pm$ 0.014	0.564	0.027
$I_{1450}/I_{1539}$	0.287 $\pm$ 0.003	0.301	0.059	0.297 $\pm$ 0.003	0.343	0.060
$I_{1240}/I_{1517}$	0.408 $\pm$ 0.004	0.512	0.028	0.407 $\pm$ 0.004	0.571	0.030
$I_{1045}/I_{1545}$	0.109 $\pm$ 0.003	0.405	0.042	0.109 $\pm$ 0.003	0.475	0.038
$I_{1080}/I_{1550}$	0.145 $\pm$ 0.004	0.397	0.047	0.143 $\pm$ 0.004	0.444	0.050
$I_{1060}/I_{1230}$	0.705 $\pm$ 0.013	0.430	0.052	0.697 $\pm$ 0.012	0.548	0.040
$I_{1170}/I_{1080}$	0.905 $\pm$ 0.017	0.504	0.044	0.918 $\pm$ 0.016	0.542	0.050
$I_{1030}/I_{1080}$	0.626 $\pm$ 0.006	0.806	0.044	0.636 $\pm$ 0.005	1.014	0.040
$I_{1080}/I_{1243}$	0.726 $\pm$ 0.014	0.457	0.045	0.717 $\pm$ 0.013	0.563	0.040
$I_{1587}/(I_{1655}+I_{1548})$	0.145 $\pm$ 0.002	0.452	0.046	0.178 $\pm$ 0.002	0.563	0.053
$I_{1156}/I_{1171}$	0.894 $\pm$ 0.007	0.450	0.053	0.898 $\pm$ 0.006	0.490	0.059
$I_{1243}/I_{1314}$	0.856 $\pm$ 0.013	0.410	0.050	0.802 $\pm$ 0.013	0.561	0.039
$I_{1453}/I_{1400}$	0.801 $\pm$ 0.006	0.434	0.043	0.737 $\pm$ 0.007	0.614	0.061

**Supplementary Table 4:** Summary of the classification accuracy using different sets of infrared spectral features.

	Train set (8-fold cross-validation)	Test Set
Plasma intensity ratios	75 %	56 %
Serum intensity ratios	85 %	61 %
Plasma (full spectra)	89 %	77 %
Serum (full spectra)	95 %	78 %

**Supplementary Table 5:** Correlation matrix of intensity ratios taken from normalised infrared spectra of serum samples. Green-shaded cell correspond to larger numbers, while the red-shaded cells correspond to low numbers.

	1635/1654	1546/1655	1655/(1655+1548)	1684/(1655+1548)	1515/(1655+1548)	2959/2931	(2855+2927)/(2962+2871)	(2851+2927)/(1655+1548)	1239/(2851+2927)	1741/1640	1740/1400	2852/1400	1450/1539	1240/1517	1045/1545	1080/1550	1060/1230	1170/1080	1030/1080	1080/1243	1587/(1655+1548)	1156/1171	1243/1314	1453/1400
1635/1654	1.00	0.43	-0.42	0.87	0.94	-0.36	0.35	0.44	-0.06	0.23	0.30	0.28	0.86	0.49	0.70	0.65	0.27	-0.51	0.05	0.27	0.85	0.80	0.75	0.766
1546/1655	0.43	1.00	-1.00	0.02	0.67	-0.04	0.04	0.10	0.09	0.02	0.04	0.01	0.19	-0.13	0.10	0.05	-0.04	-0.15	-0.17	-0.08	0.13	0.34	0.72	0.455
1655/(1655+1548)	-0.42	-1.00	1.00	-0.01	-0.66	0.06	-0.06	-0.12	-0.06	-0.04	-0.06	-0.04	-0.21	0.11	-0.12	-0.08	0.01	0.17	0.20	0.04	-0.13	-0.33	-0.74	-0.47
1684/(1655+1548)	0.87	0.02	-0.01	1.00	0.73	-0.26	0.25	0.32	0.01	0.17	0.23	0.18	0.76	0.48	0.63	0.57	0.21	-0.40	0.27	0.20	0.88	0.73	0.38	0.519
1515/(1655+1548)	0.94	0.67	-0.66	0.73	1.00	-0.25	0.24	0.33	0.04	0.14	0.20	0.17	0.74	0.29	0.60	0.53	0.21	-0.46	0.06	0.19	0.74	0.80	0.82	0.735
2959/2931	-0.36	-0.04	0.06	-0.26	-0.25	1.00	-1.00	-0.98	0.93	-0.96	-0.96	-0.98	-0.69	-0.88	-0.52	-0.62	-0.29	0.06	0.35	-0.40	-0.32	-0.26	-0.54	-0.71
(2855+2927)/(2962+2871)	0.35	0.04	-0.06	0.25	0.24	-1.00	1.00	0.98	-0.93	0.97	0.97	0.97	0.67	0.87	0.50	0.59	0.26	-0.03	-0.36	0.37	0.31	0.25	0.53	0.693
(2851+2927)/(1655+1548)	0.44	0.10	-0.12	0.32	0.33	-0.98	0.98	1.00	-0.92	0.94	0.95	0.98	0.74	0.89	0.57	0.67	0.33	-0.14	-0.39	0.43	0.38	0.27	0.59	0.754
1239/(2851+2927)	-0.06	0.09	-0.06	0.01	0.04	0.93	-0.93	-0.92	1.00	-0.93	-0.92	-0.97	-0.46	-0.75	-0.32	-0.45	-0.24	-0.07	0.45	-0.36	-0.08	0.05	-0.32	-0.51
1741/1640	0.23	0.02	-0.04	0.17	0.14	-0.96	0.97	0.94	-0.93	1.00	1.00	0.96	0.54	0.81	0.33	0.44	0.10	0.16	-0.39	0.22	0.18	0.10	0.46	0.621
1740/1400	0.30	0.04	-0.06	0.23	0.20	-0.96	0.97	0.95	-0.92	1.00	1.00	0.96	0.59	0.83	0.37	0.48	0.11	0.12	-0.39	0.23	0.24	0.15	0.50	0.669
2852/1400	0.28	0.01	-0.04	0.18	0.17	-0.98	0.97	0.98	-0.97	0.96	0.96	1.00	0.63	0.85	0.46	0.59	0.29	-0.05	-0.45	0.41	0.34	0.12	0.50	0.681
1450/1539	0.86	0.19	-0.21	0.76	0.74	-0.69	0.67	0.74	-0.46	0.54	0.59	0.63	1.00	0.78	0.83	0.83	0.46	-0.50	-0.05	0.50	0.83	0.69	0.71	0.866
1240/1517	0.49	-0.13	0.11	0.48	0.29	-0.88	0.87	0.89	-0.75	0.81	0.83	0.85	0.78	1.00	0.66	0.75	0.38	-0.27	-0.28	0.48	0.47	0.31	0.46	0.646
1045/1545	0.70	0.10	-0.12	0.63	0.60	-0.52	0.50	0.57	-0.32	0.33	0.37	0.46	0.83	0.66	1.00	0.96	0.83	-0.79	0.14	0.82	0.75	0.72	0.52	0.629
1080/1550	0.65	0.05	-0.08	0.57	0.53	-0.62	0.59	0.67	-0.45	0.44	0.48	0.59	0.83	0.75	0.96	1.00	0.84	-0.79	-0.10	0.88	0.66	0.61	0.54	0.653
1060/1230	0.27	-0.04	0.01	0.21	0.21	-0.29	0.26	0.33	-0.24	0.10	0.11	0.29	0.46	0.38	0.83	0.84	1.00	-0.86	0.03	0.98	0.38	0.40	0.22	0.279
1170/1080	-0.51	-0.15	0.17	-0.40	-0.46	0.06	-0.03	-0.14	-0.07	0.16	0.12	-0.05	-0.50	-0.27	-0.79	-0.79	-0.86	1.00	-0.01	-0.83	-0.50	-0.52	-0.32	-0.29
1030/1080	0.05	-0.17	0.20	0.27	0.06	0.35	-0.36	-0.39	0.45	-0.39	-0.39	-0.45	-0.05	-0.28	0.14	-0.10	0.03	-0.01	1.00	-0.11	0.25	0.37	-0.29	-0.25
1080/1243	0.27	-0.08	0.04	0.20	0.19	-0.40	0.37	0.43	-0.36	0.22	0.23	0.41	0.50	0.48	0.82	0.88	0.98	-0.83	-0.11	1.00	0.36	0.36	0.25	0.342
1587/(1655+1548)	0.85	0.13	-0.13	0.88	0.74	-0.32	0.31	0.38	-0.08	0.18	0.24	0.24	0.83	0.47	0.75	0.66	0.38	-0.50	0.25	0.36	1.00	0.77	0.46	0.604
1156/1171	0.80	0.34	-0.33	0.73	0.80	-0.26	0.25	0.27	0.05	0.10	0.15	0.12	0.69	0.31	0.72	0.61	0.40	-0.52	0.37	0.36	0.77	1.00	0.57	0.545
1243/1314	0.75	0.72	-0.74	0.38	0.82	-0.54	0.53	0.59	-0.32	0.46	0.50	0.50	0.71	0.46	0.52	0.54	0.22	-0.32	-0.29	0.25	0.46	0.57	1.00	0.904
1453/1400	0.77	0.46	-0.47	0.52	0.74	-0.71	0.69	0.75	-0.51	0.62	0.67	0.68	0.87	0.65	0.63	0.65	0.28	-0.29	-0.25	0.34	0.60	0.55	0.90	1

**Supplementary Table 6:** Correlation matrix of intensity ratios taken from normalised infrared spectra of plasma samples. Green-shaded cells correspond to larger numbers, while the red-shaded cells correspond to low numbers.

	1635/1654	1546/1655	1655/(1655+1548)	1684/(1655+1548)	1515/(1655+1548)	2959/2931	(2855+2927)/(2962+2871)	(2851+2927)/(1655+1548)	1239/(2851+2927)	1741/1640	1740/1400	2852/1400	1450/1539	1240/1517	1045/1545	1080/1550	1060/1230	1170/1080	1030/1080	1080/1243	1587/(1655+1548)	1156/1171	1243/1314	1453/1400
1635/1654	1.00	0.41	-0.42	0.79	0.93	-0.38	0.37	0.47	-0.05	0.25	0.32	0.27	0.85	0.46	0.66	0.63	0.25	-0.51	-0.01	0.25	0.60	0.81	0.69	0.522
1546/1655	0.41	1.00	-1.00	-0.15	0.62	-0.10	0.10	0.16	0.01	0.07	0.07	0.04	0.18	-0.19	0.06	0.07	0.04	-0.18	-0.29	0.03	0.03	0.37	0.69	0.362
1655/(1655+1548)	-0.42	-1.00	1.00	0.16	-0.62	0.13	-0.12	-0.18	0.02	-0.09	-0.09	-0.06	-0.20	0.17	-0.08	-0.09	-0.06	0.20	0.31	-0.06	-0.05	-0.37	-0.70	-0.359
1684/(1655+1548)	0.79	-0.15	0.16	1.00	0.65	-0.20	0.20	0.27	0.09	0.13	0.21	0.16	0.88	0.47	0.58	0.51	0.13	-0.36	0.28	0.11	0.53	0.63	0.26	0.355
1515/(1655+1548)	0.93	0.62	-0.62	0.65	1.00	-0.27	0.26	0.36	0.05	0.16	0.23	0.21	0.70	0.25	0.58	0.53	0.24	-0.51	-0.02	0.21	0.38	0.80	0.81	0.638
2959/2931	-0.38	-0.10	0.13	-0.20	-0.27	1.00	-1.00	-0.98	0.92	-0.96	-0.96	-0.94	-0.69	-0.84	-0.55	-0.63	-0.34	0.16	0.36	-0.45	-0.31	-0.31	-0.51	-0.416
(2855+2927)/(2962+2871)	0.37	0.10	-0.12	0.20	0.26	-1.00	1.00	0.98	-0.92	0.96	0.96	0.93	0.67	0.84	0.53	0.61	0.31	-0.13	-0.36	0.42	0.31	0.30	0.49	0.396
(2851+2927)/(1655+1548)	0.47	0.16	-0.18	0.27	0.36	-0.98	0.98	1.00	-0.90	0.94	0.94	0.94	0.75	0.85	0.59	0.68	0.37	-0.23	-0.38	0.47	0.35	0.33	0.56	0.465
1239/(2851+2927)	-0.05	0.01	0.02	0.09	0.05	0.92	-0.92	-0.90	1.00	-0.93	-0.89	-0.90	-0.45	-0.70	-0.32	-0.44	-0.28	-0.01	0.43	-0.39	-0.18	0.01	-0.26	-0.211
1741/1640	0.25	0.07	-0.09	0.11	0.16	-0.96	0.96	0.94	-0.93	1.00	0.99	0.93	0.55	0.79	0.38	0.47	0.18	0.05	-0.37	0.28	0.19	0.15	0.42	0.374
1740/1400	0.32	0.07	-0.09	0.21	0.23	-0.96	0.96	0.94	-0.89	0.99	1.00	0.95	0.59	0.82	0.43	0.52	0.20	0.00	-0.36	0.29	0.16	0.19	0.49	0.476
2852/1400	0.27	0.04	-0.06	0.16	0.21	-0.94	0.93	0.94	-0.90	0.93	0.95	1.00	0.57	0.82	0.51	0.61	0.36	-0.17	-0.40	0.45	0.05	0.14	0.53	0.38
1450/1539	0.85	0.18	-0.20	0.68	0.70	-0.69	0.67	0.75	-0.45	0.55	0.59	0.57	1.00	0.73	0.80	0.80	0.45	-0.52	-0.09	0.50	0.73	0.72	0.60	0.463
1240/1517	0.46	-0.19	0.17	0.47	0.25	-0.84	0.84	0.85	-0.70	0.79	0.82	0.82	0.73	1.00	0.65	0.72	0.37	-0.32	-0.25	0.45	0.38	0.29	0.37	0.373
1045/1545	0.66	0.06	-0.08	0.58	0.58	-0.55	0.53	0.59	-0.32	0.38	0.43	0.51	0.80	0.65	1.00	0.96	0.83	-0.82	0.13	0.81	0.49	0.72	0.54	0.522
1080/1550	0.63	0.07	-0.09	0.51	0.53	-0.63	0.61	0.68	-0.44	0.47	0.52	0.61	0.80	0.72	0.96	1.00	0.84	-0.83	-0.11	0.87	0.46	0.64	0.57	0.533
1060/1230	0.25	0.04	-0.06	0.13	0.24	-0.34	0.31	0.37	-0.28	0.18	0.20	0.36	0.45	0.37	0.83	0.84	1.00	-0.86	0.01	0.98	0.25	0.44	0.35	0.341
1170/1080	-0.51	-0.18	0.20	-0.36	-0.51	0.16	-0.13	-0.23	-0.01	0.05	0.00	-0.17	-0.52	-0.32	-0.82	-0.83	-0.86	1.00	0.04	-0.84	-0.32	-0.58	-0.45	-0.399
1030/1080	-0.01	-0.29	0.31	0.28	-0.02	0.36	-0.36	-0.38	0.43	-0.37	-0.36	-0.40	-0.09	-0.25	0.13	-0.11	0.01	0.04	1.00	-0.13	0.08	0.26	-0.30	-0.16
1080/1243	0.25	0.03	-0.06	0.11	0.21	-0.45	0.42	0.47	-0.39	0.28	0.29	0.45	0.50	0.45	0.81	0.87	0.98	-0.84	-0.13	1.00	0.30	0.42	0.35	0.318
1587/(1655+1548)	0.60	0.03	-0.05	0.53	0.38	-0.31	0.31	0.35	-0.18	0.19	0.16	0.05	0.73	0.38	0.49	0.46	0.25	-0.32	0.08	0.30	1.00	0.57	0.04	-0.206
1156/1171	0.81	0.37	-0.37	0.63	0.80	-0.31	0.30	0.33	0.01	0.15	0.19	0.14	0.72	0.29	0.72	0.64	0.44	-0.58	0.26	0.42	0.57	1.00	0.57	0.394
1243/1314	0.69	0.69	-0.70	0.26	0.81	-0.51	0.49	0.56	-0.26	0.42	0.49	0.53	0.60	0.37	0.54	0.57	0.35	-0.45	-0.30	0.35	0.04	0.57	1.00	0.849
1453/1400	0.52	0.36	-0.36	0.36	0.64	-0.42	0.40	0.47	-0.21	0.37	0.48	0.58	0.46	0.37	0.52	0.53	0.34	-0.40	-0.16	0.32	-0.21	0.39	0.85	1

Supplementary References

1. Segelstein, D. J. The complex refractive index of water. (1981).

## 3.2 Electric-field molecular fingerprinting to probe human disease

**Preface:** The following work represents the first application of electric-field-resolved molecular fingerprinting to a real-world-problem, which is cancer detection in human blood sera. For our group and myself, taking this step from basic science to a biomedical application was a huge endeavour. The majority of our team never worked on any biomedical or clinical research questions before. This meant that we had to learn the basic and advanced practices and concepts of such research.

These included aspects of study design, sample collection, and establishing clinical collaborations. Although our group has had no experience in the field of serum diagnostics based on infrared spectroscopy, we were able to establish a new collaboration network with several clinical partners. Together, we developed standard operating procedures for the management of clinical information and the collection, handling, and storage of blood samples. This way, we collected over 3000 human serum samples from cancer patients as well as with samples from healthy individuals and benign controls over the last three years.

The measurements of the collected samples with the field-resolved spectrometer itself brought along further new challenges. It has already been a leap forward when we demonstrated that field-resolved spectroscopy (FRS) beats Fourier-transform infrared (FTIR) spectroscopy in terms of sensitivity. However, the ability to repeatedly perform reproducible, high-precision measurements on biological samples presented us with yet another additional degree of complexity, which we had to manage with a first-generation laboratory device. Most importantly, the instrument had to perform reliably over extended periods of time. A particularly great challenge was to capture the fingerprints in a way they could be compared with each other. This required omitting physical errors and batch effects as well as devising ways to properly process acquired data. Not only did we have to maintain precise control over the instrument parameters at all times, but we also had to develop appropriate data pre-processing routines for standardization of the datasets.

In addition, we had to ensure that sample handling and measurement procedures were controlled as much as possible to prevent them from having a major impact on the acquired infrared fingerprints. In order to obtain high-throughput capabilities, the human blood serum samples had to be delivered automatically and reproducibly. At the same time, the schedule of the individual team members who took part in the measurements had to be matched to the workflows of both sample preparation and warm-up phase of the laser in order to achieve the highest possible measurement efficiency.

Lastly, we learned a series of pitfalls when applying machine learning algorithms for analysis of highly complex infrared fingerprints to detect cancer. A machine learning algorithm can pick up almost any data feature that is contained in a specific dataset used for training. And such a feature is not necessarily linked or correlated with the actual medical condition. For example, the control group may consist only of women and the case group only of men. In this case, the algorithm may learn to distinguish between men and women. Therefore, when designing our study cohorts to perform relevant comparisons, we had to properly balance for age and gender. In addition, we had to keep in mind that any bias from sample collection or sample handling might be taken up by the algorithm. Therefore, we standardized as many of our operating procedures as possible and randomized the order of measurements to minimize

any potential bias.

But eventually, all our hard work has borne fruit. We successfully applied FRS to the analysis of over 300 individuals' samples in a clinical study involving lung, breast, and prostate cancer patients along with matched control individuals. Applying machine learning algorithms, we obtained detection efficiencies for all cancer entities in the range of 0.63-0.84 (area under the receiver operating characteristic curve). We also found that FRS detection efficiencies are higher than those obtained with conventional FTIR spectroscopy, suggesting that the increased sensitivity of the FRS method directly translates into better detection efficiency. Currently, we are planning further measurements to validate these findings with larger cohorts and to publish the results in a peer-reviewed journal. The following section reports on the initial study, representing a first version of the planned manuscript.

# Electric-field molecular fingerprinting to probe human disease

**Preprint version (2020)**

[98]

*by*

Marinus Huber, Kosmas Kepesidis, Liudmila Voronina, Wolfgang Schweinberger, Michael Trubetskov, Cristina Leonardo, Daniel Gerz, Markus Pötzlberger, Syed A. Hussain, Ioachim Pupeza, Frank Fleischmann, Christian Stief, Jürgen Behr, Nadia Harbeck, Abdallah Azzeer, Maximillian Reiser, Ferenc Krausz, and Mihaela Žigman

**Contributions:** I took part in designing and conducting the study as well as in performing the subsequent experiments and evaluations. I wrote the majority of the manuscript.

## Electric-field molecular fingerprinting to probe human disease

M. Huber<sup>1,2</sup>, K. V. Kepesidis<sup>1</sup>, L. Voronina<sup>1</sup>, W. Schweinberger<sup>1,3</sup>, M. Trubetskov<sup>2</sup>,  
C. Leonardo<sup>1,2</sup>, D. Gerz<sup>1,2</sup>, M. Poetzlberger<sup>1</sup>, S. A. Hussain<sup>1</sup>, I. Pupeza<sup>1</sup>, F. Fleischmann<sup>1,4</sup>,  
C. Stief<sup>5</sup>, J. Behr<sup>6</sup>, N. Harbeck<sup>7</sup>, A. Azzeer<sup>3</sup>, M. Reiser<sup>8</sup>, F. Krausz<sup>1,2,4,†</sup> and M. Zigman<sup>1,2,4,†</sup>

<sup>1</sup> Ludwig Maximilians University Munich (LMU), Department of Laser Physics, Garching, Germany;

<sup>2</sup> Max Planck Institute of Quantum Optics (MPQ), Laboratory for Attosecond Physics, Garching, Germany;

<sup>3</sup> King Saud University (KSU), Department of Physics and Astronomy, Riyadh, Saudi Arabia;

<sup>4</sup> Center for Molecular Fingerprinting (CMF), Budapest, Hungary;

<sup>5</sup> University Hospital of the Ludwig Maximilians University Munich (LMU), Department of Urology;

<sup>6</sup> University Hospital of the Ludwig Maximilians University Munich (LMU), Department of Internal Medicine V, Comprehensive Pneumology Center; Member of the German Center for Lung Research;

<sup>7</sup> University Hospital of the Ludwig Maximilians University Munich (LMU), Department of Obstetrics and Gynecology, Breast Cancer and Comprehensive Cancer Center Munich (CCLMU);

<sup>8</sup> University Hospital of the Ludwig Maximilians University Munich (LMU), Department of Clinical Radiology.

<sup>†</sup> These authors have contributed equally to this work.

**A multitude of medical phenotypes are mirrored in human biofluids<sup>1-4</sup>. Robust, sensitive and parallel detection of molecules across different species carries the potential to improve current clinical diagnostics<sup>4-6</sup>. Here we present the first biomedical application of field-resolved laser spectroscopy (FRS)<sup>7</sup> as a new cross-molecular analytical method for electric-field molecular blood profiling with time-efficient workflows enabling high-throughput applications. In a proof-of-concept clinical study, we applied first-generation FRS to probe bulk liquid human blood sera from more than three hundred individuals, capturing rapidly oscillating infrared electric fields emitted simultaneously from all molecular species in the wake of an ultra-brief excitation. Machine learning algorithms enabled isolation of infrared signatures instructive for distinguishing therapy-naïve non-metastatic breast, prostate, and lung carcinoma from those of carefully-matched control individuals. Detection efficiencies in the range of 0.63-0.84 (area under the ROC curve, AUC) systematically exceed those obtained with Fourier-transform infrared spectroscopy applied to the same samples. The reported data build evidence that the coherent electric fields emanating from impulsively excited biomolecules in blood can be captured as informative “electric-field-resolved molecular fingerprints” (EMFs). Beyond contributing to the detection of cancer, they are likely to provide, more generally, a new framework for future phenotyping of biofluids.**

The way human cells, organs and bodies function is governed by the molecular composition of their contents. Multiple human phenotypes, as well as aberrations such as disease, are reflected by the molecular composition of biofluids, like circulating blood, and its cell-free phase - serum and plasma, respectively<sup>1-4</sup>. Although there is an enormous medical need for complementing current tissue biopsy-driven diagnostics with time- and cost-efficient non-invasive approaches, the challenge for modern omics-technologies still lies in achieving reproducible and robust multi-molecular detection and interpretation<sup>4,8,9</sup>. Highly sensitive and specific analytical approaches in the fields of proteomics<sup>9-11</sup>, metabolomics<sup>12,13</sup>, and genomics<sup>14-16</sup> have led to the discovery of numerous biomarker candidates. However, current omics-based identification of new candidates is limited by the set of molecular species and changes thereof that can be probed with a reasonably manageable analytical setup, ideally within a single measurement.

There is an orthogonal approach - *molecular fingerprinting*. Here, phenotype detection is based on the patterns of changes within the entire molecular landscape<sup>2,17</sup>. If that very pattern is specific enough to a state, it may contribute to the detection of a given physiology/phenotype. Differences in patterns of e.g. peptides and metabolites reflected in the spectra obtained with mass spectrometry (MS)<sup>18</sup> and nuclear magnetic resonance (NMR)<sup>19</sup> spectroscopy have shown

potential for disease detection. The combination of different omics approaches, with each targeting a specific molecular species, like proteins, metabolites etc., briefly multi-omics<sup>4,5</sup>, holds promise to improve diagnostics capabilities. However, this still requires complex and target-specific sample preparation as well as elaborate ways combining different data sets<sup>4-6,8</sup>. Broadband vibrational spectroscopy<sup>20</sup> addresses these issues by measuring the entire molecular landscape in a single cross-molecular fingerprint. Numerous studies have shown the potential of blood-based infrared spectroscopic molecular fingerprinting for disease detection<sup>21-24</sup>. Their limited sensitivity, however, restricted molecular fingerprinting to highly abundant components so far<sup>25</sup>. We recently demonstrated that field-resolved spectroscopy (FRS) is able to overcome this limitation<sup>7</sup>.

Here we report the first biomedical application of electric-field-resolved fingerprinting, a novel concept based on time-resolved measurement of the coherent electric fields emanating from vibrating molecules impulsively-excited by ultrashort infrared pulses<sup>7</sup>. We demonstrate that phenotypic snapshots of liquid blood serum can be robustly acquired from the resulting infrared *electric-field molecular fingerprint* (EMF). We find that infrared EMFs from sera enable efficient detection of lung cancer. Moreover, even in its very first implementation, FRS substantially improved the detection efficiency of breast and prostate cancer as compared to conventional Fourier-transform infrared (FTIR) spectroscopy, which had matured over decades.

#### **Infrared electric-field molecular fingerprinting of human blood serum**

Infrared vibrational spectroscopy interrogates the vibrational response of molecular bonds to optical excitation. It accesses the frequency, phase, and strength of the vibrational modes, which are specific to the molecule(s) under scrutiny and may hence allow their identification and quantification<sup>26</sup>. For complex human bioliquids, infrared electric fields emitted by thousands of different types of molecules add up coherently to form the sample's overall EMF. It delivers a pattern that reflects the sample's molecular landscape across all species. The larger the detection dynamic range, the larger the number of molecules contributing to the measured EMF and thus, the greater the depth of analysis. This may result in a more specific and sensitive detection of abnormal physiologies.

In conventional infrared absorption (e.g. FTIR) spectroscopy, the molecular fingerprints are measured by capturing time-integrated signals. Thus, weak signals of low abundant molecules may be buried in the noise of the detector and/or excitation, restricting the analysis to highly abundant molecules<sup>7,25</sup>. By contrast, FRS relies on the sudden, impulsive excitation of molecular vibrations and direct sampling of the infrared electric field emanating from the sample<sup>7,27</sup>. Because the coherent molecular response survives the ultra-brief excitation, FRS can isolate the EMF and measure it directly in a temporal window that can be free from any excitation and hence also from its noise. By this, sensitivity limitations imposed by source noise and detector dynamic range can be avoided. As a result, FRS has – already in its first implementation – outperformed state-of-the-art FTIR in sensitivity, with a detectable molecular concentration range in complex biofluids from >50 mg/ml to several hundred ng/ml<sup>7</sup>.

In the current study, we tested the new technology for medically relevant blood profiling in a prototypical clinical setting, assessing the usefulness of EMFs as a source of complementary information for cancer diagnostics. We evaluated the efficiency of electric-field fingerprinting of bulk liquid blood sera to distinguish non-metastatic (TNM stage II and III), therapy-naïve, lung, prostate and breast cancer patients (case cohorts) from age-, gender and smoking-status-matched individuals with benign conditions of the same organ (organ-specific control cohorts) as well as matched non-symptomatic healthy references (healthy control cohorts), see Fig. 1a and Extended Data Table 1. Blood samples were drawn and processed according to well-defined standard operating procedures (see Methods) to minimize pre-analytical error (Fig. 1 b).



An automated sample delivery system was applied for high-throughput electric-field fingerprinting of 329 liquid sera (Fig. 1c). The samples were excited by broadband (940-1515  $\text{cm}^{-1}$  at -20 dB intensity) mid-infrared laser pulses with a duration of 90 fs (full width at intensity half maximum) (Fig. 2a, top panel), and the molecular response was recorded with electro-optic sampling<sup>7</sup>. The acquired EMFs were used to train a machine-learning algorithm for binary classifications of the samples (Fig. 1d, e) into case and control groups.

In what follows, we discuss the characteristic properties and analyses of EMFs using the lung cancer cohort as an example. The same tools and procedures have also been applied to the two other cancer entities.

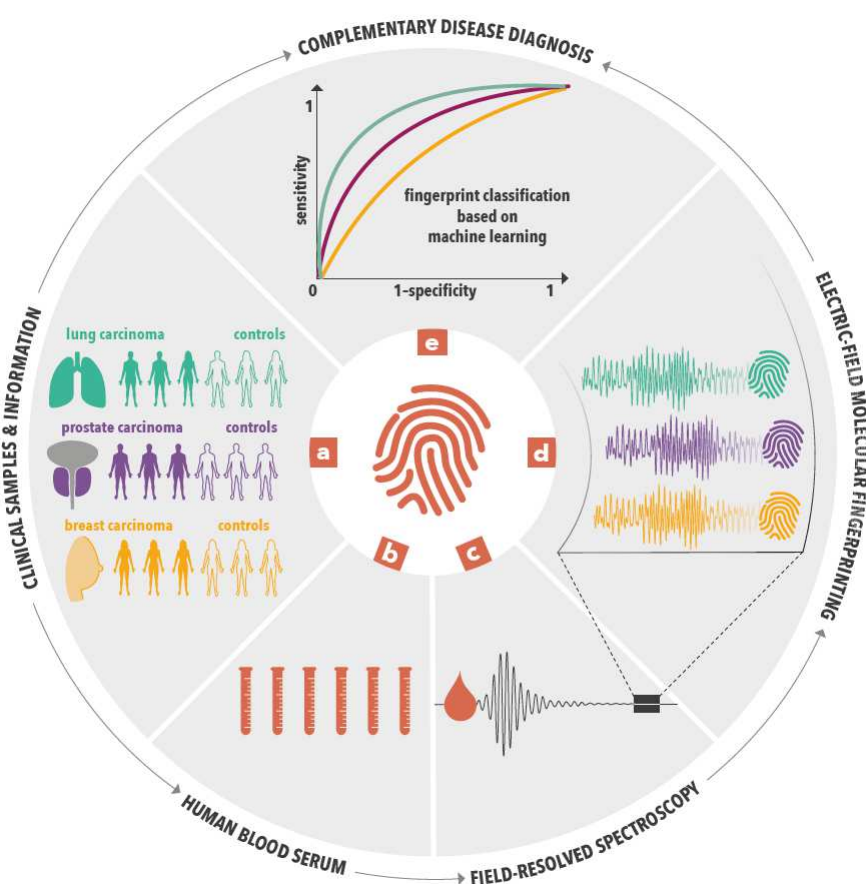


**Fig. 1 | Electric-field molecular fingerprinting workflow and clinical study design.** **a**, Designing balanced, matched cohorts of three cancer entities (lung, prostate, and breast carcinoma) at therapy naïve, non-metastatic stage and organ-specific control individuals for case-control studies. **b**, Blood samples from all individuals were drawn and sera prepared according to well-defined standard operating procedures. **c**, Field-resolved spectroscopy of liquid bulk blood sera were used to obtain **d**, electric-field molecular fingerprints (EMFs). **e**, Machine learning models were built on training data sets and evaluated on test data sets to separately evaluate the efficiency of classification for each of the three cancer entities.

### Electric-field molecular fingerprints

EMFs of serum samples were obtained from 56 lung cancer patients and 96 control subjects by subtracting the recorded signal from a water reference from that of the samples (Fig. 2a). To capture the benefits of FRS, it is instructive to analyse the EMFs in different time windows: one coinciding with the excitation and others opening later.

During the time span of the excitation pulse, no substantial differences between case and control group could be discerned (Fig. 2b). The same phenomenon was observed in the spectral domain (Fig. 2c, upper panel), as reflected by non-significant p-values for case-control separation higher than  $10^{-2}$  (Fig 2c, lower panel). Possible small differences in the EMFs that might result from variations of the molecular composition tend to be masked by intensity fluctuations of the strong excitation. Although Fourier-transformation of the entire electric field trace emitted by the sample preserves the molecular information, it also transfers the excitation noise to the spectral domain. This reflects an unfavourable measurement condition, characteristic of time-integrating spectroscopic techniques.

In contrast, FRS can circumvent this noise contribution, by allowing isolated analysis of the EMFs in a temporal window opening sufficiently late (at  $t_{opening}$ ) after the impulsive excitation (see Methods). Should there be any differences between the EMFs of case and control individuals, they offer the best chance to be observed after the (noisy) excitation disappeared and the molecular signal prevails. Figure 2b' indeed reveals significant differences between 900 fs and 1200 fs after the excitation pulse. A Fourier analysis of the EMFs temporally filtered with  $t_{opening} = 200$  fs and  $t_{opening} = 900$  fs elucidate spectral domains in which the spectral components of the EMFs from the case and control samples were robustly distinguishable with p-values of  $<10^{-10}$  (Fig. 2c' and c'', lower panel), eight orders of magnitude below those of Fig. 2c.

In conventional vibrational spectroscopy, distinct peaks in the acquired absorbance spectra can be assigned to chemical bonds and functional groups<sup>26,28</sup>. However, the number of possible assignments is limited by the spectral coverage and the width of the absorption peaks. Time-resolved spectra may provide much richer information. For small values of  $t_{opening}$ , the resulting time-filtered spectra and associated p-values yield fairly broad features (Fig. 2c), while for later times the features become narrower with their central frequency shifting (Fig. 2c' and c''). This is because vibrations associated with broad absorption peaks decay faster than those with narrow absorption peaks<sup>29</sup>. Consequently, with the temporal window opening later, vibrational modes with long-lived coherence characterized by narrow-band signatures prevail. EMFs may thus give direct access to a larger variety of spectral features, potentially serving as spectral markers associated with a particular condition (e.g. lung cancer). Further investigation of the unique information content of these time-resolved spectral markers is required to gain improved insight into the molecular origin of differences between case and control fingerprints.

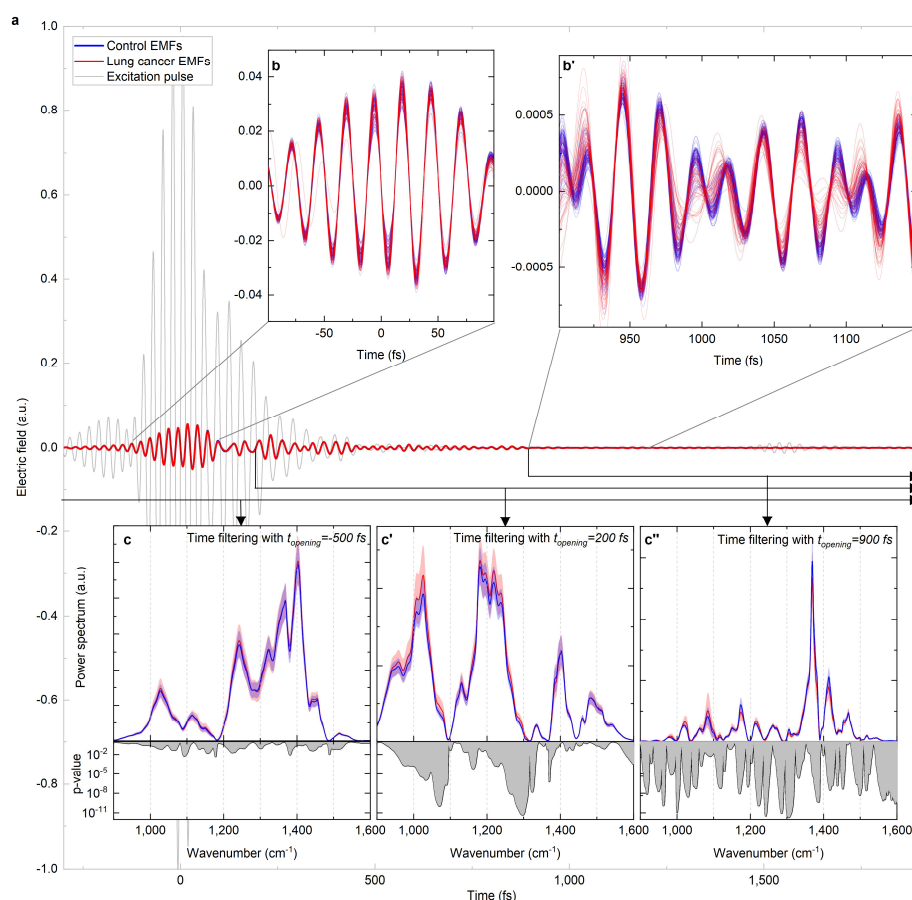


**Fig. 2 | Electric-field fingerprints of human blood sera.** *a*, Infrared electric field emanating from serum samples of control subjects (blue lines) and non-small-cell lung cancer patients (red lines), upon being excited by a few-cycle mid-infrared laser pulse (grey line). EMFs of serum samples were obtained by subtracting the recorded signal from a water reference from that of the samples. *b*, *b'*, Close-ups of case and control traces for selected time windows. *c*, *c'*, *c''* (upper traces), Power spectra of the EMFs upon transmission through a high-pass-time-filter with  $t_{\text{opening}} = -500$  fs, 200 fs and 900 fs, respectively. The two-tailed  $p$ -value of the Student's  $t$ -test between controls and lung cancer cases are depicted in the lower panels.

### Lung cancer detection

We implemented binary classification between (lung) cancer and controls by applying a support vector machine (SVM)<sup>30</sup> algorithm to the EMFs. The data was split into train and test sets, employing a 10-times repeated 10-fold cross validation. For assessing the efficiency of cancer detection, we evaluated the resulting area under the curve (AUC) of the respective receiver operating characteristic (ROC) curves for the test sets.

As discussed above, quality and information content of the recorded EMFs for case-control separation strongly depend on the selected time interval. Although a complex, optimized algorithm should be able to pick up all defining features without pre-processing (e.g. temporal

filtering) of the measured EMFs, this applies only if enough data for training are available<sup>31</sup>. Due to the limited size of our data set, we chose to perform a numerical search for identifying the optimum time window prior to classification (see Methods and Supplementary Information Section 2). This was found to span from 1050 fs to 1550 fs after the excitation, yielding an AUC of 0.84. In Fig. 3a, we depict the corresponding ROC curve (black line). To access whether our model overfits the training set, we compare the model's performance on both the train (red ROC curve) and test set (black ROC curve). The fact that the two ROC curves are nearly identical, implies that the derived model is not sensitive to small fluctuations in the training set and is therefore reliable.

Further analysis shows that the classification efficiency depends on the tumour size: models trained on T4 non-small-cell lung cancer (NSCLC) patients with larger tumours yielded an AUC about 15% higher than models trained on T3 patients with smaller tumours (Fig. 3b). This suggests that the information retrieved from the measured differences between case and control EMFs may be dominated by tumour-related signals. A larger tumour load may itself give rise to more extensive molecular changes, or larger tumours could have imposed a higher systemic response, or a combination of both may be leading to higher efficiency of detecting larger tumours.

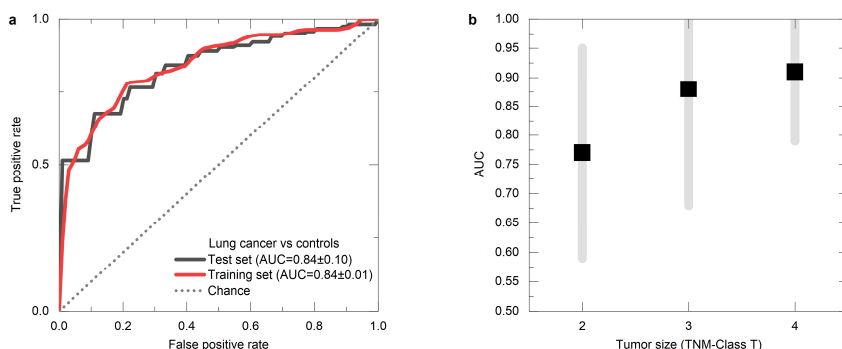


**Fig. 3 | Lung cancer detection efficiency.** *a*, ROC curve for the binary classification of infrared electric-field molecular fingerprints with SVM models (for a time window spanning from 1050 fs to 1550 fs after the excitation) of blood sera from 56 therapy naïve, non-metastatic non-small cell lung cancer (NSCLC) versus 96 reference individuals (either non-symptomatic healthy, COPD or lung hamartoma individuals). *b*, Classification efficiency (AUC, grey bars depict standard deviation) is higher in patients bearing tumours with larger diameter. T2, T3 and T4 are corresponding to 3-5 cm, 5-7 cm or > 7 cm tumour diameter, respectively. The prospective cohort did not encompass any patients with T1 tumours to be evaluated.

To identify spectral regions of EMFs most relevant for NSCLC detection, we analysed the Fourier-transformed data of the optimized time window (see also Supplementary Information Section 3). We trained Random Forest<sup>32,33</sup> models and evaluated the resulting Gini importance across the spectral range used for differentiating between the groups. We found five spectral regions of high Gini importance, marking the frequency components of the EMFs, which most significantly contributed to the classification of NSCLC (Fig. 4 left panels, Supplementary Information Section 3).

Lung cancer is often accompanied by chronic obstructive pulmonary disease (COPD). Thus, we tested whether electric-field fingerprinting, as a modality, could possibly identify any NSCLC-specific signatures, independently of COPD. Towards that end, we separated individuals from the above analysis into sub-cohorts with subjects negative (Fig. 4b, b') and positive (Fig. 4c, c') for COPD. Although NSCLC detection was less efficient in the presence

of COPD, with an AUC value dropping to 0.77 (Fig. 4c), we found three of the five spectral regions previously identified as dominant in NSCLC classification to remain instructive for classifying COPD-positive NSCLC cases vs. COPD-positive age- and gender-matched control individuals. The specificity of these three regions for the presence of NSCLC in the organism is further corroborated by the fact that they do not contribute to the classification of COPD versus non-symptomatic, healthy individuals (Fig. 4d).

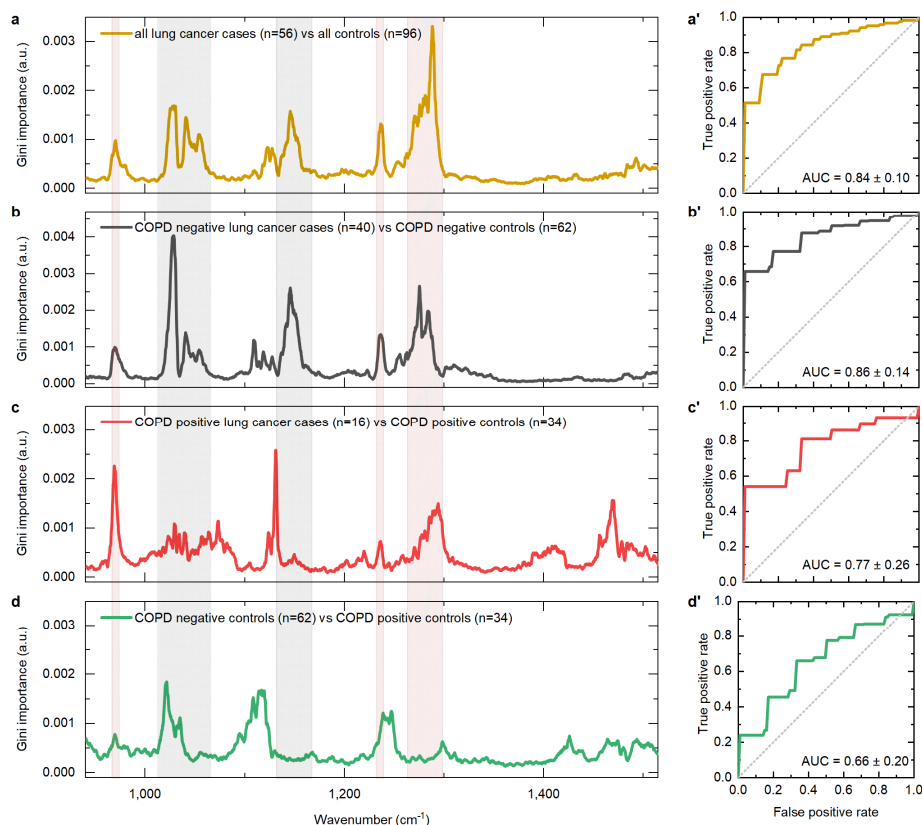


**Fig. 4 | Isolation of NSCLC infrared electric-field fingerprint regions.** (a, b, c, d) Comparison of the Gini importance across spectral fingerprints for binary classification related to different conditions. The shaded areas depict five regions of high Gini importance relevant for the classification of non-small-cell lung cancer (a). Three of the five regions (red shaded areas) are also observed when only consider COPD-negative or COPD-positive cohorts (b, c), but do not contribute to the classification of COPD-negative controls vs. COPD-positive controls (d). (a', b', c', d') ROC curves depicting the classification performance of linear SVM-based models. The plots show the mean and standard deviation of the distribution of ROC curves resulting from a repeated randomized procedure (10 times) of a 10-fold cross-validation. The mean AUC values and the corresponding standard deviation are shown in the inset.

### Reproducibility of electric-field fingerprinting

To test the robustness and technical reproducibility of electric-field fingerprinting, we prepared a second (replicate) aliquot of a randomly-selected subset of the lung cancer cohort consisting of 56 samples (26 cases, 30 controls) to serve as a hold-out test set. This fully-independent set was measured 16 months after the first measurement campaign (Supplementary Information Section 4). An SVM-based model was trained on the EFM of the remaining 96 samples (30 cases, 65 controls) from the first measurement set. Thereby, a numerical standardization procedure was applied to all EMFs to account for changes in the instrument setting. The trained model yielded a classification efficiency (AUC) of 0.83 (Extended Data Fig. 3), comparable to that obtained by a data set acquired in one and the same measurement campaign. This not only provides an additional confirmation of the reliability of the derived models, but also further delivers evidence for the feasibility of combining measurements obtained at different times in different measurement campaigns with differing instrumentation. These are essential prerequisites for large-scale studies – involving several measurement sites over several years – as well as for the real-world setting of using a previously-trained model for classification of independent samples at later times.

### Capacity to detect different cancer entities

To evaluate whether FRS has any capability of detecting cancer entities other than lung carcinoma, we performed analyses of blood sera from patients with prostate and breast cancer along with separate age- and gender-matched, organ-specific controls for each cancer entity.

Classification models trained on therapy-naïve, non-metastatic breast and prostate cancer (and matched controls) yielded AUCs of 0.63 and 0.70, respectively (Table 1). Overall, we found that lung, breast, and prostate cancer leave their dominant marks in different time windows and different regions of the time-filtered EMF spectra (Supplementary Information Section 4). This indicates that primary cancer entities of different origin tend to induce differing changes in the EMFs of blood sera.

To benchmark our approach against conventional infrared spectroscopy, we analysed the same sample set with a state-of-the-art FTIR spectrometer (Methods and Supplementary Information Section 5). For comparing the electric-field fingerprinting classification performance with that of FTIR-based fingerprinting, we confined FTIR spectroscopy to the same spectral region covered by our FRS instrument, resulting only in a small difference in FTIR-based classification efficiency (Supplementary Information Section 6). By this approach, we found that FRS yields higher AUC values for all three cancer entities. Whilst progress in lung cancer detection remains within statistical uncertainty, advances are evident for prostate and breast cancer, none of which can be detected by FTIR (Table 1). This is a first experimental indication that the improved molecular sensitivity of EMFs directly translates into higher efficiency in distinguishing medical phenotypes.

**Table 1 | Cancer detection accuracy**, in terms of area under the curve (AUC), of different cancer entities by FRS vs. FTIR fingerprinting. The results are based on EMFs from optimized time windows (Supplementary Information Section 4). The classification was performed using linear SVM based models but similar results can be obtained using Logistic Regression.

Cancer cohort (# cases / # controls)	Lung Cancer (56 / 96)	Prostate Cancer (41 / 79)	Breast Cancer (42 / 41)
Electric-field-resolved fingerprinting	0.84	0.70	0.63
FTIR fingerprinting	0.83	0.55	0.55

### Conclusions and outlook

Here, we show that electric-field-resolved molecular fingerprints (EMFs) harbour information instructive to identify human pathophysiological phenotypes. Analysing the non-cellular fraction of blood (serum) in a prototypical clinical study, EMFs allow to detect therapy-naïve and non-metastatic cancer types, a notoriously difficult medical problem<sup>34</sup>.

Our data put forward electric-field-resolved spectroscopy as a new molecular fingerprinting approach, where information of organismal states - systemic phenotypes - can be comparatively derived from oscillating infrared electric fields emitted after an ultra-brief laser pulse. The technique permits capturing a snapshot of the ensemble of chemical bonds, covering all types of biomolecules in the highly complex blood serum sample. In addition, our approach obviates the necessity to detect different types of analytes with several separate instruments or separate pre-analytical steps that all can potentially introduce analytical error. These makes electric-field-resolved fingerprinting inherently suited for robust high-throughput applications. Additionally, we have shown that EMF-based classification is still feasible for samples that were measured more than one year after the data for training of the classifier were recorded. Both aspects (high-throughput and cross-comparability over time) are pre-requisites for the application in a medical setting.

A major advantage of EMFs is that they reflect changes in the “*multi-omic landscapes*” of bioliquids. Such changes are potentially based on the heterogeneity of cancer growth<sup>35–37</sup> that might project into bioliquids, and that can be collectively captured by electric-field-resolved fingerprinting. Despite the fact that vibrational spectroscopy, in general, provides to some extent the possibility to relate spectral differences to changes in concentration of individual molecules, this is inherently not the aim of this study. Towards that end, further molecular analyses (e.g. infrared chemometrics<sup>25</sup>, complementary proteomics or metabolomics) will be necessary to understand the molecular nature underpinning the EMFs. Instead, this approach focuses on evaluating whether EMFs detected are robust and specific to a given disease.

Although we have made a first step towards identifying patterns of EMFs specific to different cancer entities, we need to acknowledge that their reproducibility is yet to be verified in future large-scale clinical studies with independent validation data sets. For assessing the generalizability of EMFs on a population scale, it will be further instructive to address the effect of a variety of confounding factors contributing to EMFs, and to test populations from multiple medical centres and additional relevant control groups.

Other analytical approaches are being predominantly molecule- and gene-centric. While they provide quantitative information on molecules of known identity, this is at the expense of complex analytical workflows. Although their integration into multi-omics analyses are progressing, the complexity of combining and analysing different datasets remains challenging<sup>4,38,39</sup>. And even though other multi-analyte, omics and multi-omics techniques for blood-based cancer detection have already yielded high detection accuracies<sup>2,3,40–44</sup>, our study reveals a simple, time- and cost-effective, label-free approach that, already in its first biomedical implementation, shows promising efficiencies for detection of common non-metastatic malignancies providing possible grounds.

The future of electric-field molecular fingerprinting holds promise for further improving sensitivity and specificity. Technical advances towards increasing the capacity to probe additional functional groups by extending spectral coverage<sup>45–47</sup>, and towards enhancing detection sensitivity to capture low-abundant molecules are both under way. The general paradigm of the reported approach could well be extended as a complementary tool for systemic phenotyping of cancer and potentially also other human physiologies.

## Methods and Materials

### Clinical study participants

We performed a multicentric, prospective study on three cancer entities (lung cancer, breast cancer and prostate cancer), including subjects with corresponding benign conditions as well as healthy volunteers. Participants provided informed written consent for the study under research study protocol # 17-182 approved by the Ethics Committee of the Ludwig-Maximillan-University (LMU) of Munich. Our study complies with all relevant ethical regulations and informed consent was obtained from all participants. The following clinical centres were involved in subject recruitment and sample collections of the prospective clinical study: Department of Internal Medicine V for Pneumology, Urology Clinic, Department of Obstetrics and Gynaecology, Breast Cancer and Comprehensive Cancer Centre Munich (CCLMU), all affiliated with the LMU. The Asklepios clinic (Gauting), and the Comprehensive Pneumology Centre (CPC) Munich were further study sites in Germany.

Analyses focus only on subjects with clinically confirmed carcinoma of lung, prostate or breast at the TNM stage II, and III<sup>48</sup>, with no metastases, prior to any cancer-related therapy, and without any other cancer occurrence. Healthy controls were non-symptomatic individuals, without any history of cancer, not suffering from any cancer-related disease nor being under any medical treatment.

Lung cancer cases were compared to matched individuals from the following groups: Chronic obstructive pulmonary disease (COPD), pulmonary hamartoma or healthy individuals matched for gender, age and smoking status. As a reference condition for the prostate cancer age-, gender- and smoking-status-matched either benign prostate hyperplasia (BPH) patients or healthy, non-symptomatic individuals were chosen. For breast cancer age-, gender, and smoking-status-matched healthy, non-symptomatic subjects were compared. Full breakdown of all participants is listed in Extended Data Table 1.

### Blood sample collection and preparation

Blood samples were collected, processed and stored using previously defined standard operating procedures: Blood draws were all performed using Safety-Multifly needles of 21G (Sarstedt) into 4.9 ml serum, centrifuged at 2.000 g for 10 minutes at 20 °C, aliquoted and frozen at -80°C within 3 hours from the time of sampling. All samples were thawed, further aliquoted for measurement and re-frozen at -80°C to ensure a constant number of freeze-thaw cycles before analysis. Before any measurement, serum aliquots were thawed at room temperature, shaken for 20 s, and spun down again. Measurements of liquid sera were performed using an automated sample delivery system for high-throughput electric-field fingerprinting. Samples were measured in a random order to avoid systematic effects during data evaluation. To measure and track experimental errors (Supplementary Information Section 7) during the measurement campaign<sup>49</sup>, quality control (QC) samples from pooled human serum (BioWest, Nuaille, France) were measured after each 5 samples. One measurement sequence contained up to 40 samples resulting in measurement time of up to 3 h.

### Electric-field fingerprinting measurements

The electric-field-resolved molecular fingerprint (EMF) measurements were performed with a spectrometer described in detail in our previous work.<sup>7</sup> Automated liquid sample handling and cleaning of the measurement cuvette was implemented with the same commercially-available autosampler (micro-biolytics GmbH) as in the FTIR measurements (see also below). Each serum sample measurement was preceded by a reference measurement on blank water and followed by automatic cleaning of the cuvette to avoid any residue or takeover. Each electric-



field trace – obtained either from reference or sample measurement – was recorded within an 8.3-ps time window (corresponding to a spectral resolution of  $4\text{ cm}^{-1}$ ) over a total measurement time of 45 s. Including the time required for sample exchange and cleaning of the cuvette, the total measurement time for one single serum sample took approximately 4 minutes.

#### **Preprocessing of EMFs**

In order to compensate for drifts of the time axis and pulse intensity between different measurements, we first performed time adjustments of pulse positions, setting the peak of the excitation to time 0 fs. Next, the energy of all excitation pulses was normalised to one. Then we minimized the discrepancy between different pulses by varying a time offset parameter. The time-domain EMFs were acquired by subtracting the reference (i.e. water) from the corresponding sample measurement. Time-filtered data was obtained by setting the recorded time-traces to 0 before  $t_{opening}$  and after  $t_{end}$ . If  $t_{end}$  is not stated, the endpoint of the recorded time-trace was considered. For the analysis in the frequency domain we performed Fourier transform of the data using fast Fourier transform algorithm.

#### **Standardization of EMFs**

For comparison between measurements taken at different times or different instrument configuration, we applied a numerical standardization procedure to the EMFs. First, a reliable and uniform subset of reference measurements was selected, and averaged reference pulse was obtained. It is considered as a standardized reference pulse. Second, all datasets were converted to the frequency domain using fast Fourier transform algorithm. Third, for each of the reference spectra a transformation converting its spectrum to the spectrum of the standardized reference pulse was obtained and applied for also for the sample measurement corresponding to this reference. This procedure converts all reference spectra to the standardized reference pulse spectrum, and all samples spectra to spectra excited by the same excitation. Last, with the help of the inverse Fourier transform standardized sample and reference pulses were represented in time domain.

#### **FTIR measurements and data pre-processing**

The spectroscopic measurements were performed with an automated FTIR device (MIRA-Analyzer, micro-biolytics GmbH) with a flow-through transmission cuvette ( $\text{CaF}_2$  with  $8\text{ }\mu\text{m}$  path length). The spectra were acquired with a resolution of  $4\text{ cm}^{-1}$  and an averaging time of 45 s to ensure a fair comparison with the EMF measurements. After sample exchange a water reference spectrum was measured to reconstruct the infrared absorption spectra. For the pre-processing of FTIR fingerprints we tested different recommendations from prior works<sup>24,50</sup>. In our case, normalization of all spectra (using either  $L_1$  or  $L_2$  norm) yielded highest classification performance. Currently, the spectral coverage of our FRS device ( $940\text{-}1515\text{ cm}^{-1}$ ) is much less than that of a state-of-the-art FTIR spectrometer. Thus, for the comparison between FTIR and FRS, all spectra were truncated to  $940\text{-}1515\text{ cm}^{-1}$ .

#### **Classification models**

The data analysis was performed using Scikit-Learn (v. 0.20.3), in Python (v.3.6.8). We trained classification models based on three algorithms: logistic regression, linear SVM and random forests. We evaluated the performance with a repeated (10-times) stratified 10-fold cross validation and its visualization using the notion of the receiver operating characteristic (ROC) curve. As an overall metric for model performance, we use the area under the ROC curve (AUC).

### Time-domain optimization of the classification models

To identify the most informative parts of the time traces, we numerically slide filters of different sizes across the entire length of the time traces and evaluate the performance (AUC) of the SVM classification (Supplementary Information Section 2). As a criterion for the optimization we defined a measure for the amount of overfitting given by the difference between the average AUC values for the train and test sets (in cross validation). A classification was considered reliable if and only if the amount of overfitting did not exceed the standard deviation of the distribution of AUC values for a given time window. From all time windows for which this requirement was satisfied, we eventually selected the one yielding the highest AUC.

### Gini importance and feature selection

Using random forests classification models with 10k decision trees we evaluated the Gini importance<sup>32,33</sup> of each feature. This enabled us to identify informative regions along the spectra, by ranking the features in terms of their relevance to a particular binary-classification problem. In addition, using the spectral features associated with the local maxima of the Gini importance as a base, we performed feature selection by recursively scoring all features using SVM models (see Supplementary Information Section 3). This allowed us to isolate the minimal number of spectral markers that yield optimal classification.

### Model evaluation using cross validation

For the evaluation of the performance of machine-learning models and for assessing the levels of overfitting, all models considered in this work were tested on hold-out test sets, which were not used for model building. Due to limited size of the data sets considered, no single train-test splits were used but instead multiple splits under k-fold cross validation. The reasoning behind this choice is that in cases of limited data sets, single train-test splits lead to very small test sets that lead to high variance in the estimated performance. This problem can be overcome by simulating the effect of a larger test set using repeated k-fold cross validation<sup>51</sup>.

### References

1. Chen, R. *et al.* Personal Omics Profiling Reveals Dynamic Molecular and Medical Phenotypes. *Cell* **148**, 1293–1307 (2012).
2. Kulasingam, V. & Diamandis, E. P. Strategies for discovering novel cancer biomarkers through utilization of emerging technologies. *Nat. Clin. Pract. Oncol.* **5**, 588–599 (2008).
3. Cohen, J. D. *et al.* Detection and localization of surgically resectable cancers with a multi-analyte blood test. *Science* (80-. ). **359**, 926–930 (2018).
4. Karczewski, K. J. & Snyder, M. P. Integrative omics for health and disease. *Nat. Rev. Genet.* **19**, 299–310 (2018).
5. Hasin, Y., Seldin, M. & Lusis, A. Multi-omics approaches to disease. *Genome Biol.* **18**, 83 (2017).
6. Yoo, B. C., Kim, K.-H., Woo, S. M. & Myung, J. K. Clinical multi-omics strategies for the effective cancer management. *J. Proteomics* **188**, 97–106 (2018).
7. Pupeza, I. *et al.* Field-resolved infrared spectroscopy of biological systems. *Nature* **577**, 52–59 (2020).
8. Malone, E. R., Oliva, M., Sabatini, P. J. B., Stockley, T. L. & Siu, L. L. Molecular profiling for precision cancer therapies. *Genome Med.* **12**, 8 (2020).
9. Geyer, P. E. *et al.* Plasma Proteome Profiling to detect and avoid sample-related biases in biomarker studies. *EMBO Mol. Med.* **11**, 1–12 (2019).
10. Geyer, P. E., Holdt, L. M., Teupser, D. & Mann, M. Revisiting biomarker discovery by plasma

- proteomics. *Mol. Syst. Biol.* **13**, 942 (2017).
11. Uzozie, A. C. & Aebersold, R. Advancing translational research and precision medicine with targeted proteomics. *J. Proteomics* **189**, 1–10 (2018).
  12. Xia, J., Broadhurst, D. I., Wilson, M. & Wishart, D. S. Translational biomarker discovery in clinical metabolomics: An introductory tutorial. *Metabolomics* **9**, 280–299 (2013).
  13. Roig, B. *et al.* Metabolomics reveals novel blood plasma biomarkers associated to the BRCA1-mutated phenotype of human breast cancer. *Sci. Rep.* **7**, 17831 (2017).
  14. Han, X., Wang, J. & Sun, Y. Circulating Tumor DNA as Biomarkers for Cancer Detection. *Genomics. Proteomics Bioinformatics* **15**, 59–72 (2017).
  15. Schwarzenbach, H., Hoon, D. S. B. & Pantel, K. Cell-free nucleic acids as biomarkers in cancer patients. *Nat. Rev. Cancer* **11**, 426–437 (2011).
  16. Abbosh, C. *et al.* Phylogenetic ctDNA analysis depicts early-stage lung cancer evolution. *Nature* **545**, 446–451 (2017).
  17. Goodacre, R., Vaidyanathan, S., Dunn, W. B., Harrigan, G. G. & Kell, D. B. Metabolomics by numbers: acquiring and understanding global metabolite data. *Trends Biotechnol.* **22**, 245–252 (2004).
  18. Borrebaeck, C. A. K. Precision diagnostics: moving towards protein biomarker signatures of clinical utility in cancer. *Nat. Rev. Cancer* **17**, 199–204 (2017).
  19. Smolinska, A., Blanchet, L., Buydens, L. M. C. & Wijmenga, S. S. NMR and pattern recognition methods in metabolomics: From data acquisition to biomarker discovery: A review. *Anal. Chim. Acta* **750**, 82–97 (2012).
  20. Baker, M. J. *et al.* Using Fourier transform IR spectroscopy to analyze biological materials. *Nat. Protoc.* **9**, 1771–91 (2014).
  21. Sala, A. *et al.* Biofluid diagnostics by FTIR spectroscopy: A platform technology for cancer detection. *Cancer Lett.* **477**, 122–130 (2020).
  22. Butler, H. J. *et al.* Development of high-throughput ATR-FTIR technology for rapid triage of brain cancer. *Nat. Commun.* **10**, 1–9 (2019).
  23. Paraskevaïdi, M. *et al.* Differential diagnosis of Alzheimer’s disease using spectrochemical analysis of blood. *Proc. Natl. Acad. Sci.* 201701517 (2017). doi:10.1073/pnas.1701517114
  24. Ollesch, J. *et al.* An infrared spectroscopic blood test for non-small cell lung carcinoma and subtyping into pulmonary squamous cell carcinoma or adenocarcinoma. *Biomed. Spectrosc. Imaging* **5**, 129–144 (2016).
  25. Perez-Guaita, D., Garrigues, S. & De La, M. Infrared-based quantification of clinical parameters. *TrAC - Trends Anal. Chem.* **62**, 93–105 (2014).
  26. Griffiths, P. R. & De Haseth, J. A. *Fourier Transform Infrared Spectrometry*. **171**, (John Wiley & Sons, 2007).
  27. Kowligy, A. S. *et al.* Infrared electric field sampled frequency comb spectroscopy. *Sci. Adv.* **5**, eaaw8794 (2019).
  28. Movasaghi, Z., Rehman, S. & ur Rehman, D. I. Fourier Transform Infrared (FTIR) Spectroscopy of Biological Tissues. *Appl. Spectrosc. Rev.* **43**, 134–179 (2008).
  29. Laubereau, a & Kaiser, W. Vibrational dynamics of liquids and solids investigated by picosecond light pulses. *Rev. Mod. Phys.* **50**, 607–665 (1978).
  30. Cortes, C. & Vapnik, V. Support-vector networks. *Mach. Learn.* **20**, 273–297 (1995).
  31. Liu, J. *et al.* Deep convolutional neural networks for Raman spectrum recognition: a unified solution. *Analyst* **142**, 4067–4074 (2017).
  32. Menze, B. H. *et al.* A comparison of random forest and its Gini importance with standard chemometric methods for the feature selection and classification of spectral data. *BMC Bioinformatics* **10**, 213 (2009).
  33. Genuer, R., Poggi, J.-M. & Tuleau-Malot, C. Variable selection using random forests. *Pattern Recognit. Lett.* **31**, 2225–2236 (2010).
  34. Etzioni, R. *et al.* The case for early detection. *Nat. Rev. Cancer* **3**, 243–252 (2003).
  35. McGranahan, N. & Swanton, C. Clonal Heterogeneity and Tumor Evolution: Past, Present, and the Future. *Cell* **168**, 613–628 (2017).
  36. Cieslik, M. & Chinnaiyan, A. M. Global genomics project unravels cancer’s complexity at unprecedented scale. *Nature* **578**, 39–40 (2020).
  37. Boyle, E. A., Li, Y. I. & Pritchard, J. K. An Expanded View of Complex Traits: From

- Polygenic to Omnigenic. *Cell* **169**, 1177–1186 (2017).
38. Tyanova, S. & Cox, J. Perseus: A Bioinformatics Platform for Integrative Analysis of Proteomics Data in Cancer Research. in *Cancer Systems Biology: Methods and Protocols* (ed. von Stechow, L.) 133–148 (Springer New York, 2018). doi:10.1007/978-1-4939-7493-1\_7
  39. Paczkowska, M. *et al.* Integrative pathway enrichment analysis of multivariate omics data. *Nat. Commun.* **11**, 1–16 (2020).
  40. Geyer, P. E. *et al.* Plasma Proteome Profiling to Assess Human Health and Disease. *Cell Syst.* **2**, 185–195 (2016).
  41. Anfossi, S., Babayan, A., Pantel, K. & Calin, G. A. Clinical utility of circulating non-coding RNAs — an update. *Nat. Rev. Clin. Oncol.* **15**, 541–563 (2018).
  42. Sajic, T. *et al.* Similarities and Differences of Blood N-Glycoproteins in Five Solid Carcinomas at Localized Clinical Stage Analyzed by SWATH-MS. *Cell Rep.* **23**, 2819–2831.e5 (2018).
  43. Xu, R. *et al.* Extracellular vesicles in cancer — implications for future improvements in cancer care. *Nat. Rev. Clin. Oncol.* **15**, 617–638 (2018).
  44. Yurkovich, J. T., Tian, Q., Price, N. D. & Hood, L. A systems approach to clinical oncology uses deep phenotyping to deliver personalized care. *Nat. Rev. Clin. Oncol.* **17**, 183–194 (2020).
  45. Butler, T. P. *et al.* Multi-octave spanning, Watt-level ultrafast mid-infrared source. *J. Phys. Photonics* **1**, 044006 (2019).
  46. Wang, Q. *et al.* Broadband mid-infrared coverage (2–17  $\mu\text{m}$ ) with few-cycle pulses via cascaded parametric processes. *Opt. Lett.* **44**, 2566 (2019).
  47. Hofer, C. *et al.* Quantum-Efficiency and Bandwidth Optimized Electro-Optic Sampling. in *2019 Conference on Lasers and Electro-Optics Europe & European Quantum Electronics Conference (CLEO/Europe-EQEC)* 1–1 (IEEE, 2019). doi:10.1109/CLEO-EQEC.2019.8873083
  48. Amin, M. B. *et al.* *AJCC Cancer Staging Manual*. (Springer, 2017).
  49. Sangster, T., Major, H., Plumb, R., Wilson, A. J. & Wilson, I. D. A pragmatic and readily implemented quality control strategy for HPLC-MS and GC-MS-based metabolomic analysis. *Analyst* **131**, 1075–1078 (2006).
  50. Trevisan, J. J., Angelov, P. P., Carmichael, P. L., Scott, A. D. & Martin, F. F. L. Extracting biological information with computational analysis of Fourier transform infrared (FTIR) biospectroscopy datasets: current practices to future perspectives. *Analyst* **137**, 3202–3215 (2012).
  51. Kohavi, R. A Study of Cross-Validation and Bootstrap for Accuracy Estimation and Model Selection. *Int. Jt. Conf. Artif. Intell.* (1995).

**Author contributions:**

M.Z. conceived the study. M.H., F.K. designed experiments. M.Z., F.K., M.R. initiated the clinical collaborations. J.B., C. S., N. H. led clinical activities. L.V., M.H. defined the study cohorts. M.H., W.S., L.V., C.L., D.G. performed the measurements. W.S., M. P., M.T., S.A.H., D.G. optimized the measurement device. K.V.K., M.H., L.V. performed data analysis. K.V.K. performed the machine-learning engineering. M.T. performed the experimental data preprocessing. I.P., M.H., W.S., S.A.H., A. A., F.K. performed and supported the instrument development. F.F. devised and supervised sample preparation workflows. M.H., F.K., M.Z., K.V.K. wrote the manuscript. All authors have discussed the results and contributed to the finalization of the manuscript.

**Acknowledgments:**

We would like to thank Sigrid Auweter, Stefan Jungblut, Jacqueline Hermann and Inna Koch for management of the clinical study; Katja Leitner, Sabine Eiselen, Beate Rank for collecting clinical samples; Matthias Uieberacker, Tarek Eissa, Eric Griessinger for help with arranging the clinical database; Daniel Meyer for preparation of samples for measurements; Ernst Fill and Ianina Kosse for valuable contributions to the experiments; Gabrielle Multhoff for help initializing the experiments; Alexander Zigman Kohlmaier for insightful discussions and critical comments.

## Supplementary Information

### Electric-field molecular fingerprinting to probe human disease

M. Huber<sup>1,2,\*</sup>, K. V. Kepesidis<sup>1</sup>, L. Voronina<sup>1</sup>, W. Schweinberger<sup>1,3</sup>, M. Trubetskov<sup>2</sup>,  
C. Leonardo<sup>1,2</sup>, D. Gerz<sup>1,2</sup>, M. Poetzlberger<sup>1</sup>, S. A. Hussain<sup>1</sup>, I. Pupeza<sup>1</sup>, F. Fleischmann<sup>1,4</sup>,  
C. Stief<sup>5</sup>, J. Behr<sup>6</sup>, N. Harbeck<sup>7</sup>, A. Azzeer<sup>3</sup>, M. Reiser<sup>8</sup>, F. Krausz<sup>1,2,4,\*†</sup> & M. Zigman<sup>1,2,4,\*†</sup>

<sup>1</sup> Ludwig Maximilians University Munich (LMU), Department of Laser Physics, Garching, Germany;

<sup>2</sup> Max Planck Institute of Quantum Optics (MPQ), Laboratory for Attosecond Physics, Garching, Germany;

<sup>3</sup> King Saud University (KSU), Department of Physics and Astronomy, Riyadh, Saudi Arabia;

<sup>4</sup> Center for Molecular Fingerprinting (CMF), Budapest, Hungary;

<sup>5</sup> University Hospital of the Ludwig Maximilians University Munich (LMU), Department of Urology;

<sup>6</sup> University Hospital of the Ludwig Maximilians University Munich (LMU), Department of Internal Medicine V, Comprehensive Pneumology Center; Member of the German Center for Lung Research;

<sup>7</sup> University Hospital of the Ludwig Maximilians University Munich (LMU), Department of Obstetrics and Gynecology, Breast Cancer and Comprehensive Cancer Center Munich (CCLMU);

<sup>8</sup> University Hospital of the Ludwig Maximilians University Munich (LMU), Department of Clinical Radiology.

† These authors have contributed equally to this work.

### Section 1: Breakdown of participants of the clinical study

We performed a prospective clinical study to evaluate the feasibility of detecting cancer by means of field-resolved spectroscopy (FRS) of impulsively-excited vibrations of the biomolecules contained in human blood. To this end, blood serum was prospectively collected from individuals from either being primarily diagnosed with a single carcinoma or belonging to the following control groups of individuals. The total number of all cancer patients from all three cancer entities is 139, and the number of all control individuals, without any malignant condition, is 190. In sum this prospective study investigated blood sera of 329 unique individuals. Note that some of the control individuals were used for multiple comparisons of different cancer cohorts (Extended Data Table 1).

Extended Data Table 1 | Participant cohort breakdown

	Breast cancer cohort		Lung cancer cohort				Prostate cancer cohort		
	Breast cancer patients (BCa cases)	Non-symptomatic, healthy individuals	Non-small-cell lung cancer (NSCLC) (LCa cases)	Patients with chronic obstructive pulmonary disease (COPD) without LCa	Lung hamartoma patients	Non-symptomatic, healthy individuals	Prostate cancer patients (PCa cases)	Benign prostate hyperplasia (BPH) patients	Non-symptomatic, healthy individuals
Number	42	41	21	26	35	35	41	40	39
Average age	58	57	63	64	64	62	63	64	63
% female	100	100	43	35	43	40	0	0	0
% active smokers	26	29	43	19	46	46	20	15	21
% ex-smokers	21	20	24	77	40	37	39	43	36
% TNM stage II	81	n/a	29	n/a	n/a	n/a	39	n/a	n/a
% TNM stage III	19	n/a	71	n/a	n/a	n/a	61	n/a	n/a

## Section 2: Methods for optimizing EMF-based classification

In order to identify regions of the time traces informative for disease detection, we trained classification models using linear SVM on different time windows of differing sizes and locations, spanning the entire time window incorporating the EMF signal. The results presented here refer to lung cancer but the procedures described remain the same when analysing the EMFs for the other cancer entities. We then evaluate the average AUC using 10 times repeated 10-fold cross validation (Extended Data Fig. 1 a) and the amount of overfitting (Extended Data Fig. 1 b), given by the difference between the resulting average AUC of the train and test set.

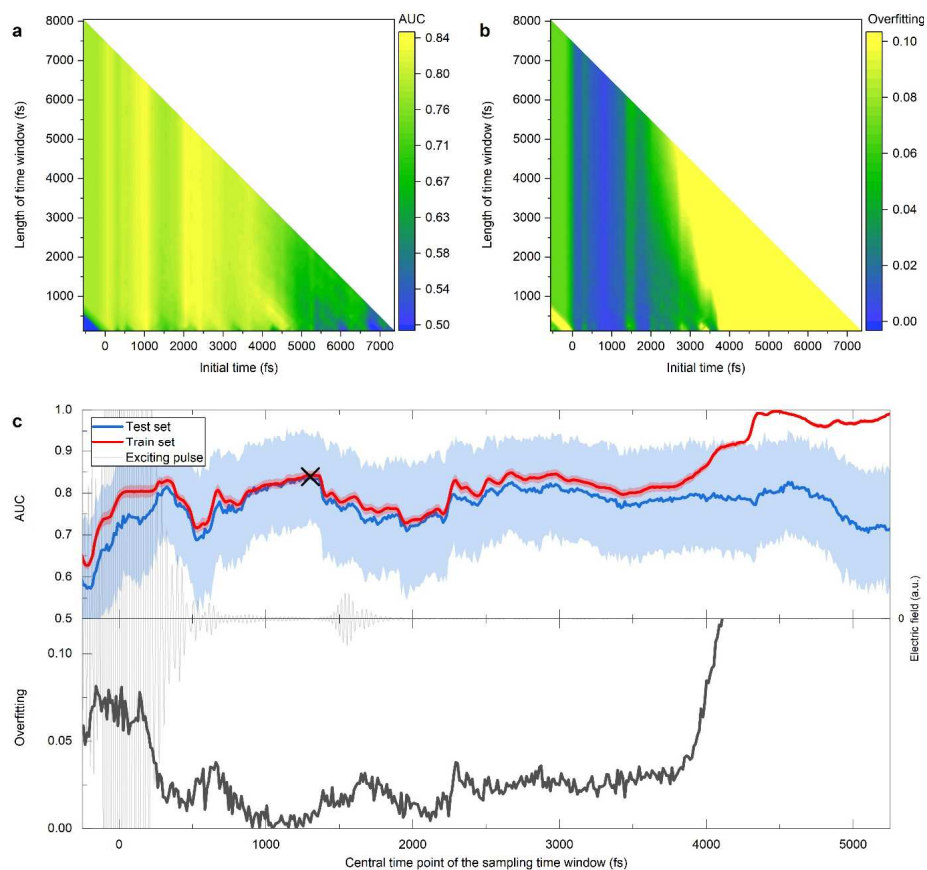
As displayed by the yellow stripe in the left bottom corner of Extended Data Fig. 1b, there is strong overfitting as long the excitation pulse has large overlap with the sampling window. This is a consequence of the fact that reading out the molecular signal in this temporal domain is plagued by substantial noise carried by the excitation pulse, as discussed in the main text. Sliding a temporal window of 495-fs duration across the entire EMF measured reveals the same behaviour, as shown on the lower panel of Extended Data Fig. 1 c. The overfitting initially decreases for increasing delay of the sliding window due to a decrease of noise with decreasing excitation signal. The temporary increases at delays around 500-700 fs and 1500-1700 fs coincide with increased background noise due to post pulses (caused by spurious reflections) depicted by the grey line in Extended Data Fig. 1c. A sampling time window starting at  $t_{opening} = 1050$  fs yields highest classification performance that corresponds to an AUC of 0.84 (Fig. 3b). Towards later times, the coherent molecular signal decays and results in an increase of overfitting and decrease of classification performance.

## Section 3: EMF spectral markers for non-small-cell lung cancer detection

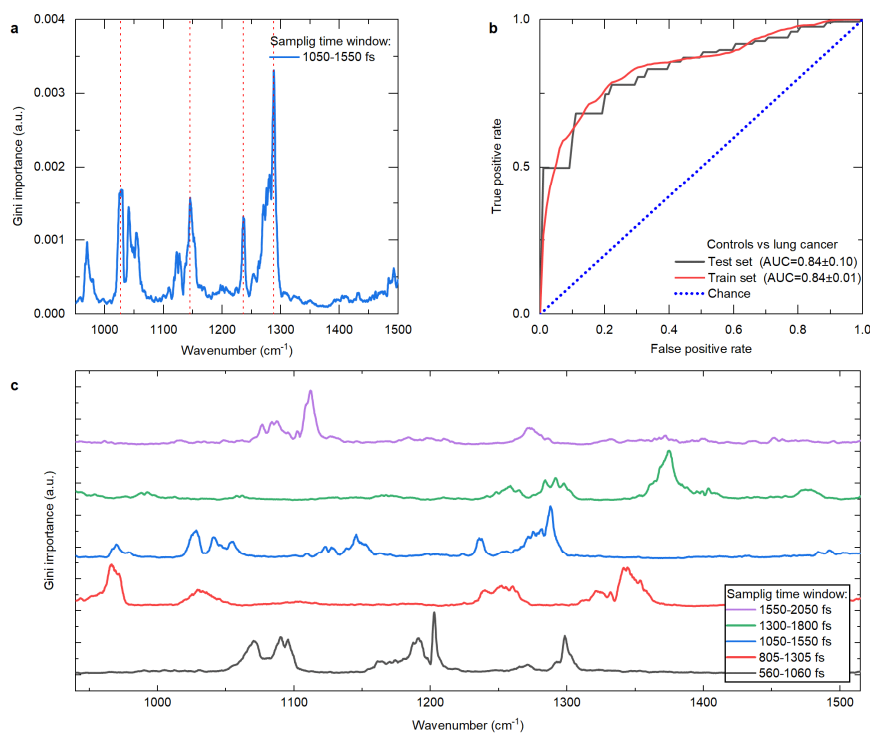
To identify spectral regions of EMFs most relevant for NSCLC detection, we analysed the Fourier-transformed data of the optimized time-window (1050 - 1550 fs for the lung cancer cohort). We derived the binary-classification-based Gini importance in the frequency domain using a Random Forest classification model with 10k estimators (Extended Data Fig. 2 a). We identified the frequencies that are associated with all local maxima of the Gini importance and used them as potential candidates of informative features. To find the optimal set of these feature (the most informative combination), we performed feature selection with a method called recursive-feature elimination using an SVM for repeated classification. This selection procedure results in a set of 4 features, located at 1054, 1145, 1236, and 1288  $\text{cm}^{-1}$ , depicted by dashed lines in Extended Fig. 2a. Using these four features for classification, an AUC of 0.84 (Extended Data Fig. 2 b) was achieved. This is identical to the value acquired by direct classification in the time domain for the same (optimized) time window with all the information contained in it. Hence, the four spectral markers identified capture the majority of cancer-specific signals contributing to classification.

As discussed in the main part of the paper, vibrations associated with broad absorption peaks decay faster in time than those with narrow absorption peaks. Therefore, analysing time-filtered spectra may give direct access to a different set of spectral features in dependence of the chosen time-window. Analysing the Gini importance for displaced time-intervals we found that the peaks appeared at different wavenumbers (Extended Data Fig 2 c) - potentially giving access to disease-related molecular information from different origin. However, the unique information content of these spectral markers needs further investigation in order to trace them back to their molecular origin and fully utilize the potential they possibly offer for further improving classification.





**Extended Data Fig. 1 | Time-domain optimization.** **a**, Colour plot depicting the dependence of the classification performance (AUC) on the selection of the sampling time window. The y axis corresponds to the initial time while the x axis to the length of the sampling time window. The colour indicates the AUC value **b**, Colour plot depicting the amount of overfitting as function of the initial time and the length of the sampling time window. The black cross indicates the time window yielding the highest AUC of 0.84. **c**, AUC and the overfitting condition respectively for a sliding time window of 500 fs.



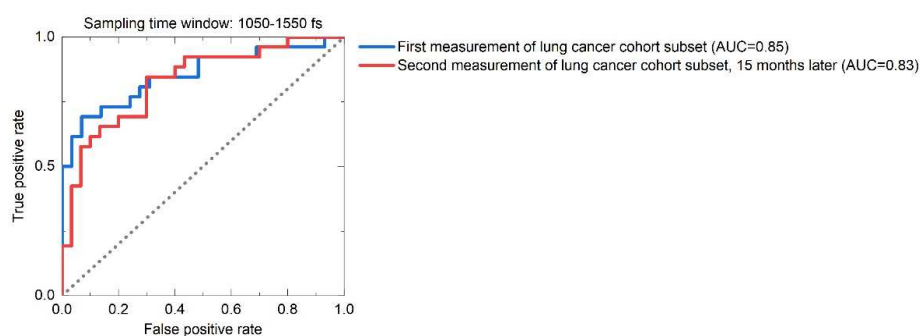
**Extended Data Fig. 2 | Spectral feature extraction and classification in the frequency domain. a,** Gini importance for the optimized time window for the detection of lung cancer. Dashed lines indicate the four spectral features that result in the optimal classification. **b,** ROC displaying the classification performance of an SVM model, based on the four optimal spectral features. **c,** Gini importance for five different sampling time windows.

#### Section 4: Reproducibility of measurements and classification over time

To evaluate the stability and technical reproducibility of our measurements, procedures and whole approach over time, we measured a second aliquot, replicate of randomly selected subset of the non-small-cell lung cancer cohort (26 cases, 30 controls) that had been initially measured one and a half year after the first measurement campaign. As these data were not integrated into initial analyses, they lend themselves for the purposes of a “true” hold-out test set. To this end, we use the fingerprints of the remaining 96 samples (30 cases, 65 controls) recorded in the first measurement campaign for training our NSCLC classification algorithm. The classifier trained this way is then used to analyse the fingerprints of the hold-out test sets, recorded in the first and the second measurement campaign. The resulting ROC curves, plotted in blue and red, respectively, are shown in Extended Data Fig. 3. Their AUC values of 0.85 and 0.83 are equivalent within the confidence intervals of the evaluations.

We would like to emphasize, that for the second round of measurements we purposely changed key parts of the FRS instrument, including dispersion compensation in the infrared pulse compressor and parameters of the nonlinear crystal used for electro-optic sampling of the infrared pulses transmitted through the samples. Therefore, the second set of measurements can be considered as to be acquired by a different instrument. In order to be able to merge and compare the two datasets, we newly devised a standardization procedure and applied it to all EMFs (see Methods).

The comparability of (A) the AUCs from the classifications with a hold-out test set (Extended Data Fig. 3) with that obtained a 10-times repeated 10-fold cross validation (Fig. 3) and (B) with each other from the first and the second measurement campaign has several important implications. (A) provides yet another confirmation of the reliability of the derived models. (B) demonstrates the possibility to combine measurements obtained with different versions of FRS instruments at different times. Both points are a prerequisite for large-scale studies over years involving several measurement sites.

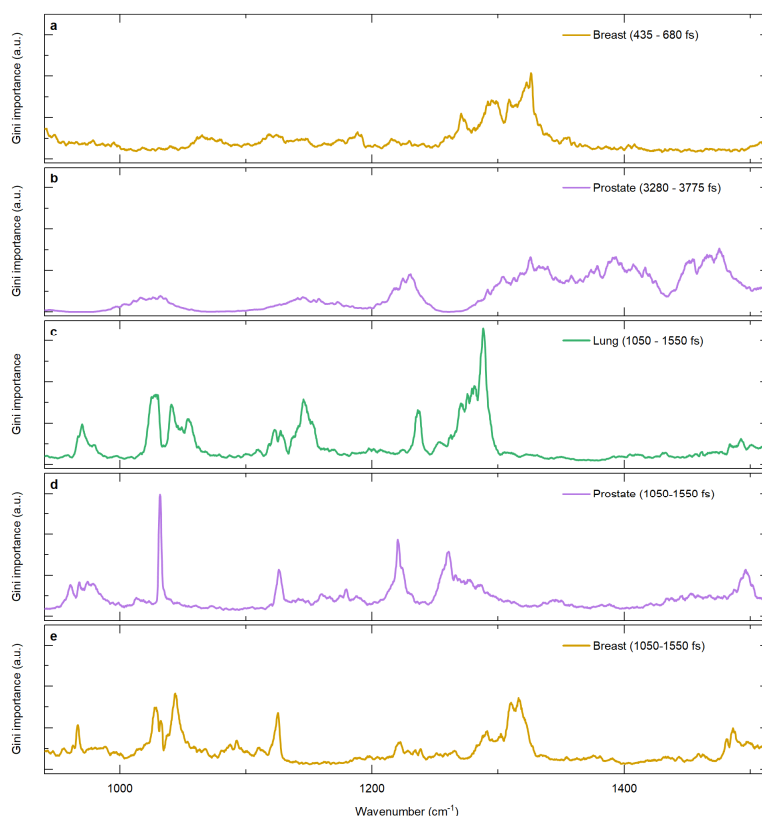


**Extended Data Fig. 3 | Reproducibility of classification over time.** ROC curve showing the classification performance of linear SVM-based models on a randomly-selected hold-out test set of 56 samples (26 cases, 30 controls), as measured in the first measurement campaign (orange curve) and one and a half year later in the second measurement campaign (blue curve). The resulting AUC values are 0.85 and 0.83 respectively. The train set consists only of measurements from the original campaign.

### Section 5: EMF spectral markers for all three cancer entities

Optimal sampling time window for EMF-based detection of each cancer entity was identified as explained in the Methods and described in more detail in the Supplementary Section 2. We found that lung, breast and prostate cancer leave their strongest marks on the EMF of blood sera in different temporal portions of EMF traces, requiring the selection of differing sampling time windows for maximizing the detection efficiency of the different cancer entities. These three different sampling time windows are as follows: breast cancer analysis: 435 - 680 fs, lung cancer analysis: 1050-1550 fs, prostate cancer analysis: 3280-3775 fs. The Gini importance of frequency components contributing to the classification has been once again evaluated in the same way as for Fig. 4 and Extended Data Fig. 2, this time for the above three sampling time windows, respectively. The results are summarized in Extended Data Fig. 4 a-c.

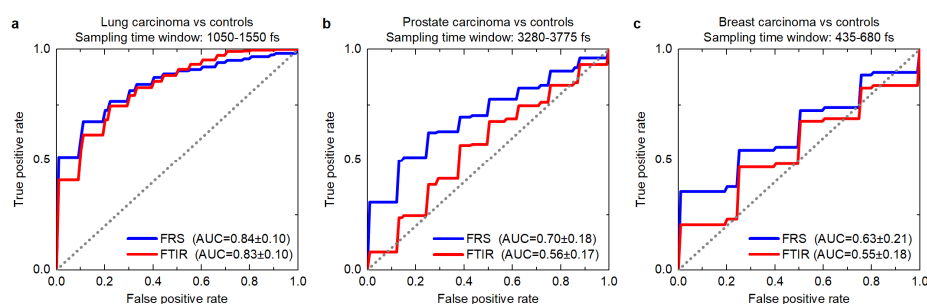
In addition, we compared the Gini importance for a common sampling time window of 1050-1550 fs. The obtained patterns (Extended Data Fig 4 c-d) differ significantly even under these unified conditions of analysis. These findings suggest that primary cancer entities of different origin induce significantly differing changes in the overall molecular landscape of blood sera. Its reflection in EMF holds promise for not only detecting but also classifying different cancer entities via electric-field molecular fingerprinting.



**Extended Data Fig. 4 | Gini importance for each studied cancer entity in the Fourier domain. a, b, c Breast, prostate and lung cancer derived from time-filtered spectra with the respective optimum time window indicated in the figure panels. c, d, e Gini importance of breast, prostate and lung cancer for time-filtered spectra between 1050 fs and 1550 fs.**

## Section 6: Classification efficiency for FRS and FTIR

To cross-compare the efficiency of detecting different cancer entities, as well as to directly evaluate and benchmark FRS against FTIR, here we list all ROC curves related to the AUC values mentioned in the main part of the paper. In the Extended Data Fig. 5, each panel depicts the two ROC curves for a case-control cohort (binary classification) for both FRS (blue line) and FTIR data (red line). In all cases, classification was performed using linear SVM and the ROC curves were evaluated using 10 time repeated 10-fold cross validation. It needs to be noted that similar results can be obtained also using logistic-regression models.



**Extended Data Fig. 5 | List of ROC curves for all cohorts. a lung cancer, b prostate cancer c breast cancer.**

## Section 7: Influence of spectral coverage on FTIR data

In order to be able to compare the classification efficiency when using the FRS data to these of FTIR, we have reduced the spectral range from  $930 - 3050 \text{ cm}^{-1}$  to  $940 - 1515 \text{ cm}^{-1}$ , which is the range of the FRS. In the Extended Data Table 3, we report the results for the FTIR evaluation using linear SVM for the full range i.e.  $930 - 3050 \text{ cm}^{-1}$  and present the resulting AUCs for 10x10-fold cross validation.

**Extended Data Table 3 | FTIR**

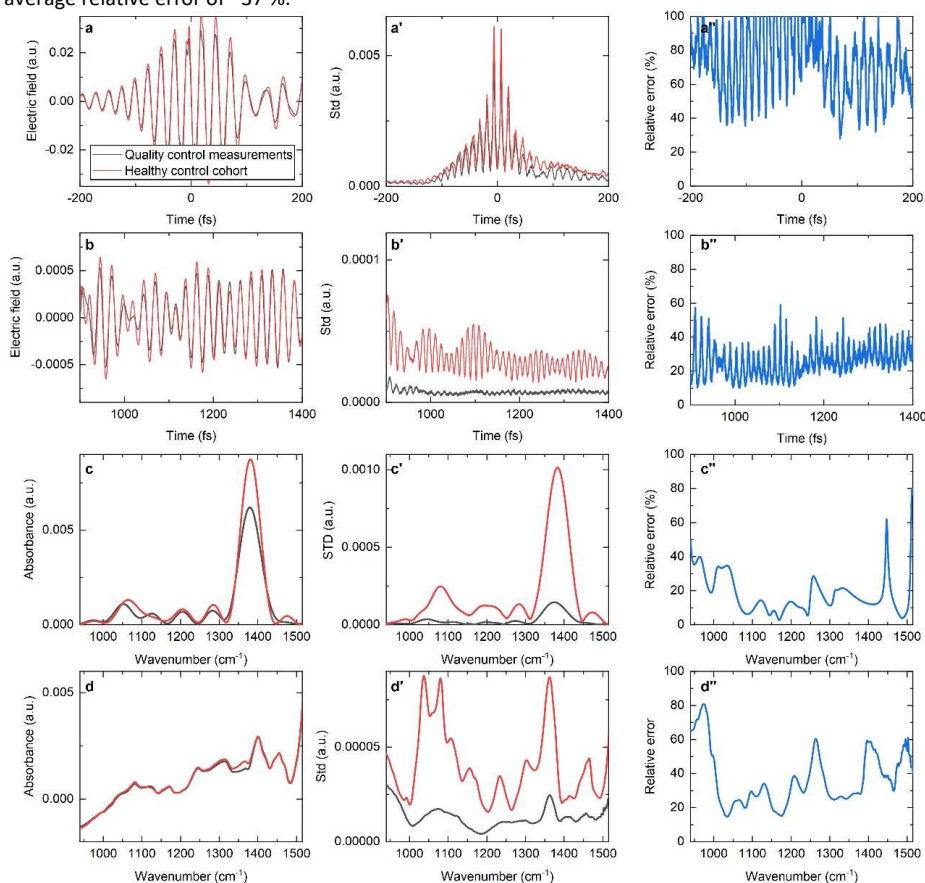
Cancer cohort	AUC (930 – 3050 $\text{cm}^{-1}$ )	AUC (940 – 1515 $\text{cm}^{-1}$ )
Lung cancer	0.84	0.83
Prostate cancer	0.61	0.55
Breast cancer	0.5	0.55

## Section 8: Measurement error vs. biological variability

We evaluated the reproducibility of infrared electric-field fingerprints obtained with FRS and infrared fingerprints acquired with FTIR, quantified their associated measurement errors and set both these into relation with the natural biological variability between healthy individuals. The measurement uncertainty was obtained by calculating the standard deviation of the repeated quality control measurements, either in the time-domain (Extended Data Fig. 6 a, b, grey lines) or in the frequency-domain (Extended Data Fig. 6 c, d, grey line). This was compared to the variability of infrared fingerprints of healthy control individuals (Extended Data Fig. 6, red lines). The relative error, defined as the ratio of the standard deviation of quality control measurements in relation to that of measurements from samples of healthy control individuals, is depicted in the right panels of Extended Data Fig. 6 as blue lines.

Time-domain analysis revealed, that during the time span of the excitation, the measured biological variability is dominated by the measurement error (Extended Data Fig. 6 a). For later times, the excitation noise is avoided, and the measurements error dropped well below the biological variability

(Extended Data Fig. 6 b). Spectral analysis of a sampling time window spanning from 900 fs – 1400 fs confirmed this finding (Extended Data Fig. 6 c). We obtained an average relative error of  $\sim 20\%$  within a wavenumber range from  $940\text{--}1515\text{ cm}^{-1}$ . Analysis of infrared fingerprints obtained with FTIR, yield an average relative error of  $\sim 37\%$ .



**Extended Data Fig. 6 | Measurement reproducibility** of time-domain traces (**a, b**) and time-filtered (between 900 – 1400 fs) spectra (**c**) obtained with FRS, as well as the reproducibility of infrared spectra obtained with FTIR (**d**). All evaluation was performed after pre-processing. The panels on the left depict the average time-trace or spectra of quality control measurements and healthy controls, respectively. The panels on the middle column show the evaluated standard deviation of these measurements and the panel on the right shows the relative error, defined as the ratio of the variability of quality control measurements and healthy controls.

# Conclusions and Outlook

## 4.1 Summary

In section 1.4 of this thesis, I formulated two main research questions, the first of which is whether "*fs-laser technology, offering broadband few-cycle infrared pulses, and the field-resolved detection thereof with electro-optic sampling (i.e. field-resolved spectroscopy), provide the means to improve sensitivity limits as compared to other emerging and established mid-infrared spectroscopy techniques*".

In chapter 2 we addressed this question and demonstrated that an improvement in sensitivity is indeed possible. Our first-generation field-resolved spectrometer already offers more than an order-of-magnitude better detection sensitivity than what is possible with state-of-the-art Fourier-transform infrared (FTIR) spectrometers. In addition, the intensity dynamic range is more than  $10^{10}$  for a measurement time of less than one minute, which is orders of magnitude higher than what is achieved with current FTIR spectrometers or quantum cascade lasers (QCL) based spectrometers. This previously unattained dynamic range was achieved by an electro-optic sampling (EOS) setup optimized for sensitivity [101] and by the fact that the measurement signal in field-resolved spectroscopy (FRS) scales linearly with the field, which effectively squares the dynamic range of the photodetector [108–110]. Besides, as discussed in detail in section 2.3, field-scaling of the measurement signal-to-noise ratio (SNR) is highly advantageous for the measurement of strongly absorbing samples, since the SNR decreases more slowly with an attenuation as it is the case for intensity-scaling. As a result, we were able to show high-quality measurements of intact living cells in water and direct measurements of living plant tissue for the first time.

The increased performance we demonstrated was made possible by a combination of technological developments and a conceptually new approach to linear (absorption) spectroscopy. The technological basis for this progress were broadband high-power fs-laser sources in the mid-infrared (MIR), which have been developed by our group [30]. Only with sufficient power it is possible to exceed detector noise, which limits the sensitivity of most FTIRs, and enter a regime where shot-noise-limited spectroscopy would be possible in principal [37].

In order to be able to benefit from the increased power of the laser source, we had to look at linear absorption spectroscopy from a different perspective. Instead of measuring the ‘missing’ part of the spectrum after interaction with the sample – a common approach in conventional absorption spectroscopy – we have studied the absorption process of impulsively-excited molecules in their natural time scale. Under the condition that the temporal duration of excitation is smaller than the lifetime of the coherent oscillations of the excited molecules,

a temporal separation between excitation and molecular response becomes possible. The molecular response, which under ideal conditions would be free from any background, can now be isolated from the excitation employing non-linear gating.

This allows the molecular information to be recorded under improved measurement conditions. Since the excitation pulse, which is orders of magnitude stronger than the molecular response, no longer reaches the detector, saturation of the latter can be avoided. That way, the full power of the excitation can be utilized. Furthermore, the molecular signal no longer needs to be detected against the background of a noisy excitation, which in turn drastically reduces the negative influence of source noise on the measurement. This approach simultaneously avoids two main obstacles (source noise and limited dynamic range of the photodetector) to further increase the sensitivity of detection. Another advantage of FRS is that it is power scalable. As a result, an increased source power can be converted directly into an improved detection sensitivity.

Furthermore, field-resolved spectroscopy can measure the electric field directly with extraordinary precision and therefore has access to the fundamental variable in the description of many systems. This in turn can facilitate the interpretation of measurement results in complex experiments. Due to all these advantages, but also due to possibilities of further technical development in the near future (see next section), we are convinced that field-resolved spectroscopy will establish itself in the field of mid-infrared spectroscopy and will improve existing applications as well as enable new applications, especially in the field of precision spectroscopy and in the investigation of highly absorbent samples.

For the second research question it was asked whether "***this newly developed field-resolved spectroscopy [can] be successfully applied to the analysis of human serum in order to detect diseases such as cancer***". An important sub-question is whether "(i) ***electric-field molecular fingerprints can be obtained reliably and robustly***", and whether "(ii) ***the increased sensitivity of field-resolved infrared spectroscopy [...] translates to higher efficiency in cancer detection***".

The answers to this particular set of questions are multi-faceted. For the sake of clarity and structure I will attempt to answer them step by step, starting with the first sub-question.

The measurements presented in section 3.2 were split into two measurement campaigns, which took place two years apart. In total more than 300 electric-field-resolved fingerprints were obtained and included into the analysis. Our evaluations revealed that data taken during the first measurement campaign can be directly compared to the data taken during the second one. In addition, we have demonstrated that a machine learning algorithm trained on the first set of measurements, can successfully perform binary classification between cases and controls from the second set of measurements. This demonstrates that our instrument as well as the developed pre-processing algorithm are operating precisely enough to obtain electric-field molecular fingerprints of human sera reliably and robustly.

Additionally, with the study presented in section 3.1, we have shown that by applying well-defined standard operating procedures for sample collection and handling, the analytical error in the measurements of infrared fingerprints can be kept significantly smaller than the natural biological variability of the latter. Furthermore, our results suggest that infrared fingerprints of individuals can be reliably acquired over time and potentially used to follow the health state of a person. Although these results were not obtained with FRS but FTIR, there is no reason for



us to believe that these findings are not transferable and to deduce that electric-field-resolved fingerprinting may be as well suited for health or possibly even treatment monitoring.

With regard to the second sub-question whether "***the increased sensitivity of field-resolved infrared spectroscopy (as compared to conventional Fourier-transform infrared spectroscopy) translates to higher efficiency in cancer detection***", first conclusions can be summarized as follows:

We obtained a higher binary classification efficiency for FRS than for FTIR for each of the three cancer entities investigated. However, in the case of lung cancer, the advantage of FRS was only slight and within the range of statistical uncertainty. For breast and prostate cancer, the improvements of classification were more significant. This is a first experimental indication that the improved molecular sensitivity of FRS is directly reflected in higher efficiency in the detection of medical phenotypes. However, it should be noted that these results were obtained with only a small cohort and should thus be confirmed in a larger cohort with more cases and controls. Furthermore, an additional validation should be performed on a leave-out test set that was only collected after the machine learning model was established.

During my doctoral studies, I realized, that the answer to the *per se* simple question whether "***field-resolved spectroscopy [can] be successfully applied [...] to detect diseases such as cancer***" depends strongly on how the question is formulated exactly, how it is framed and who asks it with which research or application interest in mind.

In this work we found that when machine learning is applied to the measured fingerprints, detection efficiencies for lung, breast, and prostate cancer in the range of 0.63-0.84 (area under the receiver operating characteristic curve) can be obtained. If we simply ask, whether we can detect cancer with *certainty*, the question would have to be answered negatively. Especially as it has to be considered that in the case of an indeterminate feasibility of detection, it is possible that molecular fingerprinting could actually measure an effect that is not clearly attributable to the presence of a tumour, although it correlates with it to a certain degree.

However, when it comes to assessing the applicability and success of the approach in actual clinical practice, the far more relevant formulation of the initial question is, whether (additional) analysis with FRS provides diagnostic advantages over established methods in a specific clinical setting. For example, the widely applied chest X-ray scan for lung cancer detection currently has a sensitivity and specificity of 78 % and 97 %, respectively [111]. For comparison, our first clinical study performed with FRS yielded a lower sensitivity and specificity of 67 % and 88 %, respectively (see section 3.2. It could therefore be concluded that FRS (at least at its current stage of development) is not clinically relevant.

However, in contrast to X-ray analysis (which involves a high radiation exposure), liquid biopsies are minimally invasive and inexpensive. In addition, blood samples are taken in suspicious cases anyway and therefore no additional blood sampling is required for an (additional) analysis with FRS. With regard to these facts, FRS (with the current detection efficiency) could already be considered as a relevant complementary tool for future clinical diagnostics today. Moreover, it still offers great potential for further improvement, given that the technology – in contrast to e.g. X-ray diagnostics – is still in its infancy.

However, several details still need to be investigated in further studies in order to be able to prove the possible applicability of our approach to a specific clinical setting. For one thing, the results obtained must be verified in a study reflecting a realistic clinical setting with a larger number of participants. For another, the cost, reliability, and user-friendliness of the method

must be examined in relation to the medical benefit. Although current proof-of-concept results provide strong foundation and promising prospects, all these and other questions have yet to be answered before a broad clinical application of FRS for cancer diagnostics can be considered.

Nevertheless, the results obtained so far are already promising. With an automated measurement with a duration of less than 5 minutes per sample, we were able to achieve high detection efficiencies comparable to conventional methods. Considering that electric-field molecular fingerprinting holds promise for further improvements in specificity by increasing the capacity to probe additional functional groups through extended spectral coverage and by enhancing detection sensitivity to capture low-abundant molecules, a further improvement of the phenotype detection efficiency can be expected. Furthermore, the general paradigm of electric-field molecular fingerprinting could potentially be extended as a complementary tool for systemic phenotyping of other relevant human physiologies.

## 4.2 Future of field-resolved spectroscopy

Although the first-generation FRS spectrometer has already achieved significant increases in sensitivity and specificity, a number of points with great potential for further substantial improvements in FRS technology can already be identified:

1. **Increasing the conversion efficiency of electro-optic sampling.** Only photons that are converted from the MIR to the near-infrared (NIR) can be detected and thus only those can contribute to the measured signal. Consequently, a high conversion efficiency is essential in order to realise the full potential of a MIR source. Furthermore, source-shot-noise-limited performance can only be achieved if all MIR photons are detected. This makes EOS with a sensitivity close to the single-photon level a prerequisite to push FRS to its fundamental limits.
2. **Increasing both power and spectral coverage of the employed MIR source.** A more intense excitation leads to a stronger molecular response, rendering the latter easier to detect. In principle, the source power can be increased until the damage threshold of the sample is reached. The broader the spectral coverage, the more types of chemical bonds can be probed simultaneously. This implies that a greater variety of molecular species can be investigated, but it also makes it easier to distinguish between the spectral signatures of different molecules (i.e. increased specificity).
3. **Minimization of the MIR background of the excitation and of molecular signals that are of no spectroscopic interest (e.g. water vapour).** This allows the informative molecular signal to be detected more directly and with less interferences.
4. **Minimize the residual fluctuations of the excitation to reduce the fluctuations in the molecular response.** This is essential, if a weak molecular signal is to be detected against the background of a strong one, since the stronger signal's fluctuations could mask the weaker signal. This is the case, for example, when low abundant constituents are to be measured in the presence of highly abundant constituents, as it is typically the case in blood serum or plasma.
5. **Recording of an excitation-independent molecular signal.** A problem that occurs when only the molecular response is recorded, is that this response depends not only on the molecular composition of the sample, but also on the excitation itself. Consequently, results from one measurement campaign might not be directly comparable to those of another, making large-scale studies challenging. A common approach to avoid this is calculating the transfer function of the sample. However, this requires a recording of the entire time trace including the noisy excitation, which may reduce the spectroscopic quality of the transfer function to a degree worse than that of the time-filtered molecular response. Therefore, either methods for noise reduction (4.) or sophisticated data processing for standardization of the molecular response are required.
6. **Reduce the complexity, costs, and footprint of the device.** These are prerequisites for making the FRS technology available to a wider public and further applications.

For most of these aspects, approaches for implementation are already emerging.

Many of the upcoming improvements will be largely based on shifting the central wavelength of the laser used for MIR generation and electro-optic sampling from 1  $\mu\text{m}$  to 2  $\mu\text{m}$ . The conversion of 2- $\mu\text{m}$  light to MIR wavelengths and vice versa is more efficient than using 1- $\mu\text{m}$  light due to the improved phase matching conditions of the available non-linear crystals. This makes few-cycle 2- $\mu\text{m}$  pulses excellent drivers for efficient and broadband mid-infrared generation (2.). First implementations demonstrated watt-scale power levels with a spectrum covering almost the entire MIR fingerprint range [112, 113].

Apart from the fact that FRS would be sensitive to a larger number of molecules, an increased spectral coverage also implies that shorter pulse durations are supported. Thus, the impulsive excitation can be compressed to an even shorter time window. If this is combined with measures to reduce the molecular background from water vapour (e.g. by improving the vacuum), the actual molecular signal can be detected over a longer time window without any disturbing MIR background (3.).

At the same time, 2- $\mu\text{m}$  gate pulses can improve the detection efficiency by more than one order of magnitude (1.). The 1- $\mu\text{m}$  system that was used for the results presented in this thesis achieved a conversion efficiency from the MIR to the NIR of 1 % in the narrowband and quantum-efficiency-optimised setting. First results with a 2- $\mu\text{m}$  EOS show that conversion efficiencies of 25 % over an extended spectral coverage can be obtained [114].

Additionally, in order for FRS to be widely and routinely used in applications, more practical considerations, such as user-friendliness as well as cost and space requirements of the spectrometer, have to be considered (6.). This is another area in which the 2- $\mu\text{m}$  technology based on Cr:ZnS/ZnSe oscillators offers great potential. First of all, Cr:ZnS/ZnSe crystals have a broad emission spectrum enabling few-cycle-pulses at watt-levels directly from the oscillator [115]. In addition, Cr:ZnS/ZnSe crystals can be effectively pumped using small semi-conductor diodes [116]. This enables a very compact oscillator design. Finally, the required optical components are relatively inexpensive compared to other available 2- $\mu\text{m}$  based system. Due to these properties, Cr:ZnS/ZnSe is already referred to as the "*Ti:Sapphire of the mid-infrared*" [116].

Current diode-pumped mode-locked Cr:ZnS/ZnSe oscillators achieve power levels up to 1 W and pulse durations of 45 fs [116]. This is not yet sufficient for the efficient generation and sampling of MIR pulses. Consequently, an amplifier and additional pulse compression are still required. Nevertheless, both footprint and complexity can already be reduced significantly as compared to the first-generation FRS spectrometer based on Yb:Yag thin-disc oscillators. If the development of Cr:ZnS/ZnSe is progressing as fast as it has been the case for the Ti:Sa technology, we can hope for significant improvements in terms of user-friendliness, cost, and space requirements in the very near future.

Another important aspect that still has a lot of potential for significant improvements is the way the sampling of the time domain signal is realized. In the current implementation the gate pulse with respect to the MIR pulse train is delayed by a mechanical stage. This has two disadvantages. Firstly, spectral acquisition takes milliseconds to seconds. As a result, fast events cannot be recorded. Secondly, most noise sources are more intense on slow time scales. These noise sources can be avoided, if the spectral acquisition is sufficiently fast (4.). In addition, a reference and sample trace could be measured quasi-instantaneously and therefore simultaneously. This would allow the sample transfer function to be obtained without additional noise, potentially providing a completely device-independent measurement result (5.).

Therefore, FRS would highly benefit from the implantation of established fast scan approaches such as dual-comb spectroscopy [36], asynchronous optical sampling [117], or fast mechanical delay lines [118]. Apart from the ability to make real-time measurements and the reduction of noise, a two-oscillator scan would allow the recording of very long-time traces (1 over the repetition rate of the oscillator to be precise), which is necessary to record the absorption lines of gases without artefacts.

But possible improvements concerning hardware are not the only areas where there is potential for significant advances. Specialized data processing for FTIR spectra has matured over decades. It is therefore not unlikely that new specialized data processing approaches will also have to be developed for the electric-field traces before their information content can be completely extracted (see also next section). In addition, approaches for the standardization of electric-field-resolved molecular fingerprints (EMFs) are necessary to enable the comparability of results between different devices and measurement campaigns (5.). Although first steps in this direction have already been investigated in this thesis (see section 3.2), further development of this standardization is certainly necessary.

When combining the above-mentioned improvements, novel applications of FRS can be envisioned. For example, in response to our *Nature* publication, Andreas Barth published a commentary article in which he suggested that with a further increase in sensitivity it would be possible to study individual molecules in liquids [119]. Apart from this, fast-scan approaches will permit the recording of electric-field molecular fingerprints on microsecond-timescales. This creates the basis for new applications studying irreversible events, such as non-reversible chemical reactions. Another promising approach is combining FRS with flow-cytometry in order to enable label-free classification of millions of cells within mere minutes. Furthermore, the nonlinear gating, which is employed in FRS, can be used not only in time but also in space. In THz time-domain spectroscopy it has already been demonstrated that EOS enables resolving structures that are below the conventional diffraction limit [120]. Bringing this concept to the MIR could pave the way towards label-free super-resolution spectro-microscopy of biological materials.

These ideas and suggestions only scratch the surface of what might be possible to achieve with this new technology and approach. Griffith's notion, that "*the number of applications [...] is limited only by the imagination of the user*" [4] rings truer than ever.

### 4.3 Future of electric-field-resolved fingerprinting

In this thesis, I outlined the first application of electric-field-resolved fingerprinting: The analysis of human serum for cancer detection. But before discussing future developments in this direction in more detail, I would like to point out the fact that the potential of electric-field-resolved fingerprinting is by no means limited to this specific application. Quite the contrary. As it has been the case for conventional infrared fingerprinting with FTIR spectrometers, the basic concepts and principles that we developed for the analysis of serum samples for cancer detection can be transferred to investigate a wide range of different biological specimen as well as further bio-medical questions. As a consequence, it is to be expected that not only disease detection, but also any other future application of electric-field-resolved fingerprinting will benefit from the anticipated technological advances of the underlying technology (see also section 4.2). The same holds true for advances in data handling, processing, and a deeper understanding of the obtained fingerprints.

Increasing the sensitivity of FRS means that the same experiment can be performed within a shorter measurement time and/or that weak molecular signals can be recorded more robustly, which facilitates the detection of low abundant molecular species in complex substances such as serum. This is important since many of the biomarkers already used in disease detection [121] are routinely found in blood serum at concentration levels well below our current detection limit. An increased spectral coverage allows additional information to be obtained. The more chemical bonds of different molecules are excited, the more clearly their characteristic signals can be distinguished from other molecular species. Thus, an increased instrument sensitivity and spectral coverage theoretically enables detection of a wider range of molecules in blood serum. This means that more molecules can contribute to the measured fingerprint, which in turn increases the probability that they contain cancer-related information and could therefore contribute to a better efficiency of cancer detection.

An important point here is the question of how this disease-relevant information can be extracted as completely as possible from the measured EMF. Data evaluation schemes and algorithms, adapted and optimized for FRS, could significantly increase the information yield. Our experiments have already shown that by time-filtering of the EMFs and including the phase information of the electric field, an improved molecular sensitivity and an increased efficiency of cancer detection can be achieved compared to the mere inclusion of intensity information. However, conventional absorption spectroscopy data evaluation principles do not facilitate that. This leads to another question regarding the information content of the EMFs: Does the direct measurement of the electric field emitted by the molecular vibrations allow access to information that is qualitatively different from the information encoded in infrared fingerprints of conventional infrared absorption spectroscopy? And if so, how can this information be extracted and used, for example, to increase the specificity of molecular detection?

Besides obtaining a deeper understanding of the nature of EMFs, extracting relevant information from EMFs and pushing the limits of the FRS technology itself, one also has to bear in mind the challenges that arise when applying the approach to a real-world setting. In the context of electric-field-resolved fingerprinting for disease detection, this means that the approach does not only have to work in a lab environment, but the technology has to robustly function at the clinics. Many of these challenges also apply to FTIR fingerprinting and have

already been discussed in section 1.3.3.

One of the major remaining challenges for the application of electric-field molecular fingerprinting is that EMFs have to become instrument- and user-independent and therefore only contain sample-related information. This is a prerequisite for large-scale applications, as measurements of these will be taken on different days, by different users with different instruments. We have done a first step in this direction by applying standardization procedures to the pulses (see section 3.2 for details). So far, this method could only be tested on EMFS obtained with a single FRS device, and no comparison could be made between EMFs obtained with other instruments. It is to be expected that a combination of further instrument development (e.g. reduction of measurement noise) on the one hand, and advanced standardization on the other hand, will be needed to isolate the pure molecular signal, which will thus be independent of both measurement instrument and user.

Even if all the developments described above could be achieved, the capacity of electric-field-resolved fingerprinting to pick up disease-specific signals from serum samples may ultimately still not be sensitive and specific enough to enable disease detection in a clinical setting. It might turn out that due to overlap of broad absorption features from various molecules, only the information of highly abundant molecules can be effectively assessed. As a consequence, FRS might only be able to contribute to disease detection in a way that is insufficient for translation into clinical diagnostics.

In this case, a promising route would be to enhance the specificity by chemical (pre-)fractionation in order to decode information from a wider range of molecules. Instead of analysing the whole sample in one single measurement, the sample can be split into several (chemical) fractions. This approach facilitates the detection of individual constituents as the individual fractions are of lower molecular complexity. This concept has been very successfully pursued by the proteomics community using mass spectrometry. Often, before the samples are measured by actual mass spectrometry, liquid chromatography is applied to split up the different chemical components. These are then measured fraction by fraction with a time delay. In this way more than 5000 different proteins of a serum or plasma sample can be identified [122].

In comparison to mass spectrometry, which usually focuses on the analysis of a selected type of molecules (e.g. proteins), FRS has the advantage that it could potentially pick up molecule-specific signals from all molecular species. In addition, FRS is sensitive to conformational changes of proteins, which are known to be indicative of e.g. Alzheimer's disease. Consequently, if liquid chromatography is successfully combined with FRS technology, not only a wide range of proteins (including their conformational changes), but also carbohydrates, lipids, and other blood constituents could potentially be analysed in a single measurement. The fact that liquid chromatography can be combined with infrared spectroscopy has already been shown by first proof-of-principle experiments with FTIR and QCL spectrometers [123, 124]. However, these applications have so far suffered from strong water absorption and limited sensitivity. Here, FRS could provide a promising new avenue to be followed given its increased sensitivity and specificity.

I would like to end this thesis with a vision. As mentioned in the previous section, it might be possible to achieve single-molecule-sensitivity in liquids by sufficient advancements in the sensitivity of FRS. When combining this assumption with the idea of a very advanced, high-throughput chemical pre-separation, FRS could potentially be able to identify and quantify

every single type of molecule contained in a (liquid) sample. Decoding the composition of complex biological samples down to every individual molecule of different chemical makeup would not only facilitate cancer detection, it would also give an unparalleled understanding of biological processes, which could be utilized in a variety of applications that are not yet foreseeable.



# References

- [1] G. Ma and H. C. Allen, *Handbook of Spectroscopy*, edited by G. Gauglitz and T. Vo-Dinh (Wiley, Aug. 2003), [10.1002/3527602305](https://doi.org/10.1002/3527602305).
- [2] J. Fraunhofer, “Bestimmung des Brechungs- und des Farbenzerstreungs-Vermögens verschiedener Glasarten, in Bezug auf die Vervollkommnung achromatischer Fernröhre”, *Annalen der Physik* **56**, 264–313 (1817) [10.1002/andp.18170560706](https://doi.org/10.1002/andp.18170560706).
- [3] R. E. Blankenship, *Molecular Mechanisms of Photosynthesis, 2nd Edition* (John Wiley & Sons, 2014), p. 312.
- [4] P. R. Griffiths and J. A. De Haseth, *Fourier Transform Infrared Spectrometry*, Vol. 171 (John Wiley & Sons, 2007).
- [5] N. Colthup, L. Daly, and S. Wiberley, *Introduction to Infrared and Raman Spectroscopy*, Third Edit (Elsevier, 1990).
- [6] J. Popp and T. G. Mayerhöfer, *Micro-Raman Spectroscopy*, edited by J. Popp and T. Mayerhöfer (De Gruyter, Feb. 2020), [10.1515/9783110515312](https://doi.org/10.1515/9783110515312).
- [7] M. Diem, P. R. Griffiths, and J. M. Chalmers, *Vibrational spectroscopy for medical diagnosis*, Vol. 40 (Wiley Chichester, 2008).
- [8] P. Lasch and J. Kneipp, *Biomedical vibrational spectroscopy* (Wiley-Interscience, 2008), pp. 318–319.
- [9] A. Barth and P. I. Haris, *Biological and biomedical infrared spectroscopy*, Vol. 2 (IOS press, 2009).
- [10] A. Barth and C. Zscherp, “What vibrations tell about proteins”, *Quarterly Reviews of Biophysics* **35**, 369–430 (2002) [10.1017/S0033583502003815](https://doi.org/10.1017/S0033583502003815).
- [11] M. J. Baker et al., “Using Fourier transform IR spectroscopy to analyze biological materials.”, *Nature protocols* **9**, 1771–91 (2014) [10.1038/nprot.2014.110](https://doi.org/10.1038/nprot.2014.110).
- [12] L. Mariey, J. Signolle, C. Amiel, and J. Travert, “Discrimination, classification, identification of microorganisms using FTIR spectroscopy and chemometrics”, *Vibrational Spectroscopy* **26**, 151–159 (2001) [10.1016/S0924-2031\(01\)00113-8](https://doi.org/10.1016/S0924-2031(01)00113-8).
- [13] F. L. Martin, J. G. Kelly, V. Llabjani, P. L. Martin-Hirsch, I. I. Patel, J. Trevisan, N. J. Fullwood, and M. J. Walsh, “Distinguishing cell types or populations based on the computational analysis of their infrared spectra”, *Nature Protocols* **5**, 1748–1760 (2010) [10.1038/nprot.2010.133](https://doi.org/10.1038/nprot.2010.133).
- [14] K. Eberhardt, C. Beleites, S. Marthandan, C. Matthäus, S. Diekmann, and J. Popp, “Raman and Infrared Spectroscopy Distinguishing Replicative Senescent from Proliferating Primary Human Fibroblast Cells by Detecting Spectral Differences Mainly Due to Biomolecular Alterations”, *Analytical Chemistry* **89**, 2937–2947 (2017) [10.1021/acs.analchem.6b04264](https://doi.org/10.1021/acs.analchem.6b04264).
- [15] Z. Movasaghi, S. Rehman, and D. I. ur Rehman, “Fourier Transform Infrared (FTIR) Spectroscopy of Biological Tissues”, *Applied Spectroscopy Reviews* **43**, 134–179 (2008) [10.1080/05704920701829043](https://doi.org/10.1080/05704920701829043).

- [16] C. Hughes and M. J. Baker, “Can mid-infrared biomedical spectroscopy of cells, fluids and tissue aid improvements in cancer survival? A patient paradigm”, *Analyst* **141**, 467–475 (2016) [10.1039/c5an01858g](https://doi.org/10.1039/c5an01858g).
- [17] A. Sala, D. J. Anderson, P. M. Brennan, H. J. Butler, J. M. Cameron, M. D. Jenkinson, C. Rinaldi, A. G. Theakstone, and M. J. Baker, “Biofluid diagnostics by FTIR spectroscopy: A platform technology for cancer detection”, *Cancer Letters* **477**, 122–130 (2020) [10.1016/j.canlet.2020.02.020](https://doi.org/10.1016/j.canlet.2020.02.020).
- [18] D. J. Anderson, R. G. Anderson, S. J. Moug, and M. J. Baker, “Liquid biopsy for cancer diagnosis using vibrational spectroscopy: systematic review”, *BJS Open* **4**, 554–562 (2020) [10.1002/bjs5.50289](https://doi.org/10.1002/bjs5.50289).
- [19] A. Barth and P. Haris, “Infrared spectroscopy - Past and present”, in *Advances in biomedical spectroscopy*, Vol. 2 (Jan. 2009), pp. 1–52, [10.3233/978-1-60750-045-2-1](https://doi.org/10.3233/978-1-60750-045-2-1).
- [20] H. A. Laitinen, “Editorial. The Seven Ages of an Analytical Method”, *Analytical Chemistry* **45**, 2305 (1973) [10.1021/ac60336a600](https://doi.org/10.1021/ac60336a600).
- [21] P. R. Griffiths, “Interferometry in the Seventies”, *Analytical Chemistry* **46**, 645A–654A (1974) [10.1021/ac60343a756](https://doi.org/10.1021/ac60343a756).
- [22] A. Rogalski, *Infrared detectors* (CRC press, 2010).
- [23] P. Kwee, B. Willke, and K. Danzmann, “New concepts and results in laser power stabilization”, *Applied Physics B* **102**, 515–522 (2011) [10.1007/s00340-011-4399-1](https://doi.org/10.1007/s00340-011-4399-1).
- [24] J. Faist, F. Capasso, D. L. Sivco, C. Sirtori, A. L. Hutchinson, and A. Y. Cho, “Quantum Cascade Laser”, *Science* **264**, 553–556 (1994) [10.1126/science.264.5158.553](https://doi.org/10.1126/science.264.5158.553).
- [25] J. Haas and B. Mizaikoff, “Advances in Mid-Infrared Spectroscopy for Chemical Analysis”, *Annual Review of Analytical Chemistry* **9**, 45–68 (2016) [10.1146/annurev-anchem-071015-041507](https://doi.org/10.1146/annurev-anchem-071015-041507).
- [26] K. Haase, N. Kröger-Lui, A. Pucci, A. Schönhals, and W. Petrich, “Advancements in quantum cascade laser-based infrared microscopy of aqueous media”, *Faraday Discussions* **187**, 119–134 (2016) [10.1039/c5fd00177c](https://doi.org/10.1039/c5fd00177c).
- [27] G. Villares, A. Hugé, S. Blaser, and J. Faist, “Dual-comb spectroscopy based on quantum-cascade-laser frequency combs.”, *Nature communications* **5**, 5192 (2014) [10.1038/ncomms6192](https://doi.org/10.1038/ncomms6192).
- [28] A. Schwaighofer, M. Montemurro, S. Freitag, C. Kristament, M. J. Culzoni, and B. Lendl, “Beyond Fourier Transform Infrared Spectroscopy: External Cavity Quantum Cascade Laser-Based Mid-infrared Transmission Spectroscopy of Proteins in the Amide I and Amide II Region”, *Analytical Chemistry* **90**, 7072–7079 (2018) [10.1021/acs.analchem.8b01632](https://doi.org/10.1021/acs.analchem.8b01632).
- [29] A. Schwaighofer, M. Brandstetter, and B. Lendl, “Quantum cascade lasers (QCLs) in biomedical spectroscopy”, *Chem. Soc. Rev.* **46**, 5903–5924 (2017) [10.1039/C7CS00403F](https://doi.org/10.1039/C7CS00403F).
- [30] I. Pupeza et al., “High-power sub-two-cycle mid-infrared pulses at 100 MHz repetition rate”, *Nature Photonics* **9**, 1–5 (2015) [10.1038/nphoton.2015.179](https://doi.org/10.1038/nphoton.2015.179).
- [31] C. Gaida et al., “Watt-scale super-octave mid-infrared intrapulse difference frequency generation”, *Light: Science & Applications* **7**, 94 (2018) [10.1038/s41377-018-0099-5](https://doi.org/10.1038/s41377-018-0099-5).

- [32] M. Seidel et al., “Multi-watt, multi-octave, mid-infrared femtosecond source”, *Science Advances* **4**, eaaq1526 (2018) [10.1126/sciadv.aaq1526](https://doi.org/10.1126/sciadv.aaq1526).
- [33] T. P. Butler et al., “Watt-scale 50-MHz source of single-cycle waveform-stable pulses in the molecular fingerprint region”, *Optics Letters* **44**, 1730 (2019) [10.1364/OL.44.001730](https://doi.org/10.1364/OL.44.001730).
- [34] F. Tittel, D. Richter, and A. Fried, “Mid-infrared laser applications in spectroscopy”, *Solid-State Mid-Infrared Laser Sources* **516**, 445–516 (2003) [10.1007/3-540-36491-9\\_11](https://doi.org/10.1007/3-540-36491-9_11).
- [35] J. Hodgkinson and R. P. Tatam, “Optical gas sensing: a review”, *Measurement Science and Technology* **24**, 012004 (2013) [10.1088/0957-0233/24/1/012004](https://doi.org/10.1088/0957-0233/24/1/012004).
- [36] I. Coddington, N. Newbury, and W. Swann, “Dual-comb spectroscopy”, *Optica* **3**, 414 (2016) [10.1364/OPTICA.3.000414](https://doi.org/10.1364/OPTICA.3.000414).
- [37] N. R. Newbury, I. Coddington, and W. Swann, “Sensitivity of coherent dual-comb spectroscopy”, *Optics Express* **18**, 7929 (2010) [10.1364/OE.18.007929](https://doi.org/10.1364/OE.18.007929).
- [38] T. Ideguchi, A. Poisson, G. Guelachvili, N. Picqué, and T. W. Hänsch, “Adaptive real-time dual-comb spectroscopy”, *Nature Communications* **5**, 3375 (2014) [10.1038/ncomms4375](https://doi.org/10.1038/ncomms4375).
- [39] M. Huber, M. Trubetskov, S. A. Hussain, W. Schweinberger, C. Hofer, and I. Pupeza, “Optimum Sample Thickness for Trace Analyte Detection with Field-Resolved Infrared Spectroscopy”, *Analytical Chemistry* **92**, 7508–7514 (2020) [10.1021/acs.analchem.9b05744](https://doi.org/10.1021/acs.analchem.9b05744).
- [40] I. Pupeza et al., “Field-resolved infrared spectroscopy of biological systems”, *Nature* **577**, 52–59 (2020) [10.1038/s41586-019-1850-7](https://doi.org/10.1038/s41586-019-1850-7).
- [41] M. Brandstetter, L. Volgger, A. Genner, C. Jungbauer, and B. Lendl, “Direct determination of glucose, lactate and triglycerides in blood serum by a tunable quantum cascade laser-based mid-IR sensor”, *Applied Physics B* **110**, 233–239 (2013) [10.1007/s00340-012-5080-z](https://doi.org/10.1007/s00340-012-5080-z).
- [42] P. Tidemand-Lichtenberg, J. S. Dam, H. V. Andersen, L. Høgstedt, and C. Pedersen, “Mid-infrared upconversion spectroscopy”, *Journal of the Optical Society of America B* **33**, D28 (2016) [10.1364/JOSAB.33.000D28](https://doi.org/10.1364/JOSAB.33.000D28).
- [43] J. S. Dam, P. Tidemand-Lichtenberg, and C. Pedersen, “Room-temperature mid-infrared single-photon spectral imaging”, *Nature Photonics* **6**, 788–793 (2012) [10.1038/nphoton.2012.231](https://doi.org/10.1038/nphoton.2012.231).
- [44] P. C. Hobbs, “Ultrasensitive laser measurements without tears.”, *Applied optics* **36**, 903–920 (1997) [10.1364/AO.36.000903](https://doi.org/10.1364/AO.36.000903).
- [45] M. Huber, W. Schweinberger, F. Stutzki, J. Limpert, I. Pupeza, and O. Pronin, “Active intensity noise suppression for a broadband mid-infrared laser source”, *Optics Express* **25**, 22499 (2017) [10.1364/OE.25.022499](https://doi.org/10.1364/OE.25.022499).
- [46] J. Li, B. Yu, W. Zhao, and W. Chen, “A Review of Signal Enhancement and Noise Reduction Techniques for Tunable Diode Laser Absorption Spectroscopy”, *Applied Spectroscopy Reviews* **49**, 666–691 (2014) [10.1080/05704928.2014.903376](https://doi.org/10.1080/05704928.2014.903376).
- [47] K. Wörle, F. Seichter, A. Wilk, C. Armacost, T. Day, M. Godejohann, U. Wachter, J. Vogt, P. Radermacher, and B. Mizaikoff, “Breath analysis with broadly tunable quantum cascade lasers”, *Analytical Chemistry* **85**, 2697–2702 (2013) [10.1021/ac3030703](https://doi.org/10.1021/ac3030703).

- [48] S. Türker-Kaya and C. Huck, “A Review of Mid-Infrared and Near-Infrared Imaging: Principles, Concepts and Applications in Plant Tissue Analysis”, *Molecules* **22**, 168 (2017) [10.3390/molecules22010168](https://doi.org/10.3390/molecules22010168).
- [49] M. De Marchi, V. Toffanin, M. Cassandro, and M. Penasa, “Invited review: Mid-infrared spectroscopy as phenotyping tool for milk traits”, *Journal of Dairy Science* **97**, 1171–1186 (2014) [10.3168/jds.2013-6799](https://doi.org/10.3168/jds.2013-6799).
- [50] D. A. Scott, D. E. Renaud, S. Krishnasamy, P. Meriç, N. Buduneli, Ş. Çetinkalp, and K.-Z. Liu, “Diabetes-related molecular signatures in infrared spectra of human saliva”, *Diabetology & Metabolic Syndrome* **2**, 48 (2010) [10.1186/1758-5996-2-48](https://doi.org/10.1186/1758-5996-2-48).
- [51] H. J. Butler, P. M. Brennan, J. M. Cameron, D. Finlayson, M. G. Hegarty, M. D. Jenkinson, D. S. Palmer, B. R. Smith, and M. J. Baker, “Development of high-throughput ATR-FTIR technology for rapid triage of brain cancer”, *Nature Communications* **10**, 4501 (2019) [10.1038/s41467-019-12527-5](https://doi.org/10.1038/s41467-019-12527-5).
- [52] M. Brandstetter, T. Sumalowitsch, A. Genner, A. E. Posch, C. Herwig, A. Drolz, V. Fuhrmann, T. Perkmann, and B. Lendl, “Reagent-free monitoring of multiple clinically relevant parameters in human blood plasma using a mid-infrared quantum cascade laser based sensor system”, *Analyst* **138**, 4022–4028 (2013) [10.1039/c3an00300k](https://doi.org/10.1039/c3an00300k).
- [53] S. Roy, D. Perez-Guaita, D. W. Andrew, J. S. Richards, D. McNaughton, P. Heraud, and B. R. Wood, “Simultaneous ATR-FTIR Based Determination of Malaria Parasitemia, Glucose and Urea in Whole Blood Dried onto a Glass Slide”, *Analytical Chemistry* **89**, 5238–5245 (2017) [10.1021/acs.analchem.6b04578](https://doi.org/10.1021/acs.analchem.6b04578).
- [54] R. Lu, W.-W. Li, B. Mizaikoff, A. Katzir, Y. Raichlin, G.-P. Sheng, and H.-Q. Yu, “High-sensitivity infrared attenuated total reflectance sensors for in situ multicomponent detection of volatile organic compounds in water”, *Nature Protocols* **11**, 377–386 (2016) [10.1038/nprot.2016.013](https://doi.org/10.1038/nprot.2016.013).
- [55] B. Mizaikoff, “Waveguide-enhanced mid-infrared chem/bio sensors”, *Chem. Soc. Rev.* **42**, 8683–8699 (2013) [10.1039/c3cs60173k](https://doi.org/10.1039/c3cs60173k).
- [56] E. Mitri, a. Pozzato, G. Coceano, D. Cojoc, L. Vaccari, M. Tormen, and G. Greci, “Highly IR-transparent microfluidic chip with surface-modified BaF<sub>2</sub> optical windows for Infrared Microspectroscopy of living cells”, *Microelectronic Engineering* **107**, 6–9 (2013) [10.1016/j.mee.2013.02.068](https://doi.org/10.1016/j.mee.2013.02.068).
- [57] H. J. Byrne, F. Bonnier, J. McIntyre, and D. R. Parachalil, “Quantitative analysis of human blood serum using vibrational spectroscopy”, *Clinical Spectroscopy* **2**, 100004 (2020) [10.1016/j.clispe.2020.100004](https://doi.org/10.1016/j.clispe.2020.100004).
- [58] K. Isensee, N. Kröger-Lui, and W. Petrich, *Biomedical applications of mid-infrared quantum cascade lasers-a review*, 2018, [10.1039/c8an01306c](https://doi.org/10.1039/c8an01306c).
- [59] D. Perez-Guaita, S. Garrigues, M. De la, and Guardia, “Infrared-based quantification of clinical parameters”, *TrAC Trends in Analytical Chemistry* **62**, 93–105 (2014) [10.1016/j.trac.2014.06.012](https://doi.org/10.1016/j.trac.2014.06.012).
- [60] P. E. Geyer, L. M. Holdt, D. Teupser, and M. Mann, “Revisiting biomarker discovery by plasma proteomics”, *Molecular Systems Biology* **13**, 942 (2017) [10.15252/msb.20156297](https://doi.org/10.15252/msb.20156297).



- [61] M. Sieger and B. Mizaikoff, “*Toward On-Chip Mid-Infrared Sensors*”, *Analytical Chemistry* **88**, 5562–5573 (2016) [10.1021/acs.analchem.5b04143](https://doi.org/10.1021/acs.analchem.5b04143).
- [62] A. Nabers, J. Ollesch, J. Schartner, C. Kötting, J. Genius, U. Haußmann, H. Klafki, J. Wiltfang, and K. Gerwert, “*An infrared sensor analysing label-free the secondary structure of the Abeta peptide in presence of complex fluids*”, *Journal of Biophotonics* **9**, 224–234 (2016) [10.1002/jbio.201400145](https://doi.org/10.1002/jbio.201400145).
- [63] A. Nabers, J. Ollesch, J. Schartner, C. Kötting, J. Genius, H. Hafermann, H. Klafki, K. Gerwert, and J. Wiltfang, “*Amyloid- $\beta$ -Secondary Structure Distribution in Cerebrospinal Fluid and Blood Measured by an Immuno-Infrared-Sensor: A Biomarker Candidate for Alzheimer’s Disease*”, *Analytical Chemistry* **88**, 2755–2762 (2016) [10.1021/acs.analchem.5b04286](https://doi.org/10.1021/acs.analchem.5b04286).
- [64] A. Nabers et al., “*Amyloid blood biomarker detects Alzheimer’s disease*”, *EMBO Molecular Medicine* **10**, 1–11 (2018) [10.15252/emmm.201708763](https://doi.org/10.15252/emmm.201708763).
- [65] C. Krafft, K. Wilhelm, A. Eremin, S. Nestel, N. von Bubnoff, W. Schultze-Seemann, J. Popp, and I. Nazarenko, “*A specific spectral signature of serum and plasma-derived extracellular vesicles for cancer screening*”, *Nanomedicine: Nanotechnology, Biology and Medicine* **13**, 835–841 (2017) [10.1016/j.nano.2016.11.016](https://doi.org/10.1016/j.nano.2016.11.016).
- [66] P. E. Geyer et al., “*Plasma Proteome Profiling to detect and avoid sample-related biases in biomarker studies*”, *EMBO Molecular Medicine* **11**, 1–12 (2019) [10.15252/emmm.201910427](https://doi.org/10.15252/emmm.201910427).
- [67] A. C. Uzozie and R. Aebersold, “*Advancing translational research and precision medicine with targeted proteomics*”, *Journal of Proteomics* **189**, 1–10 (2018) [10.1016/j.jprot.2018.02.021](https://doi.org/10.1016/j.jprot.2018.02.021).
- [68] J. Xia, D. I. Broadhurst, M. Wilson, and D. S. Wishart, “*Translational biomarker discovery in clinical metabolomics: An introductory tutorial*”, *Metabolomics* **9**, 280–299 (2013) [10.1007/s11306-012-0482-9](https://doi.org/10.1007/s11306-012-0482-9).
- [69] B. Roig, M. Rodríguez-Balada, S. Samino, E. W. Lam, S. Guaita-Esteruelas, A. R. Gomes, X. Correig, J. Borràs, O. Yanes, and J. Gumà, “*Metabolomics reveals novel blood plasma biomarkers associated to the BRCA1-mutated phenotype of human breast cancer*”, *Scientific Reports* **7**, 17831 (2017) [10.1038/s41598-017-17897-8](https://doi.org/10.1038/s41598-017-17897-8).
- [70] X. Han, J. Wang, and Y. Sun, “*Circulating Tumor DNA as Biomarkers for Cancer Detection*”, *Genomics, Proteomics & Bioinformatics* **15**, 59–72 (2017) [10.1016/j.gpb.2016.12.004](https://doi.org/10.1016/j.gpb.2016.12.004).
- [71] H. Schwarzenbach, D. S. B. Hoon, and K. Pantel, “*Cell-free nucleic acids as biomarkers in cancer patients*”, *Nature Reviews Cancer* **11**, 426–437 (2011) [10.1038/nrc3066](https://doi.org/10.1038/nrc3066).
- [72] C. Abbosh et al., “*Phylogenetic ctDNA analysis depicts early-stage lung cancer evolution*”, *Nature* **545**, 446–451 (2017) [10.1038/nature22364](https://doi.org/10.1038/nature22364).
- [73] K. J. Karczewski and M. P. Snyder, “*Integrative omics for health and disease*”, *Nature Reviews Genetics* **19**, 299–310 (2018) [10.1038/nrg.2018.4](https://doi.org/10.1038/nrg.2018.4).
- [74] E. R. Malone, M. Oliva, P. J. B. Sabatini, T. L. Stockley, and L. L. Siu, “*Molecular profiling for precision cancer therapies*”, *Genome Medicine* **12**, 8 (2020) [10.1186/s13073-019-0703-1](https://doi.org/10.1186/s13073-019-0703-1).

- [75] Y. Hasin, M. Seldin, and A. Lusic, “*Multi-omics approaches to disease*”, *Genome Biology* **18**, 83 (2017) [10.1186/s13059-017-1215-1](https://doi.org/10.1186/s13059-017-1215-1).
- [76] B. C. Yoo, K.-H. Kim, S. M. Woo, and J. K. Myung, “*Clinical multi-omics strategies for the effective cancer management*”, *Journal of Proteomics* **188**, 97–106 (2018) [10.1016/j.jprot.2017.08.010](https://doi.org/10.1016/j.jprot.2017.08.010).
- [77] M. Paraskevaïdi et al., “*Differential diagnosis of Alzheimer’s disease using spectrochemical analysis of blood*”, *Proceedings of the National Academy of Sciences* **114**, E7929–E7938 (2017) [10.1073/pnas.1701517114](https://doi.org/10.1073/pnas.1701517114).
- [78] J. Ollesch, D. Theegarten, M. Altmayer, K. Darwiche, T. Hager, G. Stamatis, and K. Gerwert, “*An infrared spectroscopic blood test for non-small cell lung carcinoma and subtyping into pulmonary squamous cell carcinoma or adenocarcinoma*”, *Biomedical Spectroscopy and Imaging* **5**, edited by K. Gerwert, 129–144 (2016) [10.3233/BSI-160144](https://doi.org/10.3233/BSI-160144).
- [79] M. Jackson, M. G. Sowa, and H. H. Mantsch, “*Infrared spectroscopy: A new frontier in medicine*”, *Biophysical Chemistry* **68**, 109–125 (1997) [10.1016/S0301-4622\(97\)80555-8](https://doi.org/10.1016/S0301-4622(97)80555-8).
- [80] G. H. Werner, J. Frueh, F. Keller, H. Greger, R. L. Somorjai, B. Dolenko, M. Otto, and D. Boecker, “*Mid-infrared spectroscopy as a tool for disease pattern recognition from human blood*”, in *Proc.spie*, Vol. 3257, edited by H. H. Mantsch and M. Jackson (Apr. 1998), pp. 35–41, [10.1117/12.306090](https://doi.org/10.1117/12.306090).
- [81] W. Petrich et al., “*Disease pattern recognition in infrared spectra of human sera with diabetes mellitus as an example.*”, *Applied optics* **39**, 3372–3379 (2000) [10.1364/AO.39.003372](https://doi.org/10.1364/AO.39.003372).
- [82] P. Lasch, M. Beekes, H. Fabian, and D. Naumann, *Antemortem Identification of Transmissible Spongiform Encephalopathy (TSE) from Serum by Mid-infrared Spectroscopy*, Dec. 2001, [doi:10.1002/0470027320.s8925](https://doi.org/10.1002/0470027320.s8925).
- [83] J. Schmitt, M. Beekes, A. Brauer, T. Udelhoven, P. Lasch, and D. Naumann, “*Identification of Scrapie Infection from Blood Serum by Fourier Transform Infrared Spectroscopy*”, *Analytical Chemistry* **74**, 3865–3868 (2002) [10.1021/ac015688s](https://doi.org/10.1021/ac015688s).
- [84] P. Lasch, J. Schmitt, M. Beekes, T. Udelhoven, M. Eiden, H. Fabian, W. Petrich, and D. Naumann, “*Antemortem Identification of Bovine Spongiform Encephalopathy from Serum Using Infrared Spectroscopy*”, *Analytical Chemistry* **75**, 6673–6678 (2003) [10.1021/ac030259a](https://doi.org/10.1021/ac030259a).
- [85] H. Fabian, P. Lasch, and D. Naumann, “*Analysis of biofluids in aqueous environment based on mid-infrared spectroscopy.*”, *Journal of biomedical optics* **10**, 031103 (2005) [10.1117/1.1917844](https://doi.org/10.1117/1.1917844).
- [86] D. I. Ellis and R. Goodacre, “*Metabolic fingerprinting in disease diagnosis: biomedical applications of infrared and Raman spectroscopy*”, *The Analyst* **131**, 875 (2006) [10.1039/b602376m](https://doi.org/10.1039/b602376m).
- [87] M. J. Baker, S. R. Hussain, L. Lovergne, V. Untereiner, C. Hughes, R. A. Lukaszewski, G. Thiéfin, and G. D. Sockalingum, “*Developing and understanding biofluid vibrational spectroscopy: a critical review*”, *Chemical Society Reviews* **45**, 1803–1818 (2016) [10.1039/C5CS00585J](https://doi.org/10.1039/C5CS00585J).

- [88] A. L. Mitchell, K. B. Gajjar, G. Theophilou, F. L. Martin, and P. L. Martin-Hirsch, “Vibrational spectroscopy of biofluids for disease screening or diagnosis: Translation from the laboratory to a clinical setting”, *Journal of Biophotonics* **7**, 153–165 (2014) [10.1002/jbio.201400018](https://doi.org/10.1002/jbio.201400018).
- [89] J. Trevisan, P. P. Angelov, P. L. Carmichael, A. D. Scott, and F. L. Martin, “Extracting biological information with computational analysis of Fourier-transform infrared (FTIR) biospectroscopy datasets: current practices to future perspectives”, *The Analyst* **137**, 3202 (2012) [10.1039/c2an16300d](https://doi.org/10.1039/c2an16300d).
- [90] J. Ollesch, S. L. Drees, H. M. Heise, T. Behrens, T. Brüning, and K. Gerwert, “FTIR spectroscopy of biofluids revisited: an automated approach to spectral biomarker identification”, *The Analyst* **138**, 4092 (2013) [10.1039/c3an00337j](https://doi.org/10.1039/c3an00337j).
- [91] M. Diem, “Comments on recent reports on infrared spectral detection of disease markers in blood components”, *Journal of Biophotonics* **11**, e201800064 (2018) [10.1002/jbio.201800064](https://doi.org/10.1002/jbio.201800064).
- [92] J. Čuklina, P. G. A. Pedrioli, and R. Aebersold, “Review of Batch Effects Prevention, Diagnostics, and Correction Approaches”, in *Briefings in bioinformatics*, Vol. 2051 (Rutgers University Press, Oct. 2020), pp. 373–387, [10.1007/978-1-4939-9744-2\\_16](https://doi.org/10.1007/978-1-4939-9744-2_16).
- [93] C. L. M. Morais et al., “Standardization of complex biologically derived spectrochemical datasets”, *Nature Protocols* **14**, 1546–1577 (2019) [10.1038/s41596-019-0150-x](https://doi.org/10.1038/s41596-019-0150-x).
- [94] L. Lovergne, P. Bouzy, V. Untereiner, R. Garnotel, M. J. Baker, G. Thiéfin, and G. D. Sockalingum, “Biofluid infrared spectro-diagnostics: pre-analytical considerations for clinical applications”, *Faraday Discuss.* **187**, 521–537 (2016) [10.1039/C5FD00184F](https://doi.org/10.1039/C5FD00184F).
- [95] M. J. Baker et al., “Clinical applications of infrared and Raman spectroscopy: State of play and future challenges”, *Analyst* **143**, 1735–1757 (2018) [10.1039/c7an01871a](https://doi.org/10.1039/c7an01871a).
- [96] J. R. Hands et al., “Brain tumour differentiation: rapid stratified serum diagnostics via attenuated total reflection Fourier-transform infrared spectroscopy”, *Journal of Neuro-Oncology* **127**, 463–472 (2016) [10.1007/s11060-016-2060-x](https://doi.org/10.1007/s11060-016-2060-x).
- [97] E. Gray et al., “Health economic evaluation of a serum-based blood test for brain tumour diagnosis: Exploration of two clinical scenarios”, *BMJ Open* **8** (2018) [10.1136/bmjopen-2017-017593](https://doi.org/10.1136/bmjopen-2017-017593).
- [98] M. Huber, K. V. Kepesidis, L. Voronina, M. Božić, M. Trubetskov, N. Harbeck, F. Krausz, and M. Žigman, “Stability of person-specific blood-based infrared molecular fingerprints opens up prospects for health monitoring”, *Nature Communications* **12**, 1511 (2021) [10.1038/s41467-021-21668-5](https://doi.org/10.1038/s41467-021-21668-5).
- [99] J. Kim and Y. Song, “Ultralow-noise mode-locked fiber lasers and frequency combs: principles, status, and applications”, *Advances in Optics and Photonics* **8**, 465 (2016) [10.1364/AOP.8.000465](https://doi.org/10.1364/AOP.8.000465).
- [100] T. Amotchkina, M. Trubetskov, S. A. Hussain, D. Hahner, D. Gerz, M. Huber, W. Schweinberger, I. Pupeza, F. Krausz, and V. Pervak, “Broadband dispersive Ge/YbF<sub>3</sub> mirrors for mid-infrared spectral range”, *Optics Letters* **44**, 5210 (2019) [10.1364/OL.44.005210](https://doi.org/10.1364/OL.44.005210).

- [101] C. Hofer, S. A. Hussain, W. Schweinberger, M. Huber, T. P. Butler, D. Gerz, N. Karpowicz, F. Krausz, and I. Pupeza, “Quantum-Efficiency and Bandwidth Optimized Electro-Optic Sampling”, in 2019 conference on lasers and electro-optics europe & european quantum electronics conference (cleo/europe-eqec) (June 2019), pp. 1–1, [10.1109/CLEOE-EQEC.2019.8873083](https://doi.org/10.1109/CLEOE-EQEC.2019.8873083).
- [102] W. Schweinberger, L. Vamos, J. Xu, S. A. Hussain, C. Baune, S. Rode, and I. Pupeza, “Interferometric delay tracking for low-noise Mach-Zehnder-type scanning measurements”, *Optics Express* **27**, 4789 (2019) [10.1364/OE.27.004789](https://doi.org/10.1364/OE.27.004789).
- [103] M. Trubetskov, M. Huber, M. Zigman, F. Krausz, and I. Pupeza, “On the Role of the Phase in Field-Resolved Spectroscopy of Molecular Vibrations”, in 2019 conference on lasers and electro-optics europe & european quantum electronics conference (cleo/europe-eqec) (June 2019), pp. 1–1, [10.1109/CLEOE-EQEC.2019.8871838](https://doi.org/10.1109/CLEOE-EQEC.2019.8871838).
- [104] P. S. Jensen and J. Bak, “Near-Infrared Transmission Spectroscopy of Aqueous Solutions: Influence of Optical Pathlength on Signal-To-Noise Ratio”, *Applied Spectroscopy* **56**, 1600–1606 (2002) [10.1366/000370202321115878](https://doi.org/10.1366/000370202321115878).
- [105] H. L. Mark and P. R. Griffiths, “Analysis of Noise in Fourier Transform Infrared Spectra”, *Applied Spectroscopy* **56**, 633–639 (2002) [10.1366/0003702021955196](https://doi.org/10.1366/0003702021955196).
- [106] A. M. Hawkrigde and D. C. Muddiman, “Mass Spectrometry–Based Biomarker Discovery: Toward a Global Proteome Index of Individuality”, *Annual Review of Analytical Chemistry* **2**, 265–277 (2009) [10.1146/annurev.anchem.1.031207.112942](https://doi.org/10.1146/annurev.anchem.1.031207.112942).
- [107] V. Kulasingam and E. P. Diamandis, “Strategies for discovering novel cancer biomarkers through utilization of emerging technologies”, *Nature Clinical Practice Oncology* **5**, 588–599 (2008) [10.1038/ncponc1187](https://doi.org/10.1038/ncponc1187).
- [108] J. J. Snyder, “Wide dynamic range optical power measurement using coherent heterodyne radiometry”, *Applied Optics* **27**, 4465 (1988) [10.1364/AO.27.004465](https://doi.org/10.1364/AO.27.004465).
- [109] G. Jarry, L. Poupinet, J. Watson, and T. Lepine, “Extinction measurements in diffusing mammalian tissue with heterodyne detection and a titanium:sapphire laser”, *Applied Optics* **34**, 2045 (1995) [10.1364/AO.34.002045](https://doi.org/10.1364/AO.34.002045).
- [110] S. Liukaityte, M. Lequime, M. Zerrad, T. Begou, and C. Amra, “Broadband spectral transmittance measurements of complex thin-film filters with optical densities of up to 12”, *Optics Letters* **40**, 3225 (2015) [10.1364/OL.40.003225](https://doi.org/10.1364/OL.40.003225).
- [111] Y. Toyoda, T. Nakayama, Y. Kusunoki, H. Iso, and T. Suzuki, “Sensitivity and specificity of lung cancer screening using chest low-dose computed tomography”, *British Journal of Cancer* **98**, 1602–1607 (2008) [10.1038/sj.bjc.6604351](https://doi.org/10.1038/sj.bjc.6604351).
- [112] T. P. Butler et al., “Multi-octave spanning, Watt-level ultrafast mid-infrared source”, *Journal of Physics: Photonics* **1**, 044006 (2019) [10.1088/2515-7647/ab4976](https://doi.org/10.1088/2515-7647/ab4976).
- [113] Q. Wang, J. Zhang, A. Kessel, N. Nagl, V. Pervak, O. Pronin, and K. F. Mak, “Broadband mid-infrared coverage (2–17  $\mu\text{m}$ ) with few-cycle pulses via cascaded parametric processes”, *Optics Letters* **44**, 2566 (2019) [10.1364/OL.44.002566](https://doi.org/10.1364/OL.44.002566).
- [114] C. Hofer et al., “Mid-infrared electric field sampling approaching single-photon sensitivity”, *Europhoton Conference 2020*, Paper Th-A1.1.



- [115] S. Vasilyev, I. Moskalev, M. Mirov, V. Smolski, S. Mirov, and V. Gapontsev, “Ultrafast middle-IR lasers and amplifiers based on polycrystalline Cr:ZnS and Cr:ZnSe”, *Optical Materials Express* **7**, 2636 (2017) [10.1364/OME.7.002636](https://doi.org/10.1364/OME.7.002636).
- [116] N. Nagl, S. Gröbmeyer, V. Pervak, F. Krausz, O. Pronin, and K. F. Mak, “Directly diode-pumped, Kerr-lens mode-locked, few-cycle Cr:ZnSe oscillator”, *Optics Express* **27**, 24445 (2019) [10.1364/OE.27.024445](https://doi.org/10.1364/OE.27.024445).
- [117] A. Bartels, R. Cerna, C. Kistner, A. Thoma, F. Hudert, C. Janke, and T. Dekorsy, “Ultrafast time-domain spectroscopy based on high-speed asynchronous optical sampling”, *Review of Scientific Instruments* **78**, 035107 (2007) [10.1063/1.2714048](https://doi.org/10.1063/1.2714048).
- [118] B. Süß, F. Ringleb, and J. Heberle, “New ultrarapid-scanning interferometer for FT-IR spectroscopy with microsecond time-resolution”, *Review of Scientific Instruments* **87** (2016) [10.1063/1.4953658](https://doi.org/10.1063/1.4953658).
- [119] A. Barth, “Infrared spectroscopy finally sees the light”, *Nature* **577**, 34–35 (2020) [10.1038/d41586-019-03866-w](https://doi.org/10.1038/d41586-019-03866-w).
- [120] F. Sanjuan, G. Gaborit, and J.-L. Coutaz, “Sub-wavelength terahertz imaging through optical rectification”, *Scientific Reports* **8**, 13492 (2018) [10.1038/s41598-018-31970-w](https://doi.org/10.1038/s41598-018-31970-w).
- [121] E. P. Diamandis, *Tumor markers: physiology, pathobiology, technology, and clinical applications* (Amer. Assoc. for Clinical Chemistry, 2002).
- [122] P. E. Geyer, N. A. Kulak, G. Pichler, L. M. Holdt, D. Teupser, and M. Mann, “Plasma Proteome Profiling to Assess Human Health and Disease”, *Cell Systems* **2**, 185–195 (2016) [10.1016/j.cels.2016.02.015](https://doi.org/10.1016/j.cels.2016.02.015).
- [123] J. Kuligowski, G. Quintás, S. Garrigues, B. Lendl, M. de la Guardia, and B. Lendl, “Recent advances in on-line liquid chromatography - infrared spectrometry (LC-IR)”, *TrAC - Trends in Analytical Chemistry* **29**, 544–552 (2010) [10.1016/j.trac.2010.03.004](https://doi.org/10.1016/j.trac.2010.03.004).
- [124] T. F. Beskers, M. Brandstetter, J. Kuligowski, G. Quintás, M. Wilhelm, and B. Lendl, “High performance liquid chromatography with mid-infrared detection based on a broadly tunable quantum cascade laser.”, *The Analyst* **139**, 2057–64 (2014) [10.1039/c3an01546g](https://doi.org/10.1039/c3an01546g).



# Danksagung

Die Realisierung eines so umfangreichen Projekts wie einer Doktorarbeit setzt immer auch die Unterstützung durch eine Vielzahl von Personen voraus. Daher möchte ich mich zu guter Letzt bei all den Menschen bedanken, die auf ganz unterschiedliche Art und Weise dazu beigetragen haben, meine Promotion erfolgreich abzuschließen.

An erster Stelle ist hier mein Doktorvater Ferenc Krausz zu nennen. Zu einem dafür, dass er die wissenschaftlichen und finanziellen Rahmenbedingungen geschaffen hat, die diese Arbeit überhaupt erst ermöglicht haben. Aber noch viel wichtiger, dass er unserer Gruppe und mir durch seine Visionen einen 'just cause' (wie er es gerne nennt) gegeben hat, der uns immer wieder daran erinnert hat, warum wir diese Forschung betreiben. Zum anderen will ich Ferenc für meine persönliche Betreuung danken. Obwohl er gleichzeitig an den verschiedensten Projekten arbeitet, hat er immer die Zeit gefunden, wichtige Forschungsfragen direkt und persönlich zu diskutieren, sich für das Projekt einzusetzen und sich für sein Gelingen zu engagieren. Zudem will ich Ferenc für seine Hartnäckigkeit und Fähigkeit zur Motivation danken. Obwohl es bei Zeiten auch anstrengend sein konnte, hat uns und mich dies immer wieder dazu angespornt, noch einen Schritt weiter zu sehen, weiter zu fragen und weiter zu denken. Insbesondere die in Abschnitt 2.2 präsentierten und Anfang 2020 in *Nature* veröffentlichten Ergebnisse wären sonst wohl nicht auf diesem Niveau publiziert worden.

Besonderer Dank gebührt auch Joachim Puceza, der den technologischen Teil meiner Arbeit betreut hat und in Sachen Beharrlichkeit und Motivationsfähigkeit Ferenc in fast nichts nachsteht. Durch diesen Ansporn haben wir die Experimente solange durchgeführt, die theoretischen Überlegungen solange ausgearbeitet und an den Manuskripten unserer Veröffentlichungen solange gefeilt, bis alles 'perfekt' war. Auch aus diesem Grund konnten wir nicht nur gute, sondern exzellente Arbeiten abliefern. Außerdem will ich Joachim für unsere Gespräche über die Wissenschaft und den Wissenschaftsbetrieb an sich danken. Auch dadurch war es mir möglich, mich sowohl als Wissenschaftler weiterzuentwickeln, als auch eigene Pläne und Visionen für die Zukunft zu entwickeln.

Als nächstes möchte ich mich ganz herzlich bei Mihaela Žigman, meiner Teamleiterin und direkten Betreuerin, bedanken, die innerhalb von Ferenc' Arbeitsgruppe für den Bereich der praktischen Anwendung der Infrarotspektroskopie zur Krebsdiagnostik verantwortlich war und ist. Ich wurde kurz nach ihr Teil von Ferenc' Gruppe und somit begannen wir beide fast gleichzeitig mit der Arbeit an und der Etablierung dieser völlig neuen Forschungsrichtung für die Krausz-Gruppe. Dies gab mir die einmalige Gelegenheit, an der Entwicklung von den Anfängen bis hin zu ersten vielversprechenden Ergebnissen mitzuwirken. Anstatt in ein bestehendes Projekt einzutreten hatte ich die Möglichkeit in eine Vielzahl von Prozessen involviert zu sein, vom Aufbau der Arbeitsgruppe, über erste Laborerarbeiten in kleinster Runde bis hin zu immer komplexer werdendem Projektmanagement und der stetigen personellen Erweiterung des Teams. Michaela erlaubte mir auch als Doktorand bereits schnell Verantwortung für das Projekt und die Gruppe zu übernehmen. So wurde ich früh in wichtige Entscheidungsprozesse mit eingebunden und hatte so die Möglichkeit das Projekt aktiv mitzugestalten. Ihr freundlicher aber bestimmter Führungsstil schufen ein so produktives wie angenehmes Arbeitsklima, insbesondere wurden Anregungen und selbst Kritik immer offen an- und ernstgenommen. Umgekehrt bereicherte sie meine eigene Arbeit regelmäßig durch hilfreiche Ideen, konstruktive Vorschläge und zahlreiche Anregungen, ohne die meine Doktorarbeit nicht in der vorliegenden Form zustande gekommen

wäre.

Als nächstes möchte ich Alexander Apolonski und Manuel Pescher danken, die mich in den ersten Monaten meiner Promotionsphase betreut und mir geholfen haben, mich zu akklimatisieren und in der Gruppe anzukommen, in das Team aufgenommen zu werden und meine ersten eigenen Schritte als Doktorand zu gehen. Mein erstes Projekt durfte ich dann mit Oleg Pronin in Angriff nehmen. Ihm möchte ich an dieser Stelle für seine Unterstützung und Anleitung bei den 'noise-eater'-Experimenten danken.

Besonderer Dank gebührt auch all meinen Kollegen, mit deren Kenntnissen und Fähigkeiten ich die ersten feldaufgelösten Spektrometer realisieren durfte. Ein großer Dank gebührt Ali, der einen Großteil des Infrsamplers 1.2 aufgebaut hat, mit welchem die meisten Messungen dieser Doktorarbeit durchgeführt wurden. Vielen Dank auch an Christina, die als 'EOS-Expertin' geholfen hat, die Empfindlichkeit der Detektion immer weiter zu steigern. Ein ganz besonderer Dank gebührt auch Wolfgang. Ich weiß nicht was er immer genau gemacht hat, aber mit Hilfe seiner 'magic fingers' war er immer wieder in der Lage auch das letzte kleine bisschen Performance aus dem System heraus zu kitzeln. Zudem war er stets hilfsbereit und hat mir immer wieder geholfen, falls ich ein Problem mit dem Laser oder der dazugehörigen Spektrometer-Software nicht lösen konnte.

Vielen Dank auch an Kilian, Markus und Jinwei, die immer mit Rat und Tat zu Stelle waren, wenn es Probleme mit dem Oszillator oder der Verbreiterungsstufe gab. Danke an Tatjana und Vova, die uns auch immer dann kurzfristig mit Spiegeln versorgt haben, wenn es wieder einmal schneller als die üblichen Wochen 'Lieferzeit' gehen musste, um unsere Zeitpläne einhalten zu können.

Besonderen Dank möchte ich auch Michael Trubetskov aussprechen. Er war eine unglaubliche Hilfe bei der Auswertung der Daten, sowohl durch sein unglaubliches Wissen als auch durch seine hilfreichen Programme, durch die ich bei der Datenauswertung unfassbar viel Zeit gespart habe. Außerdem möchte ich ihm für seine mitunter fast unangenehm treffende Kritik an unserem Vorhaben danken, die uns immer wieder dazu angehalten hat, unser Vorgehen anzupassen, zu präzisieren und einfach sauber zu arbeiten.

Unser Projekt umfasste aber nicht nur den physikalisch-technischen Teil, sondern auch die praktische Anwendung der feldaufgelösten Spektroskopie. Hier möchte ich insbesondere Lucy danken, mit der ich mir nicht nur ein Büro geteilt habe, sondern mich auch auf freundschaftlicher und wissenschaftlicher Ebene super verstehe. Dadurch war es gleich doppelt erfreulich mit ihr zu arbeiten. Danke auch an Masa und Cristina für die tolle Zusammenarbeit und die gute Stimmung und tolle Arbeitsatmosphäre.

Danke an Daniel, Wolfgang, Lucy, Ali und Cristina mit denen ich die schier endlosen Serums- und Plasamessungen durchgeführt habe. Mit euch waren sogar die Nachtschichten einigermaßen erträglich.

Kosmos möchte ich für seine unkomplizierte Art und für seine Geduld bei der Auswertung der Daten danken. Selbst nachdem mir zum x-ten Mal etwas Neues eingefallen ist, was bei der Auswertung berücksichtigt werden müsste, hat er immer wieder von vorne angefangen. Speziellen Dank an dieser Stelle auch noch einmal für die Hilfe bei der Auswertung der Daten der Longitudinalstudie, wodurch das Manuskript noch einmal deutlich aufgewertet wurde.

Daniel Meyer möchte ich danken für das Management und die Handhabung der Proben, was uns enorm viel Arbeit abgenommen hat und dafür, dass er uns immer zuverlässig mit neuen Proben versorgt hat, egal zu welchen seltsamen Zeitpunkten wir meinten, neue zu brauchen.

Frank, der immer dafür gesorgt hat, dass der Laden läuft und uns, indem er den Großteil der Organisation des Tagesgeschäfts übernommen hat, dafür gesorgt hat, dass wir Doktoranden den Kopf für die Wissenschaft an sich frei haben konnten. Außerdem möchte ich ihm noch einmal speziell für seine Hilfe bei den Zell- und Pflanzenexperimenten danken.

Ich möchte auch dem klinischen Team und den an der klinischen Studie beteiligten Patienten und Freiwilligen danken, ohne die wir keine Proben zur Untersuchung gehabt hätten.

Vielen Dank auch an Ernst Fill, der uns durch seine langjährige Erfahrung immer wieder bis dato unbedachte Querbezüge vor Augen geführt hat und uns so diverse neue Denkansätze und Perspektiven eröffnet hat, wodurch wir unseren Horizont stets erweitern konnten.

An alle jetzigen und ehemaligen Kollegen ein herzliches Dankeschön für die tolle und bereichernde Zeit! Und natürlich auch die gemeinsamen Grill- und Schafkopfabende. Es war immer eine Freude, Teil dieses Teams zu sein, welches dieses freundschaftliche und inspirierende Arbeitsumfeld erst ermöglichte. Danke für die Unterstützung, wenn es gut lief und die Motivation, wenn es zäh wurde.

Danken möchte ich außerdem der IMPRS-APS Graduate School, durch die ich die Möglichkeit erhalten habe, mich regelmäßig mit Doktoranden und Professoren verschiedener Spezialgebiete auszutauschen und damit meinen Horizont zu erweitern und meinen Projekten eine neue Dynamik zu verleihen. Insbesondere die Tagungen auf Schloss Ringberg waren jedes Jahr aufs Neue eine persönliche und fachliche Bereicherung. Besonderer Dank gebührt hier Wolfgang Zinth als Vorsitzendem meines Thesis-Advisory-Committee, der mit seiner Expertise im Bereich der Kurzzeit-Infrarotspektroskopie und seiner langjährigen Erfahrung immer ein in jeder Hinsicht bereichernder Gesprächspartner war.

Besonderen Dank möchte ich an dieser Stelle Jürgen Popp für seine Zeit und seinen Aufwand aussprechen, der sich dazu bereit erklärt hat, als Zweitgutachter dieser Dissertation zu fungieren. Darüber hinaus möchte ich mich noch bei den Professoren Joachim Rädler, Armin Scrinzi, Hartmut Ruhl und Jan Lipfert bedanken, die sich bereit erklärt haben Teil meines Prüfungskomitees zu sein.

Danken möchte ich zu guter Letzt natürlich auch meiner Familie, die mich auf meinen akademischen Weg von Anfang an voll und ganz unterstützt hat. Zunächst meinen Eltern, die mir stets alle Freiheiten gelassen und jede meiner Entscheidungen mit vollster Unterstützung begleitet haben. Ganz besonders möchte ich meiner Frau Kristin danken. Dafür, dass sie mich immer unterstützt hat. Dafür, dass ich mich auf sie immer blind verlassen kann. Dafür, dass sie sich mit mir zusammen entschieden hat, während unserer beiden Promotionen eine Familie zu gründen und es mir trotzdem ermöglicht hat meine Promotion mehr oder weniger ungebremst zu Ende zu bringen. Zudem will ich meinem Sohn Kaspar danken, dessen Lachen mich jeden Tag wieder mit Freude erfüllt hat. Als letztes will ich noch meinem ungeborenen zweiten Kind danken, dass es sich mit der Geburt tatsächlich noch so viel Zeit gelassen hat, dass diese Arbeit noch vor seiner Geburt in den Druck gehen konnte.